Microstructural Development in High-Nitrogen Stainless Steels

John W. Simmons
B.S., Cal. Poly. St. Univ., SLO, 1982
M.S., Oregon Graduate Institute of Science & Technology, 1990

A dissertation submitted to the faculty of the
Oregon Graduate Institute of Science & Technology
in partial fulfillment of the
requirements for the degree
Doctor of Philosophy
in
Materials Science and Engineering

January 1993

The dissertation "Microstructural Development in High-Nitrogen Stainless Steels" by John W. Simmons has been examined and approved by the following Examination Committee:

David G. Atteridge, Thesis Advisor
Associate Professor

James C. Rawers, Thesis Co-Advisor
Adjunct Faculty Member

Paul Clayton
Professor

Jack H. Devletian
Professor

ACKNOWLEDGEMENTS

First of all, I would like to thank the U.S. Bureau of Mines, Albany Research Center, and particularly my supervisor, Dr. John Dunning, for providing financial support during the course of this research.

Special thanks are due to my research advisor, Dr. Dave Atteridge, for the time, patience, and attention that he devoted to me and my work during the four-plus years that I spent at OGI. I am grateful to my co-advisor, Dr. Jim Rawers from the Bureau of Mines, for devoting a large amount of his time to my research and for the friendship we developed. Thanks are also extended to the other members of my dissertation committee, Dr. Jack Devletian and Dr. Paul Clayton, for their time and effort in reviewing the manuscript.

Cooperation is an essential part of any successful research project and I would like to thank all of the students, staff, and faculty in the Materials Science and Engineering Department with whom I interacted during my tenure at OGI. I would like to give special thanks to Dan, Vivek, Rick, and Qinghua who make this world a much better place.

TABLE of CONTENTS

LIST of TABLES

LIST of FIGURES

ABSTRACT

Microstructural Development in High-Nitrogen Stainless Steels

John W. Simmons, PhD

Supervising Professor: David G. Atteridge

Replacing carbon in stainless steels with nitrogen has distinct advantages. Nitrogen is a stronger austenite stabilizer, more potent solid-solution strengthener, and has greater solubility than carbon. Recent advances in processing technologies have made it possible to produce alloys with nitrogen levels approaching 1 wt%. Successful use of these newly developed advanced materials in engineering applications requires a thorough understanding of their microstructural development and resulting mechanical properties. In this work, in-depth microstructural analysis and structure/property correlation studies were performed on thermomechanically processed high-nitrogen austenitic stainless steels.

In an Fe-20Cr-5Mn-5Ni-3Mo alloy containing 0.7 wt% N, all of the nitrogen was dissolved interstitially in the austenite by annealing at temperatures above 1100°C. However, precipitation of Cr-rich Cr_2N occurred sequentially at grain boundaries (GBs), by cellular decomposition, and finally, by transgranular precipitation during isothermal aging at 600-1075°C. Precipitation kinetics were most rapid at 900-950°C where GB nucleation occurred within 0.01 hour. Cold-working, prior to aging, increased GB, and most dramatically, transgranular precipitation kinetics. Cellular precipitation development, however, was retarded in deformed materials in favor of transgranular precipitation. The presence of GB and cellular

Cr_2N precipitates induced intergranular and transgranular embrittlement. Nitrogen-based alloys were also shown to be susceptible to sensitization (GB Cr-depletion) caused by the precipitation of Cr_2N. Prior deformation significantly increased the rate of sensitization development and induced transgranular Cr-depletion. Niobium additions resulted in the presence of insoluble transgranular Nb-rich nitrides (NbCrN) which significantly reduced the room temperature impact properties of annealed materials.

This work showed that although large amounts of interstitial nitrogen can be dissolved in austenite to increase strength levels, rapid precipitation of Cr_2N occurs during exposure at elevated temperatures. Their presence can adversely affect mechanical properties and leads to material sensitization which may cause alloy susceptibility to intergranular corrosion and/or intergranular stress-corrosion cracking. It was also demonstrated that nitride precipitation kinetics and morphologies can be altered/engineered through thermomechanical processing.

INTRODUCTION

Austenitic stainless steels (SSs), based primarily on the Fe-Cr-Ni ternary system and utilizing carbon as the primary strengthening agent (AISI 300 series), have been of major engineering importance for over 60 years.[1] These materials exhibit excellent corrosion resistance, ductility, and are non-magnetic. They are used in the nuclear, chemical, petroleum, and transportation industries. The primary disadvantage of carbon-alloyed austenitic SSs is their relatively low-strength.

Replacing carbon in SSs with nitrogen has certain advantages because nitrogen is a stronger austenite stabilizer, more potent solid-solution strengthener, and has greater solubility than carbon. In the last ten years, nitrogen alloying has received increased attention primarily because advances in nitrogen steel processing technologies have made it possible to produce materials with nitrogen contents approaching 1 wt%. An austenitic SS can be considered "high-nitrogen" if it contains more than 0.4 wt% nitrogen.[2]

The main driving force in the development of high-nitrogen austenitic SSs is the attainment of higher yield strengths (YSs) than can be achieved in materials alloyed with carbon. The effect of increasing nitrogen concentrations on the YS of austenitic SSs is shown in *Figure 1*. High-nitrogen steels have much higher YSs, as much as three to four times greater, than the AISI 300 series steels. These higher strength levels enable high-nitrogen austenitic SSs to be used in certain applications as replacement materials for more expensive nickel-base super-alloys.

Industrial applications for high-nitrogen austenitic SSs include the power-generating industry, ship building, railways, cryogenic processes, chemical equipment, pressure vessels, and the petroleum and nuclear industries.[3] A few of the specific applications where their use is either being applied or considered are: (1) Bolt

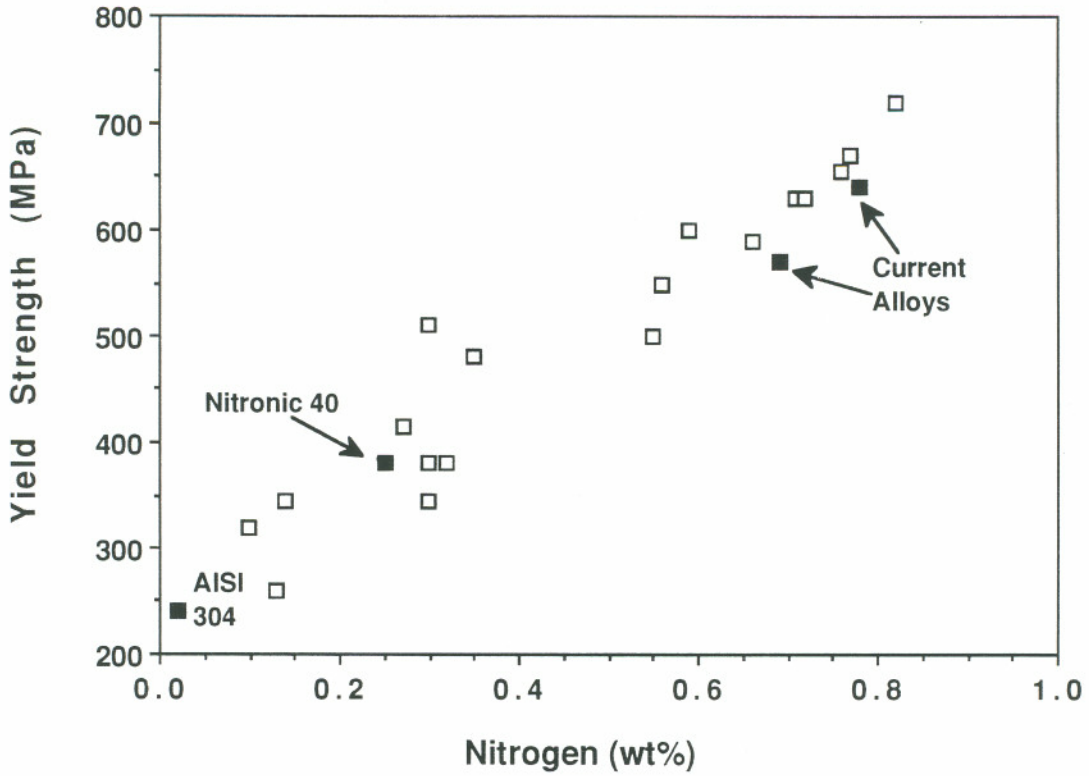

Figure 1. Effect of increasing nitrogen concentrations on yield strength in austenitic stainless steels of varying base compositions.

materials for high-strength and high-temperature applications in which YS values in excess of 900 MPa are required; (2) Power generator retaining rings which must have high YSs (>600 MPa), adequate ductility, high strain hardening potential, low magnetic permeability, and favorable stress-corrosion and pitting resistance;[4] and (3) Superconducting magnet housings which require structural alloys that can withstand the large magnetic forces of superconducting magnets, have low potential for martensite formation, high elastic moduli, low thermal and electrical conductivities, and excellent fracture toughness at cryogenic temperatures.[5,6]

High-nitrogen steels contain supersaturated nitrogen levels even though the solubility of nitrogen in austenite is as much as 10-100 times greater than that of carbon. Recent studies[7-12] have shown that high-nitrogen SSs are prone to the

precipitation of Cr-rich nitrides (Cr_2N), much the same as the 300 series SSs are susceptible to Cr-rich carbide precipitation ($Cr_{23}C_6$). It is well known that the 300 series SSs become sensitized when precipitation of Cr-rich carbides takes place during aging and causes Cr-depletion in the adjacent matrix. Sensitized materials are susceptible to intergranular corrosion (IGC) and intergranular stress corrosion cracking (IGSCC) in certain environments. Carbide precipitation also has a detrimental effect on the mechanical properties of the 300 series SSs.[13-19]

Successful use of high-nitrogen austenitic SSs in engineering applications can be achieved only after a thorough understanding of their microstructural formation and structure/property relationships are developed. Of special interest is austenite stability during thermal and deformation processing, and material susceptibility to nitride precipitation and sensitization development. The presence of nitrides may promote ductility losses and precipitation results in lower levels of interstitial nitrogen with corresponding reductions in YS. Microstructural development, austenite stability, and structure/property relationships in these newly developed advanced materials, containing high levels of nitrogen, are presently not well understood.

The objective of this research was to develop an understanding of microstructural development in high-nitrogen austenitic SSs during thermomechanical processing, with an emphasis on the following:

(1) Precipitate reaction kinetics and precipitate characterization including identification, morphology, and location.

(2) Sensitization susceptibility.

(3) Material response to deformation and its effects on precipitation and sensitization kinetics.

(4) The effect of microstructure on mechanical properties, determined through impact toughness testing.

BACKGROUND

MATERIAL PROCESSING

Until recently, the solubility of nitrogen in liquid iron was a limiting factor in the production of high-nitrogen steels. The solubility of nitrogen in pure liquid iron (1600°C) at atmospheric pressure is only 0.045 wt%.[20,21] If solubility in the melt is exceeded, then the excess nitrogen is simply evolved as nitrogen gas. Solubility in liquid iron-based alloys can be enhanced by increasing the pressure of nitrogen gas above the liquid metal and through the judicial choice of alloying additions.

Nitrogen Solubility in Liquid Metals

Nitrogen solubility in liquid iron alloys has been studied extensively by a number of researchers.[20-23] According to the work of Sieverts,[24] the solubility of a diatomic gas in a liquid metal (under constant temperature) is proportional to the square root of the partial pressure of the gas over the melt. The reaction depends upon the breakdown of the diatomic gas molecules to atomic species which can be absorbed into the melt. The solubility of nitrogen in liquid iron-base metals has been shown to follow Sieverts' law and can be described by the reaction given below:

$$\left(\frac{1}{2}N_2\right)_{gas} \rightleftharpoons N_{dissolved} \qquad [1]$$

The reaction equilibria is defined by:

$$\Delta G = -RT\ln K_{eq} \qquad [2]$$

where T is the temperature in Kelvin, R the gas constant, and K_{eq} the equilibrium constant for the reaction defined by the equation:

$$K_{eq} = \frac{a_N}{\sqrt{P_{N_2}}} = \frac{\%N f_N}{\sqrt{P_{N_2}}} \qquad [3]$$

where a_N is the chemical activity of nitrogen, P_N is the partial pressure of nitrogen gas, and f_N is the activity coefficient of nitrogen. The activity of gaseous nitrogen is taken to be equal to the square-root of its partial pressure.

The infinitely dilute solution of nitrogen in pure iron is taken as the standard state. This means that if the solubility of nitrogen in liquid iron follows Sieverts' law, f_N is equal to one and the solubility is proportional to the square root of the nitrogen pressure over the melt. In this case f_N is defined as:

$$\lim_{\%N \to 0} \frac{a_N}{\%N} = f_N = 1 \qquad [4]$$

The addition of alloying elements to pure liquid iron at constant temperature and pressure results in a change of nitrogen solubility and activity as compared to nitrogen solubility in the binary iron-nitrogen system, with f_N defined by:

$$f_N = \left[\frac{\%N\,(pure\,Fe)}{\%N\,(alloy)}\right]_{P_{N_2},T} \qquad [5]$$

Changes in the solubility of nitrogen with alloying additions are taken into account by activity coefficients which correlate the effect of additive elements (X_i) with the activity of nitrogen. Activity coefficients can be derived using the following relations:

$$\log f_N = \log f_N^N + \log f_N^{X_i} \qquad [6]$$

$$\log f_N = e_N^N \%N + e_N^{X_i} \%X_i + r_N^{X_i} \%X_i^2 + ... \qquad [7]$$

where the e's and r's are interaction parameters in the first and second order and define the effect of each alloying element (X_i) on the activity of nitrogen. The second-order interaction parameter corrects for cases in which a non-linear relationship exists between $\log f_N$ and the alloying element addition (wt%). This usually occurs at higher nitrogen concentrations (pressures). Equations [1] through [7] were obtained from the work of Pehlke and Elliott[20] and Satir-Kolorz and Feichtinger.[21]

Effect of Pressure and Alloy Additions

Relationships defined by equations [1] through [7] have been used, along with experimental results, to determine the effects of pressure and alloying additions on nitrogen solubility.[20-23,25-27] Satir-Kolorz and Feichtinger[21] have recently shown that the solubility of nitrogen in pure iron follows Sieverts' law for pressures up to at least 50 bar (~50 atm). The solubility of nitrogen in pure iron (1600°C) reaches about 0.28wt% at a pressure of 50 bars.

First-order interaction parameters, determined by Satir-Kolorz and Feichtinger[21] for a number of important alloying elements, are shown in *Table 1*. With reference to equation [7], a negative interaction parameter for a particular element means that the presence of the element increases the solubility of nitrogen in the melt. Elements with a positive interaction parameter decrease nitrogen solubility. Also listed in *Table 1* are equivalent factors based on the influence of chromium on nitrogen solubility, which is defined as unity. Chromium was used as a reference since it has a strong effect on nitrogen solubility and is the most important alloying element in austenitic high-nitrogen SSs.

Nitrogen solubility is enhanced by Ti, Zr, V, Nb, Cr, Mn, and Mo, listed in decreasing order of solubility enhancement. Elements that reduce nitrogen solubility include Ni, Al, Si, P, B, C, and N. These elements are listed in order, with Ni having the smallest, and N the greatest negative effect on its own solubility. Carbon

TABLE 1 - Interaction Parameters (e_N) and Cr-equivalent Factors (Cr_N)		
Element	e_N	Cr_N
Ti	-0.930	19.40
Zr	-0.630	13.13
V	-0.098	2.05
Nb	-0.050	1.05
Cr	-0.048	1.00
Mn	-0.024	0.50
Mo	-0.013	0.27
Ni	0.011	-0.22
Al	0.040	-0.85
Si	0.043	-0.90
P	0.048	-1.00
B	0.083	-1.73
C	0.118	-2.46
N	0.130	-2.70

also has a very strong negative influence on nitrogen solubility. The effect of C and N on nitrogen solubility has been attributed to strong repulsive forces between nitrogen atoms, and between nitrogen and carbon atoms.

Although nickel is an important austenitizing element in SSs, its negative influence on nitrogen solubility has lead to reductions in the nickel levels in most high-nitrogen alloys. Manganese, also an austenite stabilizer, is added to increase the solubility of nitrogen. Nitrogen is a strong austenite stabilizer and significantly reduces the amount of nickel required for this purpose.

At high Cr and N levels there is a strong deviation from Sieverts' law. As nitrogen concentrations increase, the distance between nitrogen atoms in the lattice

decreases, until eventually the interaction between nitrogen atoms negatively influences its own solubility. Sieverts' law is valid even to very high pressures for Fe-Ni alloys and for other element additions that don't enhance nitrogen solubility. This is because nitrogen concentrations are so low, at even very high pressures, that interaction between nitrogen atoms is not a factor.

It is interesting to note that many of the elements which have the greatest positive influence on nitrogen solubility, Ti, Zr, V, and Nb, are also strong nitride forming elements. Although these elements increase nitrogen solubility in liquid alloys, they also have strong tendencies to form nitrides. Since maximum nitrogen solid-solubility is generally of prime importance in austenitic alloys, their concentrations are usually kept low. Chromium, on the other hand, has a strong positive influence on nitrogen solubility, but has only moderate nitride forming tendencies. Manganese and molybdenum also increase nitrogen solubility and do not have strong tendencies to form nitrides. Thus, Cr, Mo, and Mn provide the best compromise between enhancement of nitrogen solubility in the liquid and tendency to form nitrides in the solid.

Elements with strong nitride forming tendencies do not always enhance nitrogen solubility in liquid iron alloys. For example, Al, Si, and B all have strong nitride forming tendencies but also decrease the solubility of nitrogen in iron alloys. It appears that more complex interactions, such as those between substitutional atoms and iron, also influence the effect that a particular element has on nitrogen solubility.

Feichtinger[28] noted that the position of an element in the periodic table, relative to iron, determines its effect on nitrogen solubility. All of the elements to the right of iron have been found to have a negative influence on nitrogen solubility, being rather strong for elements B, Si, C, and P. Feichtinger explained this phenomena on the basis of the atoms' ability to provide an electron exchange with iron atoms. He proposed that if an element delivers electrons to the outer shell of the iron atom, nitrogen solubility decreases because its interaction with the iron atom is adversely affected.

Processing Technologies

Increased gas pressure can be utilized to enhance nitrogen pick-up in solid materials. This technique has been used successfully in powder metallurgy applications. However, the kinetics of nitrogen pick-up during the gas-solid reaction are rather slow compared to direct alloying in liquid metal because they depend on gas permeability in the powder pack and nitrogen diffusion in the solid. Thus, the following discussion focuses on processing of liquid iron-based alloys, which is most viable for commercial production of high-nitrogen materials.

Enhanced nitrogen levels have been obtained by melting under high nitrogen pressures using the following methods: (1) pressurized induction furnace, (2) pressurized plasma furnace, (3) purging of nitrogen gas in a pressurized ladle configuration, (4) hot-isostatic-pressure (HIP) melting, and (5) pressurized electroslag remelting (PESR). Although there are a variety of processing methods and equipment, there are two basic mechanisms by which nitrogen is transferred to the melt. These are nitrogen pick-up via the gas phase and introduction of nitrided metals or compounds directly into the liquid slag or metal.

The first four techniques mentioned above rely on nitrogen pick-up at the gas/metal interface. Nitrogen absorption kinetics are time-dependent since they rely on the breakdown of the diatomic nitrogen gas to atomic nitrogen (gas/metal reaction) and nitrogen diffusion in the liquid. In these processes, important parameters controlling the kinetics of nitrogen pick-up are the surface area of the gas/metal interface, melt temperature, liquid convection, and pressure of nitrogen in the system. Due to slow reaction kinetics and melt convection problems materials produced by high-pressure induction, plasma, or HIP melting have been prone to nitrogen segregation. These techniques have therefore been limited to laboratory-scale ingots. The PESR technique does not suffer from these limitations and is currently being used in the commercial production of high-nitrogen steels.

In PESR, the nitrogen pressure above the melt merely serves to keep the desired amount of nitrogen in the molten metal. Nitrogen is added continuously during remelting in the form of granulated nitrogen additives (nitrides) to a consumable electrode base alloy produced by conventional means or by remelting composite electrodes comprised of a steel-tube outer jacket and a sintered or cast high-nitrogen core.[28-31] Continuous feeding of granulated high-nitrogen additives into the slag is the most cost effective method of nitrogen alloying and is the method primarily used. Possible nitrogen bearing additives are FeCrN (8-10 wt%N), CrN (4-10 wt%N), and SiN (25-30 wt%N). Silicon-nitride is generally preferred because it contains the highest nitrogen concentrations. To achieve the desired nitrogen levels would require using excessive volumes of the other possible additives which would produce high Cr levels in the alloys. A PESR unit capable of 20-ton ingots that uses a water cooled stationary copper mold, has a movable hood, and capable of 4.2 MPa over-pressure, is currently in operation.[29]

STRENGTHENING of STAINLESS STEELS

Solid-Solution-Strengthening

The effect of substitutional and interstitial alloying element additions on the YS of austenitic SSs is shown in *Figure 2*. Substitutional elements which stabilize the ferrite structure (W, Mo, V, Si, and Cr) have a small positive effect on strength while austenite stabilizing elements (Cu, Co, Mn, and Ni) have little, or, as in the case of nickel, a negative effect on YS. Interstitial elements (N, C, and B) increase the strength of austenitic materials much more than substitutional elements and nitrogen is more effective than any other element.[29]

A disadvantage of carbon-alloyed austenitic SSs is their low potential for grain size hardening.[32] In contrast, nitrogen has been found to have a significant effect on grain size hardening. The effect of grain size ($\bar{L}$) on the YS ($\sigma_{0.2\%}$) in nitrogen steels

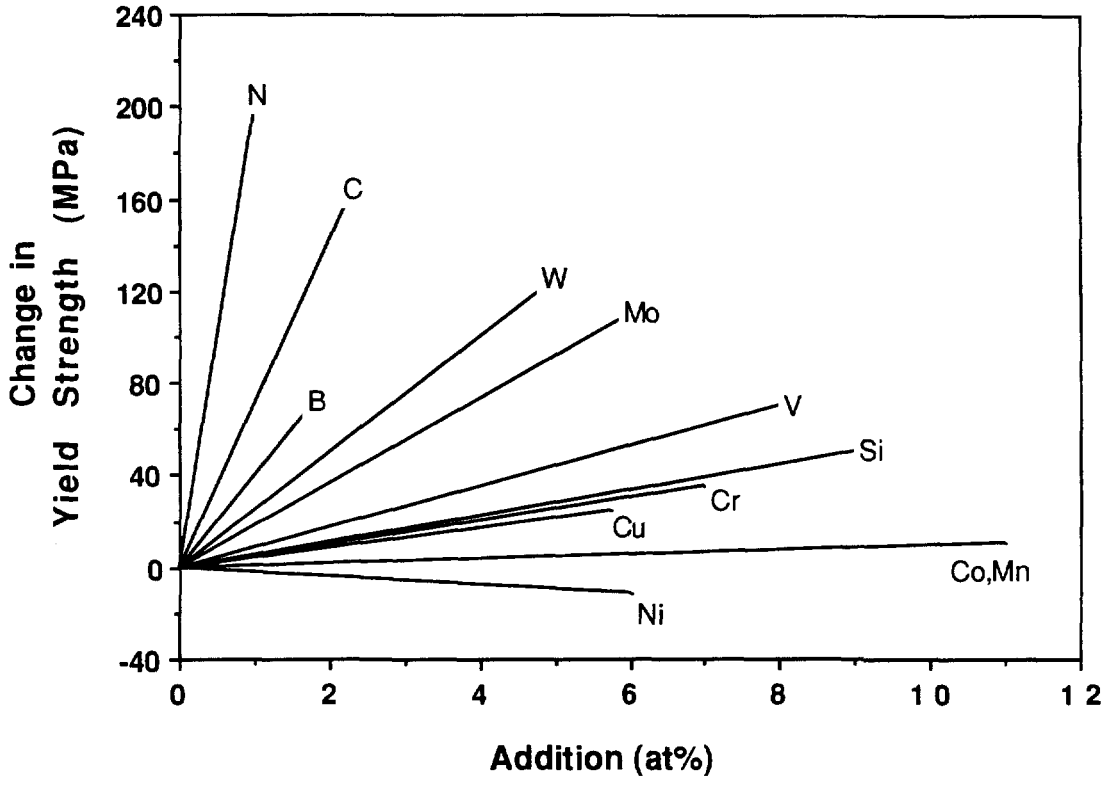

Figure 2. Change in yield strength of austenitic stainless steels due to alloying additions of individual elements.[29]

has been the focus of a number of investigations[32-38] that utilized the Hall-Petch relation:

$$\sigma_{0.2\%} = \sigma_r + \frac{K_y}{L^{1/2}} \qquad [8]$$

The second term on the right side of equation [8] is the contribution of the grain boundaries (GBs) to the YS which includes the constant, K_y, and σ_r is the YS for very large grain sizes.

Flow stresses of austenitic SSs have been shown to increase linearly with increasing nitrogen content (reference *Figure 1*).[32,33,36,38] Although increases in flow stress due to nitrogen solid-solution strengthening is dominant, grain size hardening

due to increasing nitrogen contents is also significant. For example, Werner et al.[32,8] found that reducing the grain size from 100 to 10 μm increases the YS by more than 100 MPa at room temperature in a steel with 0.6 wt% N. They reported that in a conventional austenitic SSs the increase would be at least 50% less, due to the small value of K_y. Simultaneously, solid solution hardening by the same amount of nitrogen was found to increase the YS by about 400 MPa.

Effect of Temperature on Yield Strength

The temperature dependency of flow stress in nitrogen alloyed austenitic SSs is considerably different than in materials alloyed with carbon, at temperatures both above and below room temperature.

Flow stresses in carbon-alloyed materials decrease steadily with increasing temperatures in the range of 200-600°C.[39] The effectiveness of nitrogen as a solid-solution strengthening agent seems to be less affected by increasing temperatures. The work of Byrnes et al.[33] and Norstroms[38] showed that only small decreases in flow stress occurs in high-nitrogen SSs as a function of increasing temperature between 250 and 600°C. These observations result from short-term testing and do not take into account creep behavior in this temperature range. Although the mechanism involved is not clearly understood, this phenomenon may be caused by a chemical interaction between nitrogen and dislocations as a result of the formation of Suzuki atmospheres. This was proposed by Gavrilijuk et al.[40] who cited an internal friction study which showed a correlation between austenite strain aging, as a function of increasing temperature, and the pinning of dislocations.

Carbon-alloyed austenites show only small increases in flow stress with decreasing temperatures down to 4K. In contrast, flow stresses in high-nitrogen alloys increase dramatically with decreasing temperature. The effect of nitrogen on flow stress is only about 20% greater than that of carbon at 295K, but at 4K nitrogen increases strength about 300% more than carbon.[29]

The effect of nitrogen on flow stress with decreasing temperature is similar to what occurs in body-centered cubic (bcc) metals and contrasts sharply with the behavior of face-centered cubic (fcc) substitutional solid solutions.[33] High-nitrogen austenitic SSs actually exhibit a ductile-to-brittle transition at low temperatures. This behavior is highly unusual for fcc materials and is dependent on whether the YS or the cleavage strength is reached first.[41] Cleavage with the lowest fracture stress is expected to occur along {100} planes. However, Harzenmoser et al.[42] reported that cleavage fracture in nitrogen alloyed austenitic materials occurs along {111} planes. This is considered as fracture along concentrated slip bands, not true cleavage. They proposed that a strong slip concentration is necessary for slip band fracture, as would be caused by the formation of planar dislocation arrays and reduced cross-slip.

Some substitutional elements also have a measurable effect on the temperature dependence of the flow strength in nitrogen alloys. Steels alloyed with Fe-Cr-Mn-N exhibit significant embrittlement at cryogenic temperatures, but the effect is lessened with additions of Mo and Ni which enhance toughness.[43] The slope for the increase in YS with decreasing temperature is lowered by increasing nickel concentrations which decrease flow stresses at temperatures down to 4K, resulting in significant increases in plasticity.[42]

The above findings have resulted in changes in alloying trends for high-nitrogen steels with applications at cryogenic temperatures. Trends, which were to remove nickel almost entirely from high-nitrogen materials, have been reversed and alloys with increasing combinations of Mo and Ni are being considered for low-temperature applications.

Effect of Nitrogen on Deformation Structures

Murr[44] reported that carbon-alloyed SSs, such as Type 304, have low stacking fault energies (SFEs) (21 mJ/m^2) and deformation structures generally characterized by planar dislocation arrays and reduced cross-slip. Dislocation structures in low SFE

SSs are different than in high SFE fcc materials such as nickel (SFE ~ 128mJ/m^2), which are characterized by cell-type dislocation structures and predominant cross-slip.

It is universally reported in the literature that austenitic SSs show an increased tendency to form planar dislocation structures with increasing nitrogen concentrations.[33,42,45] Planar dislocation structures reduce the ability of a material to cross-slip and lead to enhanced strain hardening, slip-band formation, and deformation twinning. Planar slip is also expected to increase the GBs efficiency as a dislocation obstacle and may help to explain the effect of nitrogen on grain size hardening.[42]

Planar slip is generally associated with low SFE materials and this would lead one to assume that increases in nitrogen concentrations decrease SFE. Decreases in SFE result in wider partial dislocation separation, more planar dislocation structures, and reduced cross-slip.[29] The stacking fault width is inversely proportional to SFE and the stress for nucleation of deformation twins proportional to SFE. Thus a lower SFE would increase the tendency for both features.[46] However, evidence of planar slip is not, in and of itself, an indication of a material with a low SFE and there is general disagreement in the literature as to the cause of the increased tendency for planar slip in high-nitrogen SSs. Planar dislocation structures have also been observed to form in high SFE materials. In high SFE materials, planar slip has been attributed to short-range order (SRO).[47]

Gerold and Karnthaler[45] attributed the occurrence of planar slip to be due to any of the following three parameters: (1) low SFE, (2) high YS, and (3) the presence of SRO. They proposed that SRO or short-range-clustering in solid solutions are the primary factors causing planar slip and that low SFEs or a high YS are only of minor importance. Short-range-ordering in high-nitrogen alloys would presumably occur between Cr and N which have a strong affinity for one another.[33,48] Obstacles to resolving the current dispute are the lack of evidence for SRO and disagreement on the effect of nitrogen on SFE.

Researchers are divided on the effect of nitrogen on SFE, some report that nitrogen increases the SFE of austenite[48,49], others[2,29,40] report decreasing SFE with

increasing nitrogen. However, there is little direct experimental evidence to support either conclusion. Few SFE measurements have been made in austenitic SSs as a function of nitrogen composition. Reports of increased SFEs with increasing nitrogen levels rely on observations that no evidence of dislocation splitting or of dislocation pairs were found in nitrogen alloys.[48] Conclusions of lower SFEs with increased nitrogen levels are primarily based on observations of planar slip, high work hardening rates, and deformation twinning.

Stoltz and Vander Sande[46] directly measured SFEs in a series of Fe, 18-21%Cr, 6-7%Ni, 8-9%Mn, 0.10-0.06%C alloys with nitrogen levels from 0.21 to 0.52% (all listed as wt%) from dislocation node measurements using TEM. They reported that nitrogen additions lowered the SFE from 53 mJ/m^2 at 0.21 wt%N to 33 mJ/m^2 at 0.24 wt%N and that further increases to 0.52 wt% N did not markedly change the SFE. They reported that no SFs or deformation twins were observed in the 0.21 wt% alloy, but alloys with 0.24 wt% and greater, had increased tendencies for SF formations, extended dislocations, and planar slip. It is unlikely that a small shift in nitrogen concentration, from 0.21 to 0.24 wt%, resulted in a 20 mJ/m^2 decrease in SF energy, while additional nitrogen up to 0.52 wt% had little or no effect. Their work is inconclusive and does not clarify the effects of increasing nitrogen contents on SFE.

Austenitic SSs exhibit increased strain hardening rates with increased nitrogen concentrations as a result of planar dislocation structures and reduced cross-slip.[2,4] Thus, cold-working has become a very effective method for further strength increases, above those of solid-solution strengthening. Extremely high yield strengths (over 1000 MPa) have been achieved in cold worked SSs with high-nitrogen levels. [4,40]

Formation of both alpha-prime (α') and deformation-induced epsilon (ϵ,hcp) martensite in austenitic materials is inhibited by nitrogen additions. Austenite stability is significantly enhanced by nitrogen and the formation of α' does not occur in high-nitrogen materials, even at cryogenic temperatures. However, since SFE is related to

the free-energy difference between the fcc principal structure and the hcp structure, constant, or reduced, SFEs and the suppression of the $\gamma \rightarrow \epsilon$ martensite transformation with increasing nitrogen contents is contradictory.[29]

Although the mechanisms involved have not been clearly identified, it is evident that higher levels of nitrogen in austenitic SSs increase the tendency for planar slip, reduce cross-slip, and enhance cold working and deformation twinning.

Comparison of Strengthening By Nitrogen and Carbon

Solid-solution-strengthening theories predict that the largest contributions to the flow stress of solid-solutions result from the resistance to the movement of mobile dislocations. This depends primarily on the atomic size difference between solvent and solute (lattice dilation due to solvent) and differences between their elastic properties (local modulus effects).[50]

The lattice dilation of austenite by dissolved nitrogen is slightly smaller than, but almost equal to, the dilation produced by carbon. The rates of linear increase of the lattice parameter with dissolved nitrogen and carbon are nearly equal to each other and are generally considered to be dependent on the total dissolved interstitial elements (C + N) without differentiating between carbon and nitrogen.[51] It is clear that differences in C and N influences on flow stresses cannot be accounted for by lattice dilation effects. Also, Reed and Simon[6] concluded that the significance of modulus changes in affecting interstitial strengthening was small and that this could not account for the observed differences between C and N alloying.

One point of general agreement is the difference in dislocation structures formed in alloys with increasing nitrogen contents. The tendency towards more planar dislocation structures with increasing nitrogen concentrations has already been explored. Phenomena such as strain aging, SRO of Cr and N, and differences between the behavior of C and N in the iron lattice, with respect to electronic structure and bonding, need to be studied further.

PRECIPITATION REACTIONS

Nitrogen Solid-Solubility

The primary advantage of nitrogen-alloying is that the solid-solubility of nitrogen in austenitic SSs is much greater than that of carbon. In an Fe-18Cr-8Ni austenitic SS at 800°C the solubility of carbon is less than 0.01 wt% while the nitrogen solubility is approximately 0.2 wt%.[52,53] This means that higher interstitial concentrations and greater solid-solution strengthening can be achieved using nitrogen instead of carbon, and with less tendency for precipitation. However, recent trends have been to produce high-nitrogen austenitic materials with nitrogen contents between 0.4 and 1 wt%, which are above the nitrogen solid-solubility limit. It is important to determine if thermomechanical processing treatments produce nitride precipitation in high-nitrogen alloys. The degree to which precipitation occurs depends upon the thermodynamics and kinetics of precipitation which are controlled by alloy composition and material processing (temperature/time dependent).

Ultimately, nitrogen solubility is determined by the nitrogen concentration in the austenite in thermodynamic equilibrium with the nitride (i.e. the solubility of a given nitride). The tendency of a second-phase precipitate to form can be estimated from the free energy (ΔG_f) and enthalpy (ΔH_f) of formation. Thermodynamic data for nitride formation from pure substances is shown in *Table 2*. The more negative the values of ΔG_f and ΔH_f, the greater the tendency for formation. This thermodynamic data can only be used as a guide because the free energies of these phases are complex functions of material composition and temperature. In the absence of strong nitride forming elements such as Ti, Zr, Nb, B, Al, and Si, the initial precipitate formed in high-nitrogen austenitic SSs is generally Cr_2N.[7-12]

In contrast to nitrogen solubility in liquid metals, there is not much specific data available in the literature regarding nitrogen solid-solubility as a function of material composition. Kikuchi and co-workers[9,10,53,54] have studied nitrogen solubility

TABLE 2 - Enthalpies (ΔH_f) and Free Energies (ΔG_f) of Nitride Formation at 298K

Compound	$-\Delta H_f$ (kJ)	$-\Delta G_f$ (kJ)
Si_3N_4	745.1	622.2
ZrN	365.5	336.2
TiN	336.6	308.1
AlN	318.6	287.1
BN	254.1	---
Nb_2N	248.6	---
NbN	234.0	---
VN	217.3	---
Mn_5N_2	201.8	156.2
Mn_4N	126.9	---
CrN	123.1	96.7
Cr_2N	114.7	93.8
Mo_2N	69.5	70.8
Fe_4N	10.9	-4.2
Ni_3N	-0.8	-27.2
Fe_2N	3.8	---

and precipitation reactions in high-nitrogen Fe-Cr-Ni austenites. They determined nitrogen solubility in the austenite matrix in equilibrium with Cr_2N at 1,000°C to be 0.353 and 0.271 wt% for base materials of Fe-25Cr-20Ni and Fe-25Cr-28Ni, respectively. This is significantly greater than the solubility of carbon. Comparison of nitrogen and carbon solubility in Fe-Cr-Ni alloys is illustrated in *Figure 3*.

Additions of elements such as Ti, Nb, Zr, Al, B, and Si (strong nitride formers) to Fe-Cr-Ni-(Mn-Mo) austenites promote nitride precipitation and lower the

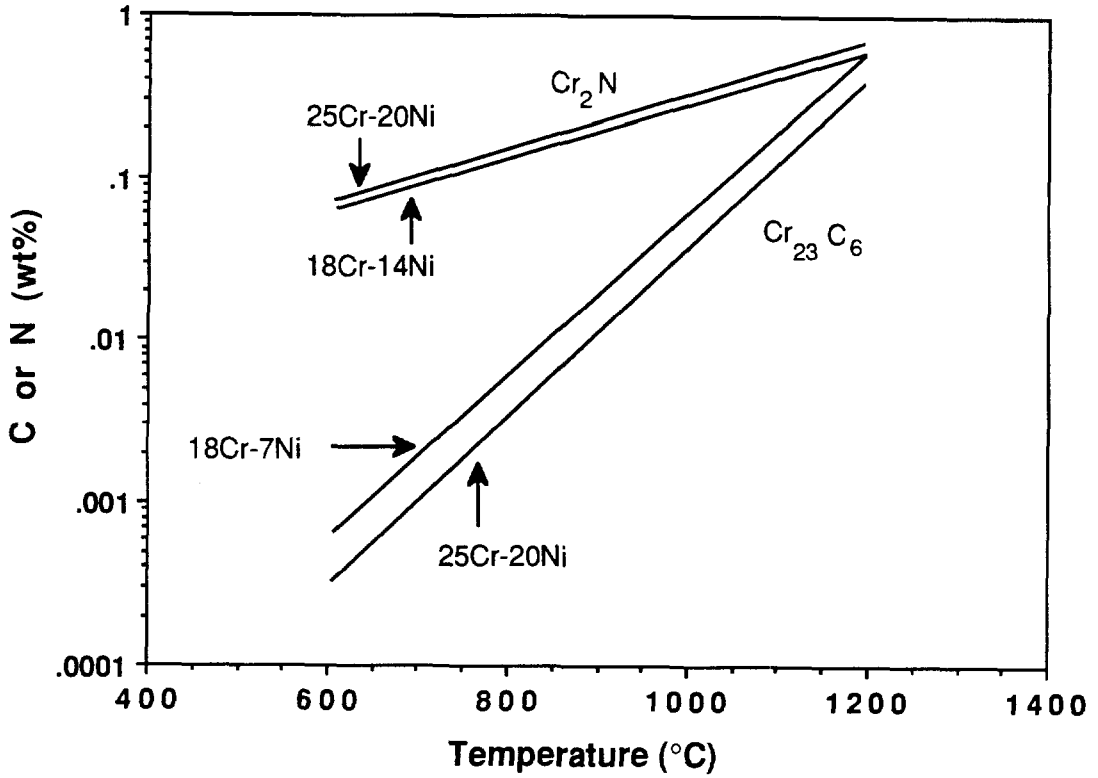

Figure 3. Comparison of nitrogen and carbon solubility in austenite in thermodynamic equilibrium with Cr_2N and $Cr_{23}C_6$, respectively.

solubility of nitrogen in austenite. Kikuchi et al.[53] reported that nitrogen solubility in austenite increases with increasing Cr, Mo, and Mn concentrations and decreases with increasing Ni contents. Normally, it would be expected that all nitride forming elements would decrease the solubility of nitrogen. This seemingly unusual feature of the solubility was ascribed to be due to the strong composition dependence of the Cr and N activity coefficients.

Nucleation Thermodynamics

The free energy change associated with the nucleation of a new phase (ß) from a solid-solution of matrix (α) has the following contributions: (1) At temperatures

where the ß phase is stable, the creation of a volume of ß will cause a volume free energy reduction of $V\Delta G_V$; (2) Creation of an α/ß interface will result in a free energy increase of $A\gamma$, where A is the interfacial area and γ is the energy per unit area of boundary; (3) The transformed volume (ß) will not fit properly into the space originally occupied by the matrix, this results in a misfit strain energy (ΔG_S) per unit volume of ß formed; and (4) If the creation of a precipitate nucleus results in the destruction of a defect, some free energy (ΔG_d) will be released thereby reducing the activation energy barrier for nucleation. Thus, the total free energy change for heterogeneous nucleation is given as:[55]

$$\Delta G_{het} = -V(\Delta G_V - \Delta G_S) + A\gamma - \Delta G_d \qquad [9]$$

The net result of all this is that nucleation in solids is almost always heterogeneous because of the ΔG_d factor, and generally occurs at specific high-energy sites. Preferred sites for second-phase nucleation include non-equilibrium defects such as grain boundaries, incoherent and coherent twin boundaries, stacking faults, inclusions, dislocations, and slip-band intersections. This has been confirmed experimentally for a number of systems such as carbide ($Cr_{23}C_6$) precipitation in austenitic SSs which occurs sequentially at ferrite/austenite interfaces, GBs, incoherent twin boundaries, and coherent twin boundaries.

Nitride Precipitation

In high-nitrogen austenitic SSs based on the Fe-Cr-Ni-Mn alloy system the primary precipitate formed is Cr_2N. Kikuchi et al.[9,10,53,54] studied precipitation reactions in a series of Fe-Cr-Ni alloys with nitrogen contents up to about 0.6 wt% at temperatures between 600 and 1050°C. They found that precipitation of Cr_2N (hcp structure) occurred at GBs and by a discontinuous (cellular) precipitation mechanism. After longer aging times (generally greater than 100 hours) the Cr_2N nitride transformed to a π-phase nitride (ß-manganese structure) which Kikuchi et al.

described as the equilibrium precipitate in high-nitrogen Fe-Cr-Ni alloys. Crystal structure data for these nitrides is given in *Appendix A*. The Cr_2N nitride was considered to be an intermediate phase in Fe-Cr-Ni alloys. Matrix nitrogen concentrations in quasi-equilibrium with Cr_2N were greater than for matrix/π-phase and the π-phase contains more nitrogen than Cr_2N. Substitution of Cr by Mo and/or Si apparently stabilizes the π-phase. They also concluded that the nickel concentration in the alloy must exceed about 10 wt% for the π-phase nitride to become stable.[53]

Cellular precipitation of Cr_2N in Fe-Cr-Ni alloys has been extensively studied by Kikuchi et al.[9,10,53,54] Most of the previous studies of cellular precipitation have involved binary substitutional systems. Kikuchi et al. described this type of cellular precipitation as the "typical" cellular precipitation and cellular precipitation of Cr_2N as a "general" cellular reaction. Cellular precipitation of Cr_2N occurs by decomposition of the supersaturated austenite matrix (γ_1), to an austenite matrix with a different composition (γ_2), and Cr_2N. The reaction can be described as $\gamma_1 \rightarrow \gamma_2 + Cr_2N$. Cellular precipitation products are lamellar and have a morphology which is very similar to pearlite formed in carbon steels. Nucleation of Cr_2N occurs at GBs and growth occurs into one of the adjacent austenite grains.

Growth in "typical" cellular precipitation systems is a steady state process while cellular precipitation of interstitial compounds, such as Cr_2N, is a non-steady state process. The growth features of these two types of cellular precipitation reactions are compared in *Table 3*. The important growth features of Cr_2N cellular precipitation are summarized as follows:

(1) The migration rate of cell boundaries decreases with reaction time and cell growth stops even when a large portion of the specimen remains supersaturated with nitrogen. Only partial decomposition of the specimen occurs and cellular precipitation is incomplete.

TABLE 3 - Growth Features of Cellular Precipitation[9]		
Growth Features	Typical (1)	General (2)
Final Volume Fraction of Cell	100%	Less than 100%
Migration Rate of Cell Boundary	Constant	Decreases with Growth
Interlamellar Spacing	Constant	Increases with Growth
Fraction of Precipitate Within Cell	Constant	Decreases with Growth
Average Composition Within Cell	Constant	Increase in Solute
Composition of Untransformed Matrix	Constant	Decrease in Solute
Long-Range Diffusion	No	Faster Diffuser (N)
(1) Cellular precipitation in substitutional binary solutions (2) Cellular precipitation of Cr_2N involving interstitial nitrogen		

(2) The nitrogen concentration averaged over an entire cell becomes greater than that of the initial supersaturated austenite matrix and correspondingly the nitrogen concentration in the untransformed matrix decreases with cell growth.

The cell boundary migration rate and Cr_2N interlamellar spacing are chiefly determined by the degree of nitrogen supersaturation in the untransformed matrix. Long-range diffusion of nitrogen into the cell from the untransformed matrix reduces the driving force for the reaction. This slows the migration rate of the cell boundary with increasing growth and results in increasing Cr_2N interlamellar spacing with cell development.[10]

Intermetallic Formation

Bechtoldt and Vacher,[56] showed that intermetallic phases such as chi (χ), sigma (σ), and laves (η) are thermodynamically stable phases in high-purity Fe-Cr-Ni-Mo alloys. Structures and typical compositions of these intermetallic phases, taken from the available literature, are given in *Table 4*. Carbon additions result in the

TABLE 4 - Intermetallic Phases in Austenitic Stainless Steels			
Phase	Structure	Lattice Parameter (nm)	Composition[58]
Sigma (σ)	Tetragonal	a = 0.8799 c = 0.4544	FeCr
		a = 0.9188 c = 0.4812	Fe(CrMo)
Chi (χ)	bcc (α-Mn)	a = 0.8920	$Fe_{36}Cr_{12}Mo_{10}$
		a = 0.8878	$(FeNi)_{36}Cr_{18}Mo_4$
Laves (η)	Hexagonal	a = 0.4744 c = 0.7725	Fe_2Mo

precipitation of carbides (usually $M_{23}C_6$) which precedes intermetallic formation. Formation of intermetallic phases is expected to be slower than carbides/nitrides due to the slow diffusion of substitutional elements compared to interstitial carbon/nitrogen. Intermetallic formation is strongly dependent upon material composition, aging temperature, and prior thermomechanical processing.

Nucleation of intermetallic phases occurs at high energy interfaces such as GBs and incoherent twin boundaries, or second phases, such as oxide inclusions.[57,58] Cold working accelerates intermetallic formation, probably through the activation of high-energy nucleation sites (dislocations and faults) and enhanced substitutional diffusion by dislocation short-circuiting.[58]

Weiss and Stickler[58] determined time-temperature-precipitation (TTP) curves for second phase reactions in 316 SS. For all aging temperatures below 900°C, the first detectable precipitate consisted of $M_{23}C_6$ carbides followed at longer aging times by the precipitation of χ, η, and σ phases. In 316 alloys, the χ-phase has the highest temperature stability and forms in the shortest times. They found that intermetallic formation occurred at the shortest times at temperatures of 750°C for χ, 725°C for η,

and 675°C for σ. Formation of χ and σ phases is more rapid in 316 than in 304 alloys because Mo additions promote their stability and accelerate precipitation.

All three intermetallic phases (σ, χ, and η) have broad homogeneity ranges (high tolerance for metal atom exchange) and their phase compositions and temperature ranges of stability are not the same in every alloy system.[58] Sigma phase reportedly has no solubility for carbon and therefore its formation is retarded by carbon additions. Thier et al.[59] reported that the laves phase, similarly to sigma phase, has no solubility for carbon. This was contradicted by Wiegand and Doruk,[60] who reported that laves phase has some solubility for carbon. Apparently the χ-phase structure can accommodate larger amounts of interstitials than either σ or η and can behave as a carbide of the type $M_{18}C$[61].

Several investigators have reported that increasing carbon contents retard the formation of these intermetallic phases in favor of the precipitation of $Cr_{23}C_6$ carbides.[57,58,62] This seems reasonable for the case of σ and η which may have a low solubility for carbon, but seems to be a contradiction for χ-phase which has some solubility for carbon. However, this phenomenon can be explained on the basis of competition for nucleation sites. Since carbide formation is more rapid due to the fast diffusion of carbon, nucleation of all intermetallic phases, even those that can incorporate some interstitial elements into their structure, will be retarded because there are less nucleation sites available.

It is likely that intermetallic formation in high-nitrogen SSs will follow similar trends to what has been observed for carbon-alloyed materials with similar base compositions. However, the high concentrations of interstitial nitrogen present in these new materials may act to retard intermetallic formation if nitrogen solubility in their structures is limited. Long-term aging studies are necessary to determine the specific roll of intermetallic phases in high-nitrogen alloys.

SENSITIZATION

Austenitic SSs become sensitized when Cr-rich carbides ($Cr_{23}C_6$) precipitate at grain boundaries causing the formation of a Cr-depleted region in the adjacent matrix.[63-66] Sensitization, characterized by grain boundary Cr-depletion (GBCD), is a controlling factor causing susceptibility of austenitic SSs to IGC and IGSCC. Bain and his co-workers[1] were the first to recognize the association between carbide precipitation, Cr-depletion, and the susceptibility of austenitic SSs to IGC and IGSCC. The existence of a Cr-depletion zone in sensitized materials has been experimentally confirmed by numerous investigators.[67-69]

The degree of sensitization (DOS) of a material is controlled by the width of the GB Cr-depletion zone and the equilibrium chromium concentration (Cr-minimum) at the precipitate/matrix interface. These parameters are controlled by the large difference between the lattice diffusivities of chromium and carbon (in effect, Cr-diffusion kinetics) and the thermodynamics of carbide precipitation.

In order for a material to be considered sensitized, the equilibrium chromium concentration at the precipitate/matrix interface must be below a critical value and a sufficiently wide Cr-depletion zone has to exist in the adjacent matrix. Strawstrom and Hillert[70] concluded that type 304 and 316 SSs are sensitive to IGC only when there is a Cr-depletion zone with a minimum chromium content at the GBs of about 13 wt% Cr and a width greater than about 20 nm. Bruemmer[71] concluded that this critical chromium content was about 14 wt%.

Effect of Nitrogen on Sensitization

Additions of less than 0.16 wt% nitrogen to carbon-alloyed austenitic SSs have been found to delay sensitization. However, nitrogen concentrations above this level tend to promote sensitization.[65,66]

Briant et al.[72] suggested that nitrogen may act to retard nucleation and or growth of carbides at GBs and increase the time for sensitization. This could possibly be accomplished by nitrogen segregation to GBs. Site competition between nitrogen and carbon atoms could interfere with carbon segregation to the boundaries and retard carbide nucleation. Mozhi et al.[65] and Betrabet et al.[66] proposed that the presence of nitrogen causes an increase in the equilibrium chromium concentration at the carbide/matrix interface. For a given amount of carbide precipitation, this would decrease the DOS of a material. Betrabet et al. also proposed that nitrogen additions decrease matrix Cr-diffusivity thereby retarding carbide growth kinetics.

Betrabet et al.[66] concluded that increases in sensitization noted for nitrogen contents above 0.16 wt% were caused by Cr-carbides precipitating discontinuously, which resulted in GB migration and wider Cr-depletion zones. In the studies cited above, in which nitrogen levels above 0.16 wt% caused enhanced sensitization, no mention of nitride precipitation was made. It is possible that nitride (Cr_2N) precipitation occurred along with carbide precipitation and that it enhanced sensitization development. It may also be possible to form mixed carbo-nitrides, but no positive identification of these has been reported. Aside from the effect of nitrogen on sensitization in carbon alloys, sensitization in high-nitrogen steels, with low carbon levels, can be expected to occur due to the precipitation of Cr_2N nitrides. This is because the same conditions that promote sensitization in carbon-alloyed SSs also exist in materials alloyed with nitrogen. However, sensitization of high-nitrogen steels, due to the precipitation of Cr-rich Cr_2N nitrides, has not been reported.

Sensitization development in nitrogen-alloyed austenitic SSs should essentially be analogous to the sensitization of materials alloyed with carbon. In austenitic materials with low-carbon and high-nitrogen levels, the degree of sensitization achieved will be controlled by the thermodynamics of nitride precipitation and Cr-depletion kinetics. Cr-depletion kinetics are controlled by chromium diffusivity since the diffusivity of nitrogen in austenite, being interstitial, is much faster than that of chromium, and is on the same order as that of carbon. The remaining question is

whether or not equilibrium interfacial Cr-concentrations between matrix and nitride, within the temperature range for precipitation, are low enough to promote sensitization.

Thermodynamics of Cr_2N Precipitation

As stated previously, the free energy of formation (ΔG) can be used to indicate whether or not precipitation of a second phase from solid-solution is thermodynamically favorable. The driving force for precipitation becomes stronger as the free energy for the given reaction becomes more negative. Consider the following reaction:

$$x\,M + y\,N = M_x N_y \qquad [10]$$

where M and N are elements forming the M_xN_y compound with the stoichiometry defined by the constants x and y. The free energy of the reaction at equilibrium can be expressed as:

$$\Delta G = -RT \ln K_{eq} \qquad [11]$$

where K_{eq} is the equilibrium constant for the reaction and is defined as:

$$K_{eq} = \frac{a_{M_xN_y}}{(a_M)^x\,(a_N)^y} \qquad [12]$$

where the a's represent the activities of the elements in the solid-solution and in the second phase, and the second phase itself. The above equation is valid for precipitation of $M_{23}C_6$ carbides in SS as well as for precipitation of Cr_2N nitrides. An

assumption can be made that the nitrides consist only of Cr and N. The equilibrium reaction for the formation of Cr_2N can then be written as:

$$K_{eq} = \exp\left(\frac{-\Delta G}{RT}\right) = \frac{a_{Cr_2N}}{(a_{Cr})^2 (a_N)} \qquad [13]$$

Under standard conditions, the activity of the product phase, in this case Cr_2N, is unity. Precipitation and reaction equilibria are controlled by the activities of Cr and N. The activities of Cr and N in the matrix are related to their concentrations by activity coefficients (γ) which can be expressed as:

$$a_i = \gamma_i X_i \qquad [14]$$

The matrix chromium concentration (X_{Cr}) in thermodynamic equilibrium with the Cr_2N is:

$$X_{Cr} = \frac{1}{(K_{eq})^{1/2} (\gamma_{Cr}) (\gamma_N X_N)^{1/2}} \qquad [15]$$

This value (X_{Cr}) represents the chromium concentration at the nitride/matrix interface. Diffusion along the GBs, which act as high-diffusivity paths, is much faster than diffusion in the matrix. Thus, when precipitate spacing is sufficiently small, equilibrium in the GB is achieved and the entire boundary has a chromium level defined by X_{Cr}. As described previously, the value of X_{Cr} has a controlling influence on the DOS.

Quantitative modeling or prediction of sensitization development in nitrogen alloys would require information regarding the values of activity coefficients for Cr and N. Values for γ_{Cr} and γ_N are not currently available in the literature. Most values for γ_{Cr} in carbon-alloyed materials were developed over a period of time since they were based on corrosion test data.[73]

There are several important points to note concerning *equation [15]* and the factors controlling the minimum chromium concentration at the GBs. As the activity

coefficients for Cr and N, and the bulk composition of N increase, the Cr-minimum decreases. Decreasing X_{Cr} values increase material DOS. Although the absolute values of X_{Cr} will be different for equilibrium conditions between matrix and carbides, versus matrix and nitrides, values for X_{Cr} should vary similarly as functions of temperature and bulk interstitial concentrations for the two situations. At higher aging temperatures, the chromium concentration in equilibrium with $Cr_{23}C_6$ increases.[68] Also, as precipitation and growth of carbides/nitrides continues, the carbon/nitrogen content in the matrix decreases. This leads to increasing interfacial Cr-minimums (X_{Cr} values) with aging time, while the width of the depleted zone continues to increase. Eventually, although stable precipitates are present, no Cr-depletion zone exists. This phenomenon is referred to as desensitization.[70,71,73,74]

Desensitization (Self-Healing)

It has been known for more than fifty years that the corrosion resistance of sensitized austenitic SSs can be restored if aging is continued for a long time within the sensitization temperature regime. According to the depletion-zone theory, desensitization is due to the diffusion of chromium into the depleted zone from the matrix and/or from an increase in GB Cr-minimums. As the nitrogen content in the interior of the grains decreases, the nitrogen activity decreases, and the Cr content increases at the matrix/nitride interface. Desensitization actually occurs simultaneously with precipitation. The annealing time required for healing is predicted to vary quadratically with the grain size of the material.[70,71,75]

Cr-depletion Kinetics

Development of a Cr-depletion zone has already been attributed to the large differences between the rate at which chromium and the interstitial element (carbon or nitrogen) arrive at the growing precipitate. Since the mass transport of chromium is

much faster in the GBs than in the lattice, a Cr-depletion zone of uniform width can be assumed to develop along the whole length of the boundary, as shown schematically in *Figure 4*. Experimental evidence suggests that the concept of a uniform Cr-depletion zone may not be valid for certain conditions, but that overall, it is a good approximation.[68]

Thorvaldsen and Salwen[76] formulated an equation describing the depletion zone shown in *Figure 4* using the following solution of Fick's second law:

$$C_x = X_{Cr} + (C_1 - X_{Cr})\ erf\left[\frac{X}{2\sqrt{D_{Cr}t}}\right] \qquad [16]$$

where t is the aging time, D_{Cr} the volume diffusion coefficient of chromium, C_x the matrix Cr composition at a given distance (x) from the GB, and X_{Cr} and C_1 represent the equilibrium solute concentration at the boundary (Cr-minimum) and the bulk chromium concentration, respectively. The width of the Cr-depletion zone (W_{Cr}) at C_1 can be estimated from the quantity:

$$W_{Cr} \approx 2\sqrt{D_{Cr}t} \qquad [17]$$

The solution above is only valid in the early stages of aging, prior to healing. It is clear from *equation [16]* and *Figure 4* that the Cr-depletion profile is controlled by the Cr-minimum present at the GB, and the volume diffusion of chromium.

Measurement of the Degree of Sensitization

The DOS depends directly on the width of the Cr-depletion zone and the equilibrium chromium concentration (X_{Cr}) at the GBs, not merely on the presence of precipitates. Therefore, experimental techniques used to measure sensitization need to be sensitive to the presence of Cr-depletion, not merely the presence of carbides or nitrides.

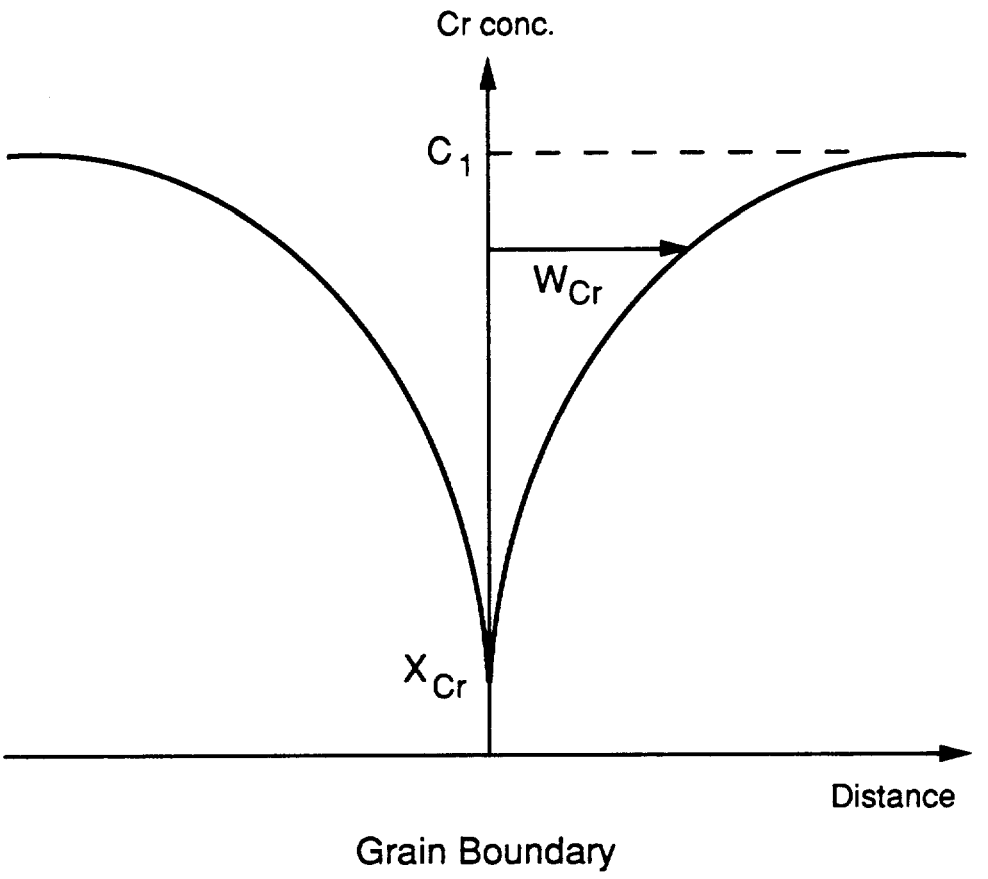

Figure 4. Schematic representation of the chromium concentration across a grain boundary segment between Cr_2N nitride precipitates.

Commonly used methods for measuring the DOS of austenitic SS materials are the ASTM Recommended Practices for Detecting Susceptibility to Intergranular Attack in Stainless Steels (ASTM A 262, Practices A & E),[77] the more recently developed electrochemical potentiokinetic reactivation (EPR) test,[78,79] and direct measurement of the Cr-depletion at GBs using analytical electron microscopy (AEM) techniques.

The EPR test method has been shown to be sensitive to Cr-depletion (sensitization) in carbon-alloyed austenitic SSs. The EPR technique is currently the most quantitative test for DOS measurement and can detect low sensitization levels which are of primary concern for industrial applications.[78,80] The EPR test can also

be performed quickly and non-destructively as compared to other methods of sensitization determination.

It is reasonable to assume that if Cr-depletion zone development occurs as a result of Cr_2N nitride precipitation in high-nitrogen materials, then these materials would be subject to attack during EPR testing. The EPR test, and direct measurement of Cr-depletion using AEM, are described in the following sections.

Electrochemical Potentiokinetic Reactivation Test

The single loop EPR test method consists of developing potentiokinetic curves of a polarized specimen by the use of a controlled potential sweep from the passive region to the active region (reactivation). A passive film is first formed on the specimen surface and then break-down of this film is characterized as GB attack occurs in the Cr-depleted regions during reactivation.[81] Passivation is due to the formation of a protective oxide film and results in a reduction of the anodic dissolution rate of the electrode involved in corrosion. Reactivation is the disruption of a passive film by electrochemical methods.[79] Non-sensitized SSs exhibit a low current density during the reactivation step resulting from the stability of the passive film. However, sensitized SSs show a high current density due to breakdown of the passive film in Cr-depleted regions near GBs.[82]

The nomenclature used in the single loop EPR test include the open circuit corrosion potential of the sample (Ec), the reactivation charge Q [total charge value in coulombs (coul.), this is the integrated area below the reactivation peak], the peak current density in the active state (Ip), and the Flade potential (E_B), which marks the start of passive film breakdown during reactivation. The integrated Q value is normalized by specimen surface area and grain size and results in the normalized charge value Pa (coul./cm^2). The Pa value is known as the DOS value determined by the EPR test.[78,82]

The EPR test provides an indirect measurement of the amount of Cr-depletion at GBs. Bruemmer[71], for Type 304 and 316 steels, correlated experimentally measured GB Cr-depletion (width and minimum) to DOS data and determined that although the GB Cr-minimum has an effect on DOS values, depletion width controls its magnitude in most cases. These direct measurements of depletion indicated that only regions below about 12.5 to 13.5 wt% Cr were attacked during EPR testing. It was determined that the EPR test does quantitatively indicate Cr-depletion and that significantly different widths and minimums can produce the same DOS value.

Direct Measurement of Cr-Depletion

The best technique for directly measuring the width of the Cr-depletion region and minimum chromium concentrations at GBs is AEM using a scanning transmission electron microscope (STEM) equipped with an energy dispersive X-ray spectrometer. This approach has been utilized by a number of investigators.[69,71,74,83] Significant variations in Cr-depletion profiles and chromium minimums between GBs exist within most materials. This is primarily due to the fact that precipitation is not a homogeneous phenomena. Precipitate growth rates, spacings, and morphologies, as well as Cr-depletion zone development, can vary significantly from boundary-to-boundary.[71,74]

Direct measurement of Cr-depletion profiles using AEM techniques requires a large amount of time and expense. Also, it is difficult to examine a statistically meaningful number of GBs to obtain bulk sensitization information from each sample since boundary-to-boundary variations exist. Direct measurement of GB chromium concentrations at GBs is not possible without matrix effects on the results because the sampling size is much greater than the width of the GBs. The particular equipment used defines the spatial resolution attainable and this affects the degree to which Cr-depletion can be mapped.

DEFORMATION EFFECTS on PRECIPITATION REACTIONS

Increasing levels of plastic deformation lead to increasing dislocation densities and defect structures. Defect structures formed as a result of material deformation can include GB ledges, slip-bands, stacking faults, deformation twins, and martensite. Dislocation and defect structures formed vary as functions of the temperature at which deformation occurs, material composition, and strain type, rate, and level.

Microstructural changes resulting from material deformation can accelerate solid-state reaction kinetics through enhanced substitutional diffusion and by decreasing the free energy barrier to nucleation. Enhanced substitutional diffusion of elements such as chromium, is postulated to occur through a dislocation pipe diffusion mechanism.[84-89] The effectiveness of diffusion enhancement due to dislocation pipe diffusion is expected to increase with increasing dislocation density. Higher chromium diffusivities are expected to lead to more rapid nitride precipitation and more rapid development of the Cr-depletion zone (an increase in sensitization kinetics). The kinetics of desensitization are also expected to increase.

Heterogeneous nucleation occurs preferentially at high-energy defect sites because the partial destruction of a high energy site creates a negative energy term (ΔG_d) which causes a reduction in the activation energy barrier for nucleation. Deformation induced defect structures formed at GBs (e.g. ledges) may accelerate nucleation at GBs which are already preferred sites for precipitation. The activation of transgranular nucleation at high-energy deformation induced defect sites is also likely.

Prior cold work has been shown experimentally to accelerate the rate of $M_{23}C_6$ carbide precipitation and sensitization development in austenitic SSs.[90-95] Deformation induced transgranular precipitation, due to martensite formation and dislocation structures, has been observed in 304 and 316 SSs.[90-94] Although martensite was shown to have a dramatic effect on carbide precipitation and

sensitization kinetics in type 304 SS,[94] it should not be a factor in high-nitrogen austenitic materials which are very stable and not generally susceptible to martensite formation.

The effect of strain on microstructure, precipitation kinetics, and precipitate characteristics such as density, location, and morphology is expected to be a function of strain level and aging temperature/time. Higher aging temperatures may initiate strain recovery and/or recrystallization which would result in lower dislocation densities and anneal-out defect structures. Deformation effects on increasing precipitation and sensitization kinetics in type 316 SS have been shown to be reduced by high temperature exposure.[90]

EXPERIMENTAL PROCEDURES

The experimental procedures used in the current work are summarized in *Figure 5*. The flow-chart of *Figure 5* illustrates, for both heats of material, thermal and deformation processing, microstructural analysis, Charpy V-notch (CVN) impact testing, and grain boundary Cr-depletion (sensitization) measurements. The flow-chart is intended to give an over-view of the work done and not specific details.

INITIAL MATERIALS

Two high-nitrogen austenitic stainless steels (Fe-Cr-Ni-Mn-Mo), were employed in this study. The compositions of these two heats of materials are listed in *Table 5*. The commercial designations for these two heats of materials, DE 257 and DPSC 2100, will be used throughout this manuscript.[1] The base compositions of these heats were quite similar. However, heat DE 257 contained small additions of strong nitride forming elements, Nb, V and Al, and also more bulk nitrogen than DPSC 2100, 0.78 wt% compared to 0.69 wt%.

Both materials were produced in PESR furnaces, heat DE 257 was produced as a 100 kg billet in a small pilot plant facility while heat DPSC 2100 was produced as an 8 ton ingot in a full-scale commercial facility. The details of the PESR method for producing high-nitrogen steels were presented in an earlier section.

The 100 kg billet of heat DE 257 and a similar-sized section from heat DPSC 2100 were forged, prior to being received by OGI, at a temperature estimated to be

---

[1] Material obtained from Krupp Steel, Vereinigte Schmiedewerke GmbH, Essen, Germany.

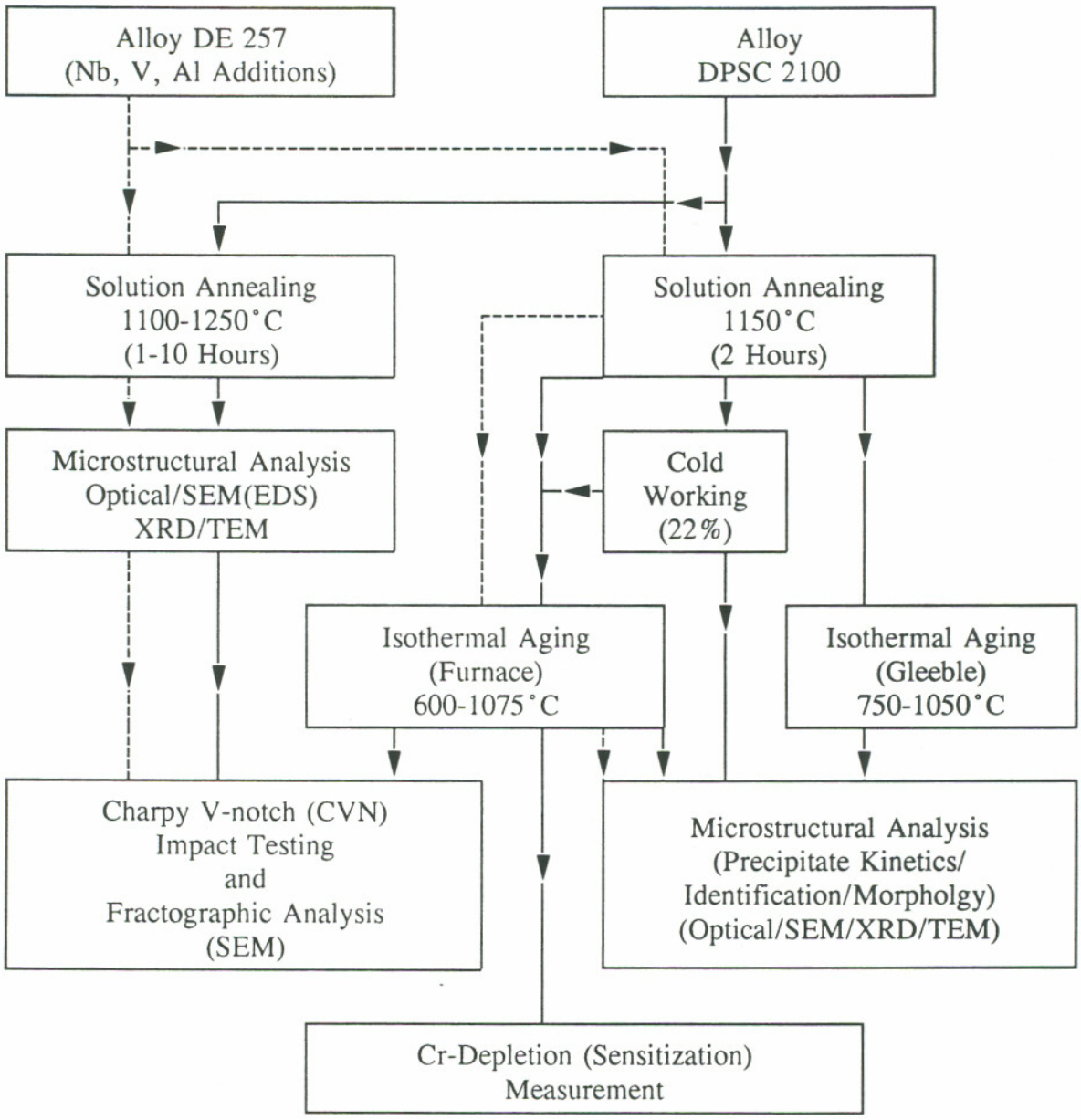

Figure 5. Flow-chart illustrating experimental procedures used in the processing, testing, and analysis of materials from heats DE 257 and DPSC 2100.

TABLE 5 - Compositions (wt%) of Heats DE 257 and DPSC 2100		
Element	DE 257	DPSC 2100
Cr	21.9	19.3
Ni	4.2	5.2
Mn	5.1	5.2
Mo	3.2	2.9
Si	0.83	0.86
Al	0.02	<0.003
V	0.09	0.03
Nb	0.13	<0.01
C	0.026	0.024
N	0.78	0.69
Fe	Bal.	Bal.

between 1000 and 1075°C to produce billets with a square cross-section of 70x70 mm^2. The DE 257 material was received in a final size of 70x70x200 mm^3 (8 kg) and the DPSC 2100 material as 70x70x1600 mm^3 (60 kg).

Sectioning of billets

The billets were sectioned as shown in *Figure 6* for removing Charpy V-notch impact testing specimens. Microstructural examination of the three primary billet directions after solution annealing at 1150°C for 2 hours revealed that the grain structures of both materials were uniform and virtually equal in all three directions. Therefore, subsequent microstructural examinations, from both heats of material, were conducted on samples taken from the front face of the square section billets.

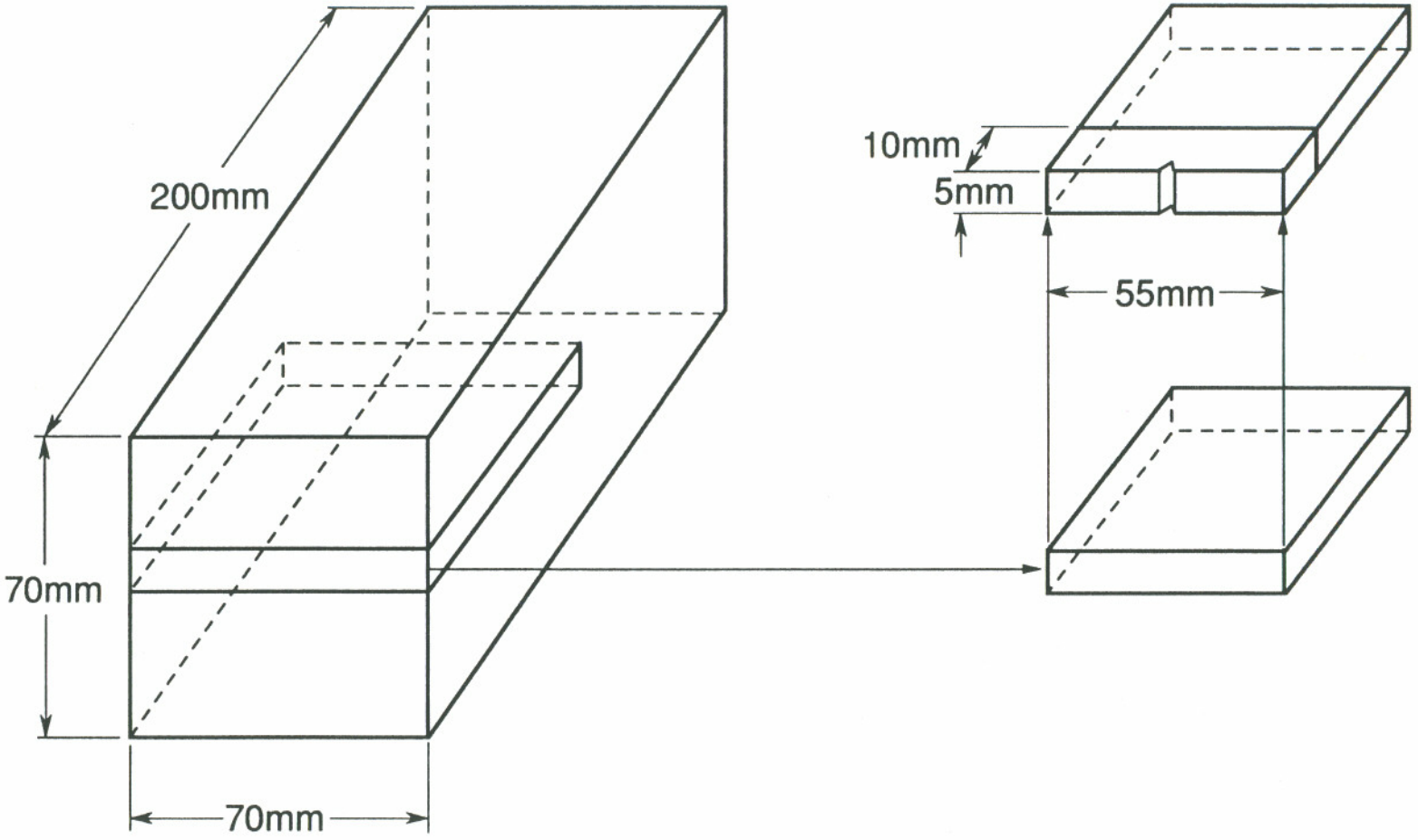

Figure 6. Schematic showing sectioning of billets from heats DE 257 and DPSC 2100 and orientation of Charpy V-notch impact specimens.

Bulk Composition Analysis

The bulk compositions of the commercially produced heats provided by the manufacturer are shown in *Table 5*. In addition, these heats were analyzed by spark emission spectroscopy for the elements listed in *Table 5*, except nitrogen, and the results compared to those provided by the material producer. Compositions provided by the manufacturer were within $\pm$ 2-5% of those measured by spark emission spectroscopy (percentage of difference between the two measurements).

Nitrogen Analysis

In the course of the present study, total nitrogen content of samples was measured by inert carrier gas fusion using a Leco Nitrogen-Oxygen-Determinator, model TC 436. Samples were sliced from bulk materials using a high-speed cut-off saw equipped with an ultra-thin (0.5 mm) blade and liquid coolant. Using this technique, small material volumes were removed for analysis without excessive heating. The sample size used for nitrogen analysis was between 0.2 to 0.3 grams. Standard materials with known nitrogen contents, similar to the sample being analyzed, were used to calibrate the equipment.

ISOTHERMAL AGING and DEFORMATION

Furnaces

Solution annealing treatments up to temperatures of 1150°C, and all furnace aging treatments, were carried out in a refractory brick-lined electric muffle furnace (Lucifer brand) with an operating range from 500-1200°C. The constant temperature zone of the furnace was measured using a shielded K-type thermocouple inserted through a small hole in the furnace door. To insure that the samples to be heat

treated were at the same temperature as the monitoring thermocouple, a refractory brick was positioned in the center of the furnace and the samples placed on it. There was excellent correspondence between the temperature displayed by the furnace controller (measured by the furnace control thermocouple) and the monitoring thermocouple. The constant temperature zone in the furnace maintained a temperature within $\pm$ 5°C of the programmed temperature.

Solution annealing at temperatures of 1200 and 1250°C was done in a refractory brick-lined furnace at the Bureau of Mines Albany Research Center, Albany, Oregon. Temperature measurement in this case was achieved by a K-type wire-thermocouple (shielded with a high-temperature refractory) placed in the center of the furnace, where the samples to be heat treated were also located.

Gleeble Thermal Simulator

A computer-controlled Gleeble thermal simulator, model 1500, was used to achieve accelerated heating rates which could not be obtained by furnace heating. Each specimen was held between two water-cooled stainless steel grips and directly heated by its own electrical resistance by passing current through it. A 10 mm (diameter) round specimen geometry was used for Gleeble thermal cycle studies. A specimen length of approximately 115 mm was used with about 20 mm of each end of the bar located within the grips.

In the Gleeble, the maximum temperature within the specimen exists at mid-span between the grips. The longitudinal thermal gradient profile along the sample is primarily dependent upon the length of the sample (distance between the grips), its thermal conductivity, and thermal conduction through the jaws themselves. The feedback signal necessary for closed loop control of the current and accurate temperature control was obtained from a fine wire K-type (chromel-alumel) thermocouple welded to the specimen at mid-span. Each thermocouple wire was independently welded to the specimen surface using a parallel separation distance

between the wires of about 1 mm. This method is preferred to welding of the thermocouple wires together at the surface with a single bead. Using a single bead increases the surface area of the junction resulting in greater surface cooling effects that can cause increased errors in temperature measurement.

Thermal Profiles for Furnace Aging

Heating rates of samples (10x10x10 mm^3) in the Lucifer furnace were measured in order to determine the minimum aging time which could be used without sample heating time significantly influencing the thermal aging treatment. A 3 mm diameter hole was drilled into the center of the block and a K-type thermocouple wire shielded with a high temperature refractory cloth was spot-welded to the bottom of the hole. The hole was subsequently filled with a ceramic-filled epoxy.

The block of material with attached thermocouple was placed into the center of the furnace and the furnace door was closed on the attached wire. As tight a seal as possible was made with the furnace door so as to avoid heat loss. Temperature measurements were taken every fifteen seconds using a hand-held digital thermometer connected to the thermocouple. Specimens reached furnace temperature in just over three minutes as shown in *Figure 7.* Time to reach temperature was independent of the furnace temperature and was only a function of the samples size and material thermal conductivity. This is because the sample size was very much smaller than the furnace and the drop in the furnace temperature during sample insertion was negligible.

Thermal Profiles for Gleeble Thermal Treatments

To help assure a constant temperature zone of at least 6 mm (0.5 inches) in the Gleeble, stainless steel jaws were used to reduce heat conduction through the grips. To determine the approximate size of the isothermal zone in the specimens, a

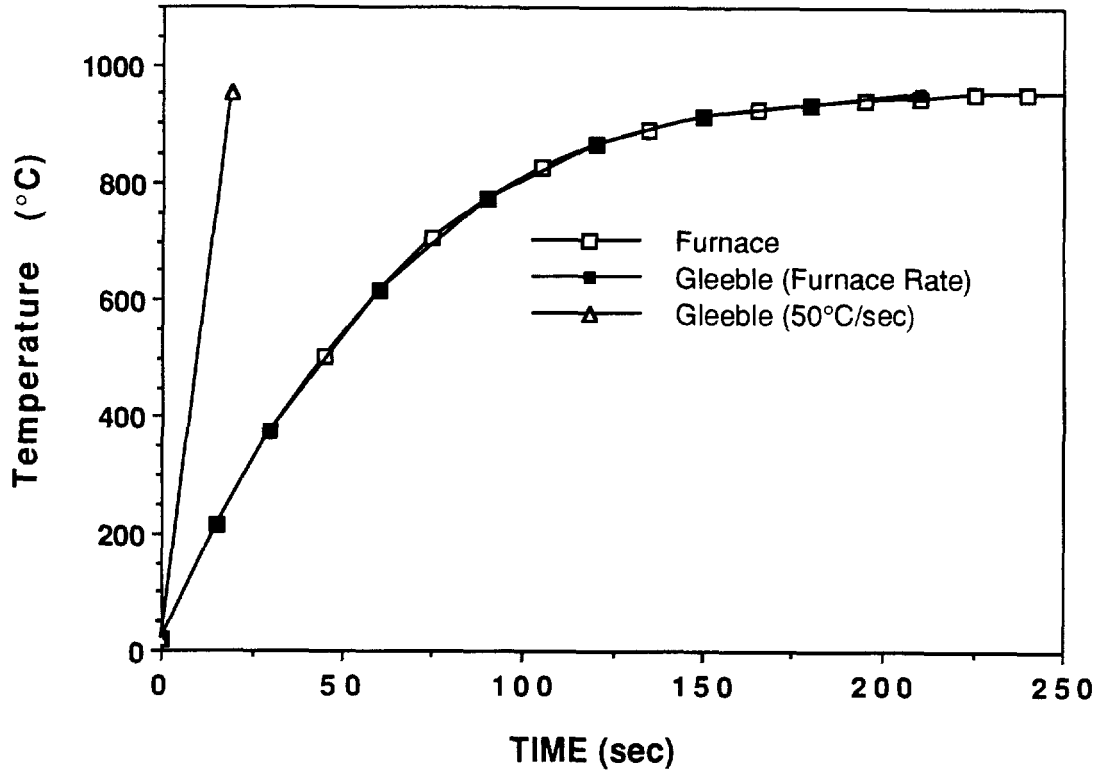

Figure 7. Heating rate profiles for aging in furnace, accelerated heating in the Gleeble, and simulation of furnace heating in the Gleeble.

thermocouple was placed at 3 mm from mid-span (in addition to the controlling thermocouple at specimen mid-span), and monitored during heating to 1050°C. No temperature difference was measured between the thermocouples at mid-span and at 3 mm. Thus, it was concluded that the experimental conditions were sufficient to provide a total isothermal zone of at least 6 mm.

Gleeble thermal cycles consisted of heating a sample to a particular target temperature where it was isothermally held for a specified length of time, after which it was cooled by a continuous blast of argon gas at a pressure of 30 psi. Basically, two types of heating were employed. The first was linear heating of samples to the isothermal hold temperature at an accelerated heating rate of 50°C/s so as to minimize or eliminate heating rate influences on the precipitation characteristics of the

material at the isothermal hold temperature of interest *(Figure 7)*. In the second, a heating rate was designed to mimic the heating rate of samples observed in the furnace aging. This was done by segmenting the heating into a series of different linear heating rates so that the resulting heating profile would correspond closely to the sample heating measured in the furnace *(Figure 7)*.

Effect of Solution Annealing on Nitrogen Content

To determine acceptable procedures for solution annealing and isothermal aging of the high-nitrogen materials, experiments were conducted to determine the effects of atmosphere used during thermal aging on the final nitrogen contents of samples. Due to the relatively small sample sizes being employed for thermal treatments, gain or loss of nitrogen in the materials, as a function of atmosphere, needed to be determined and then minimized by using optimized thermal processing procedures.

Considering the diffusion kinetics of nitrogen, the greatest gain or loss of nitrogen should occur at the highest annealing temperatures. Samples (10x10x10 mm^3) were annealed at 1150 or 1200°C under three different conditions: (1) encapsulation in quartz tubes with a nitrogen backfill; (2) encapsulation in evacuated quarts cylinders; and (3) heat treatment in air. The samples were annealed for one hour and then water quenched. After removal of any oxide scale on the surface of the samples by wet grinding, thin slices were cut at incremental depths of approximately 1 mm, starting at the specimen surface with a high-speed cut-off saw and a 0.5 mm thick blade. The bulk nitrogen content of each slice was then determined using the Leco analyzer.

A significant increase in the nitrogen content near the surface was observed for samples heat treated in nitrogen backfilled quartz crucibles, even to about 2.5 mm in depth. A slight nitrogen pick-up was observed in the first 1 mm from the surface for samples heat treated in air at 1150°C. No change in the bulk nitrogen content was

detected for samples heat treated at 1150°C in evacuated quartz crucibles. These results are shown in *Table 6.*

It was concluded that annealing the high-nitrogen materials in nitrogen backfilled quartz crucibles could significantly increase the nitrogen composition of small samples. Heat treating in air and in evacuated quartz crucibles both had an insignificant effect on the nitrogen concentration, even in very small samples, except that heat treatment in air caused significantly more surface oxidation, especially at temperatures above 1100°C. Therefore, subsequent solution annealing heat treatments (1100°C and above) were done with samples encapsulated in evacuated quartz crucibles. Furnace aging treatments of these samples at temperatures between 600 and 1075°C were subsequently done in air.

Solution Annealing Studies

Solution annealing effects on grain growth, microstructural/chemical heterogeneity, and impact toughness were studied by annealing samples from heats DE 257 and DPSC 2100 at temperatures between 1100 and 1250°C, for times between 0.5 and 10 hours. This study was also necessary in order to produce solution annealed microstructures suitable for subsequent isothermal aging and TEM analysis.

Cold Working

The effect of prior cold work on the isothermal aging characteristics of heat DPSC 2100 was studied. This was carried out by first solution annealing two plates of the material (dimensions of 60x80x15 mm^3) in air at 1150°C for 2 hours. The top and bottom of each plate was then milled to obtain a final thickness dimension of 10 mm. The plates were subsequently rolled at ambient temperature at the US Bureau of Mines Albany Research Center to obtain a 22% reduction in thickness.

TABLE 6 - Nitrogen Composition as a Function of Heat Treatment Condition/Atmosphere

Material/ Condition	Atmosphere	Section*	N (wt%)
DE 257	As-forged	----	0.77 - 0.79
DE 257 1150°C 1 hr	Air	1	0.80
		2	0.79
		3	0.79
		4	0.79
DE 257 1150°C 2 hrs	Vacuum	1	0.76
		2	0.77
		3	0.77
DE 257 1050°C 10 hrs	Nitrogen	1	0.85
		2	0.78
		3	0.78
DE 257 1250°C 1 hr	Nitrogen	1	0.87
		2	0.80
DPSC 2100	As-Forged	----	0.68 - 0.70

* Section equals distance in from edge of sample in mm not including blade thickness of 0.5 mm

Isothermal Aging

Effects of isothermal aging on precipitation characteristics were studied for alloys DE 257 and DPSC 2100 solution annealed at 1150°C for 2 hours. Square sections (10x10x10 mm^3) were encapsulated in quartz tubes, evacuated, sealed, and annealed, followed by water quenching. In addition, the aging characteristics of the cold-rolled material from heat DPSC 2100 were studied.

Furnace aging (isothermal) was conducted in the temperature range of 600-1075°C for times from 0.1 hour to as long as 30 hours. Isothermal aging in the Gleeble thermal simulator was conducted at temperatures of 750-1050°C for times ranging from 0.01 hour (36 seconds) to 1 hour. Tables showing the specific aging treatments employed are located in *Appendix B*.

MICROSTRUCTURAL CHARACTERIZATION

Prior to microstructural characterization (e.g. optical, XRD, or electron microscopy) heat treated samples were sectioned or ground to a depth of about 2 mm to remove any surface effects of heat treatment and possible nitrogen gain/loss and oxidation at the sample surface.

Optical Microscopy

Metallographic Preparation

Samples for metallographic examination were mounted in a thermosetting compound (Bakelite) and wet ground using water and SiC abrasive papers with grit sizes of 120, 240, 400, and 600. Intermediate polishing was done successively with 6 and 1 μm diamond pastes on low-nap synthetic cloths using an oil-based lubricant. Final polishing was done using a Leco finipol automatic polishing unit and a 0.05 μm cerium-oxide polishing solution.

Etching

Several etchants were used to reveal the microstructural features of the two commercial heats studied. The etchant procedure used depended upon the material condition as well as the information desired. A common multipurpose electrolytic

etchant used for austenitic stainless steels is an aqueous 10% oxalic acid solution. When applied to solution annealed materials with no secondary phases present and no grain boundary segregation, oxalic acid etches the grains of the material based on crystallographic orientation and does not attack grain boundaries. However, oxalic acid is known to vigorously attack GB Cr-rich carbides. In the current work, it was determined that oxalic acid also attacks nitrides (Cr_2N) and was therefore used to detect the early precipitation of GB nitrides. On the other hand, a solution of 10% HCl/methanol, used electrolytically, was found to attack the austenite phase, but not the Cr-rich Cr_2N nitrides. This etchant was used to prepare samples with larger volume fractions of nitrides for metallographic and SEM examination. An aqueous solution of 60% HNO_3 was used to etch (electrolytically) the grain boundaries of materials prior to grain size measurement. This solution tends to provide better grain boundary attack of SSs than other etchants and does not generally attack twin boundaries.

Examinations

Metallographically prepared specimens were examined and photographed at magnifications ranging from 50 to 1,000X magnifications using a Nikon Epiphot inverted metallograph. Samples were examined with normal bright-field illumination, Nomarski interference contrast, and polarized light.

Grain Size Measurements

Since complete GB etching of solution annealed austenitic SSs is not possible because the GBs are not aggressively attacked by known etchants, the solution annealed materials were aged at 800°C for one hour prior to grain size measurement. This heat treatment provided almost 100% coverage of the grain boundaries by Cr-rich Cr_2N nitrides which assured attack during etching. The samples were

electrolytically etched with an aqueous solution of 60% HNO_3. Grain growth at this temperature was assumed to be negligible.

The ASTM grain size of each specimen was measured using the three-circle method outlined in ASTM E 112.[96] The test pattern for grain size measurement consisted of three concentric circles having a total circumference of 500 mm. The pattern was successively applied to at least five blindly selected areas from each sample and the number of grain boundary intersections counted for each area. The ASTM grain size number and mean intercept distance (average grain diameter in microns) were subsequently determined using the charts, graphs, and procedures outlined in ASTM E 112.

Image Analysis

Microstructural features were quantitatively analyzed using a Leco Model 2001 image analysis unit connected to the Nikon Epiphot metallograph. Image analysis was used to measure inclusion counts in annealed materials and area fractions of second phases. At least twenty fields, blindly chosen, were used for each analysis and the results averaged to obtain the final numbers.

X-ray Diffraction Analysis

One of the methods used for identification of primary and precipitate phases in the materials was X-ray diffraction (XRD). Specimens were analyzed using Ni filtered Cu-K_α radiation and accepted XRD analysis procedures. Two methods of sample preparation were utilized to extract precipitate phases from the two alloys prior to powder diffraction analysis of the residues. In one case, a 1:1 solution of $HCl:H_2O$ was used to dissolve the matrix. In the second method, electrolytic dissolution of the matrix was achieved using a solution of 10% HCl/methanol. The residues were filtered onto a glass micro-fiber filter and washed with methanol.

Scanning Electron Microscopy

Energy dispersive X-ray spectroscopy (EDS) microanalyses of inclusions in the materials were performed using a JEOL JSM35 scanning electron microscope. An electron microprobe analyzer, equipped with a wavelength dispersive X-ray spectrometer (WDS), was also used for inclusion analysis at the US Bureau of Mines Albany Research Center. Examination of metallographically prepared specimens and fractographic analysis of impact specimens was conducted using a Zeiss digital scanning electron microscope (DSM960).

Transmission Electron Microscopy

Specimens for TEM were prepared by electric-discharge-machining (EDM) 3 mm diameter cylinders from each material. Slices (250 μm thick) were cut from the cylinders using a high-speed cut-off saw equipped with a 0.5 mm thick bonded Al_2O_3 abrasive blade and sufficient liquid cooling so as to avoid heating of the samples. Slices were mounted on 25 mm diameter aluminum blocks using a low-temperature melting wax. The slices were subsequently ground to 50-100 μm in thickness using wet grinding techniques and SiC abrasive papers finishing with a 600 grit finish on each side of the disks.

The 3 mm diameter disks, with a 600 grit finish, were subsequently twin-jet electropolished using a Mark 2 model Metalthin unit. Electropolishing was done using a solution consisting of 144 ml methanol, 36 ml H_2SO_4, and 20 ml glycerin. Polishing was done at room temperature, a jet speed setting of 4.25, 6 volts, and currents of about 44-52 mA.

For comparative purposes, thin sections were cut from bulk specimens using the high-speed cut-off saw described above, and the microstructures compared to specimens removed by EDM. Also, EDM materials were metallographically prepared

and examined for heating effects. Results of metallographic examination and comparative TEM indicated that no microstructural changes were induced in the materials due to the EDM process.

Carbon Extraction Replicas

Nitrides were removed from the materials for analysis using carbon extraction replication. Metallographically polished specimens were electrolytically etched using a 10% HCl/methanol solution which etched the matrix and left the carbides in relief. A thin layer of carbon (estimated to be 30-60 nm in thickness) was then evaporated onto the samples. The surface of each sample was scored into small squares (about 1-2 mm) and subsequently etched electrolytically with an aqueous 10% oxalic acid solution to dissolve the metal matrix and loosen-up the carbon film. When the carbon started to separate from the surface, the samples were immersed in water and the carbon replica floated on the surface. The carbon extractions were then captured on 3 mm diameter copper TEM grids.

Equipment and Analysis Procedures

A majority of the TEM analyses were conducted using a Hitachi H800 200 KeV analytical electron microscope. The H800 has capabilities for EDS analysis, imaging in standard bright and dark field TEM modes, obtaining selected area electron diffraction patterns (SADPs), secondary electron imaging, and STEM. Calibration of the camera lengths for electron diffraction for specified operating conditions was carried out using a thin film sputter deposited gold on holey carbon film standard. A limited amount of the TEM work was conducted on a 100 Kev JEOL 100CX analytical TEM/STEM. Unless otherwise stated, the procedures and analysis techniques employed for the TEM work were standard techniques listed in many textbooks.

TIME-TEMPERATURE-PRECIPITATION CURVES

Time-temperature-precipitation (TTP) curves were generated to determine the precipitation kinetics in the commercially produced high-nitrogen steels. Two basic approaches are generally used in determining the onset of a given phase reaction, in this case precipitation from a super-saturated solid solution. In the first case, the onset of precipitation is defined by the first observation of a precipitate/phase detectable using a given analytical technique. In the second case, onset would be determined by the presence or formation of a given volume fraction of the second phase. The reaction TTP curve would thus be defined by progression of the given reaction to a certain percentage of completion.

In the current study, TTP curves for precipitation of a particular phase (Cr_2N), were defined as a function of where precipitation took place. This was done for (1) grain boundary precipitation, (2) cellular decomposition of the austenite which resulted in a lamellar structure, and (3) transgranular precipitation. Onset of precipitation for all three cases was defined by the first detectable precipitation using a given technique. This method was preferred because the confidence was high for detecting precipitation at extremely low volume fractions in the present materials. For instance, grain boundary precipitates could be detected when they were present at less than 5% of the grain boundaries. Cellular precipitation could be detected when present at volume fractions of less than 0.5%.

GRAIN BOUNDARY CHROMIUM-DEPLETION

Indirect Measurement

The DOS of each test specimen was measured using the single-loop EPR test and the testing methods proposed by Clarke et al..[78,97] The nomenclature and definition of terms for EPR testing were outlined in a previous section. Normalized

charge values [Pa (coul./cm^2)], which corrects for grain size differences between samples, were calculated although all samples tested had identical grain sizes. This is because it has become standard practice to report the DOS in terms of the Pa value. The integral charge value, Q, was normalized to the grain boundary area (GBA) of each test specimen to obtain the Pa value, using the following relationship outlined by Clarke et al.:[78]

$$Pa\ (coul/cm^2) = \frac{Q}{(GBA)} \qquad [18]$$

where GBA is the grain boundary area (cm^2) defined by the following equation:

$$GBA = As[5.1\ x\ 10^{-3}\ \exp(0.35X)] \qquad [19]$$

where As is the masked specimen area (cm^2) and X is the ASTM grain size of the material.

The electrochemical test cell (corrosion cell) used for EPR testing consisted of a specimen holder, reference electrode (SCE, saturated calomel electrode), counter electrode (graphite), and working electrode (sensitized specimen).

The standard heat treat specimens described previously were used for EPR testing. A SS screw was attached to the backside of each specimen as an electrical connection. The specimens were subsequently mounted in an epoxy resin (room temperature cured), metallographically prepared using standard practices and silicon-carbide abrasive papers of 120 through 600 grit sizes, and final polished with 6 and 1 micron diamond pastes on nylon cloths. A circular area (6 mm dia. circle) of each sample was masked off for EPR testing using a specially prepared tape. The specific parameters of the EPR test are listed in *Table 7.*

After the test cell was set-up with the sample in-place and the electrolyte at the proper temperature, the EPR test was performed in the following manner: (1) the open-circuit corrosion potential (Ec) of the working electrode vs. SCE was measured; (2) the sample was passivated at an Ep of +200 mv for 2 minutes; (3) the

reactivation scan was performed by sweeping the potential of the sample from the Ep to Ec at a rate of 3 volts/hour; and (4) the area of the reactivation peak was integrated during the reactivation scan to obtain the total charge value, Q.

Direct Measurement

Analysis of chromium composition profiles at GBs was done using the Hitachi H800 operated in the STEM mode at 200 KeV with the X-ray analysis done using an EDS detector and Tracor Northern Model 5500 computer system. The spot size was estimated to be less than 25 nm measured from micrographs of contamination spots produced on the specimen surface by the electron beam operating in the STEM spot mode. Quantitative calculations of the compositions of the materials were made using software developed for the Tracor Northern system which could deconvolute the overlapping Cr-Kα and Mn-Kα peaks.

A special isothermal aging treatment was conducted on a solution annealed (1150°C for 2 hours) DPSC 2100 specimen in order to create a sample with wide nitride spacing on the GBs (high-temperature aging) and low GB Cr-minimum values (low temperature aging). It was believed that measurement of GBCD would be easier in this "specially" heat treated sample compared to samples isothermally aged at one particular temperature. The sample was first aged at 1050°C for 1 hour in order to produce a GB structure which consisted of nitrides which had a finite but definite spacing (i.e. not a continuous GB nitride structure). However, this heat treatment temperature (1050°C) was expected to be much higher than that which would produce matrix Cr-depletion. Therefore, the sample was subsequently heat treated at 750°C for 1 hour, followed by aging at 650°C for 1.5 hours. It was anticipated that this special heat treatment would produce a material condition where GBCD due to the precipitation of Cr-rich Cr_2N nitrides, if present, could be directly measured.

TABLE 7 - Parameters of EPR Testing	
Sample Surface Finish	1 μm Diamond Polish
Electrolyte	0.5M H_2SO_4 + 0.01M KSCN
Electrolyte Temperature	30°C +/- 1°C
Corrosion Potential (Ec)	-0.22 to -0.33 volts
Passivation Potential (Ep)	+0.200 volts
Reactivation Scan Rate	3 volts/hour
Instrument	Instruspec Model WC-5 Metal Sensitization Detector

CHARPY V-NOTCH IMPACT TESTING

A Tinius Olsen Charpy impact testing machine was used to measure the impact toughness of solution annealed and aged materials using the procedures outlined in ASTM E 23-86.[98] Reduced thickness, standard subsized (Type A) Charpy specimens (55x10x5 mm^3) were used since annealed SS materials are known to possess very high impact toughness at room temperature and the ultimate limit of the testing machine was 350 joules. The specimen orientation relative to the original billets was shown in *Figure 6*. Impact testing was done at ambient temperature.

RESULTS and ANALYSIS

SOLUTION ANNEALED MATERIALS

Microstructure

Grain growth as a function of solution annealing temperature/time for heats DE 257 and DPSC 2100 is illustrated in *Figure 8*. Grain size measurements are listed in *Table 8*. After annealing at 1100°C for 1 hour, the average grain size of heat DPSC 2100 was 47 microns compared to 29 microns for heat DE 257. For comparable heat treating temperatures and times throughout the range 1100 to 1250°C, grain sizes for heat DPSC 2100 were consistently larger than for heat DE 257. Comparison of grain growth for the two alloys at 1150°C for times between 0.5 and 10 hours shows that the rate of grain growth was faster for heat DPSC 2100 *(Figure 9)*. The percentage change in average grain diameter from 1150°C/0.5 hours to 1150°C/10 hours for heat DPSC 2100 was 105%, while it was only 27% for heat DE 257.

Large volume fractions of transgranular second-phase particles were present in DE 257 materials (alloyed with strong nitride formers Al, Nb, and V) in the as-forged state and after solution annealing. In contrast, the DPSC 2100 material contained very few inclusions. This is illustrated in the optical micrographs of *Figures 10 and 11*. After solution annealing at 1150°C for 2 hours, significantly more inclusions were present in heat DE 257 than heat DPSC 2100 *(Figure 11)*. In the as-forged condition and after solution annealing at temperatures below 1150°C, the inclusions in heat DE 257 were segregated into clusters *(Figure 10a)*. Thus, these materials contained regions of high and low inclusion densities and the inclusions were not

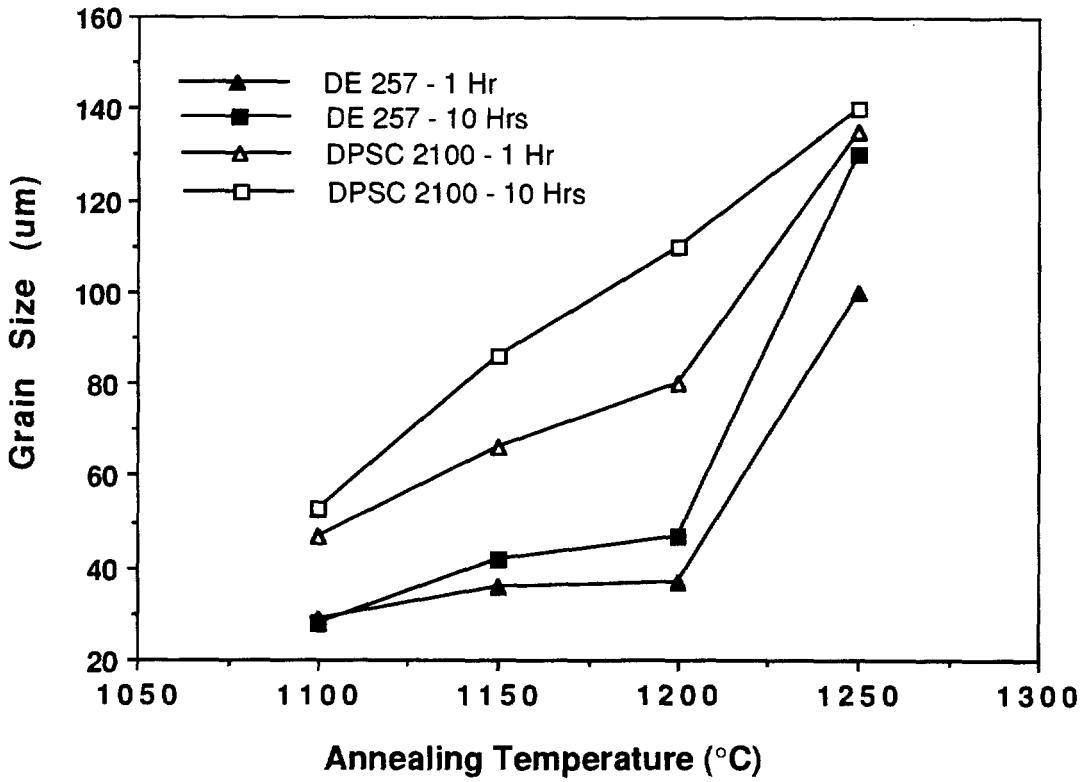

Figure 8. Grain size as a function of solution annealing temperature and time (1 and 10 hours) for heats DE 257 and DPSC 2100.

evenly distributed. Solution annealing at temperatures between 1150 and 1250°C for times longer than about 0.5 hours, reduced the amount of inclusion clustering in heat DE 257 materials (compare micrographs of *Figure 10a and 10b).*

For the purposes of this manuscript, the term inclusion will be used to define second-phases present in as-forged materials that were retained, at least to some degree, after solution annealing. This will hopefully eliminate confusion of these phases with precipitates which formed during aging treatments, after solution annealing.

Chemical analyses (using WDS and EDS) showed that about 90% of the second phase particles in Heat DE 257 were Nb-rich. Results of X-ray diffraction analysis indicated that only one phase was present in extracted residues of annealed

TABLE 8 - Grain Size as a Function of Solution Annealing				
Solution Annealing (°C - Hours)	DE 257		DPSC 2100	
	ASTM #	(μm)	ASTM #	(μm)
1100 - 0.5	6.6	33	5.8	42
1100 - 1.0	6.7	29	5.5	47
1100 - 10	6.8	28	5.2	53
1150 - 0.5	6.6	33	5.0	55
1150 - 1.0	6.5	36	4.6	66
1150 - 2.0	5.9	40	4.2	72
1150 - 10	5.8	42	3.8	86
1200 - 1.0	6.2	37	4.0	80
1200 - 10	5.5	47	3.1	110
1250 - 1.0	3.3	100	2.6	135
1250 - 10	2.7	130	2.4	140

DE 257 materials, a Nb-rich nitride (Z-phase), designated NbCrN. *Figure 12* shows XRD spectra typical of extracted residues from solution annealed DE 257 materials. This phase has previously been reported to form in steels with base compositions similar to DE 257.[99-101]

Hughes[99] reported the NbCrN nitride to have a tetragonal crystal structure with $a = b = 0.6784$ *nm* and $c = 0.736$ *nm* (P4/nmm space group), with a compound structure $(CrFeMn)_4(NbMo)_3N_3$. Jack and Jack[100] reported the same nitride (samples taken from Hughes' work) to have a tetragonal structure (P4/nmm space group) with a = b = 0.3037 nm, c = 0.7391 nm, and a compound structure of $Nb_2Cr_2N_2$. Their results are essentially the same since they result in the same d-spacings being reported for the phase, with very minor differences.[100]

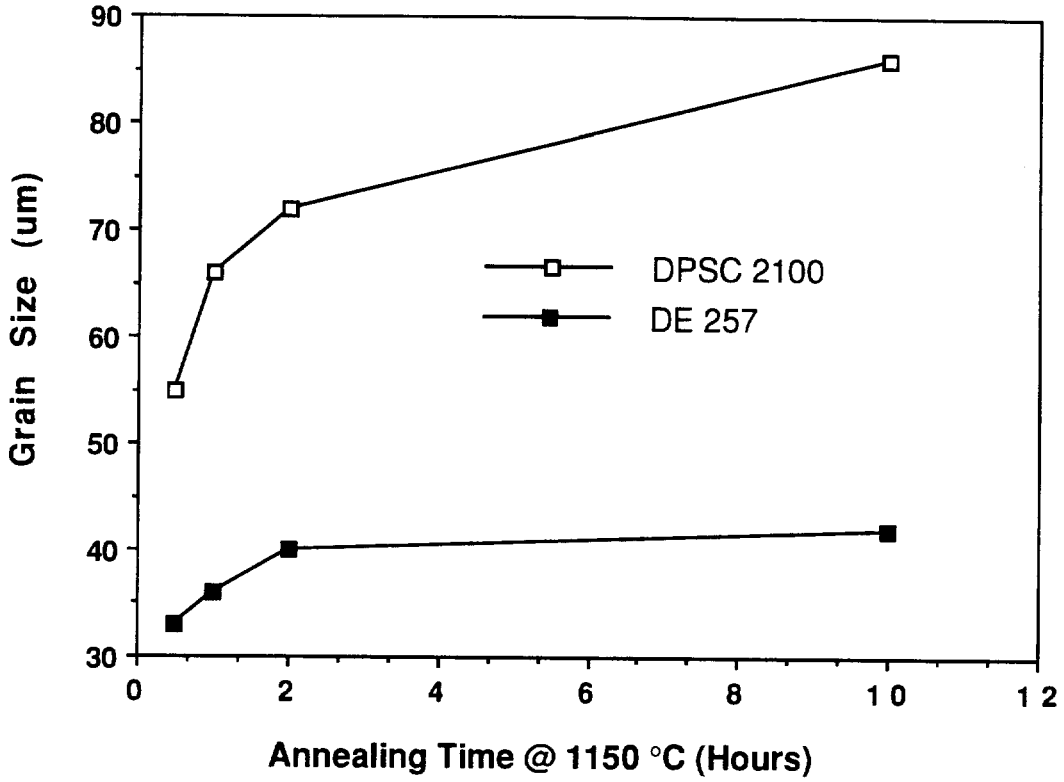

Figure 9. Grain size as a function of solution annealing time at a temperature of 1150°C for heats DE 257 and DPSC 2100.

Results of thin-section TEM and SADP analyses correlated well with the XRD results. Electron diffraction patterns and d-spacing measurements taken from Nb-rich precipitates in DE 257 materials solution annealed at 1150 and 1250°C matched with d-spacings and computer generated diffraction patterns for the NbCrN nitride. Bright-field (BF) TEM micrographs and representative diffraction patterns from the inclusions are presented in *Figure 13* and indexed diffraction patterns shown in *Appendix C.*

Chemical analysis by STEM/EDS of the metallic species in the precipitates (from extraction replicas) correlated very well to the compositions reported for this phase by Hughes[99] as shown in *Table 9.* The analysis by Hughes was done on bulk

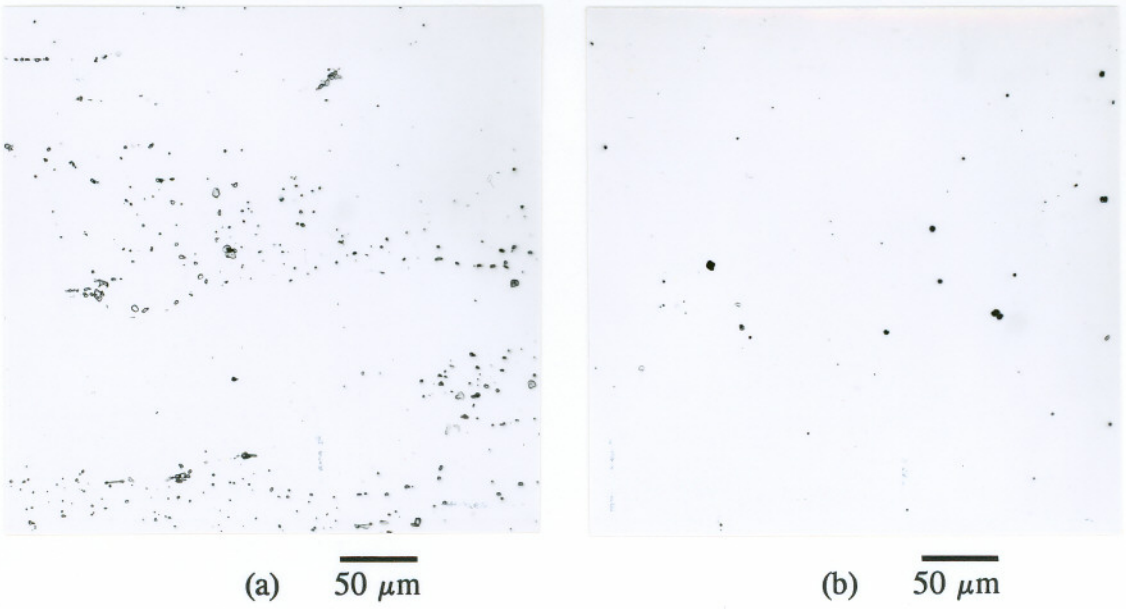

Figure 10. Optical micrographs of un-etched specimens from heat DE 257 solution annealed at (a) 1100°C for 1 hour and (b) 1250°C for 10 hours.

extracted samples and therefore a full composition analysis, including carbon and nitrogen, was obtained.

It should be noted that the NbCrN nitrides did not form as a result of solution annealing, but were present in the as-forged DE 257 material. The NbCrN nitrides were observed to slowly dissolve during solution annealing, however, dissolution was incomplete. Nb-rich (NbCrN) nitrides were still present in samples heat treated at temperatures as high as 1250°C for 10 hours. Heat treating at higher temperatures to attempt to achieve total dissolution was considered to be impractical.

Nitride solubility was studied as a function of annealing temperature/time by measuring the density of precipitates in samples using image analysis of metallographically prepared sections. These results are given in *Figure 14 and Table 10*. The density and total number of precipitates decreased with increasing annealing temperature and was much less after annealing at 1250°C for 10 hours than after annealing at 1100°C for 1 hour (reference *Figure 10 and Table 10*). It is apparent from the graph of *Figure 14* that the total number/density of precipitates did not

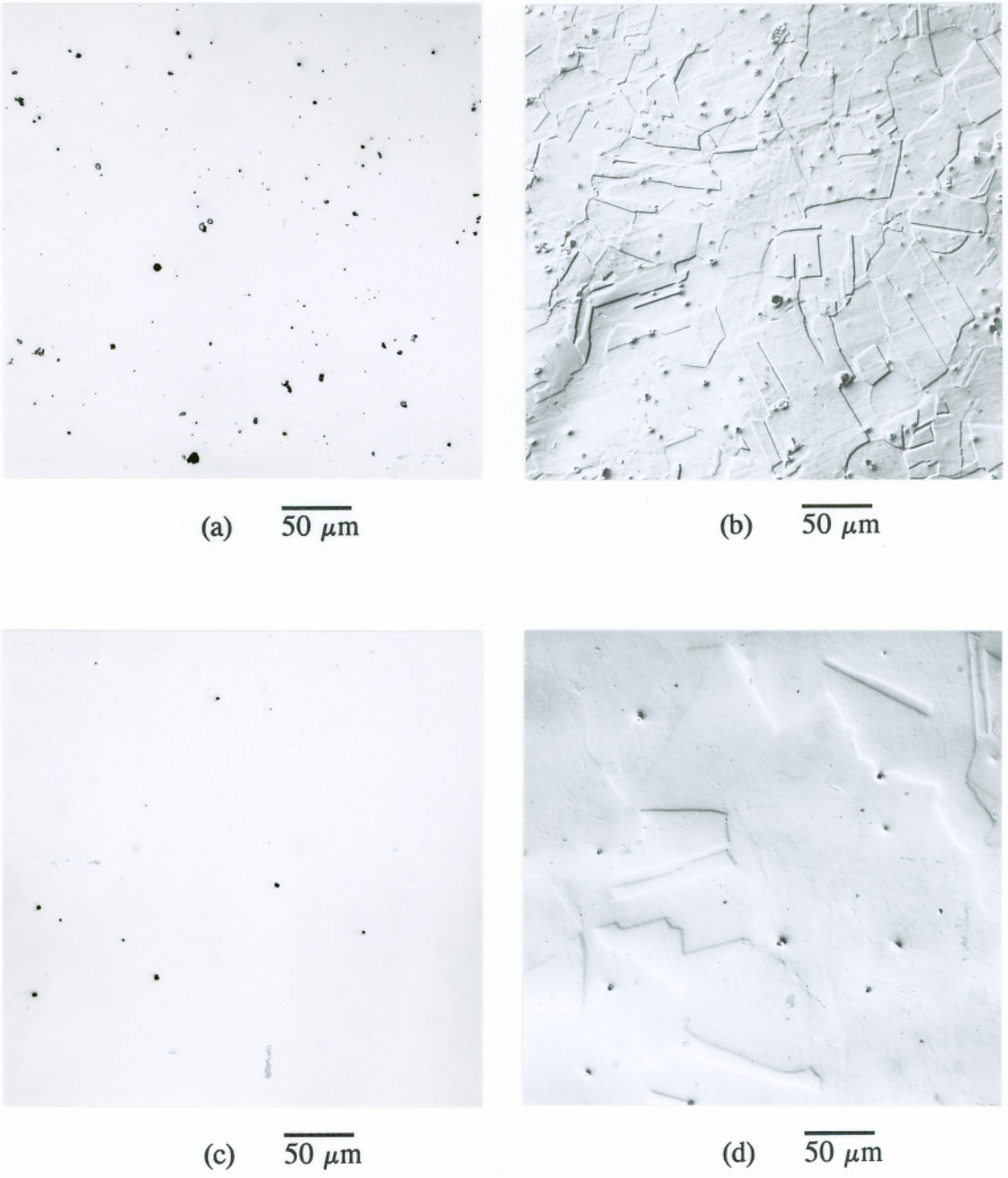

Figure 11. Optical micrographs of specimens from heats (a,b) DE 257 and (c,d) DPSC 2100 solution annealed at 1150°C for 2 hours [(a,c) un-etched, (b,d) etched electrolytically with 10% oxalic acid].

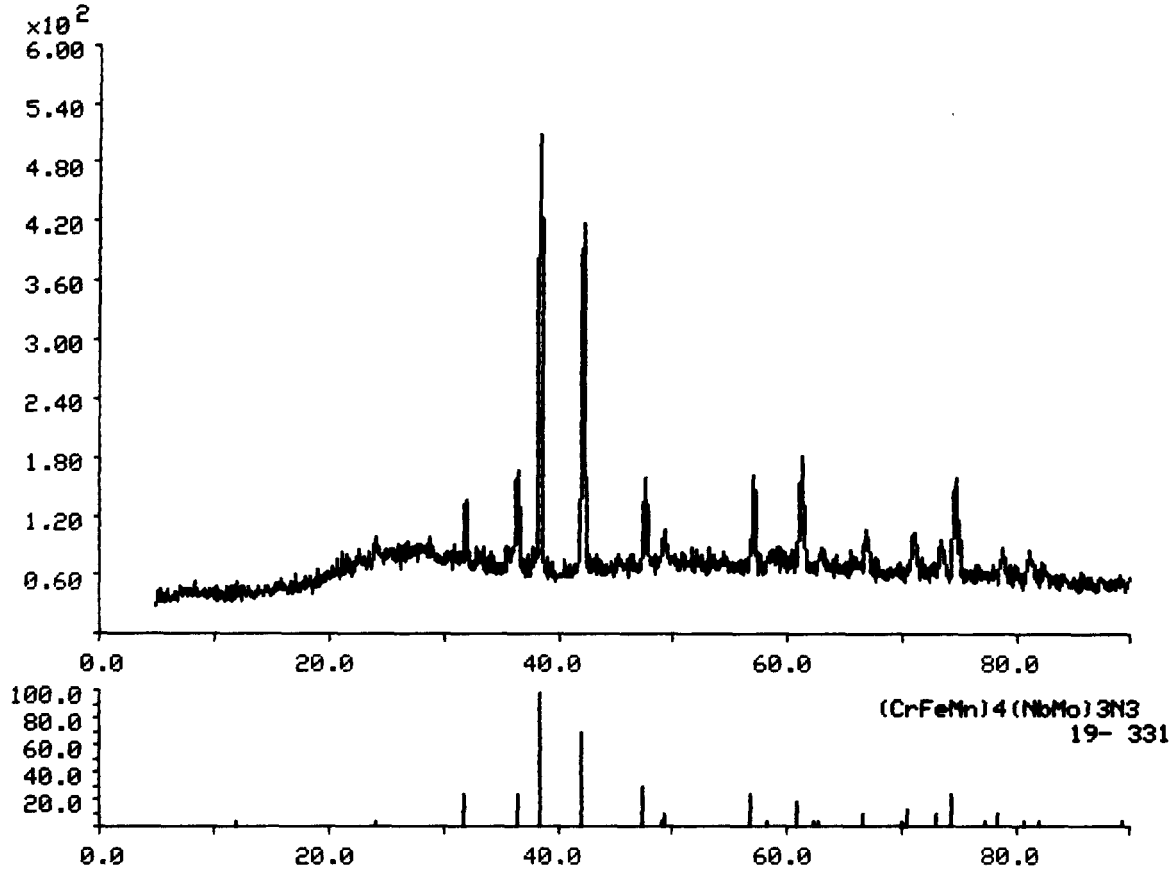

Figure 12. X-ray powder diffraction spectra for extracted residue from heat DE 257 solution annealed at 1150°C for 2 hours.

significantly decrease from solution annealing at 1250°C as compared to 1200 or 1150°C, except for very short times. The standard deviations for the density measurements are quite large, especially for short annealing times. However, microscopic observations revealed that precipitate clustering was significantly reduced by annealing at higher temperatures and/or longer times. The large standard deviations for precipitate counts at low annealing temperatures and short times also indicated that precipitate clustering was significant and influencing measurement statistics *(Table 10)*. At higher annealing temperatures, and/or longer times at a given temperature, the measurement statistics were much more consistent indicating that the precipitate segregation/clustering was essentially eliminated.

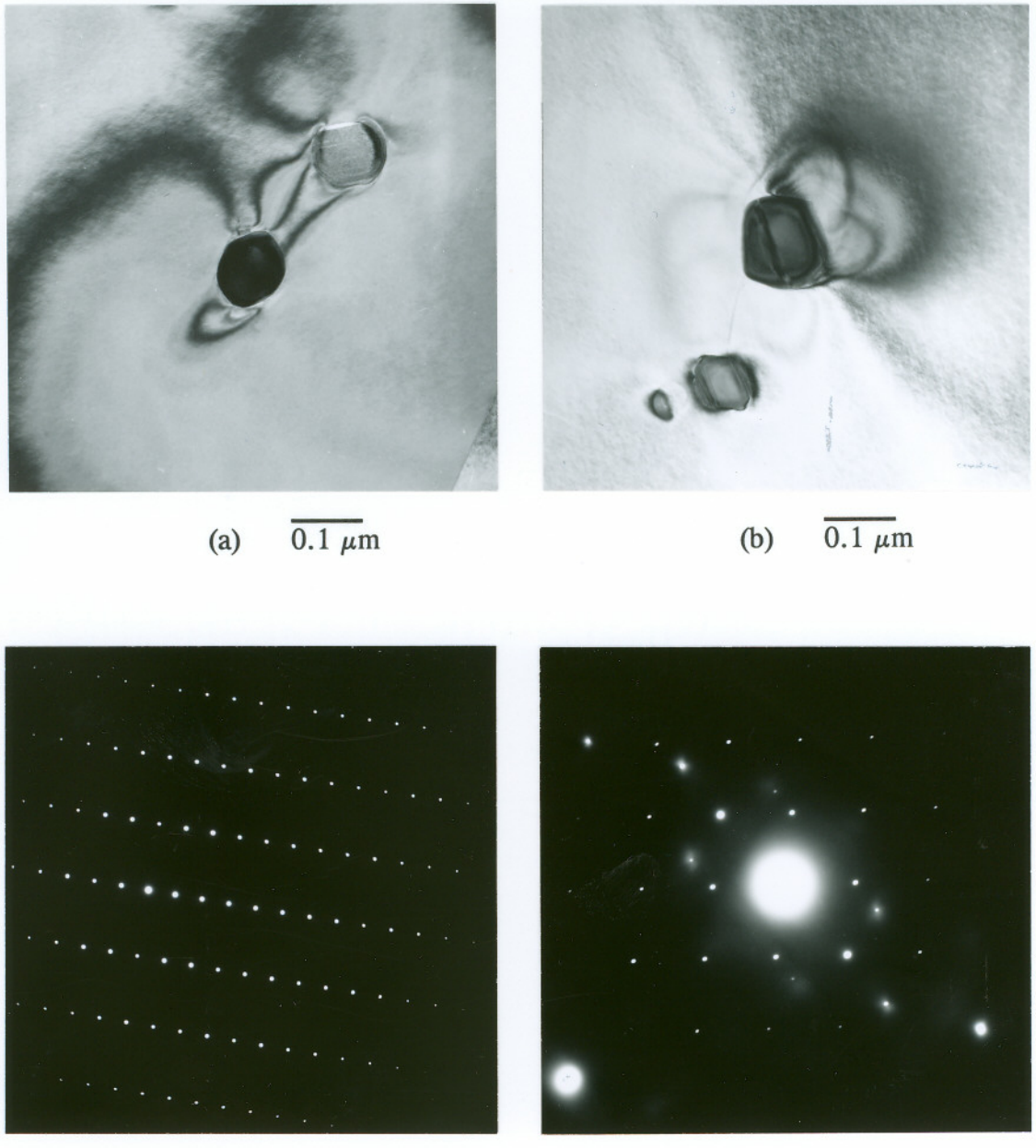

Figure 13. TEM bright-field micrographs (a,b) of NbCrN nitrides present in solution annealed materials from heat DE 257. Electron diffraction patterns of NbCrN nitrides at zone axis (c) [100] and (d) [111].

TABLE 9 - NbCrN (Z-Phase) Precipitate Compositions			
Element (wt%)	Hughes[99]	DE 257*	DE 257**
Nb	44.9	52.0	49.0
Cr	22.9	30.5	28.6
Mo	3.8	6.7	6.3
Fe	5.1	5.8	5.3
V	---	3.3	3.0
Mn	2.2	ND	ND
Ni	0.3	0.5	0.4
Si	---	1.2	1.0
C	0.2	---	---
N	6.4	---	6.4

* Actual Analysis
** Normalized Assuming Nitrogen Content of 6.4 wt%
ND = Not Detected

Impact Toughness

Room temperature impact toughness of DE 257 and DPSC 2100 materials was measured as a function of solution annealing temperature/time with the results shown in *Table 11* and *Figure 15* (NOTE - results are for 1/2 thick Charpy impact specimens). For purposes of comparison, the room temperature impact energy of an annealed AISI type 316 SS is also shown in *Figure 15*.

As-forged DE 257 materials and those annealed at 1050°C had extremely low impact toughness values at room temperature *(Figure 16)*. The as-forged materials contained a large amount of Cr_2N, present primarily at GBs, which caused the low impact energies observed. Since the Cr_2N was not dissolved by annealing at 1050°C, samples annealed at this temperature also had very low impact toughness values. The

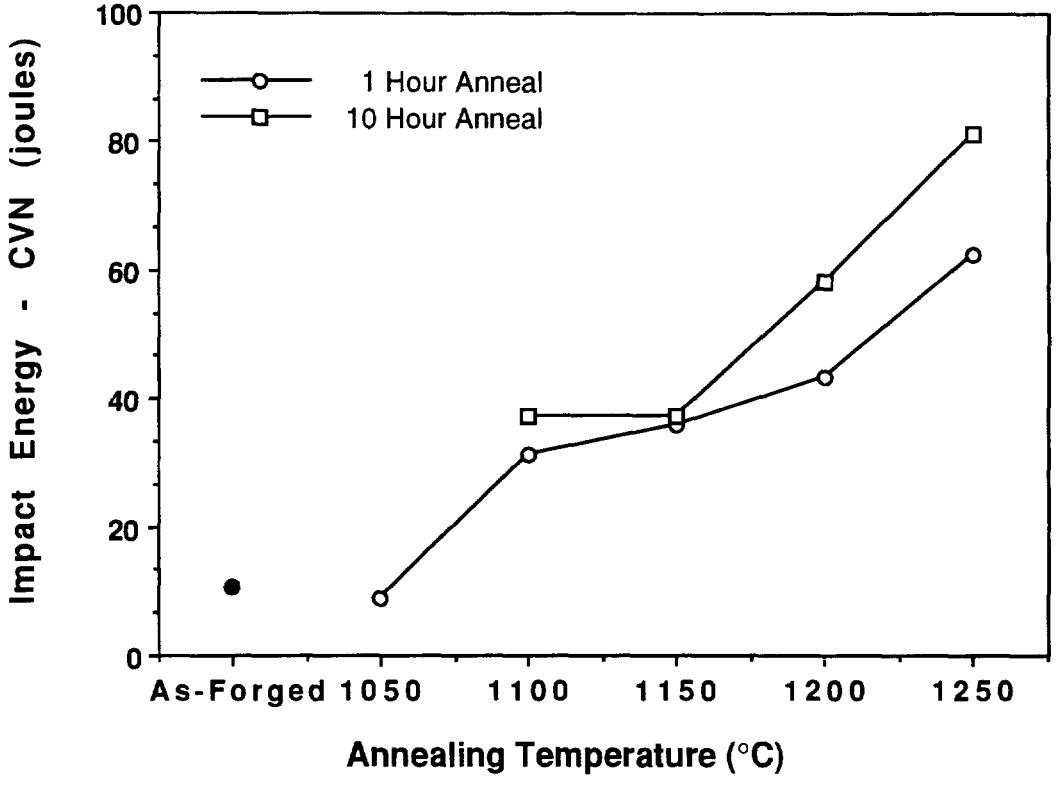

Figure 14. Concentration of precipitates in heat DE 257 as a function of annealing temperature and time (1 and 10 hours).

impact toughness of heat DE 257 materials increased consistently with increasing annealing temperature. Charpy values also increased slightly with increased time at a given annealing temperature. The graph of *Figure 16* shows the impact energies of DE 257 materials as a function of annealing temperature for times of 1 and 10 hours.

The DE 257 material condition which had the highest impact toughness (81 J) was heat treated at the highest temperature, for the longest time (1250°C for 10 hours). This material also had the fewest Nb-rich inclusions and the smallest amount of inclusion clustering. Heat DE 257 samples solution annealed at 1150°C/2 hours had CVN values of only 36 J compared to heat DPSC 2100 at 144 J. The impact toughness of the DE 257 material with the highest value of 81 J was still well below the DPSC 2100 material solution annealed at 1150°C/2 hours (CVN of 144 J).

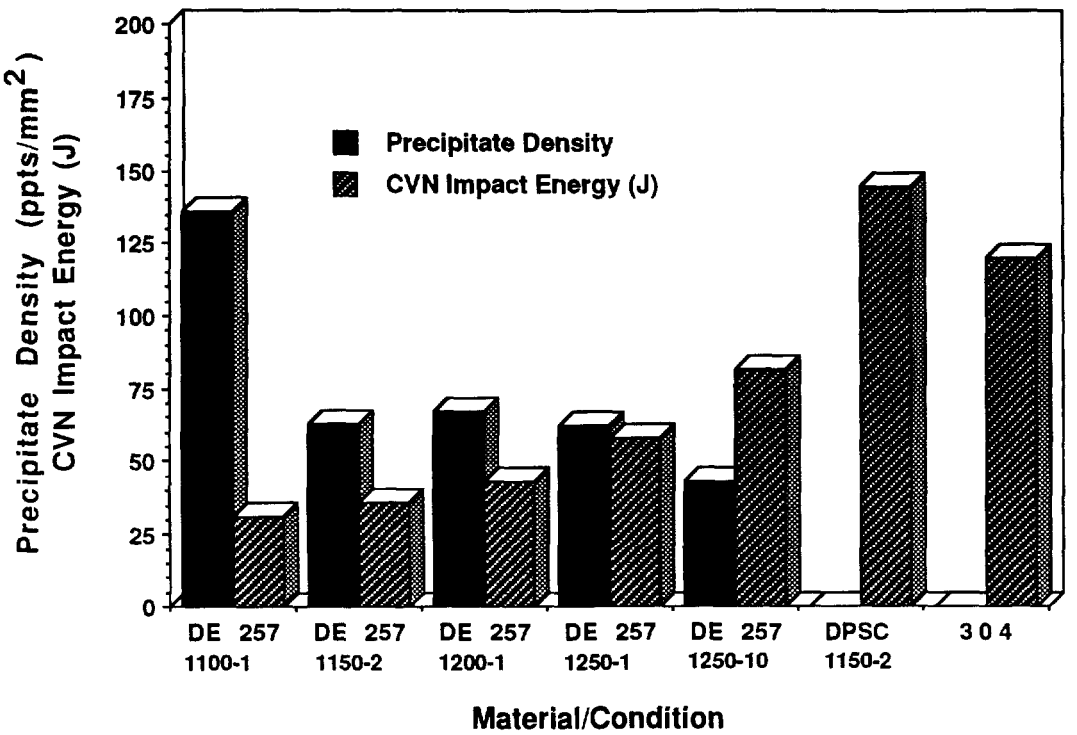

Figure 15. Comparison of impact toughness values (CVN) of solution annealed materials from heats DE 257 and DPSC 2100.

Representative micrographs from the fractographic analyses of impact specimens from solution annealed DE 257 and DPSC 2100 materials are shown in *Figures 17 and 18.* All of the samples from both heats of materials failed in a ductile manner by micro-void coalescence. However, large voids, which contained a high density of inclusions, were present on the fracture surfaces of heat DE 257 samples. Failure in annealed DE 257 specimens occurred by low-energy fracture through inclusion clusters which produced large voids that were connected by ductile fracture of the matrix. Regions characterized by brittle fracture through inclusions were evident in all DE 257 materials, such as those heat treated at 1100°C for 1 hour *(Figure 17a, 17b)*, 1250°C for 10 hours *(Figure 17c, 17d)*, and 1150°C for 2 hours *(Figure 18a, 18b)*. Qualitatively, it can be stated that the number of inclusions

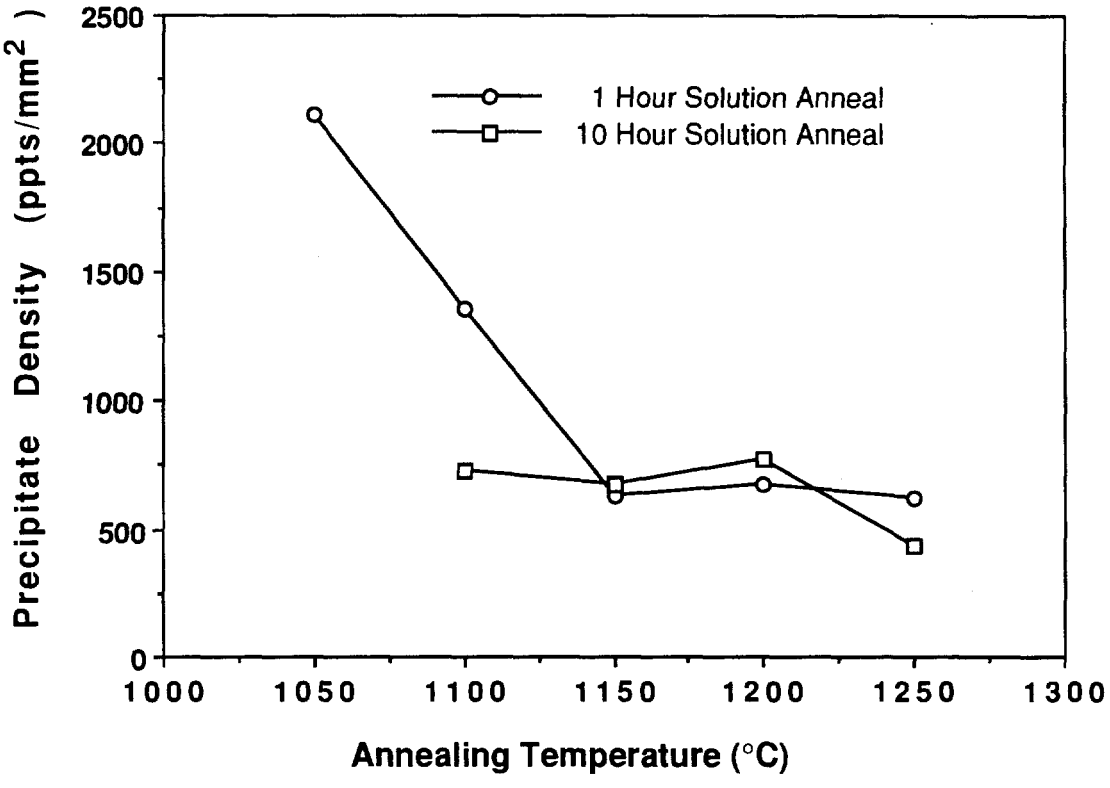

Figure 16. Charpy V-notch values for heat DE 257 materials as a function of annealing temperature and time.

present on fracture surfaces of heat DE 257 samples decreased with increasing solution annealing temperatures and increasing impact energies. As shown in *Figure 18c and 18d*, inclusions were not observed on the fracture surface of heat DPSC 2100 annealed at 1150°C for 2 hours.

TABLE 10 - Heat DE 257 Precipitate Counts Effect of Solution Annealing				
Solution Annealing (°C - Hours)	Precipitate Counts (400x)	Standard Deviation	PPTS #/mm^2 (10^2)	Area (%)
As-Forged	50.76	32.56	11.3	0.525
1050 - 1.0	94.88	27.88	21.1	0.548
1050 - 10	318.4	39.02	70.8	2.06
1100 - 0.1	53.04	16.14	11.8	0.541
1100 - 0.5	64.76	17.57	14.4	0.708
1100 - 1.0	61.12	21.05	13.6	0.747
1100 - 10	32.76	6.16	7.3	0.318
1150 - 0.1	44.52	12.11	9.9	0.348
1150 - 0.5	41.24	6.07	9.2	0.444
1150 - 1.0	28.12	6.21	6.3	0.398
1150 - 2.0	29.72	8.76	6.6	0.394
1150 - 10.0	30.04	4.91	6.7	0.371
1200 - 0.1	55.36	20.05	12.3	0.698
1200 - 1.0	30.40	7.67	6.7	0.529
1200 - 10	34.84	7.44	7.7	0.432
1250 - 0.1	38.56	8.25	8.6	0.479
1250 - 1.0	28.72	5.62	6.2	0.481
1250 - 10	19.52	4.81	4.3	0.287

TABLE 11 - Charpy Impact Toughness of Annealed Materials*

Material	Annealing (°C - Hours)	CVN Energy joules (ft-lbs)
DE 257	As-forged	10.8 (8.0)
	1050 - 1	8.8 (6.5)
	1100 - 1	31.2 (23.0)
	1100 - 10	37.3 (27.5)
	1150 - 2	35.9 (26.5)
	1150 - 10	37.3 (27.5)
	1200 - 1	43.4 (32.0)
	1200 - 10	58.3 (43.0)
	1250 - 1	62.3 (46.0)
	1250 - 10	81.3 (60.0)
DPSC 2100	1150 - 2	144.4 (106.5)

* Testing done at ambient temperature

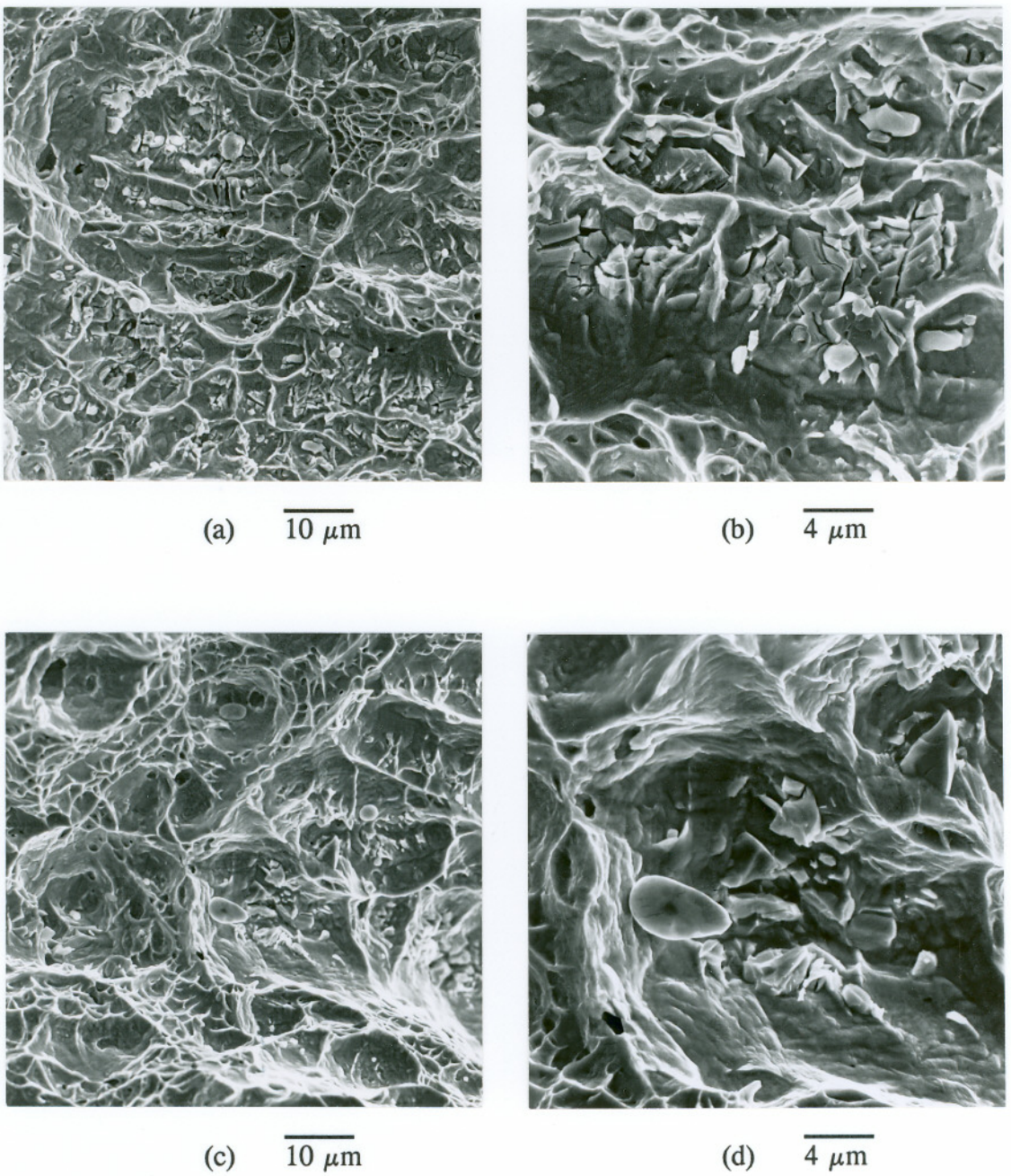

Figure 17. Scanning electron fractographs of impact specimens from heat DE 257 solution annealed at (a,b) 1100°C for 1 hour and (c,d) 1250°C for 10 hours.

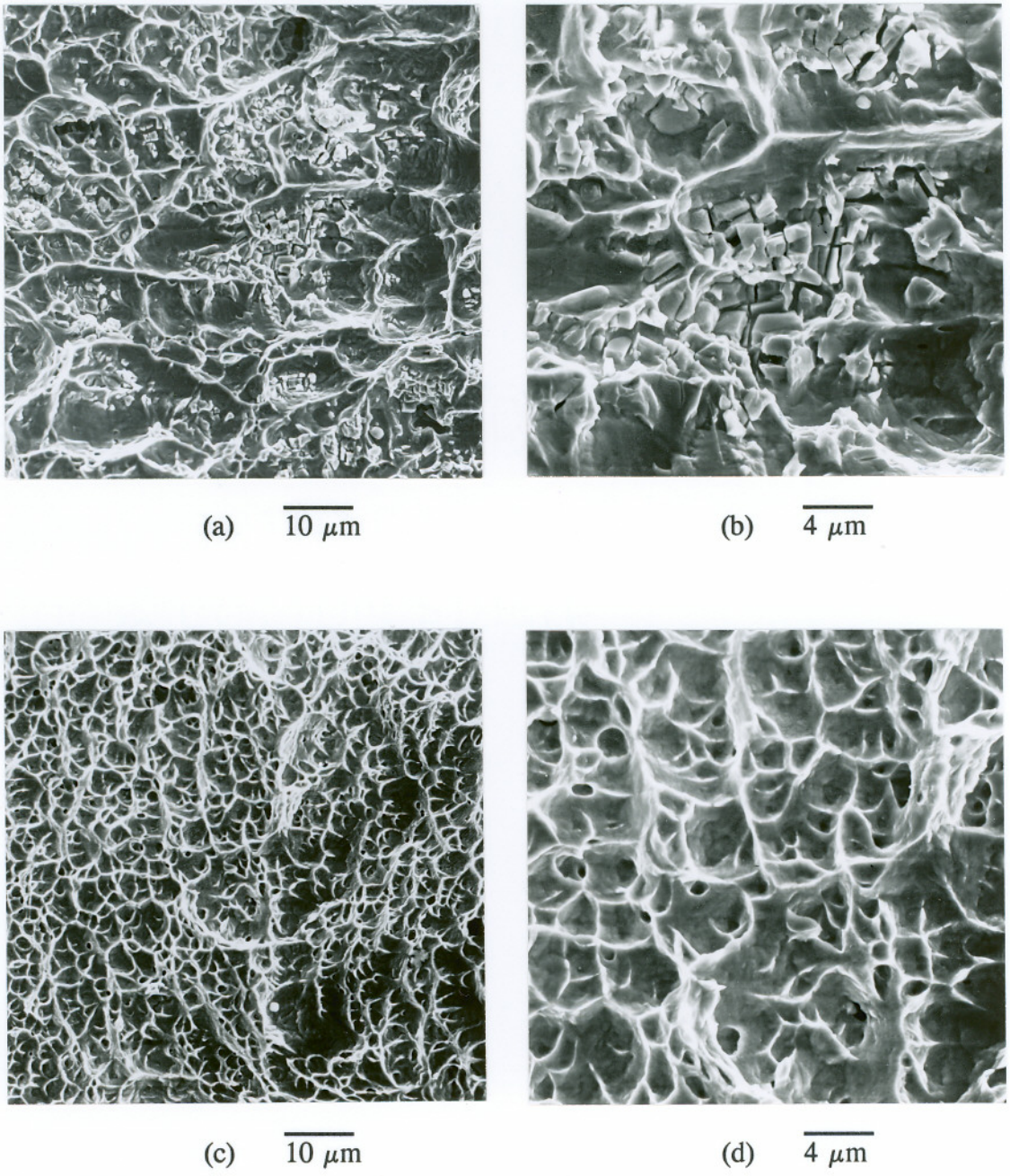

Figure 18. Scanning electron fractographs of impact specimens from materials solution annealed at 1150°C for 2 hours from (a,b) heat DE 257 and (c,d) heat DPSC 2100.

ISOTHERMALLY AGED MATERIALS

Microstructural development (precipitation) in solution annealed materials from heats DE 257 and DPSC 2100 as a result of isothermal aging at temperatures between 600 and 1075°C, for times up to 30 hours, is presented in this section. The results include general microstructural observations, phase identification, morphology, and precipitate analysis using TEM/STEM/EDS.

Microstructures - General

Optical micrographs presented in this section are intended to give the reader a general feel for the structures obtained in heats DE 257 and DPSC 2100 after isothermal aging. Due to the large number of material conditions studied for the two heats (over 100), micrographs will be shown which illustrate general trends or are representative of specific microstructural characteristics.

Optical micrographs taken from heats DE 257 and DPSC 2100 materials aged at temperatures from 750 to 1000°C for one hour are shown in *Figures 19, 20, and 21*. Precipitation of Cr-rich nitrides (Cr_2N) occurred at GBs and within austenite grains. Precipitation within the austenite matrix occurred through two mechanisms. In the first, cells of austenite and Cr_2N, morphologically similar to pearlite in steels, were formed through the cellular decomposition of austenite (discontinuous precipitation). Cellular precipitation nucleated at grain boundaries and subsequent growth occurred into one of the austenite grains. Also, transgranular nucleation and growth of individual precipitates of Cr_2N occurred. All of these structures will be detailed further in subsequent sections.

The micrographs of *Figure 19* illustrate GB precipitation in the two alloys. As detailed earlier, the oxalic acid solution used to etch the materials attacks the Cr_2N precipitates present at the boundaries. Therefore, the degree to which the boundary is etched gives an indication of the amount of precipitate coverage at the GBs. After

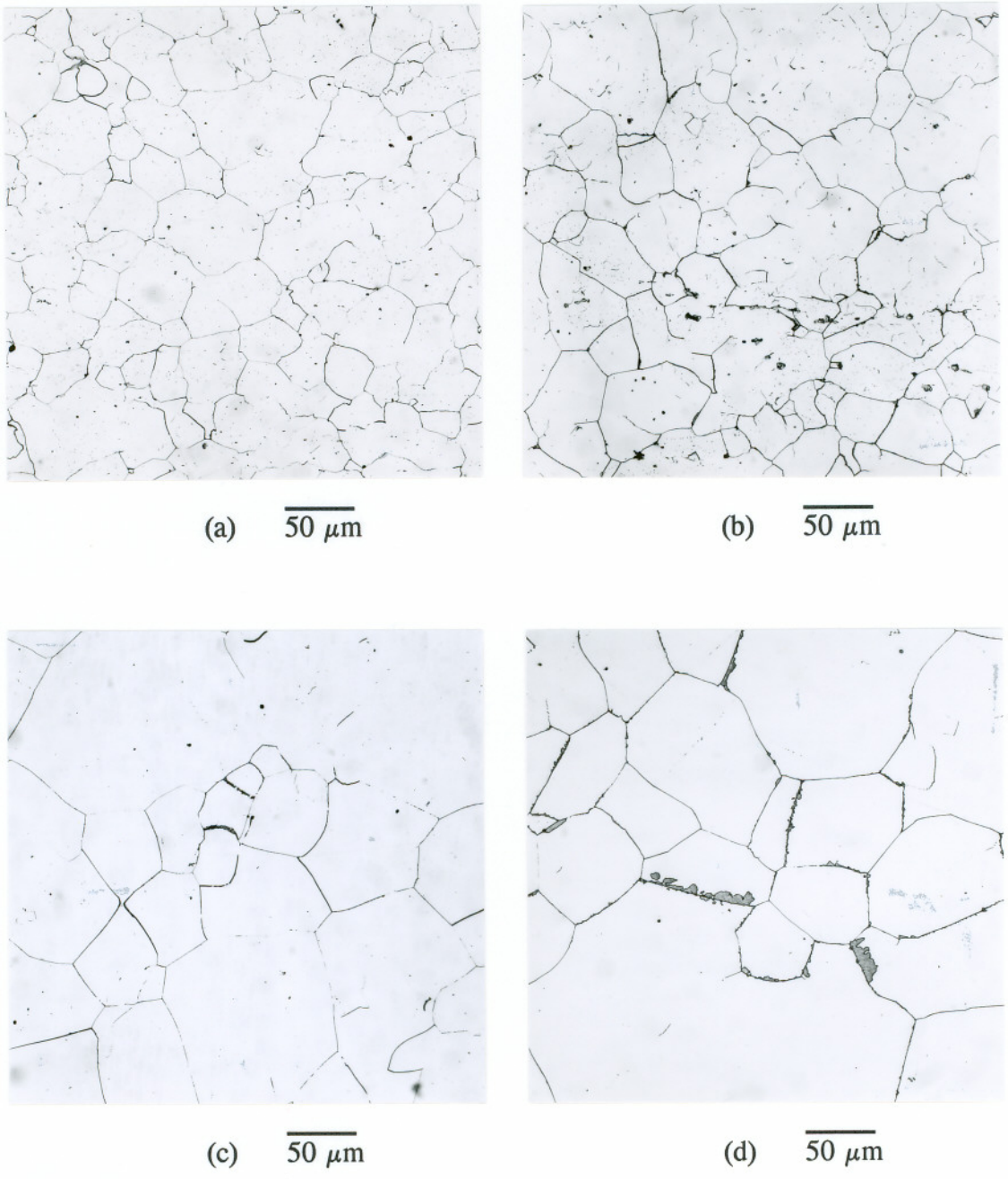

Figure 19. Optical micrographs from heats (a,b) DE 257 and (c,d) DPSC 2100 aged for 1 hour at (a,c) 750°C and (b,d) 800°C.

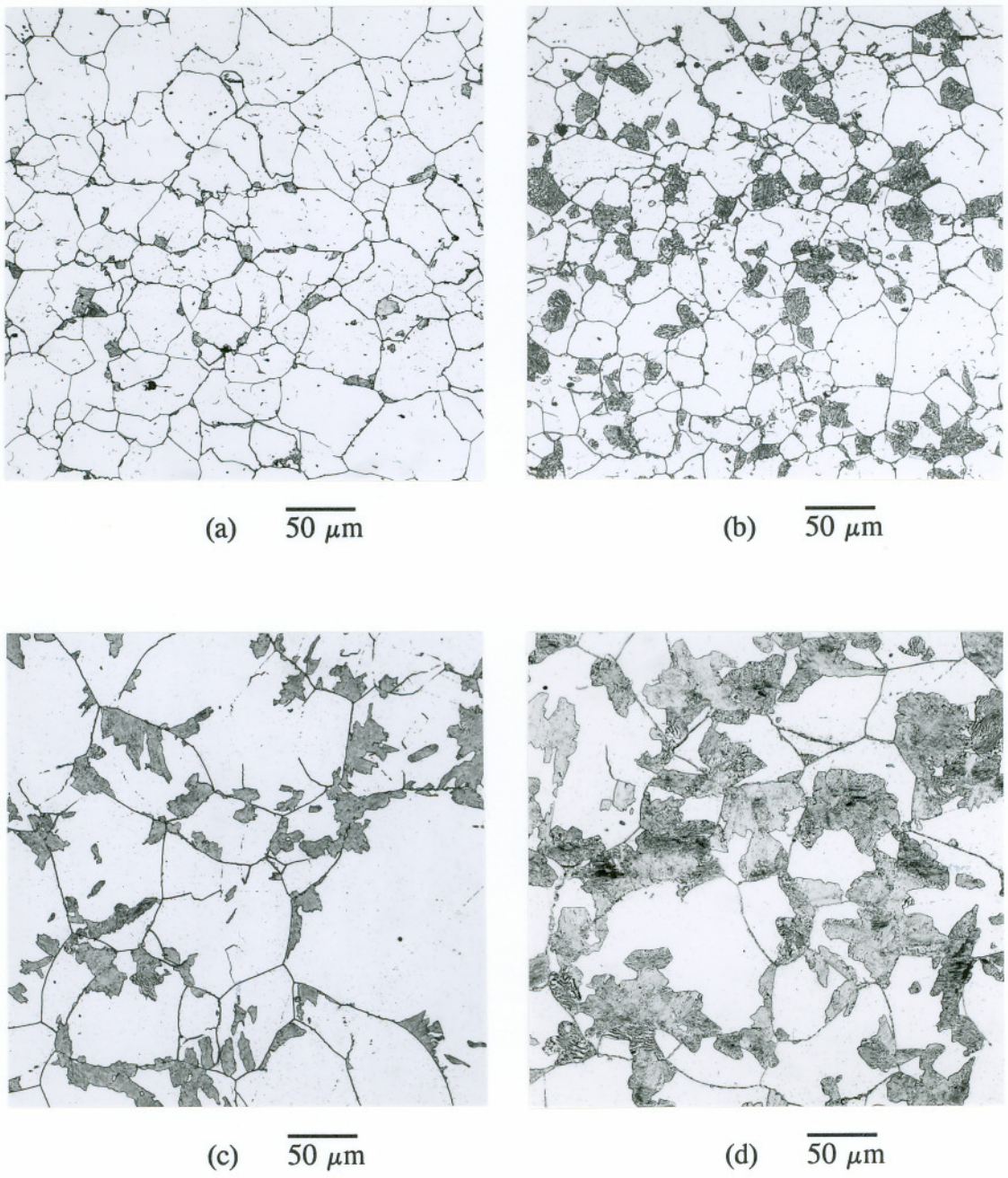

Figure 20. Optical micrographs from heats (a,b) DE 257 and (c,d) DPSC 2100 aged for 1 hour at (a,c) 850°C and (b,d) 900°C.

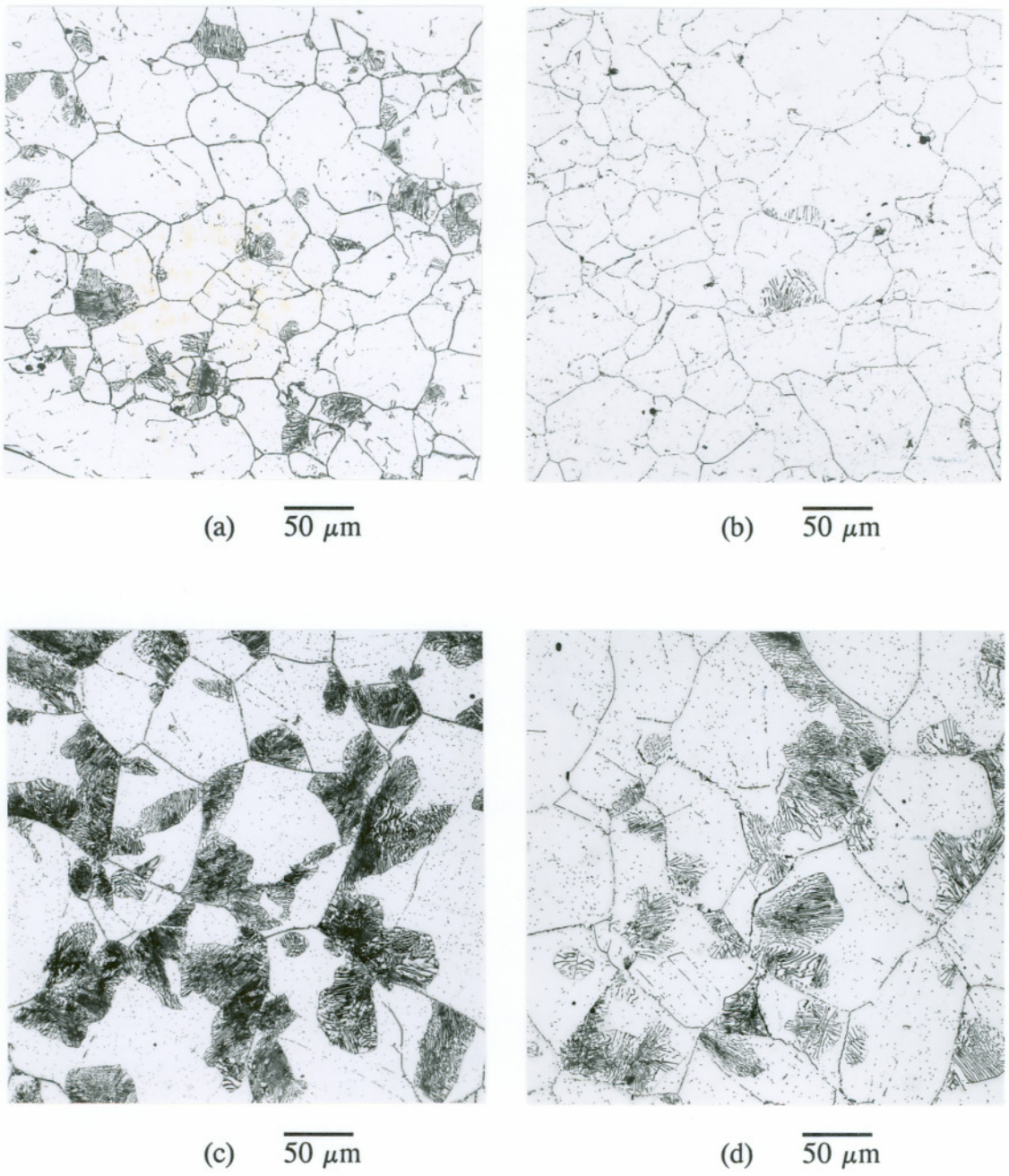

Figure 21. Optical micrographs from heats (a,b) DE 257 and (c,d) DPSC 2100 aged for 1 hour at (a,c) 950°C and (b,d) 1000°C.

aging for 1 hour at temperatures above 750°C and below 1050°C, basically 100% coverage of the GBs was evident. In addition to grain boundary precipitation, significant cellular precipitation of Cr_2N can be seen in the micrographs of *Figures 20 and 21*, taken at temperatures between 850°C and 1,000°C. Cellular and transgranular precipitation of Cr_2N are illustrated in the micrographs of *Figure 22*, taken from heat DPSC 2100 aged at 950°C for 10 hours. Grain boundary precipitation in the two alloys occurred at temperatures as high as 1075°C (*Figure 23*).

X-ray Diffraction Analysis

Results of XRD analyses on extracted residues from selected DE 257 and DPSC 2100 materials are tabulated in *Table 12*. For bulk materials dissolved in a 1:1 HCl/H_2O solution, the Cr_2N present was dissolved, but the NbCrN nitrides were not. In contrast, NbCrN nitrides, known to be present in heat DE 257 for all material conditions, was not detected in extraction residues made by dissolving the material electrolytically with a 10% HCl/methanol solution. Apparently, the electrolytic process used to dissolve the matrix using the 10% HCl/methanol solution, also dissolved the NbCrN nitrides present in the DE 257 materials. The Cr_2N nitrides were not dissolved during the electrolytic dissolution process using the 10% HCl/methanol solution. X-ray diffraction analyses confirmed that nitrides (Cr_2N) were present in all heat DPSC 2100 samples aged at temperatures between 700 and 1,000°C. After aging heat DPSC 2100 materials for 1 hour at either 900 or 1,000°C, Cr_2N was the only precipitate phase detected. Austenite (γFe) was present in most residues analyzed because preferential GB etching and subsequent grain fall-out occurred during electrolytic dissolution. Typical XRD spectra obtained from the powder extraction residues are shown in *Figures 24 and 25*.

After aging both heats (DE 257 and DPSC 2100) for 10 hours at 900°C, additional spectral peaks, in addition to the Cr_2N, were present. The extra peaks,

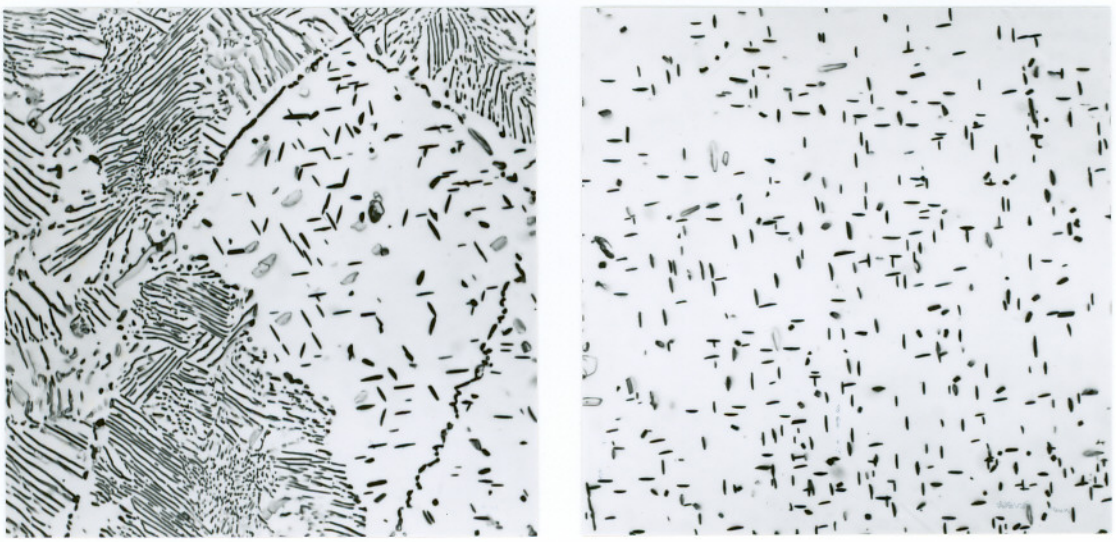

Figure 22. Optical micrographs of heat DPSC 2100 material aged for 10 hours at 950°C.

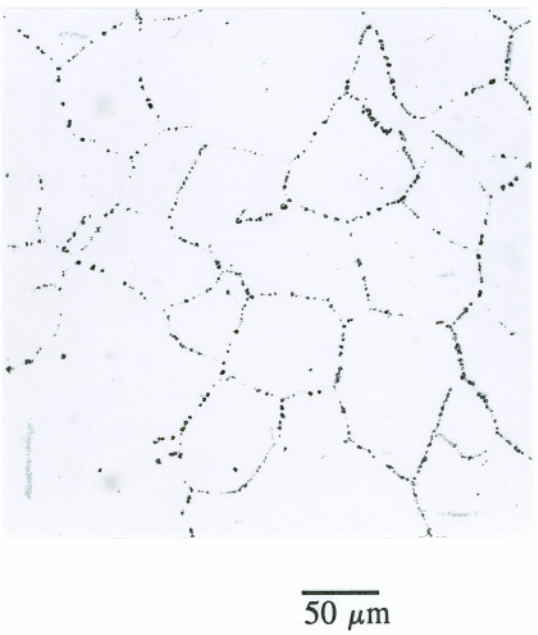

Figure 23. Optical micrograph showing grain boundary precipitation in material from heat DPSC 2100 aged at 1075°C for 1 hour (un-etched).

TABLE 12 - XRD Analysis of Aged Materials*			
Material	Aging (°C - Hours)	Dissolution Technique	Results
DE 257	800 - 10	10% HCl	Cr_2N + γFe (χ-Phase)
	900 - 1	1:1 HCl	NbCrN (Cr_2N - Dissolved)
	900 - 10	10% HCl	(NbCrN - Dissolved) Cr_2N (χ-Phase)
DPSC 2100	700 - 10	10% HCl	Cr_2N + γFe
	800 - 3	10% HCl	Cr_2N + γFe
	900 - 1	10% HCl	Cr_2N + γFe
	CW 900 - 1**	10% HCl	Cr_2N + γFe
	900 - 10	10% HCl	Cr_2N + γFe (χ-Phase)
	1000 - 1	10% HCl	Cr_2N + γFe

* Materials solution annealed at 1150 °C for 2 hours
** CW = Cold Rolled After Solution Annealing

matched with data from the literature, were determined to be due to the presence of an intermetallic, chi (χ) phase. Two χ-phase compounds, with identical crystal structures (cubic, space group I-43m), but slightly different compositions, were found in the literature. These had compositions of $Cr_{12}Fe_{32}Mo_7Ni_7$ (JCPDS-ICDD card # 33-395),[102] and $Cr_{12}Fe_{36}Mo_{10}$ (JCPDS-ICDD card # 31-401)[102], with almost identical lattice parameters reported as 0.8899 nm and 0.8900 nm, respectively. Essentially, there is little distinguishable difference between the two χ phases, except that one contains nickel.

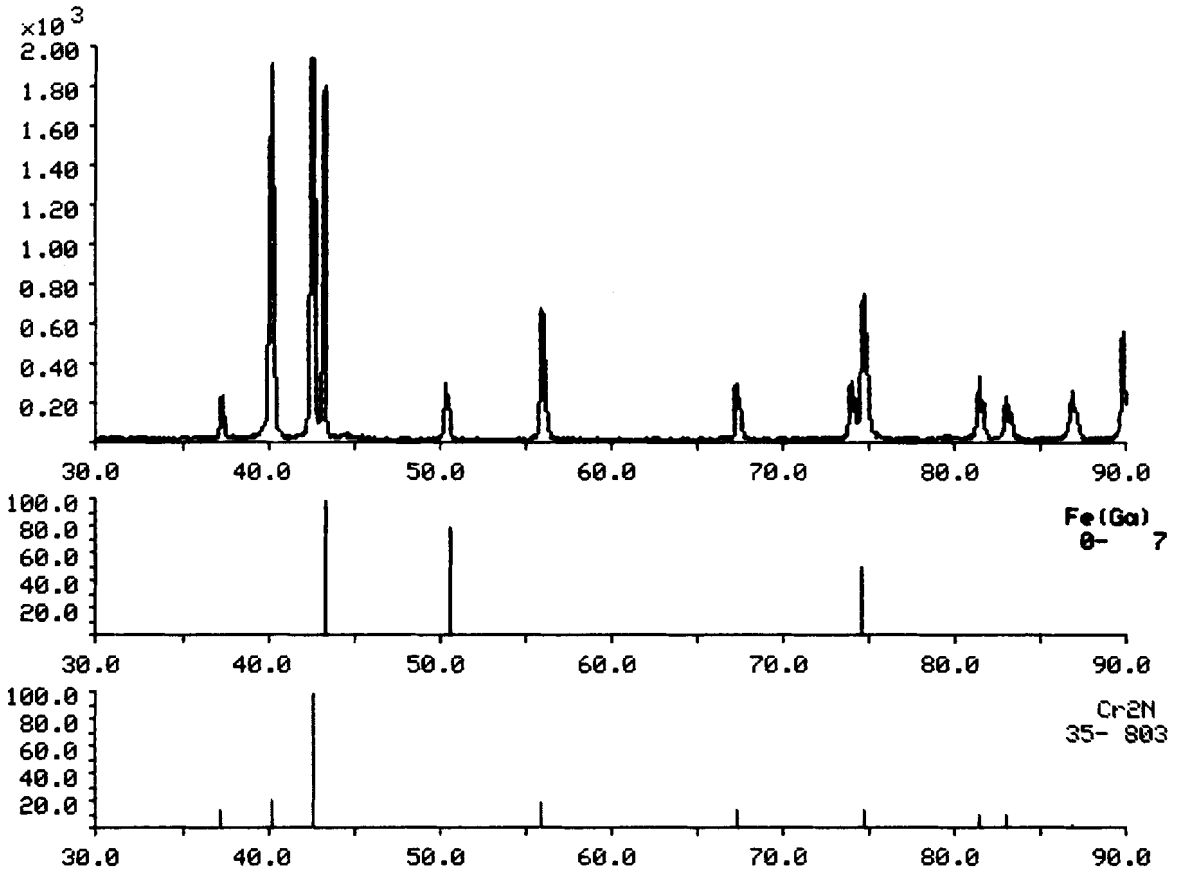

Figure 24. X-ray powder diffraction spectra for extracted residue from heat DPSC 2100 material aged at 900°C for 1 hour.

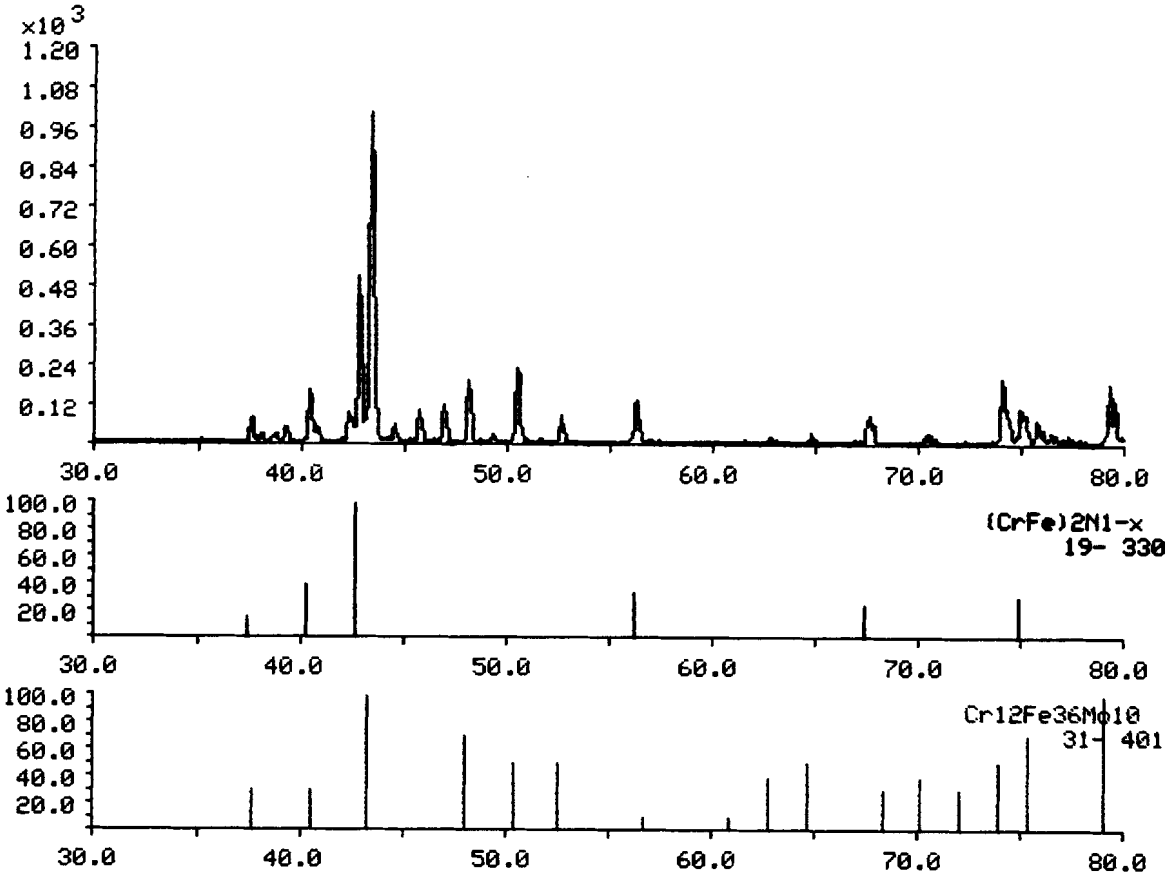

Figure 25. X-ray powder diffraction spectra for extracted residue from heat DPSC 2100 material aged at 900°C for 10 hours.

Grain Boundary Cr_2N Precipitation

Nucleation (onset) of GB precipitation was defined through metallographic examination of specimens etched electrolytically with an aqueous solution of 10% oxalic acid. Oxalic acid is known to directly attack Cr-rich $M_{23}C_6$ carbides in austenitic stainless steels. In this work, chromium-rich Cr_2N nitrides were also found to be susceptible to attack/dissolution by oxalic acid etching. It was determined that GB precipitation of Cr_2N could be detected when precipitates were present on less than 5% of the available boundaries.

The optical micrographs of *Figure 26 (a,b)* illustrate the early detection of GB precipitation for a DPSC 2100 sample heat treated at 800°C for 0.1 hours (6 minutes). The optical micrograph shown in *Figure 26a* was taken with bright-field illumination and the micrograph of *Figure 26b* was taken using Nomarski interference contrast. Slight attack of the sample surface is shown in *Figure 26a* and this attack is shown to be present at grain boundaries (GB grooving) in *Figure 26b*. The surrounding grain and twin boundaries did not show any attack. Examination of this sample using TEM confirmed the presence of precipitates at isolated grain boundaries as shown in *Figure 26 (c,d)*.

Time-temperature-precipitation diagrams for GB precipitation of Cr_2N in heats DPSC 2100 and DE 257 are shown in *Figures 27 and 28*. Grain boundary precipitation of Cr_2N occurred in heat DPSC 2100 at temperatures from 600 to 1075°C and heat DE 257 from 650 to 1075°C. Grain boundary precipitation did not occur in heat DE 257 materials at a temperature of 600°C for aging times up to 30 hours. It took slightly longer for GB precipitation to develop in heat DE 257, at least for temperatures up to 750°C. Despite these minor differences, GB precipitation characteristics for the two alloys were quite similar.

Near the nose of the TTP curve (900 and 950°C), isolated GB precipitation was observed in DPSC 2100 samples aged in the Gleeble for times as short as 0.01 hours (36 seconds). It should be kept in mind that specimens from DE 257 were heat

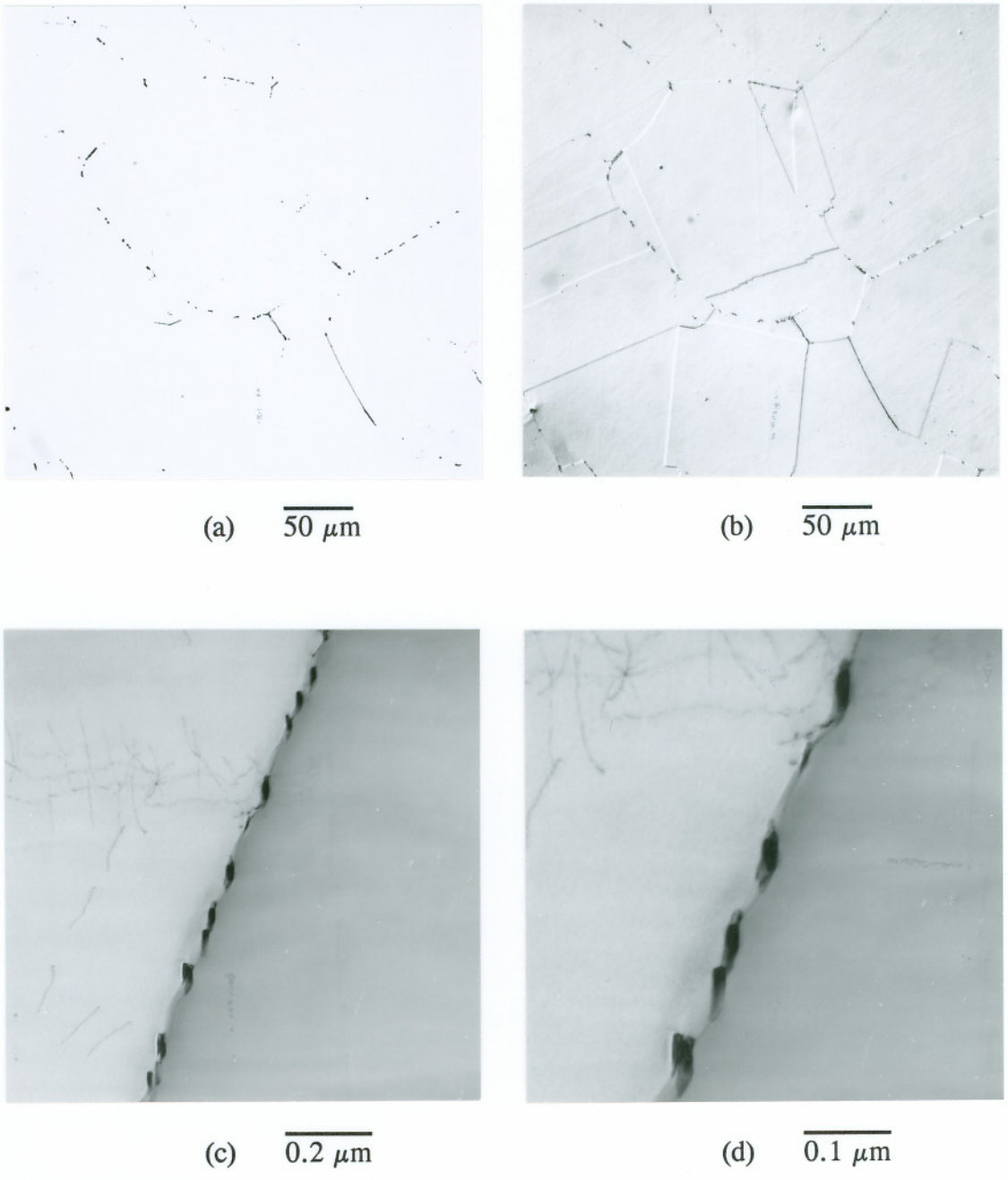

Figure 26. Optical (a,b) and TEM-BF micrographs (c,d) of grain boundary Cr_2N precipitation in heat DPSC 2100 specimens aged at 800°C for 0.1 hour. Photograph in (b) taken with Nomarski interference contrast.

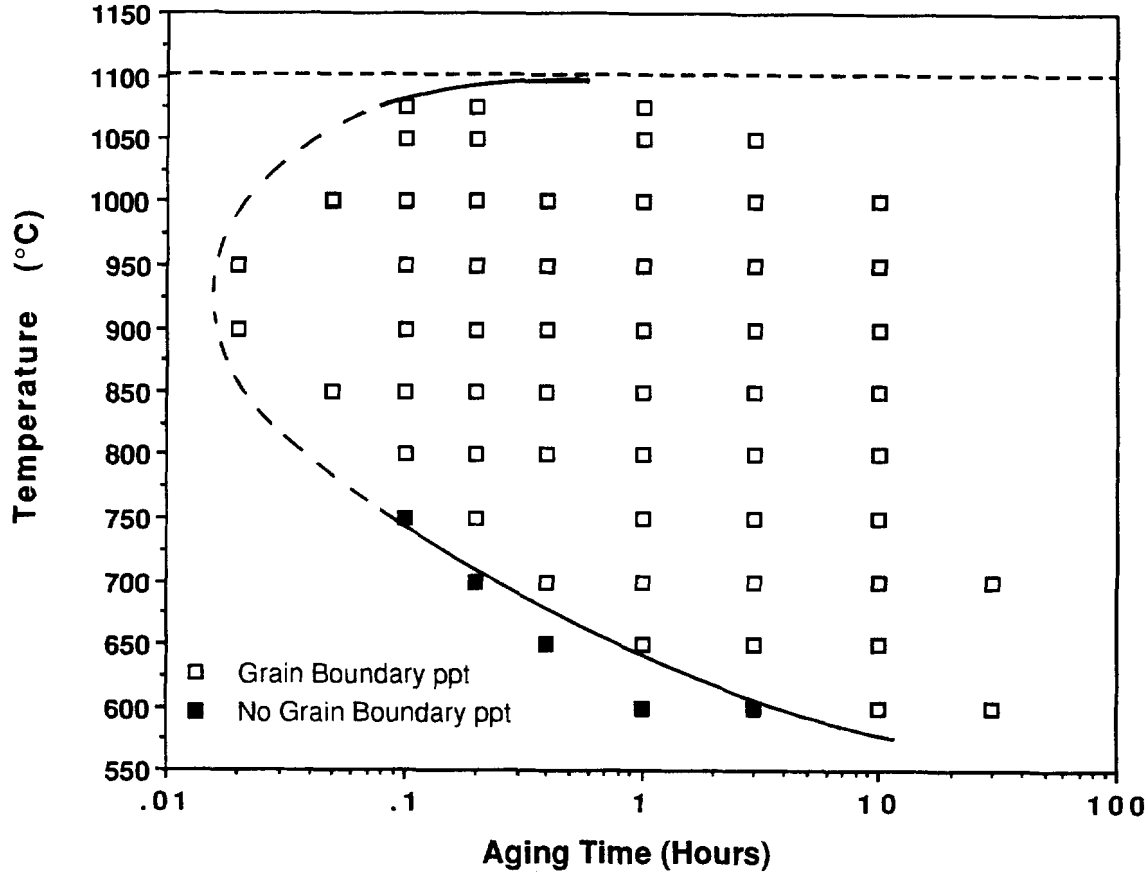

Figure 27. Time-temperature-precipitation curve for grain boundary precipitation in heat DPSC 2100.

treated for a minimum time of 0.1 hour (6 minutes) while DPSC 2100 were materials thermal cycled in the Gleeble for times at temperature as short as 0.01 hour (36 seconds). Therefore, the response of material DE 257 at short times can only be assumed to follow similar trends as for lower temperatures. Heat treatments were not conducted at temperatures below 600°C and complete dissolution of the precipitates occurred at 1100°C.

An example of grain boundary Cr_2N nitride precipitates present is shown in *Figure 29a* (DPSC 2100 aged at 1050°C/1 hour). Three SADPs from the grain boundary precipitates in this sample are shown in *Figure 29 (c-d)*. Indexed schematics of these SADPs are shown in *Appendix C*.

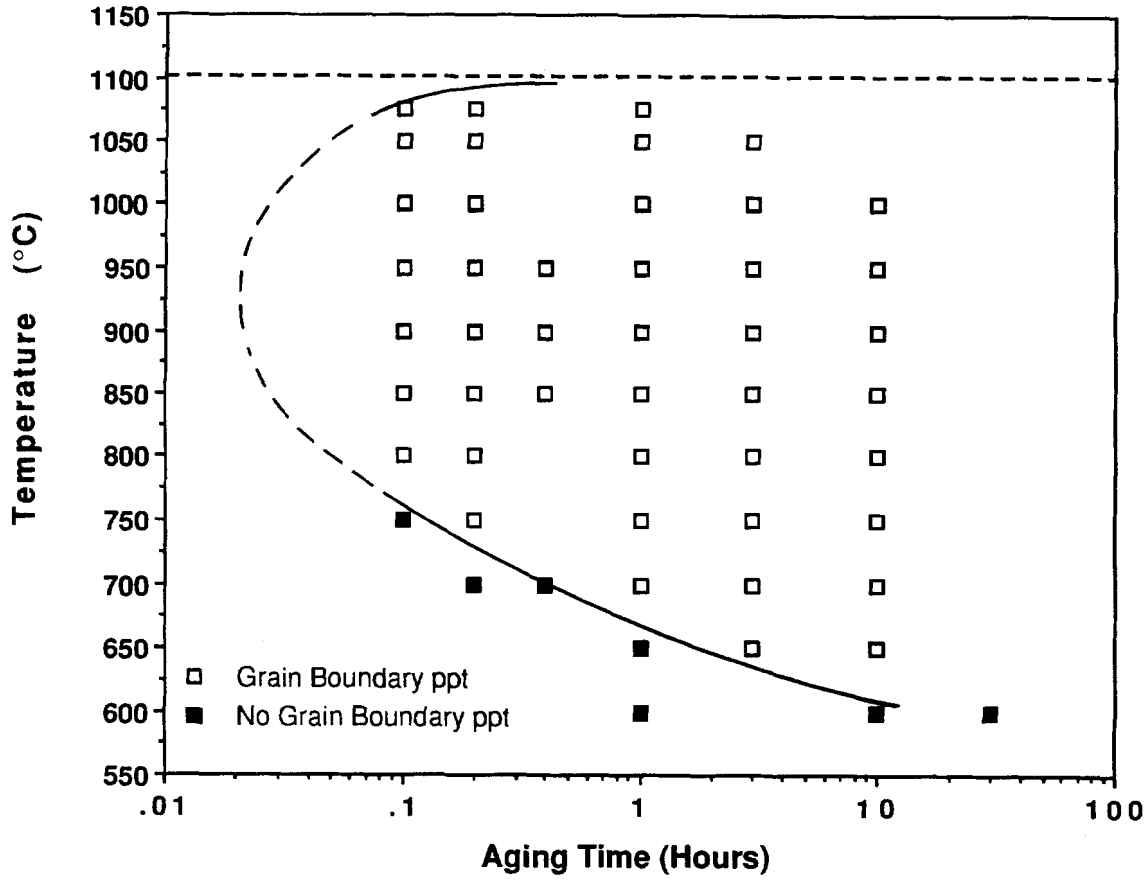

Figure 28. Time-temperature-precipitation curve for grain boundary Cr_2N precipitation in heat DE 257.

Generally, GB precipitates were identified as Cr_2N by TEM analysis by using EDS to confirm that they were Cr-rich, and through SADP analysis. Computer generated diffraction patterns (zone axis patterns) were generated for the specific camera constants used in the TEM (calibrated with a gold standard) and compared to those obtained experimentally. Thus, d-spacings and angles were measured experimentally and compared to known values. Good correlation was obtained between the experimental electron diffraction analyses and Cr_2N crystal structure data, computer generated SADPs, and XRD analyses.

High-densities of Cr_2N were present at GBs in both heats of material at very short aging times (0.1 hour) for temperatures between 800 and 1000°C. Generally, for short aging times (0.1 hour), high density nitride areas were confined to a limited

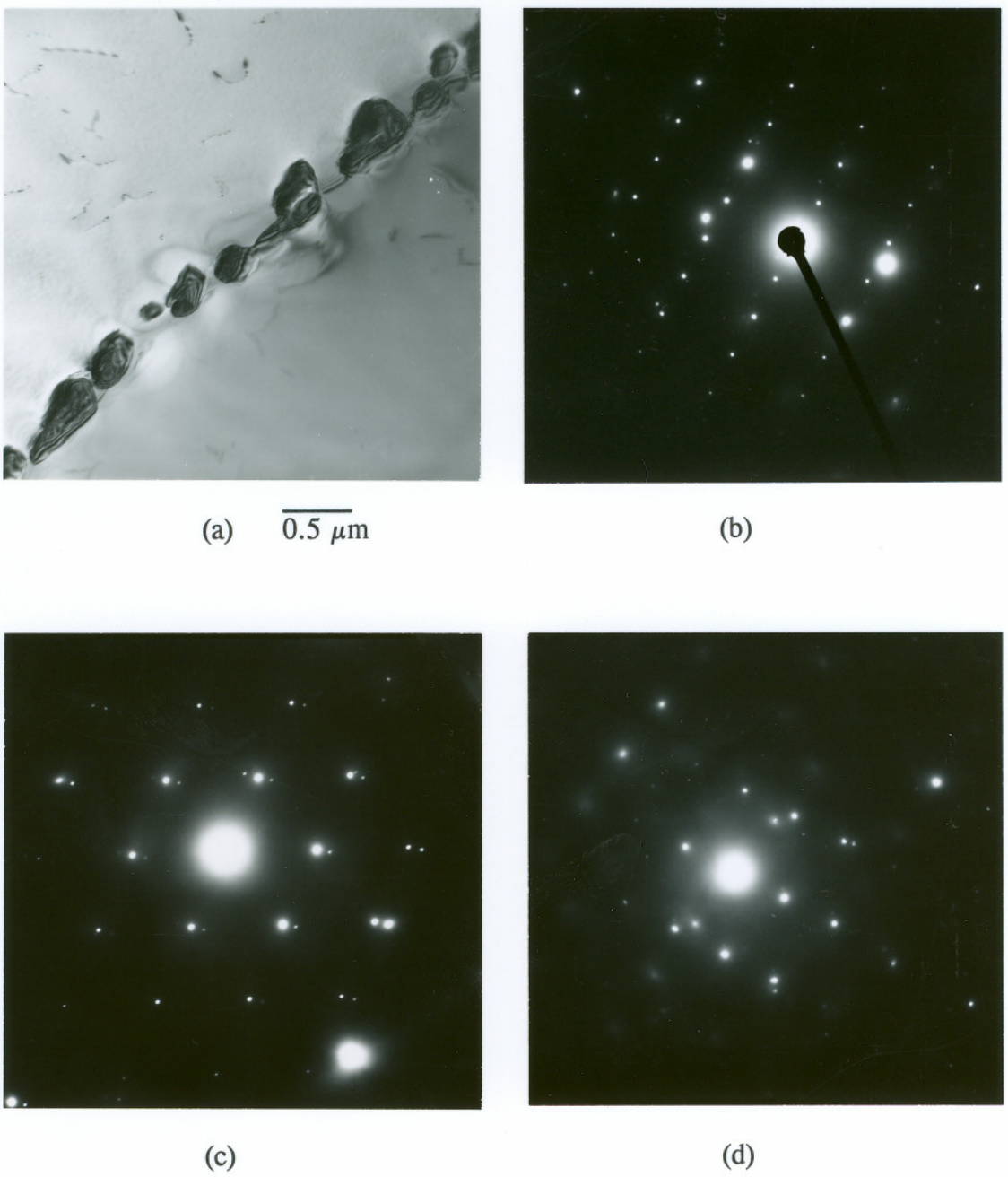

Figure 29. TEM bright-field micrograph (a) of Cr_2N grain boundary precipitates in heat DPSC 2100 material aged at 1050°C for 1 hour. Electron diffraction patterns of nitrides taken at zone axis (a) $[1\bar{1}00]$, (c) $[1\bar{1}03]$, and (d) $[20\bar{2}3]$.

number of GBs. Thus, some GBs were activated and contained a large number of precipitates while other GBs were not and didn't contain any precipitates.

An example of the high-density of Cr_2N precipitates which formed at GBs in a short period of time is shown in *Figure 30* for a sample heat treated at 850°C/0.1 hour (DPSC 2100). The GB shown is at an inclined angle with respect to the thin foil and electron beam. For this area, the matrix and Cr_2N appear to have an orientation relationship *(Figure 30b)*. However, this relationship was not observed for all GB precipitates. In materials heat treated at higher temperatures or for longer times, an orientation relationship between the matrix and GB precipitates was not generally observed. More in-depth TEM studies of materials heat treated at a variety of temperatures/times would be required to determine whether or not a relationship exists.

The size and spacing of GB precipitates generally increased with increasing heat treatment temperature and/or time. The size and spacing of precipitates was found to be particularly sensitive to aging temperature. This is illustrated in the secondary electron micrographs of *Figure 31* for specimens heat treated for 3 hours at 850°C *(a,b)* and 1050°C *(c,d)*. Aging at lower temperatures (<1000°C) produced nearly continuous nitride coverage on GBs, while aging at temperatures at 1000°C or above resulted in larger nitrides with finite spacing. Examples of GB nitrides are shown in *Figure 32* for DPSC 2100 samples heat treated at temperatures of 700, 800, 900, and 1000°C.

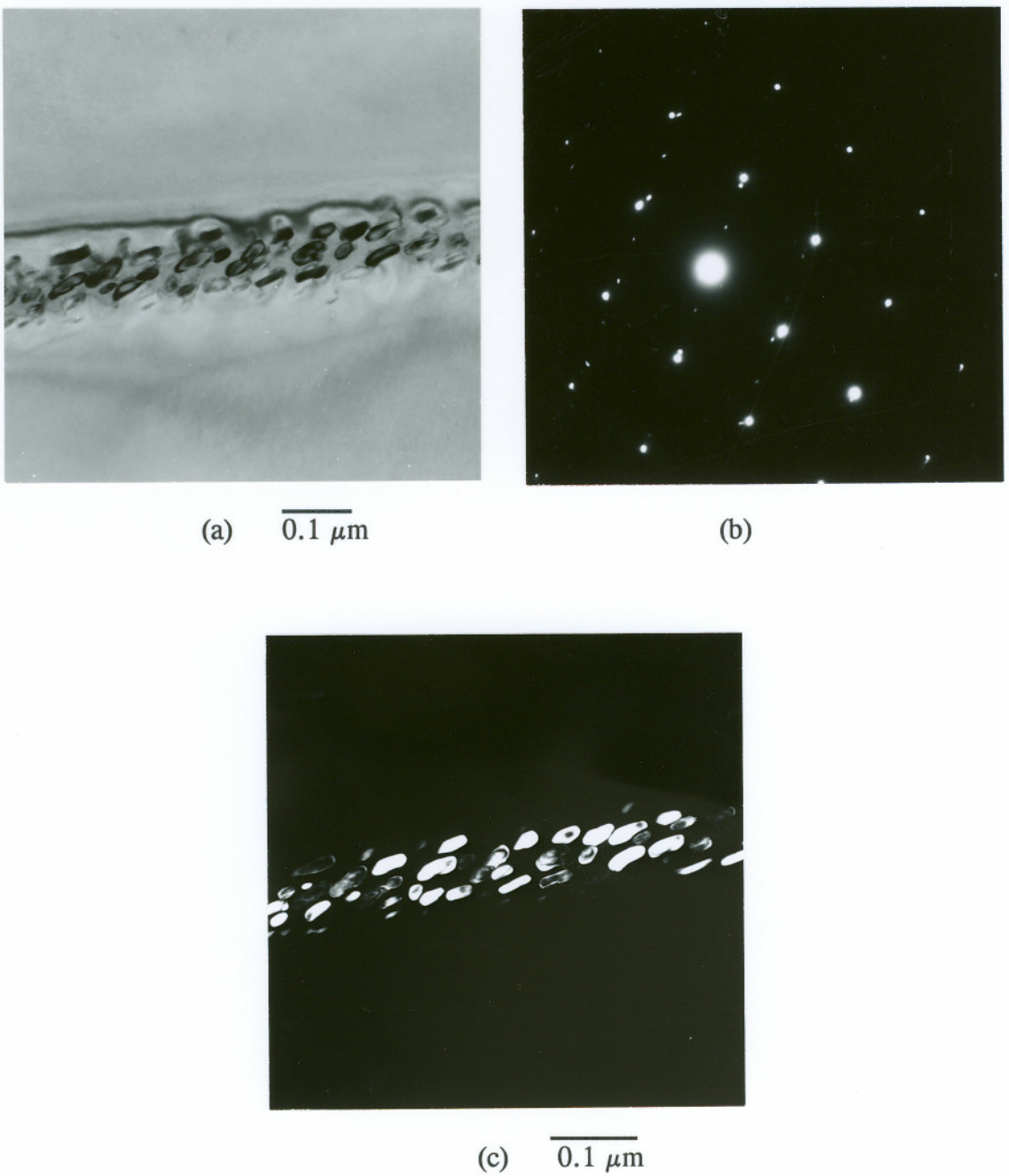

Figure 30. TEM bright-field micrograph (a) of Cr_2N grain boundary precipitates in heat DPSC 2100 material aged at 850°C for 0.1 hour. Electron diffraction pattern of nitrides from (a) taken at zone axis (b) $[1\bar{1}00]$. TEM-CDF micrograph (c) of (a) using $(11\bar{2}1)$ reflection.

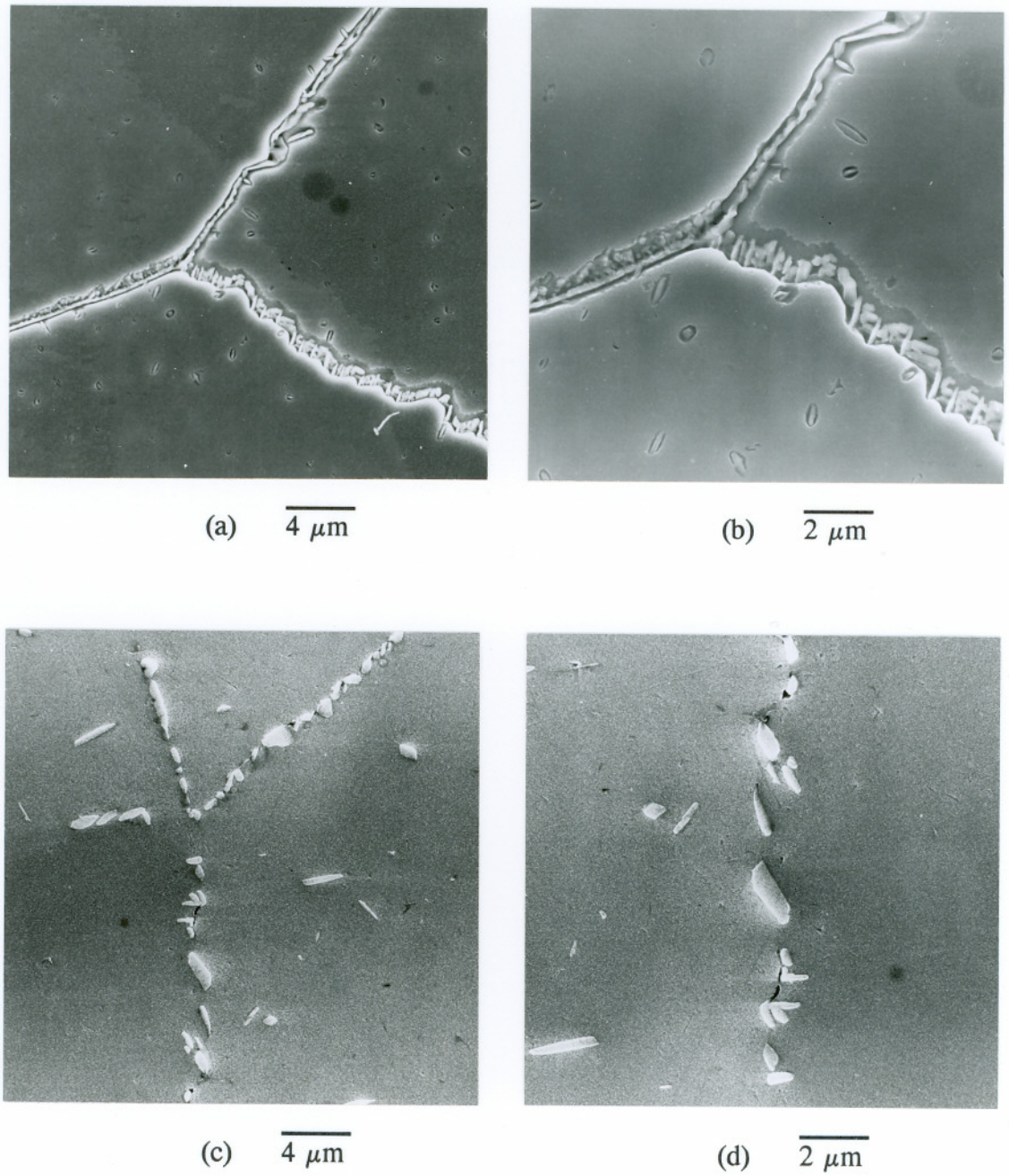

Figure 31. Scanning electron micrographs of grain boundary Cr_2N nitrides in heat DPSC 2100 samples aged for 3 hours at (a,b) 850°C and (c,d) 1050°C. Samples electrolytically etched in 10% HCl/methanol solution.

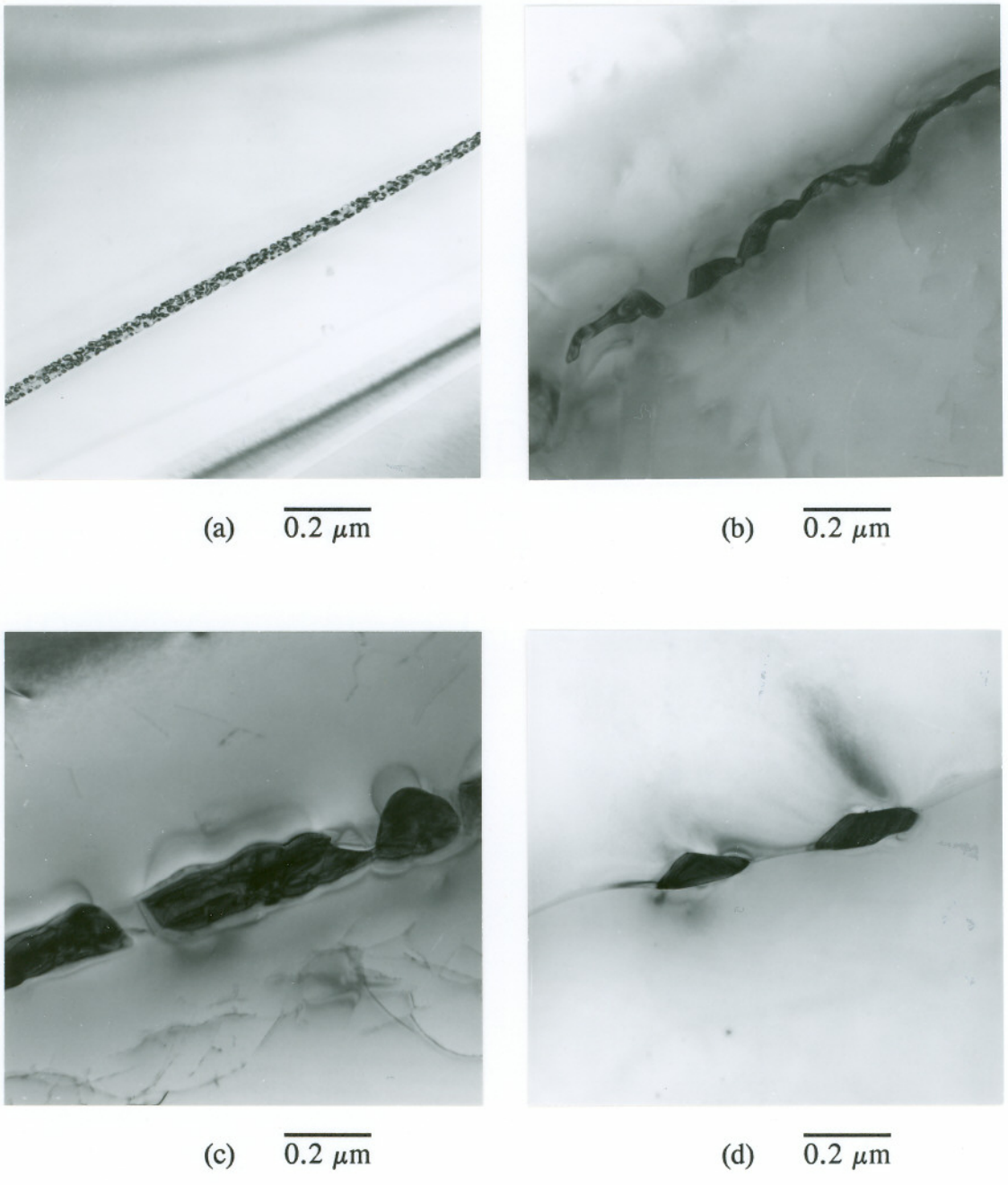

Figure 32. TEM bright-field micrographs of Cr_2N grain boundary precipitates in heat DPSC 2100 specimens aged at temperatures of (a) 700°C, (b) 800°C, (c) 900°C, and (d) 1000°C.

Cellular Cr_2N Precipitation

Nucleation and Development

Nucleation (onset) of cellular precipitation was defined through examination of metallographically prepared and etched specimens using optical and scanning electron microscopy. Under optical examination, GB nucleated cells appeared, in the early stages of development, as a changing of the usually linear GBs, to GBs having a jagged appearance, as illustrated in *Figure 33a*. Examination of areas such as this in the SEM revealed the early development of cellular Cr_2N precipitation *(Figure 33b)*. Using SEM examinations, it was estimated that cellular precipitation could be detected in samples with cell volume fractions of less than 0.5%. Using the SEM analysis of metallographically prepared specimens, the onset of cellular precipitation was clearly differentiated from GB precipitation.

Time-temperature-precipitation diagrams for cellular precipitation of Cr_2N in heats DPSC 2100 and DE 257 are shown in *Figures 34 and 35*. Cellular precipitation was detected for specimens aged in the temperature range of 750-1000°C for heat DE 257 and 700-1000°C for heat DPSC 2100. However, the development of cellular precipitation was significantly different for the two heats of material, occurring faster, and to a greater degree, in heat DPSC 2100. This was particularly evident for aging at 1000°C (reference *Figure 21*). Cellular precipitation nucleated in heat DE 257 at 1000°C, but no further cell growth occurred with increasing aging time at this temperature. At all temperatures, cell nucleation occurred at shorter times in heat DPSC 2100 than in DE 257.

Over-all cellular precipitation development for the two heats of material is shown in the graphs of *Figure 36*. In these graphs, cellular precipitate coverage (volume % cells as a fraction of sample total, remainder being the austenite matrix) is plotted as a function of aging time and temperature. The characteristics of cell development are further illustrated in the graphs of *Figure 37* and compared for the

two heats of material in *Figure 38*. Cellular precipitation occurred over a wider temperature range for heat DPSC 2100 and cell development (amount of cellular precipitation for a given aging temperature/time) was also much greater for this alloy. Maximum cell coverage reached over 40%, while for heat DE 257, the maximum coverage was less than 30%. Also, cell development in heat DE 257 dropped off significantly for temperatures either below, or above, 900°C, and was much less at 950°C as compared to 900°C. The characteristics of cell development in DPSC 2100 were very similar at 900 and 950°C.

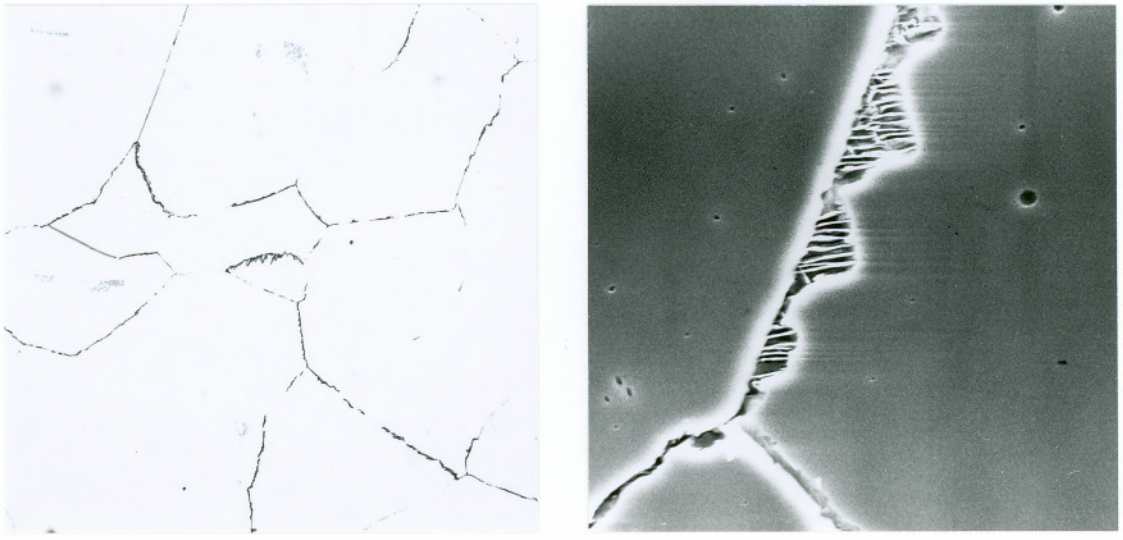

Figure 33. Optical micrograph (a) showing possible precipitate nucleation in heat DPSC 2100 materials isothermally aged at 850°C for 0.1 hour. Secondary electron micrograph (b) of same specimen from (a) illustrating early cellular precipitation development.

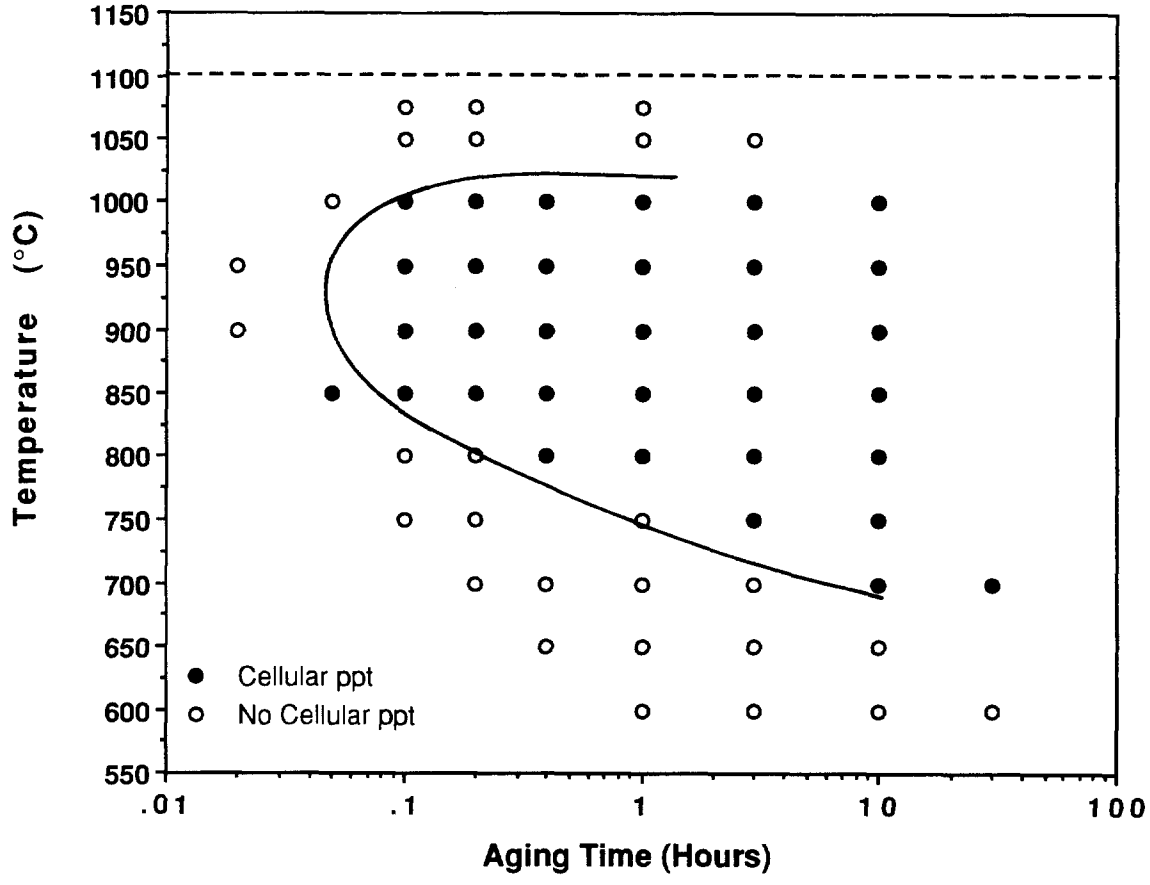

Figure 34. Time-temperature-precipitation curve for cellular precipitation of Cr_2N in heat DPSC 2100.

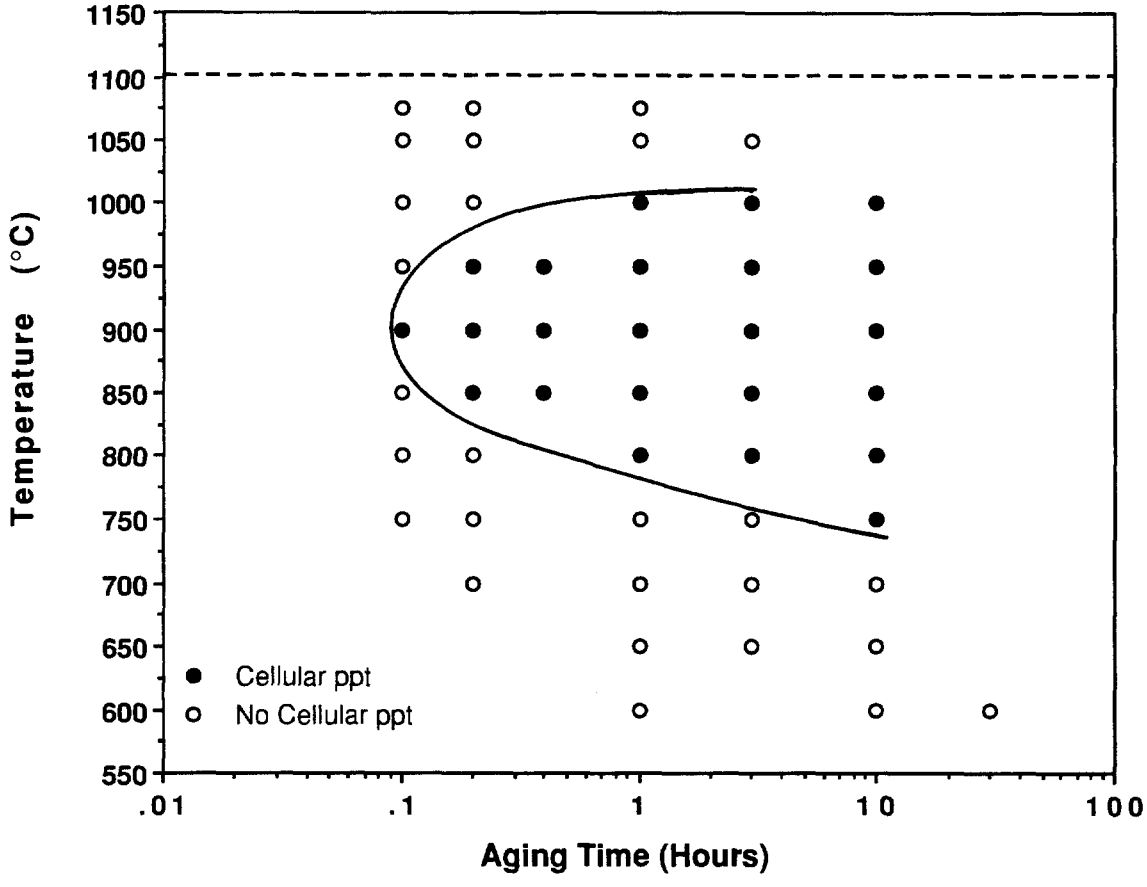

Figure 35. Time-temperature-precipitation curve for cellular precipitation of Cr_2N in heat DE 257.

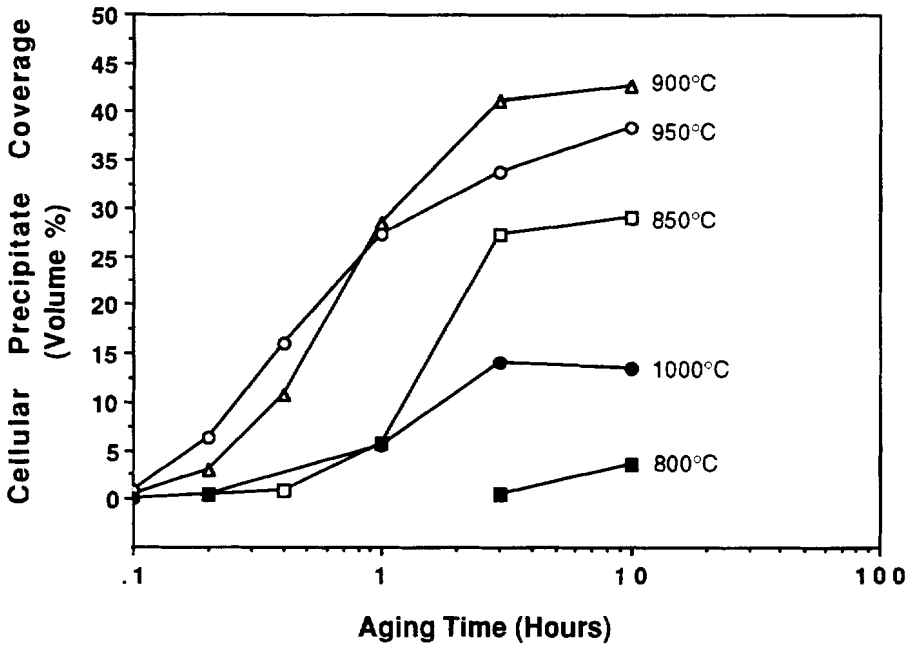

(a)

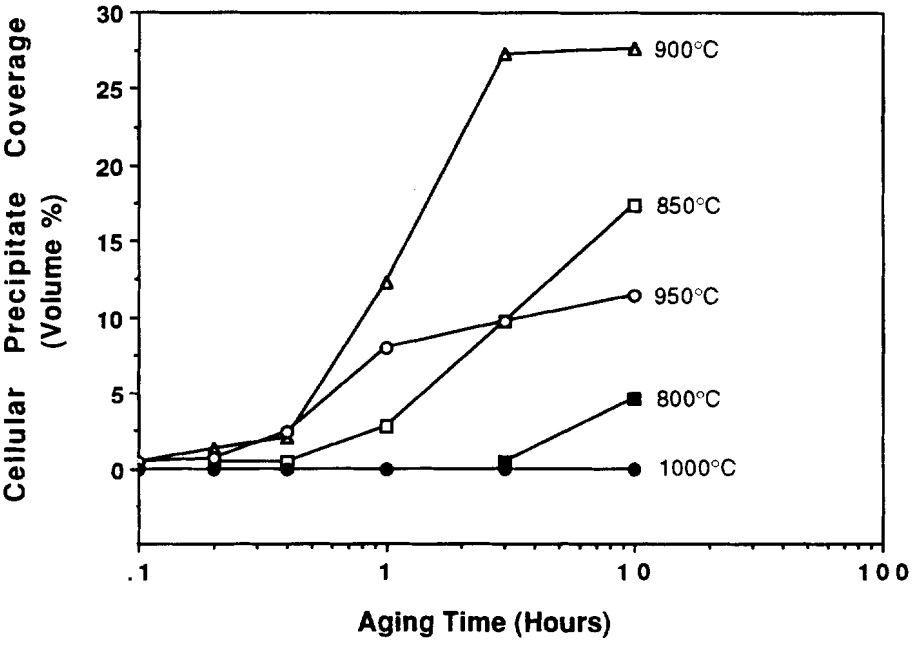

(b)

Figure 36. Cellular precipitate coverage as a function of aging time at temperatures of 800-1000°C for (a) heat DPSC 2100, and (b) heat DE 257.

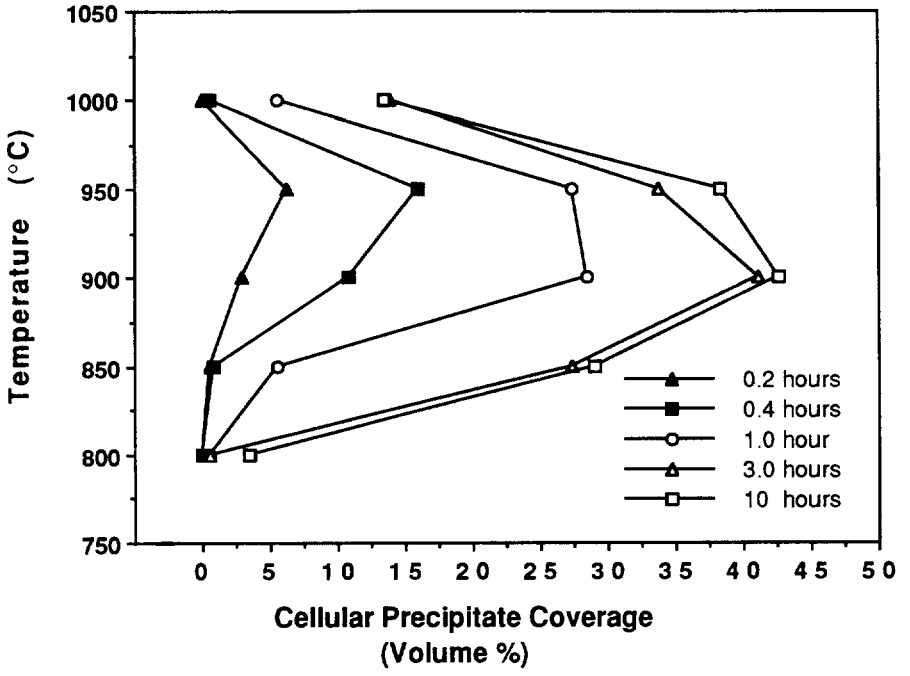

(a)

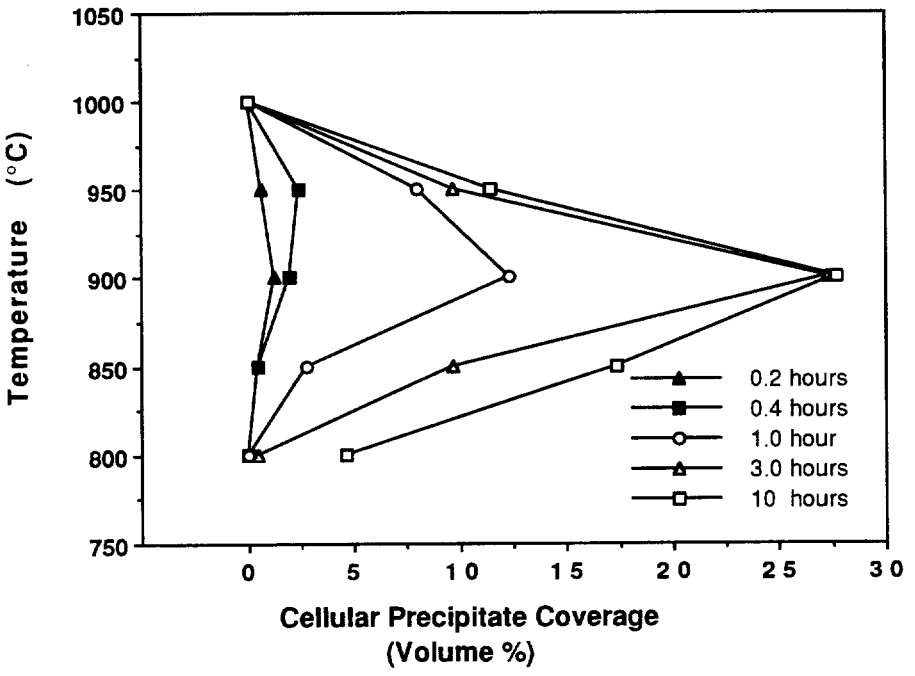

(b)

Figure 37. Cellular precipitate coverage as a function of aging temperature for aging times from 0.2 to 10 hours for (a) heat DPSC 2100, and (b) heat DE 257.

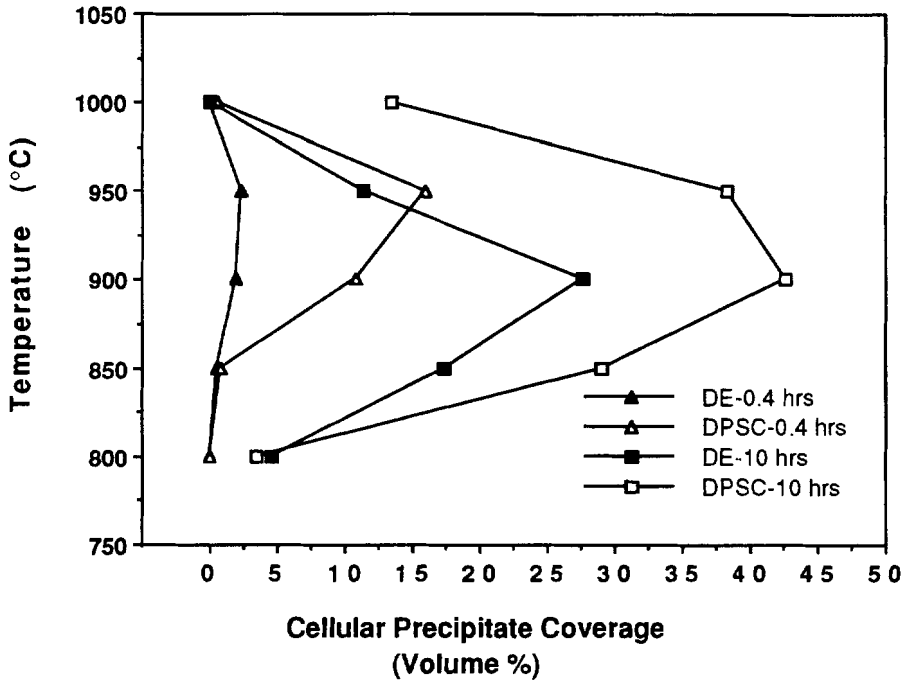

(a)

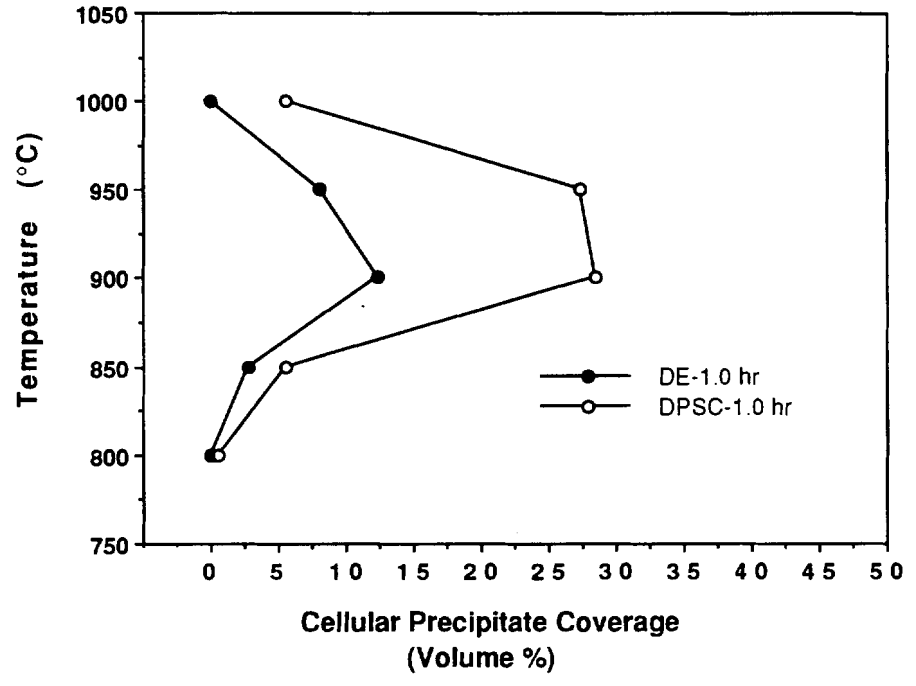

(b)

Figure 38. Cellular precipitate coverage in alloys DPSC 2100 and DE 257 as a function of aging temperature for aging times of (a) 0.4 and 10 hours, and (b) 1 hour.

Precipitate Characteristics

As described previously, the microstructure within the cells consisted of alternating regions of austenite and Cr_2N lamellae (reference *Figure 22*). The spacing of Cr_2N lamellae within cell colonies was observed, at least qualitatively, to increase with increasing aging temperature. For example, nitride lamellae spacing at 850°C *(Figure 39a)* was significantly finer than spacing at 1000°C *(Figure 39d)*. The lamellae spacing, at a given temperature, was found to be larger for heat DE 257 than DPSC 2100 (compare *Figure 39b* to *Figure 39e*). Lamellae characteristics (length, growth direction, and spacing) varied considerably within each cell and therefore a more quantitative description of these parameters was not considered to be feasible.

Typical austenite and Cr_2N lamellae present within the cellular precipitation products for both heats of material are illustrated in the TEM micrographs and SADP shown in *Figure 40*. An orientation relationship, detailed in the following section, was found to exist between the Cr_2N within the cellular precipitate region and the austenite matrix.

Nucleation of cellular precipitation occurs at austenite GBs and growth of the cell develops as interface migration occurs and Cr_2N lamellae grow into the adjacent austenite matrix. The Cr_2N lamellae maintain a crystallographic orientation relationship with the austenite grain from which growth occurs, not with the lattice of the austenite grain the lamellae are growing into. This behavior is illustrated in the TEM-BF micrograph of a growing cell and associated diffraction patterns of *Figure 41*.

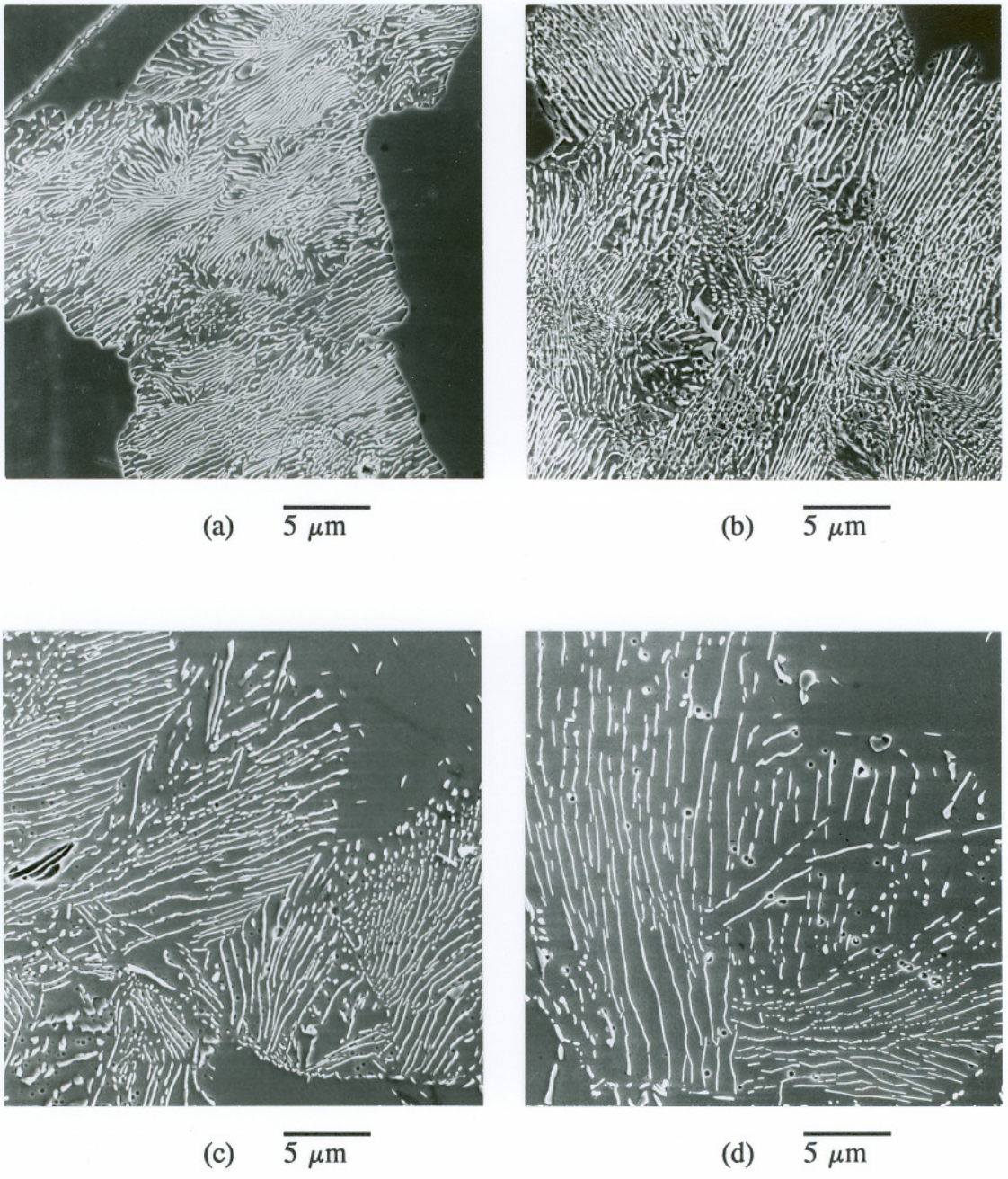

Figure 39. Scanning electron micrographs of metallographically prepared specimens showing cellular precipitation typical of heat DPSC 2100 specimens aged at (a) 850°C, (b) 900°C, (c) 950°C, and (d) 1000°C (electrolytically etched with 10% HCl/methanol).

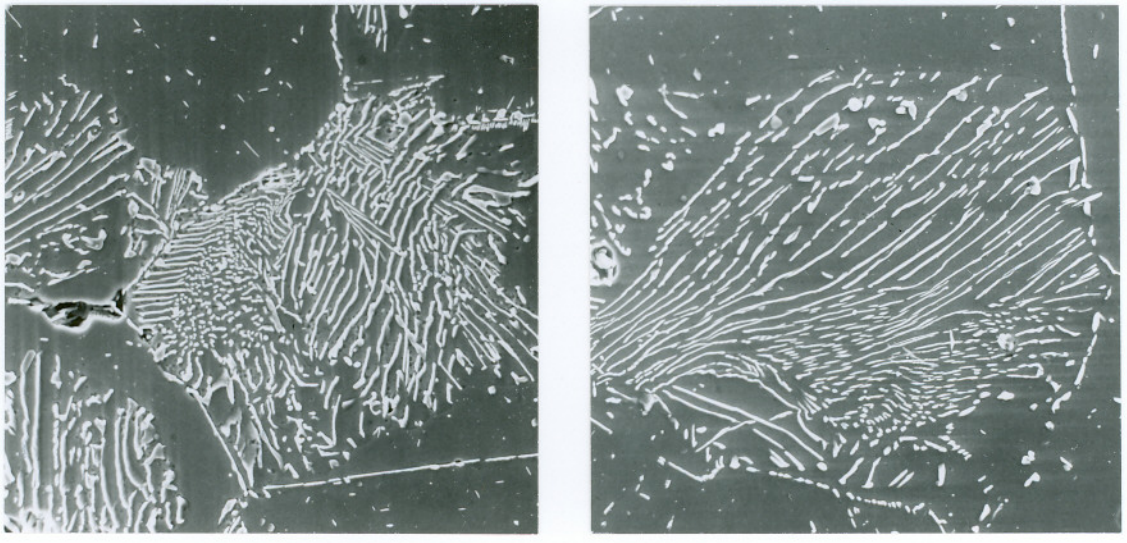

(e) 5 μm (f) 5 μm

Figure 39 (cont.) Scanning electron micrographs of metallographically prepared specimens showing cellular precipitation typical of heat DE 257 specimens aged at (e) 900°C and (f) 950°C.

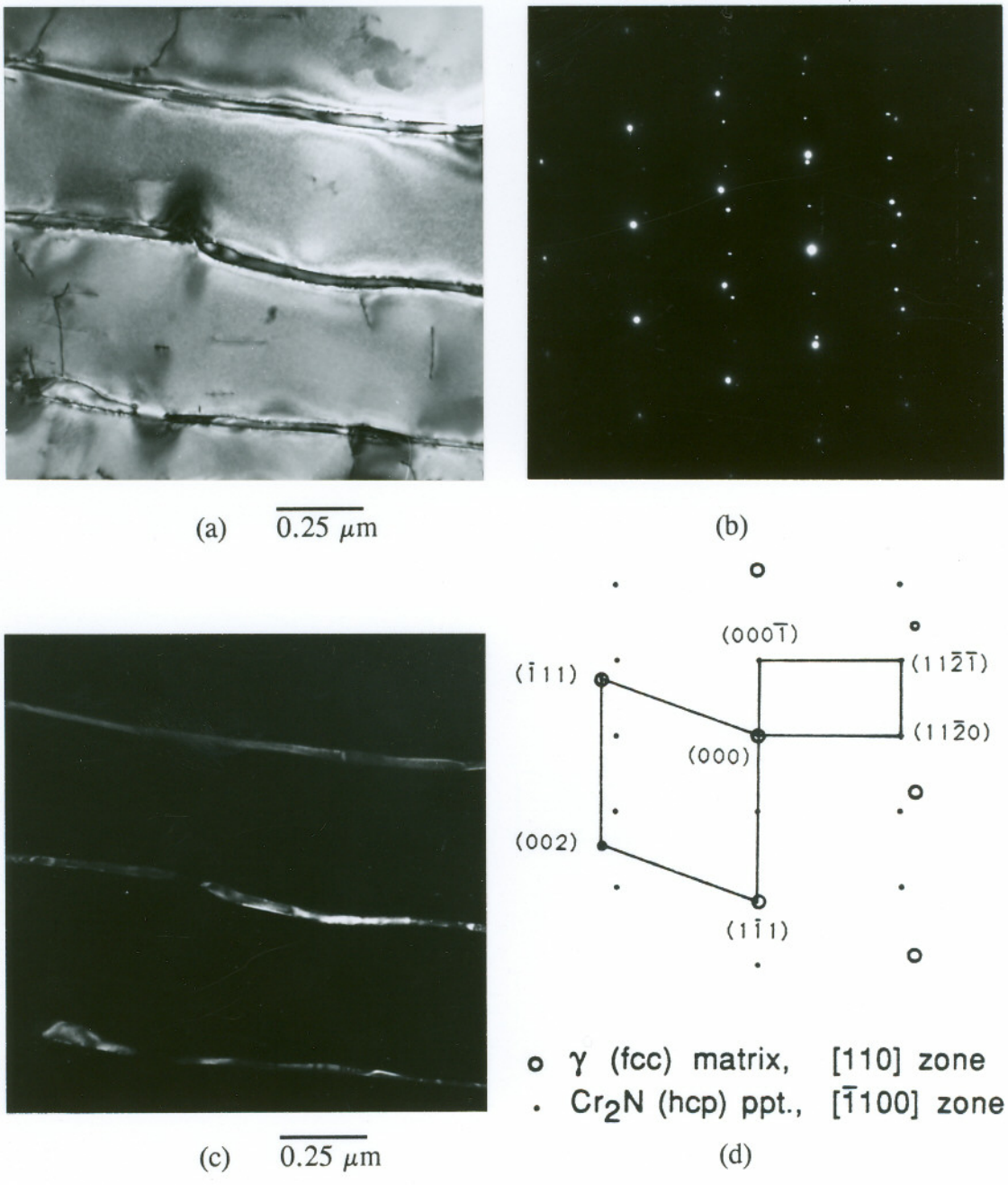

Figure 40. Cellular precipitation in heat DPSC 2100 materials aged at 950°C for 10 hours. TEM micrographs (a) bright-field, (b) SADP of matrix and Cr_2N lamellae (ZA [110]γ//[$\bar{1}$100]Cr_2N), and (c) dark-field micrograph of (a) using (0001) reflection. Schematic of (b) shown in (d).

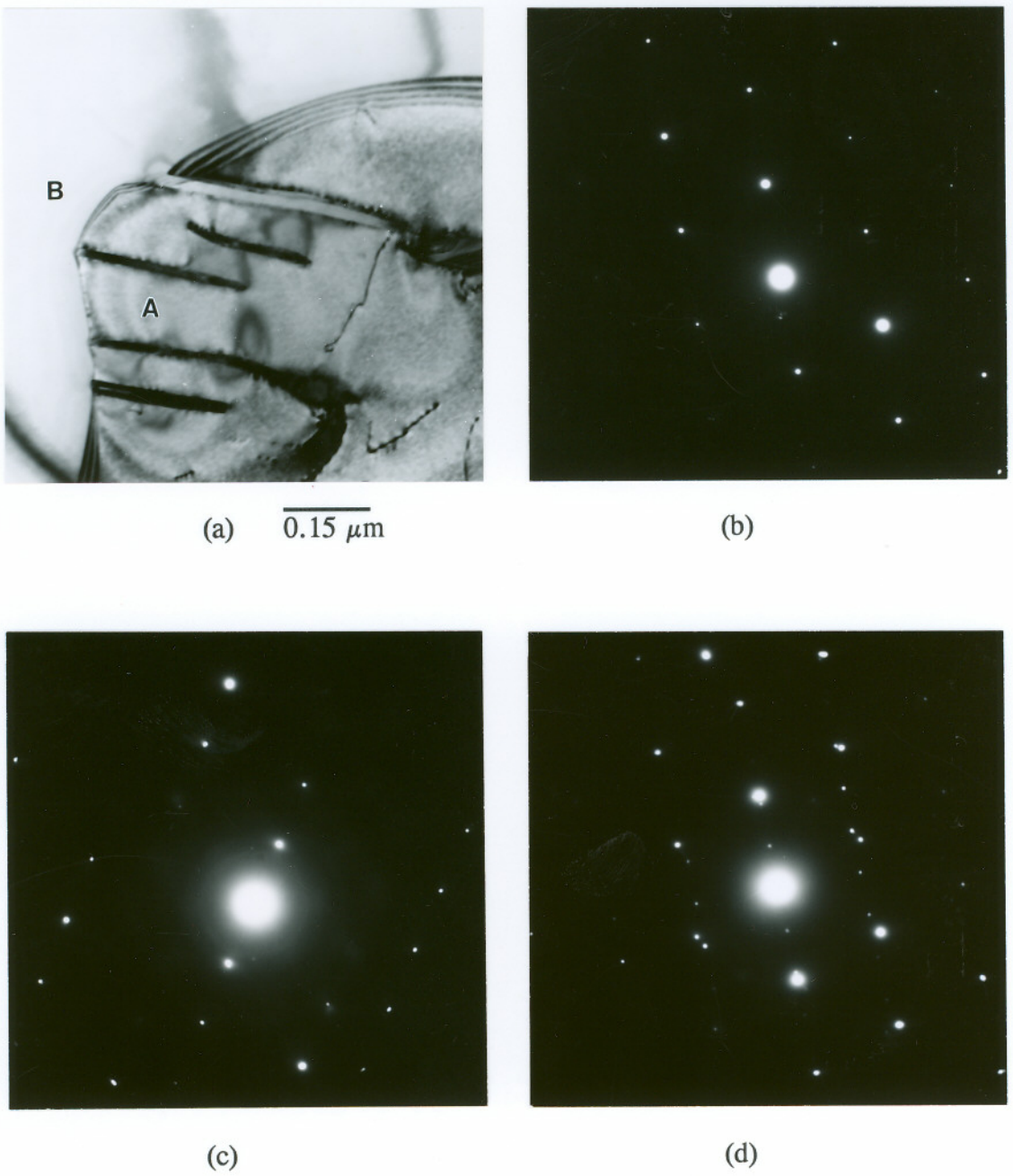

Figure 41. TEM-BF micrograph (a) of early cell development in DPSC 2100 material aged at 900°C for 0.1 hour. SADPs of (b) matrix in which Cr_2N growth occurred [labeled A in (a)] ZA[110]γ, (c) austenite that cell is growing into [labeled B in (a)], and austenite matrix of (b) plus Cr_2N (ZA [110]γ//[$\bar{1}$100]Cr_2N).

Transgranular Cr_2N Precipitation

Nucleation and Development

Determination of the onset (nucleation) of transgranular precipitation in the high-nitrogen materials was more difficult than for GB and cellular precipitation of Cr_2N because transgranular precipitation did not occur until GB and cellular precipitates were fully developed. Also, detection of transgranular precipitates in the early stages of development by optical microscopy is difficult because of the small size and low density of precipitates present.

The presence of transgranular precipitates was determined through SEM examination of metallographically prepared samples etched electrolytically with 10% oxalic acid. These results were subsequently confirmed with TEM analyses of selected specimens.

The secondary electron micrographs shown in *Figure 42*, taken from DPSC materials heat treated for 3 hours at 950 and 1050°C, illustrate the transgranular precipitates observed in the SEM. The sample aged at 950°C had a relatively high density of precipitates which were also visible by optical microscopy. However, transgranular precipitation in the 1050°C specimen could not be positively identified optically due to the low density of precipitates present. Also, in the early stages, precipitates are only present in some of the grains sectioned, not all of them. The onset of transgranular precipitation was defined by the first detectible precipitates using SEM examinations such that precipitates were not observed in a sample aged for the next shorter time.

Time-temperature-precipitation diagrams for transgranular precipitation of Cr_2N in heats DPSC 2100 and DE 257 are shown in *Figures 43 and 44*. Transgranular precipitation was detected in specimens aged in the temperature range of 850-1050°C for heat DE 257 and 700-1050°C for heat DPSC 2100. Transgranular precipitation in heat DPSC 2100 occurred over a wider temperature range, and at

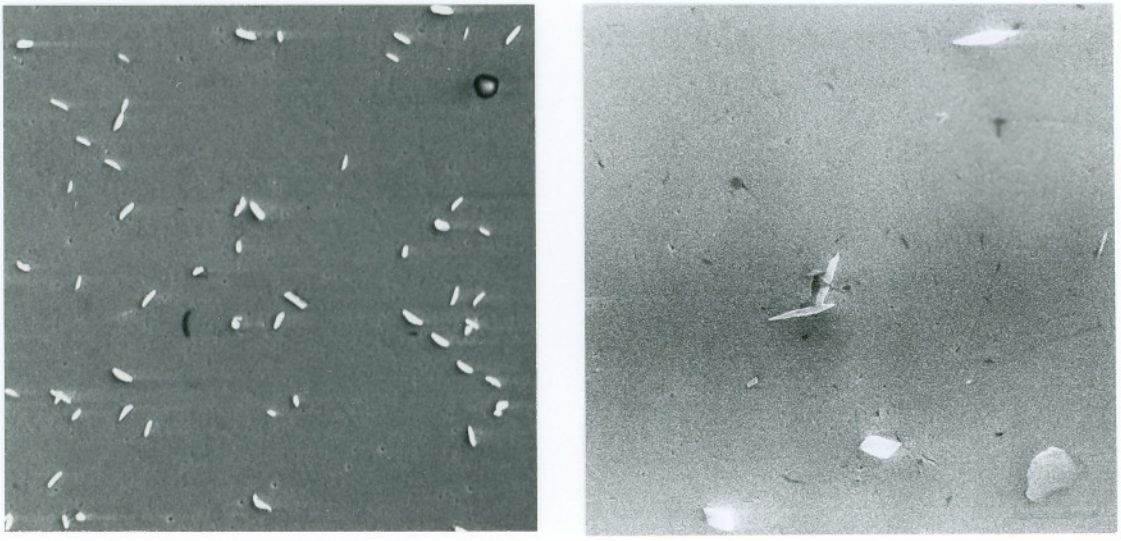

Figure 42. Scanning electron micrographs from metallographically prepared specimens of heat DPSC 2100 material aged for 3 hours at (a) 950°C and (b) 1050°C.

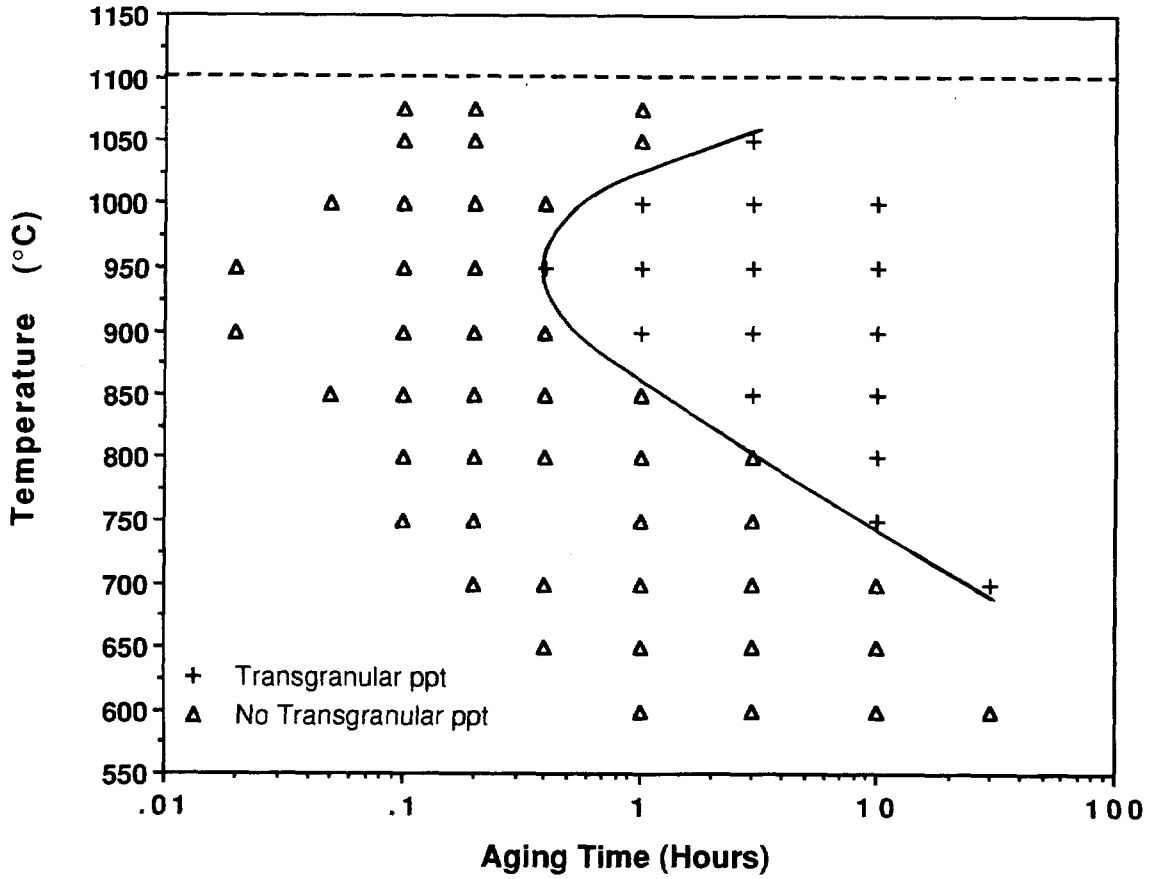

Figure 43. Time-temperature-precipitation curve for transgranular precipitation of Cr_2N in heat DPSC 2100.

earlier times for a given aging temperature. However, near the nose of the TTP curve, the actual time difference between the two heats for the onset of precipitation was insignificant.

Precipitate Characteristics

No differences were observed between the morphologies or structures of the transgranular precipitates formed in the two heats of material. General features of the precipitates are illustrated in the TEM micrographs shown in *Figures 45 and 46.*

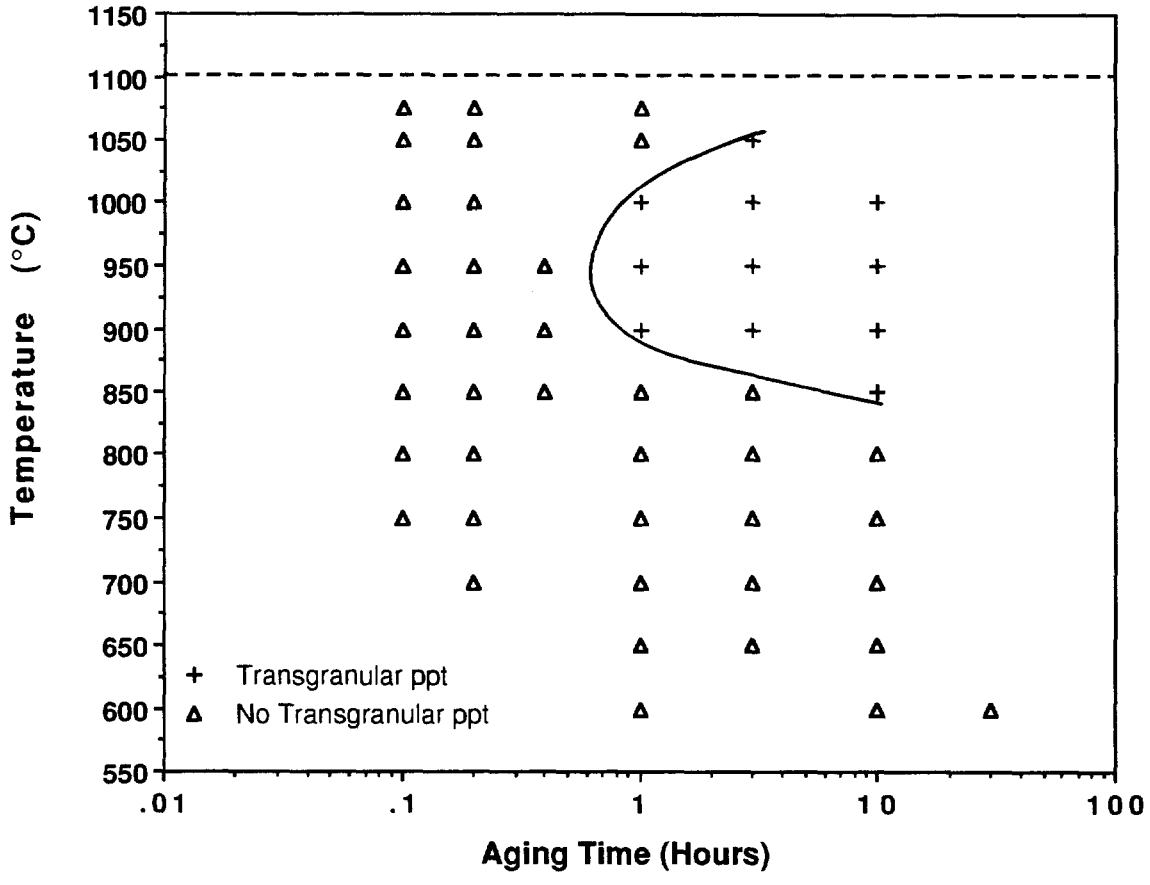

Figure 44. Time-temperature-precipitation curve for transgranular precipitation of Cr_2N in heat DE 257.

Transgranular precipitates formed in the shape of platelets *(Figure 46)* and were found to have maximum dimensions (DPSC material aged at 950°C/10 hours) of approximately 2.5 μm in length and 0.3 μm thick.

Three SADPs taken from the austenite matrix and transgranular Cr_2N are shown in *Figures 47 and 48*. These patterns were taken with the austenite matrix oriented to give zone axis patterns of [110] *(Figure 47)*, [$\bar{1}$12] *(Figure 47c)*, and [$\bar{1}$11] *(Figure 48)*. The Cr_2N electron diffraction patterns associated with these matrix patterns were found to correspond to zone axis for the Cr_2N of [$\bar{1}$100] *(Figure 47a)* and [$\bar{1}\bar{1}$20] *(Figure 47c)*, for austenite at [110] and [$\bar{1}$12], respectively. For the austenite at [$\bar{1}$11], the Cr_2N gave a pattern close to [5 5 $\bar{1}\bar{0}$ 6], but not exact. These

results correspond to a generalized orientation relationship between the Cr_2N and austenite matrix described as:

$$\{111\}\gamma//\{0001\}Cr_2N \text{ and } <110>\gamma//<\bar{1}100>Cr_2N$$

This orientation relationship is illustrated by the stereogram shown in *Figure 49* centered on [110] and [$\bar{1}$100]. Individual stereographic projections for the two crystals are located in *Appendix C*. Schematic electron diffraction patterns for the γ/Cr_2N system were computer generated assuming the orientation relationship listed above. Excellent correlation was obtained between these computer generated patterns and the ones obtained experimentally as shown for the individual patterns with zone axis of [110]γ *(Figure 47b)*, [1$\bar{1}\bar{2}$]γ *(Figure 47d)*, and [$\bar{1}$11]γ *(Figure 48b)*.

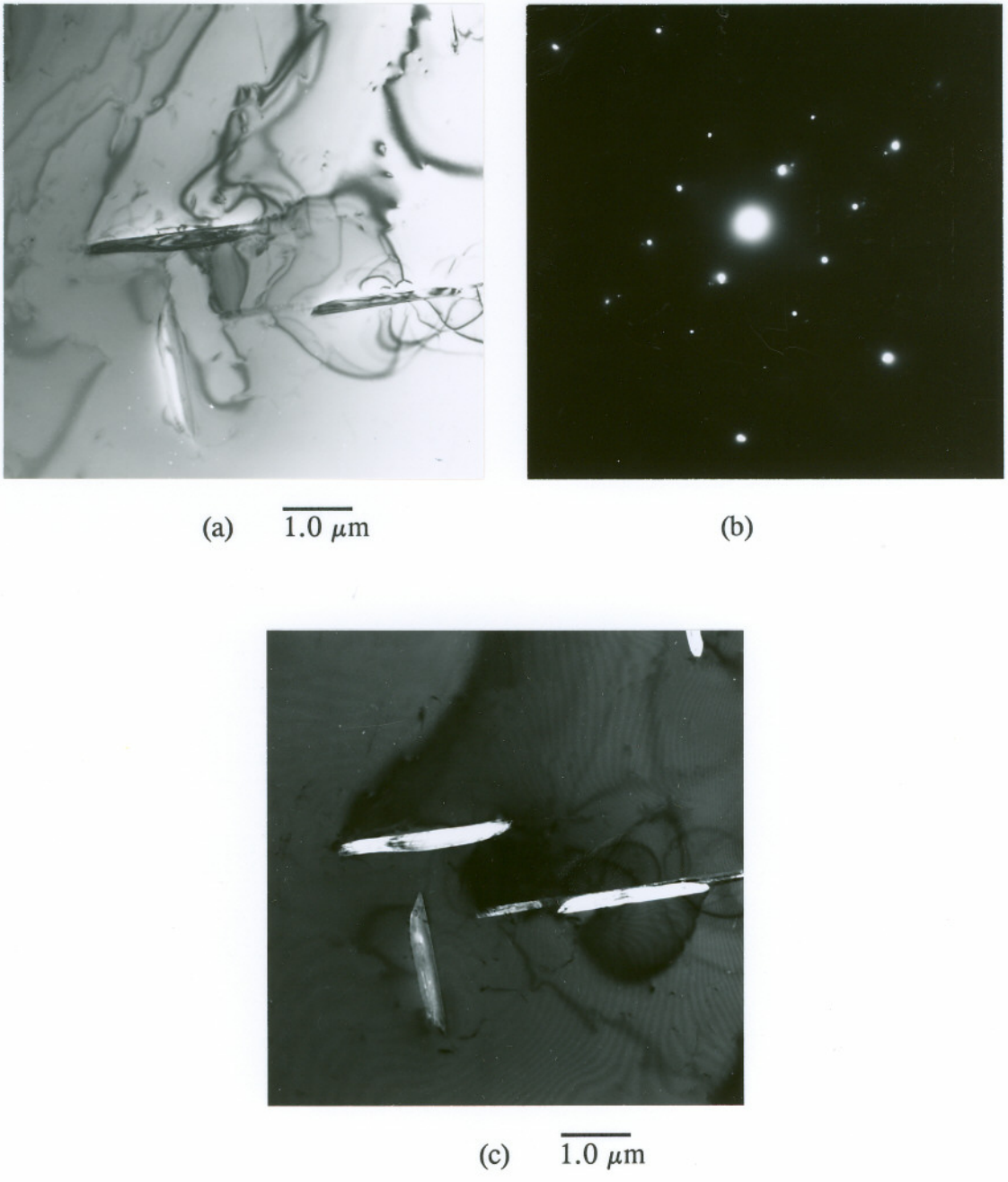

Figure 45. TEM bright-field micrograph (a) showing transgranular Cr_2N precipitates in DPSC 2100 material aged at 950°C for 10 hours. SADP (b) taken from Cr_2N shown in (a) with ZA $[3\bar{2}1\bar{3}]$. TEM-CDF micrograph (c) of (a) using $(11\bar{2}1)$ reflection.

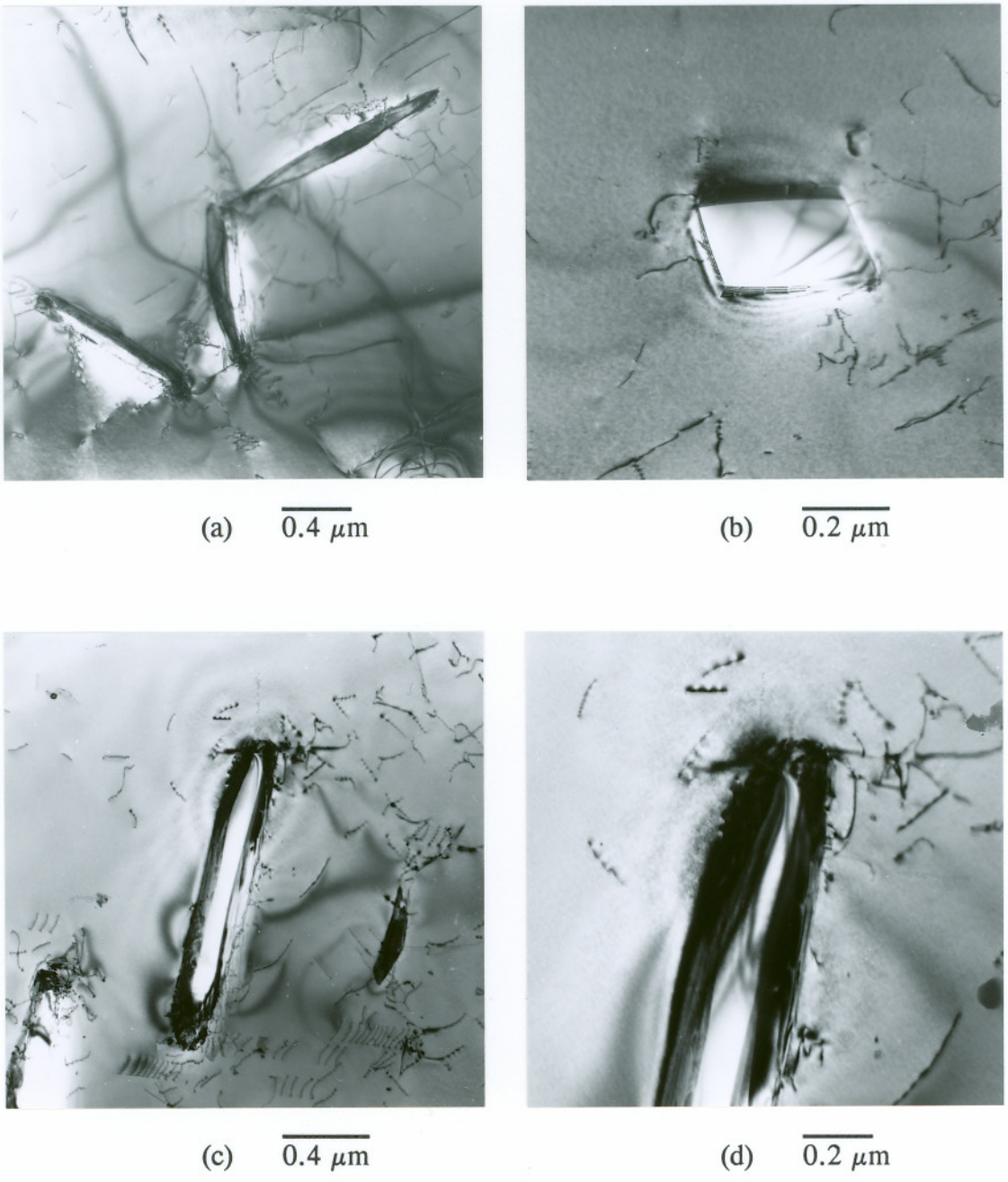

Figure 46. TEM-BF micrographs showing typical transgranular Cr_2N precipitates present in aged DPSC 2100 and DE 257 materials.

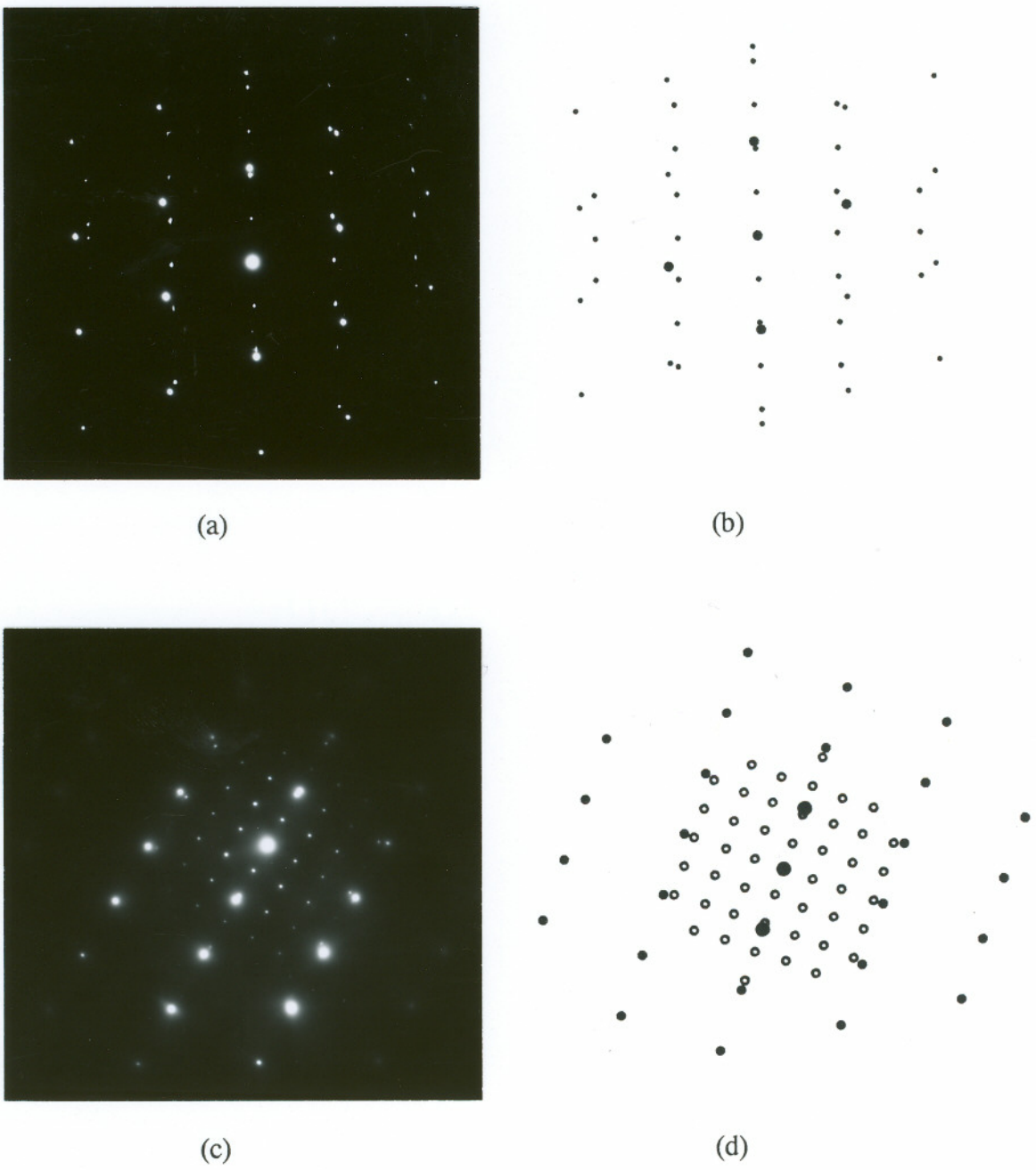

Figure 47. SADPs taken from transgranular Cr_2N precipitates and austenite matrix with ZA of (a) $[110]\gamma//[\bar{1}100]Cr_2N$ and (c) $[1\bar{1}\bar{2}]\gamma//[11\bar{2}0]Cr_2N$. Computer generated patterns (b,d) for SADPs of (a,c) assuming orientation relationship of $[110]\gamma//[\bar{1}100]Cr_2N$ and $(1\bar{1}1)\gamma//(0001)Cr_2N$.

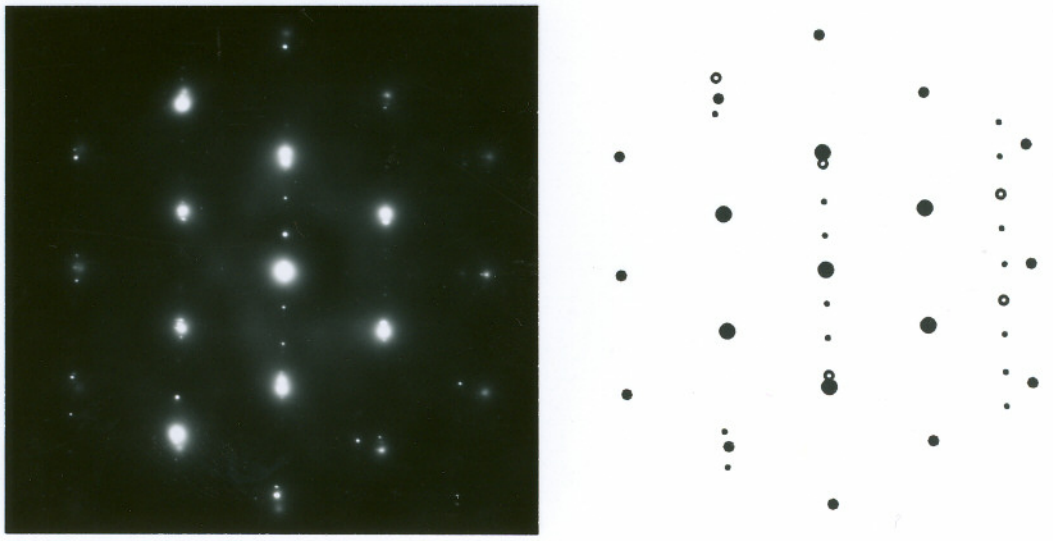

(a) (b)

Figure 48. SADP taken from transgranular Cr_2N precipitates and austenite matrix with ZA of $[\bar{1}11]\gamma$ and Cr_2N close to $[5\ 5\ \bar{1}\bar{0}\ 6]$. Computer generated pattern (b) for SADP of (a) assuming orientation relationship of $[110]\gamma//[\bar{1}100]Cr_2N$ and $(1\bar{1}1)\gamma//(0001)Cr_2N$.

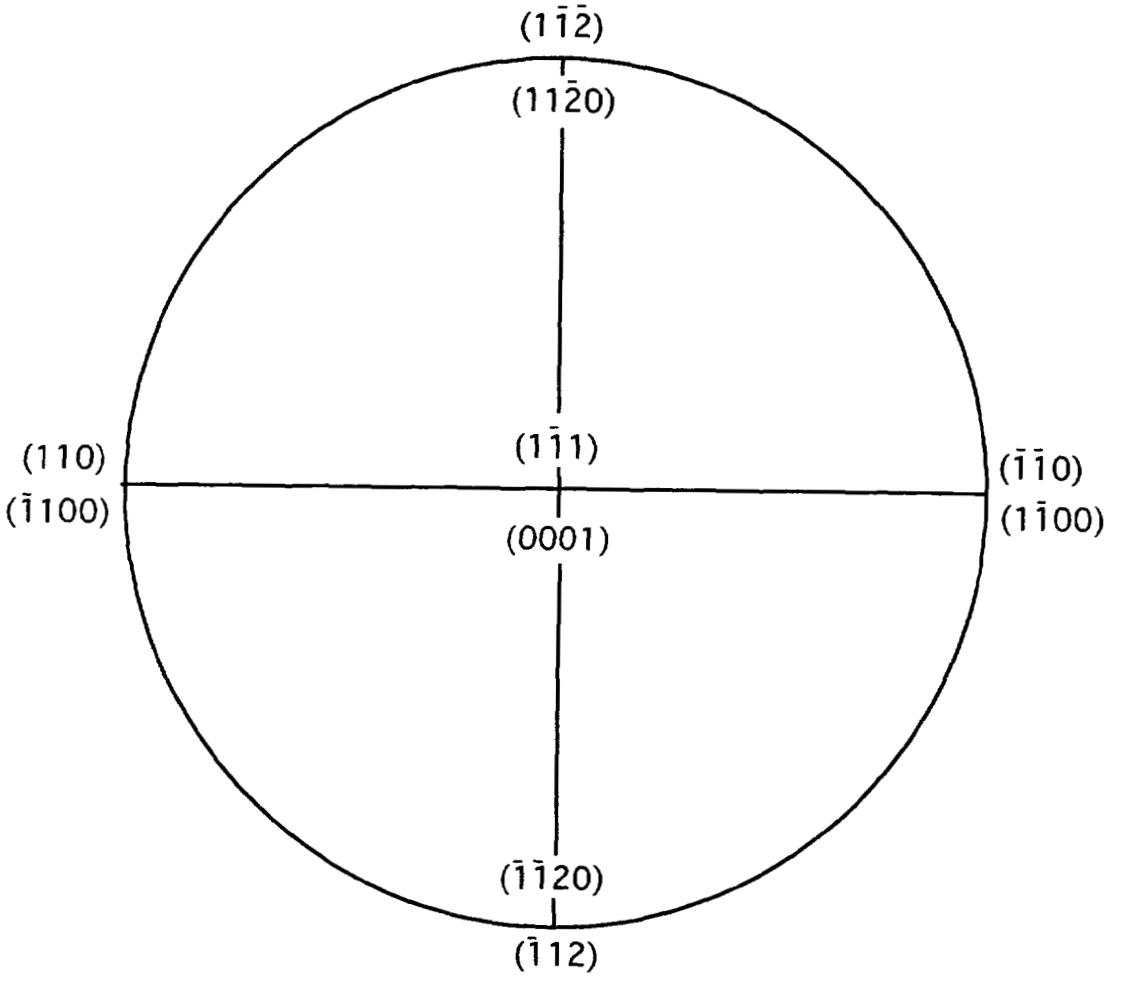

Figure 49. Stereographic representation of the orientation relationship between the austenite and Cr_2N precipitates of $[110]\gamma//[\bar{1}100]Cr_2N$ and $(1\bar{1}1)\gamma//(0001)Cr_2N$.

Over-All Time-Temperature-Precipitation Diagrams

Individual TTP diagrams developed for GB, cellular, and transgranular precipitation of Cr_2N were combined and resulted in over-all TTP diagrams for heats DPSC 2100 and DE 257 presented in *Figures 50 and 51*, respectively. Time-temperature-precipitation behavior for the two alloys was found to be quite similar, except for minor differences as specifically discussed in prior and subsequent sections. Precipitation of Cr_2N at GBs, by cellular decomposition, and within the matrix (transgranular) occurred at shorter times for given aging temperatures in heat DPSC 2100 than in heat DE 257.

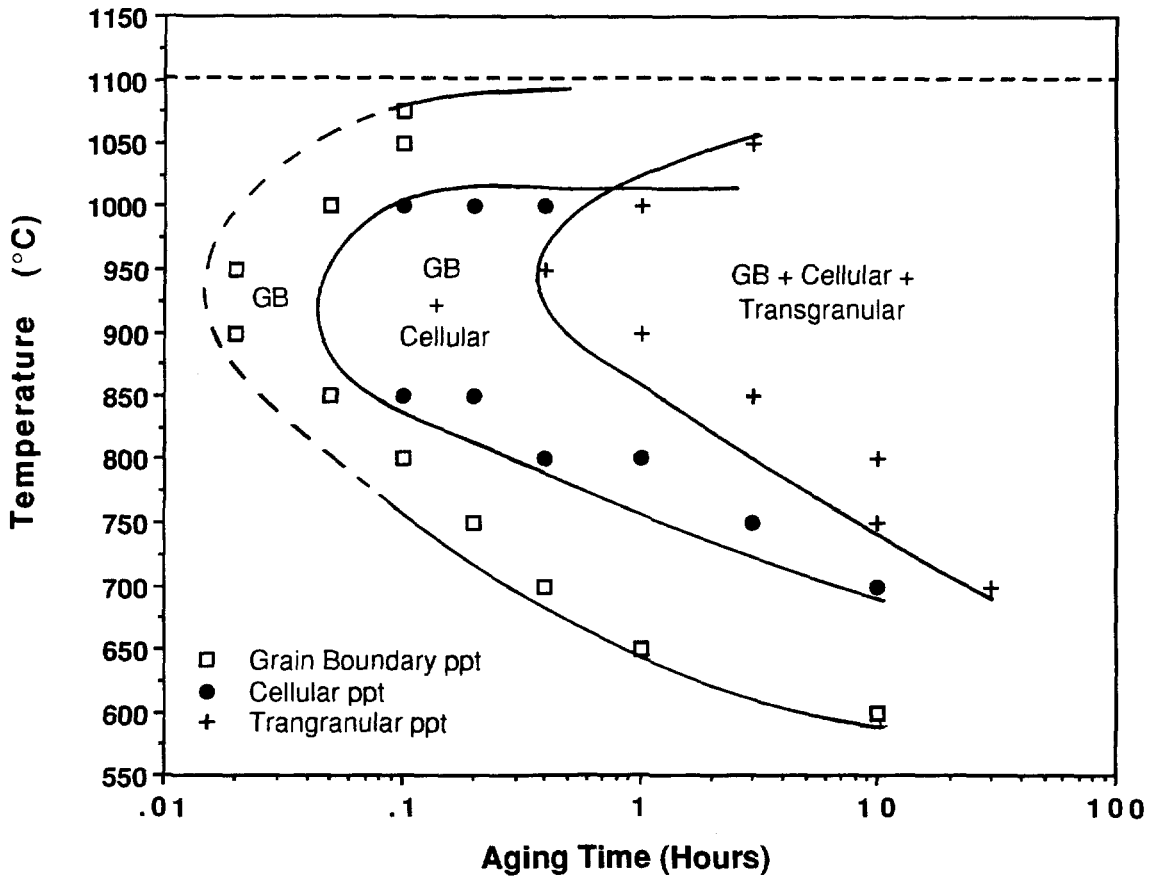

Figure 50. Time-temperature-precipitation curve for grain boundary, cellular, and transgranular precipitation in heat DPSC 2100.

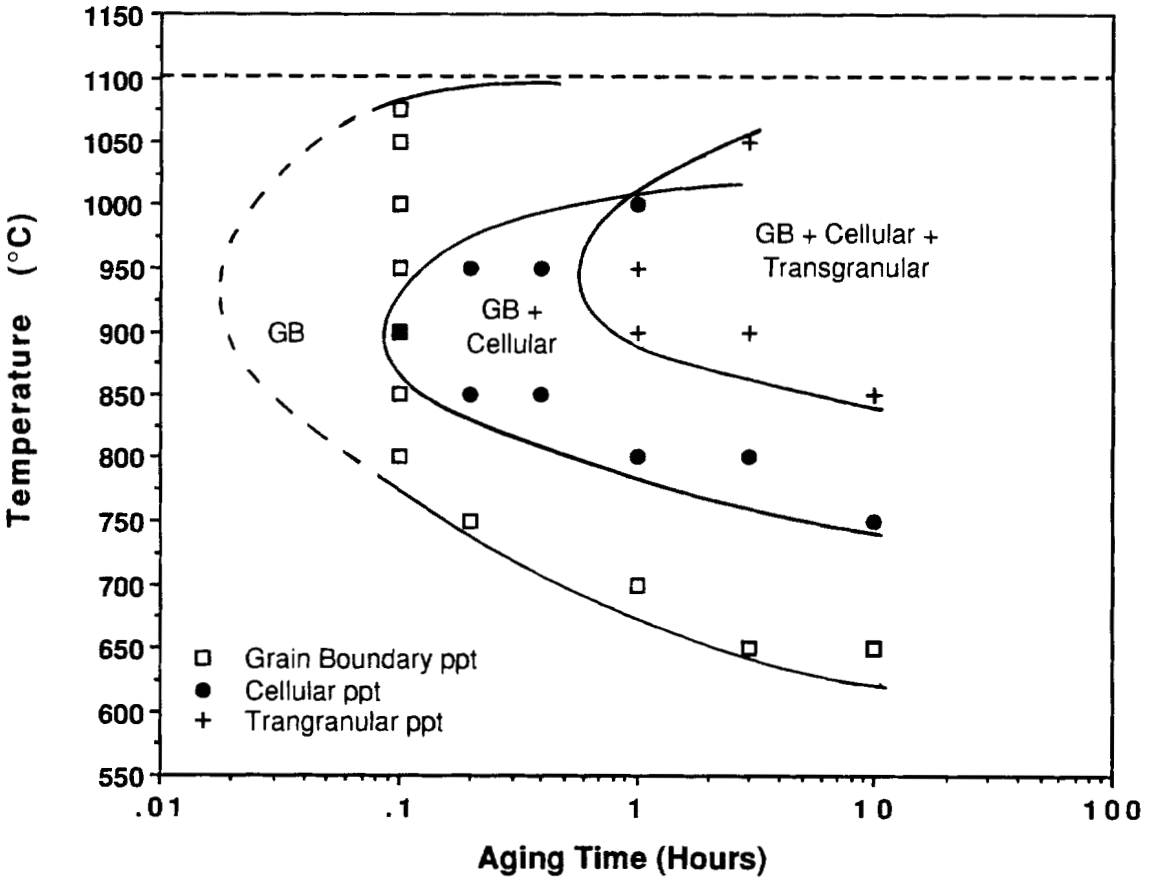

Figure 51. Time-temperature-precipitation curve for grain boundary, cellular, and transgranular precipitation of Cr_2N in heat DE 257.

Precipitate Composition Analysis

Compositions of GB and lamellar Cr_2N from both heats of material, analyzed by STEM/EDS, are tabulated in *Table 13*. Only the metallic species present in the precipitates could be analyzed and the results were normalized to 100%.

Generally, the compositions of the Cr_2N precipitates did not vary as a function of base material composition or precipitate location (GB versus cellular). For materials aged at temperatures between 800 and 1000°C, the precipitates were Cr-rich, containing about 90 wt% Cr, and also Mo, Fe, Si, and V. Grain boundary precipitates in DE 257 material aged at 700°C/1 hour contained considerably less chromium (only about 76 wt% Cr) than precipitates heat treated at higher temperatures. This would seem to indicate that precipitates in an earlier stage of development, might be richer in Fe, Mo, and Si than precipitates which are further developed. However, more work would be required to determine a correlation between aging temperature/time and precipitate compositions.

Transgranular precipitates from heat DPSC material aged at 950°C for 10 hours were analyzed in-situ and were found to be Cr-rich. Qualitatively, good correlation was found between compositions of transgranular and GB precipitates, measured in-situ.

Precipitation of χ-Phase

Precipitates, with measured d-spacings which matched the χ-phase results from XRD, were found to be present at grain boundaries and within the austenite matrix of cellular decomposition products in DE 257 and DPSC materials aged for 10 hours at 900°C. Typical TEM-BF from these precipitates are shown in *Figure 52* along with SADP taken at zone axis of [111], and [110]. Indexed diffraction patterns corresponding to those shown in *Figure 52 (c,d)* are located in *Appendix C*. These precipitates were detected in isolated sample regions and were present in much

TABLE 13 - Composition of Metallic Elements in Cr_2N						
Material/ Condition	Precipitate Location	Composition (wt%)				
		Cr	Mo	Fe	Si	V
DPSC	GB	89.1	6.7	3.4	0.4	0.5
900°C/0.2 hr	Pearlite	89.7	4.7	3.3	1.6	0.7
DPSC	GB	90.5	4.8	3.1	0.6	0.9
900°C/1 hr	Pearlite	90.3	5.2	3.3	0.5	0.7
DPSC	GB	90.2	4.6	3.5	0.2	1.5
900°C/10 hrs	Pearlite	90.4	6.0	2.2	0.1	1.3
DPSC	GB	89.8	4.3	4.5	---	1.3
1000°C/10 hrs	Pearlite	89.7	4.4	4.5	---	1.2
DE 257 700°C/1 hr	GB	76.0	10.8	6.4	5.8	1.0
DE 257 800°C/1 hr	GB	90.4	4.4	2.8	0.9	1.3
DE 257 800°C/10 hrs	Pearlite	89.3	3.3	3.6	2.7	1.1

smaller volume fractions than Cr_2N. The χ-phase was not detected by either XRD of powder residues or by TEM analysis in samples heat treated for less than 10 hours.

Compositions of several χ-phase precipitates, such as those shown in *Figure 52*, were measured in-situ in the TEM using EDS. The average composition (wt%) of the precipitates analyzed was 54Fe-24Cr-19Mo-2Ni-1Si. This composition is very similar to the composition (52Fe-21Cr-22Mo-5Ni) for a χ-phase reported by Weiss and Stickler[58] in a 316 alloy. The nickel content of the χ-phase precipitates in the DPSC 2100 and DE 257 alloys was measured to be somewhat lower than that in the 316 alloy and may reflect the level of nickel in the bulk alloy.

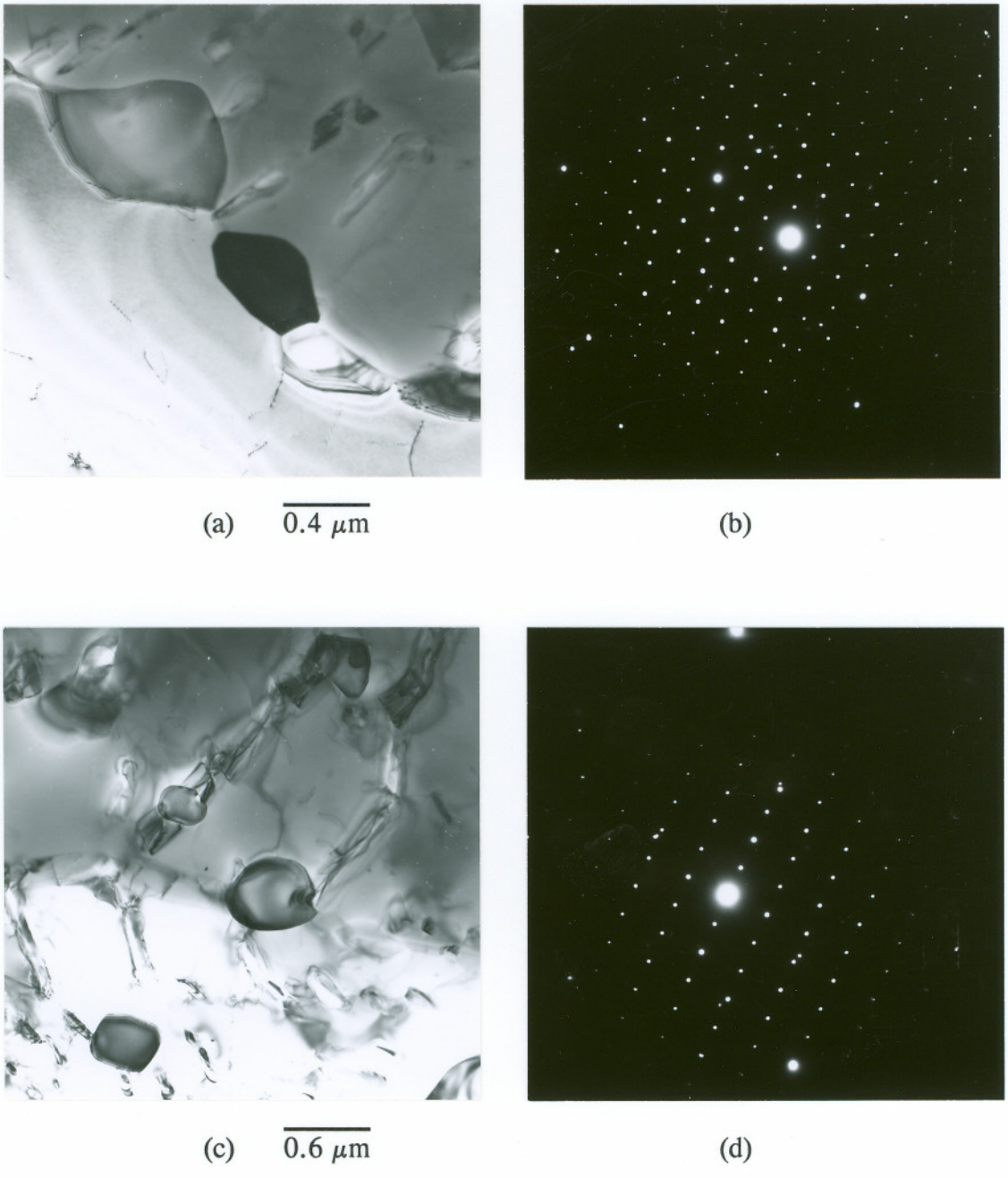

Figure 52. TEM-BF micrographs of χ-phase precipitates located at (a) austenite grain boundary and (c) within region of cellular decomposition. SADPs (b) from precipitate in (a) at ZA $[111]\chi$, and (d) from precipitate in (c) at ZA $[110]\chi$.

STRAIN EFFECTS on ISOTHERMAL AGING

General Microstructures

General microstructural features of the cold-rolled DPSC 2100 material, before and after aging at temperatures ranging from 700 to 1000°C, are shown in the optical micrographs of *Figures 53 and 54.* All of the specimens were photographed after electrolytic etching with 10% oxalic acid.

It is important to note that GBs and grain interiors of the as-rolled material were not preferentially etched by the oxalic acid solution. This indicated that the initial DPSC 2100 cold rolled material was not susceptible to attack by oxalic acid etching and that this etchant could be used to determine the presence of Cr_2N in cold worked materials, after thermal aging, as it was for solution annealed materials.

Lineal features within grain interior regions of cold-rolled and aged materials were etched as shown in the optical micrographs of *Figures 53 and 54.* These regions corresponded to the presence of long needle-like transgranular precipitates (Cr_2N) present in the aged materials as confirmed by SEM and TEM examinations. The SEM micrographs of *Figure 55* show transgranular precipitates formed after aging at 850°C for 10 hours in DPSC 2100 solution annealed and cold rolled materials. The formation of elongated, needle-like precipitates in cold rolled materials is typified in the SEM micrograph of *Figure 55d.* This is in comparison to the short, platelet precipitates formed in annealed materials *[Figure 55 (a,b)].*

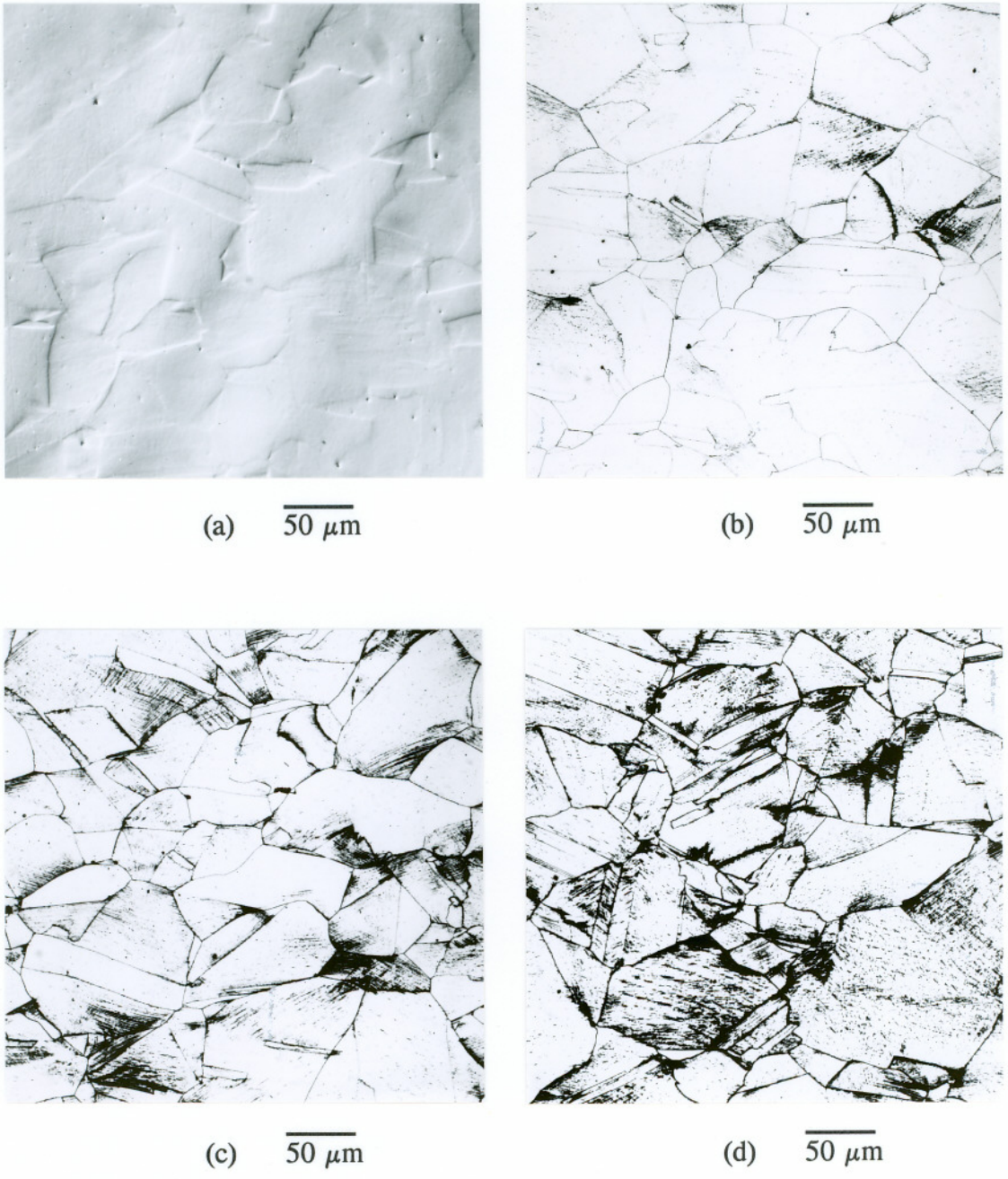

Figure 53. Optical micrographs from cold-rolled heat DPSC 2100 material (a) as cold-rolled, and after aging for 1 hour at temperatures of (b) 700°C, (c) 750°C, and (d) 800°C (electrolytically etched with 10% oxalic acid).

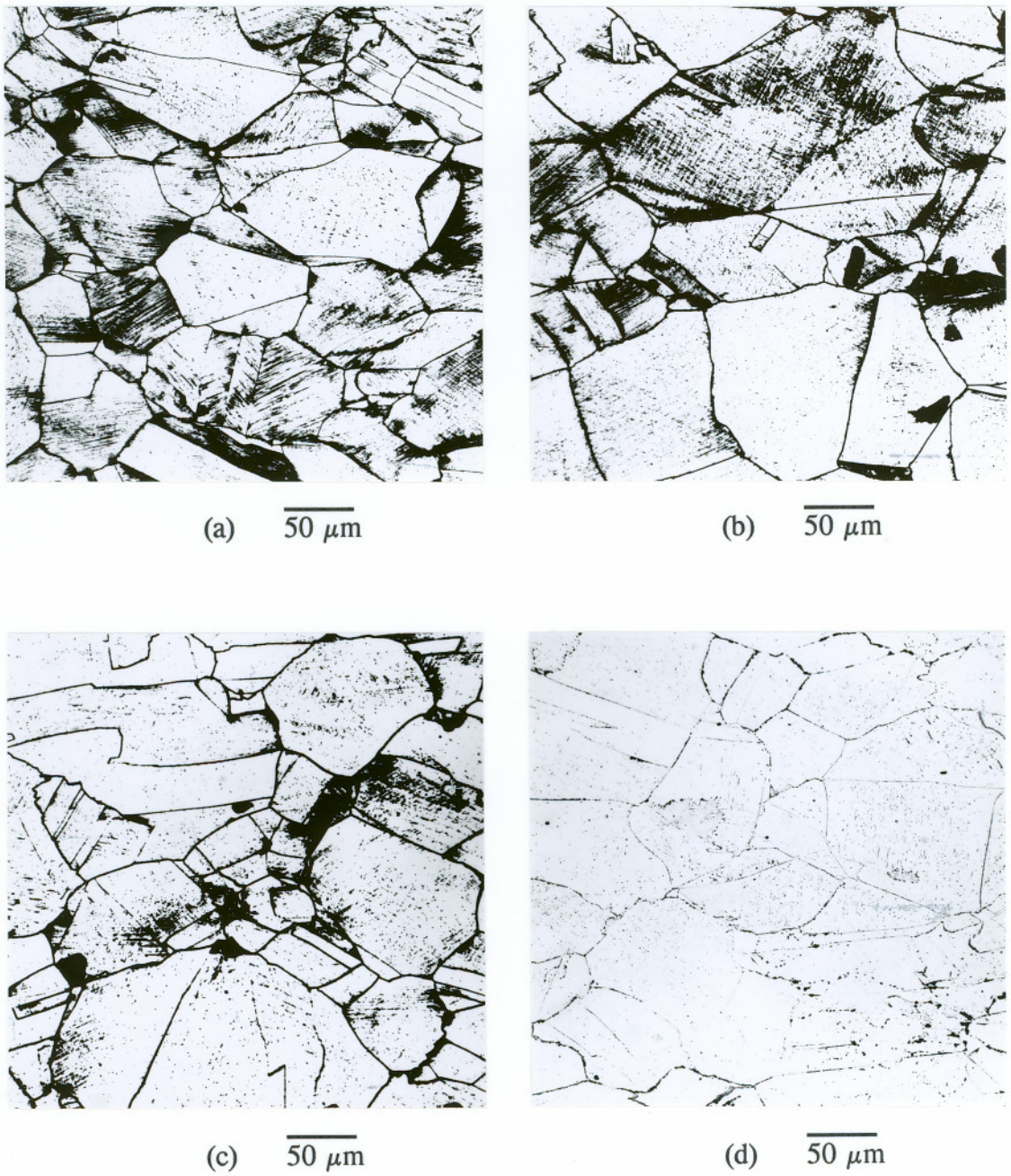

Figure 54. Optical micrographs from cold-rolled heat DPSC 2100 materials after aging for 1 hour at temperatures of (a) 850°C, (b) 900°C, (c) 950°C, and (d) 1000°C (electrolytically etched with 10% oxalic acid).

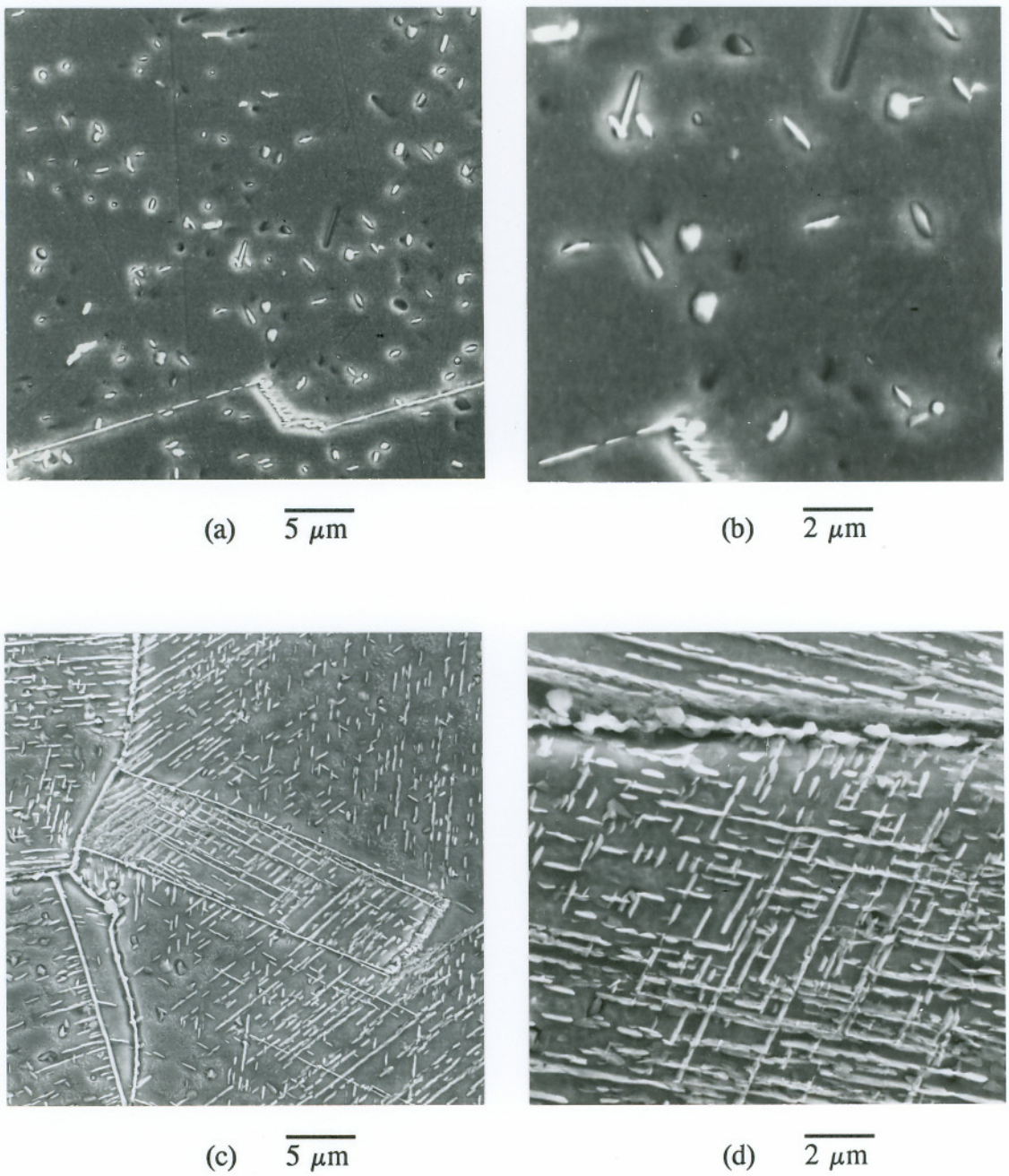

Figure 55. Secondary electron micrographs from heat DPSC 2100 materials aged at 850°C for 10 hours. Material in (a,b) aged in solution annealed condition and (c,d) cold-rolled prior to aging.

Prior deformation substantially accelerated the onset of transgranular precipitation of Cr_2N for all temperatures below 1000°C and GB precipitation below 800°C. This is illustrated by the TTP diagrams of *Figures 56 and 57* which compare the onset of GB and transgranular precipitation for annealed and cold-rolled materials. For annealed DPSC 2100 materials, rapid GB precipitation occurred at times of less than 0.1 hour at temperatures between 800 and 1075°C, and in less than 0.01 hour at 900 and 950°C. This rapid GB precipitation precluded study of deformation induced acceleration of GB development at these temperatures. However, GB precipitation was definitely accelerated in cold-rolled materials at temperatures below 800°C.

Deformation caused enhancement of transgranular precipitation and shifted the TTP curve to much shorter times and lower temperatures *(Figure 57)*. Deformation had little effect on the kinetics of transgranular precipitation at temperatures of 1000°C and above *(see Figure 54d)*. Transgranular precipitation in cold-rolled materials occurred at relatively short times at temperatures below 700°C. This aging treatment did not induce any transgranular precipitation in annealed materials. Nucleation times at temperatures between 800 and 950°C could not be determined using furnace aging treatments due to rapid precipitation (less than 0.1 hour).

The development of cellular precipitation was clearly retarded in cold-rolled materials. For example, very few cells were observed for samples aged at 900°C for an aging time of 1 hour *(Figure 54b)*. This aging treatment produced almost 30 volume% cells in solution annealed materials *(see Figure 20d)*. Cellular precipitation development in cold-rolled materials could not be quantified due to the large volume of transgranular precipitates present.

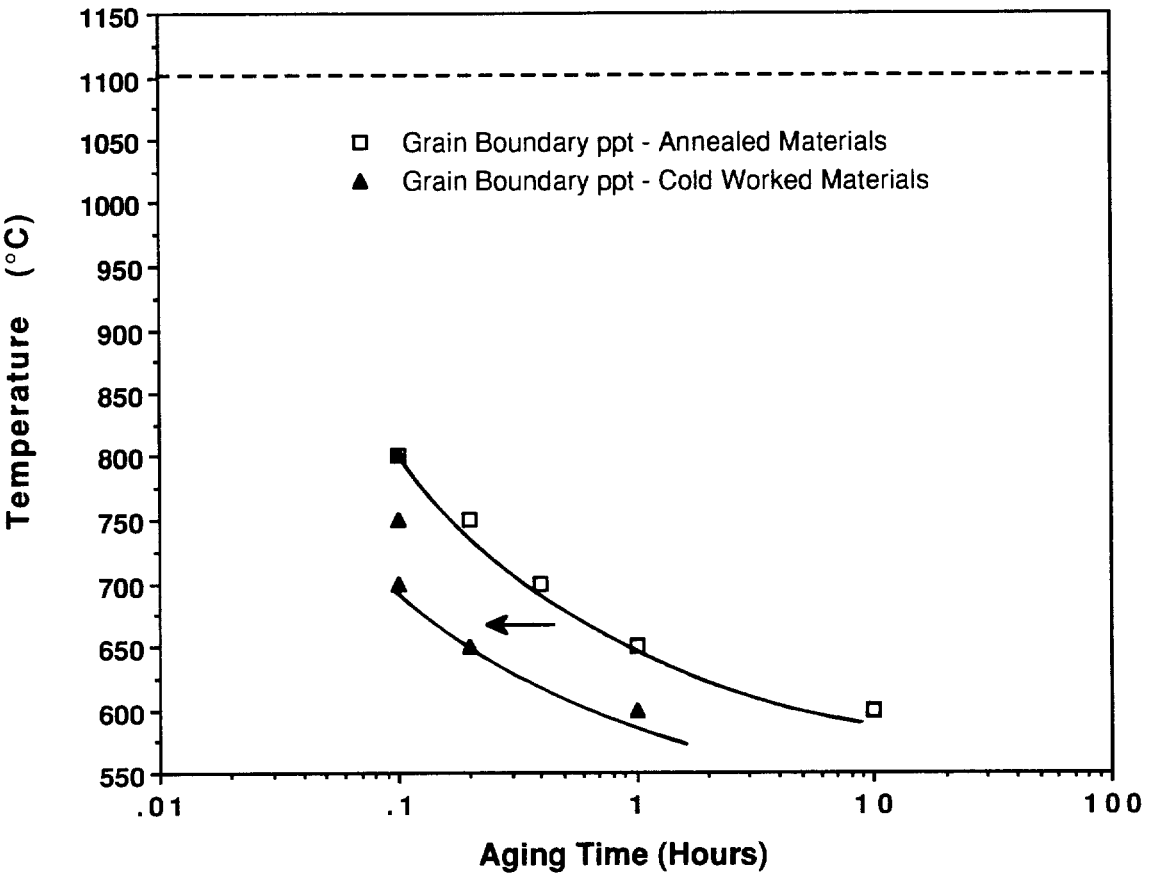

Figure 56. Effect of prior deformation on the time-temperature-precipitation characteristics of grain boundary Cr_2N precipitation in heat DPSC 2100.

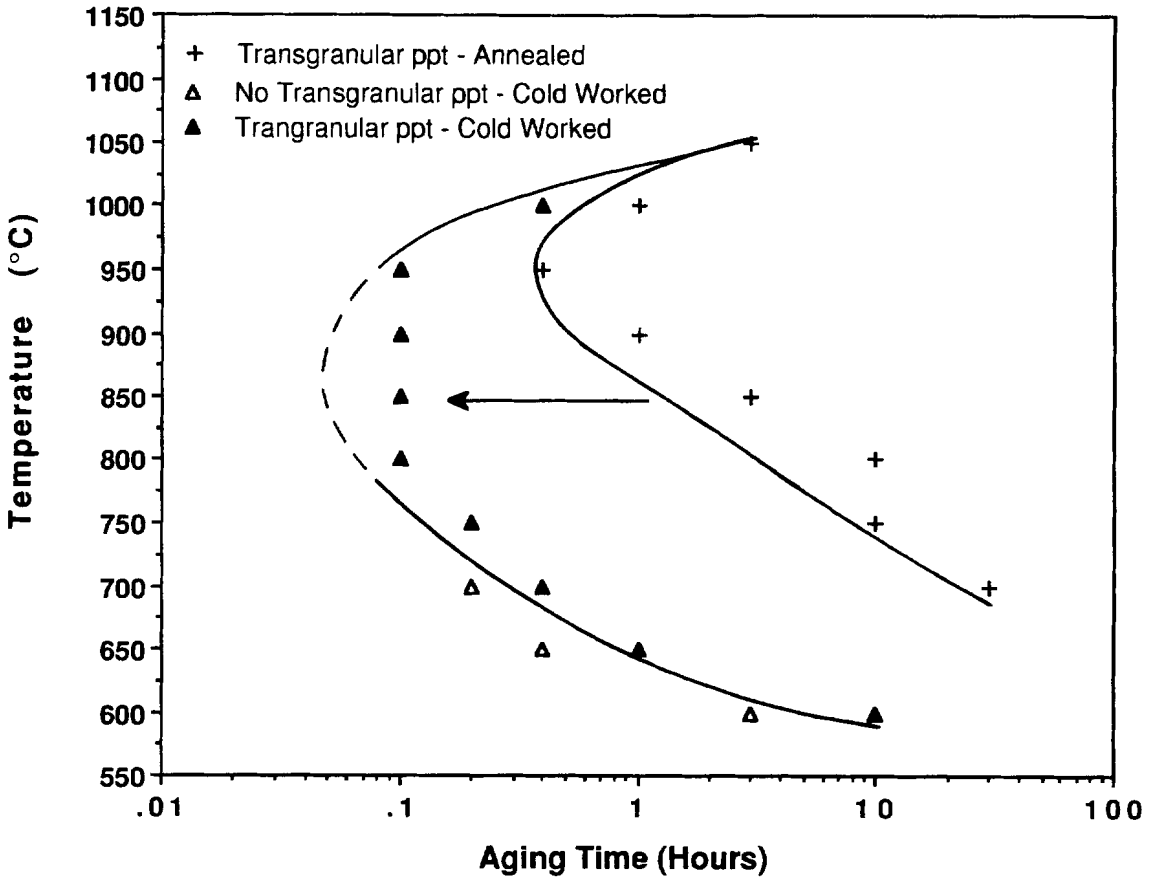

Figure 57. Effect of prior deformation on the time-temperature-precipitation characteristics of transgranular Cr_2N precipitation in heat DPSC 2100.

Transmission Electron Microscopy

Initial Deformation Structure

The initial cold-rolled material contained a high density of dislocation tangles, slip-bands, and deformation twins. Planar dislocation arrays, in which individual dislocations could be identified, were not observed, but instead, concentrated slip-bands were formed due to the high degree of deformation in the material. Dislocation cell structures were not observed. One of the primary deformation mechanisms in the cold-rolled material was deformation twinning. Cold-rolled materials contained a high density of deformation twins as shown in *Figure 58*. The habit plane for twinning was {111} and occurred along <112> directions as expected for fcc materials. Individual deformation twins were very thin (approximately 0.01 μm) and appeared to extend over entire grains.

Aged Structures

Transgranular precipitates (Cr_2N), representative of cold-rolled materials aged at temperatures between 600 and 950°C, are shown in the TEM micrographs of *Figures 59 and 60*. The examples shown were taken from a cold-rolled specimen aged at 900°C for 1 hour. Comparison of the precipitates shown in *Figure 59* to those shown in *Figure 60* illustrate the fact that the needle-like precipitates were not equal in width and thickness. No evidence of deformation twins was observed in samples aged at 900 or 1000°C. Twins were present in samples aged at 700°C, but their density was not as high as in the un-aged cold-rolled material.

In samples aged at 900°C, it was determined that the elongated precipitates of Cr_2N formed along <112> directions, parallel to the deformation twins *(Figure 60a)*. Apparently, Cr_2N precipitation occurred along the deformation twins. However, due to the absence of twins in these samples, direct observation of the

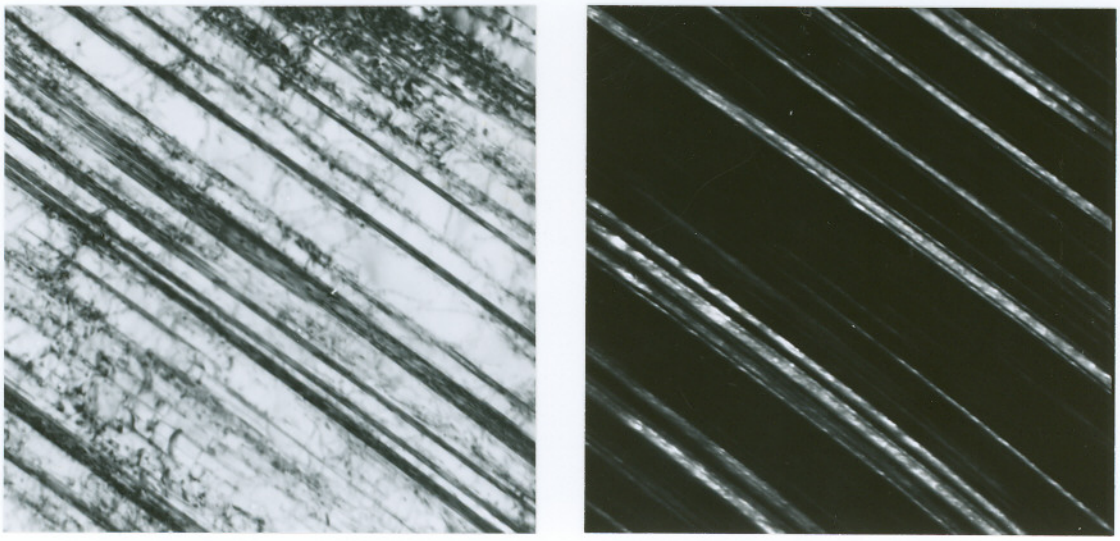

(a) 0.1 μm (b) 0.1 μm

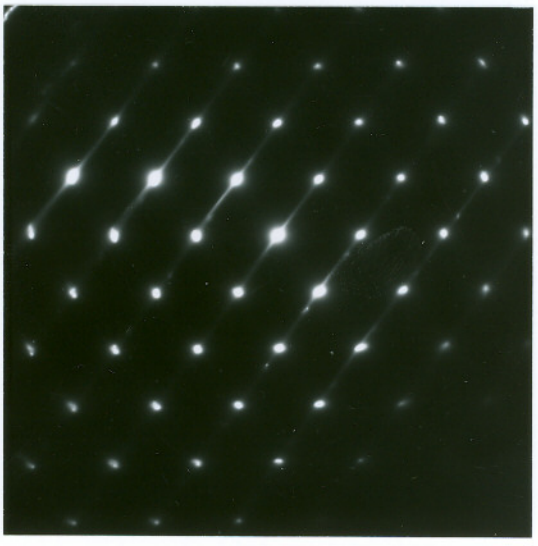

(c) ZA [110]γ

Figure 58. TEM micrographs taken from cold-rolled DPSC 2100 material showing the deformation twinning predominant. TEM-CDF micrograph in (b) was taken using (111)γ twin reflection. Streaks in SADP are due to twins and are perpendicular to the $\{111\}\gamma$ habit plane.

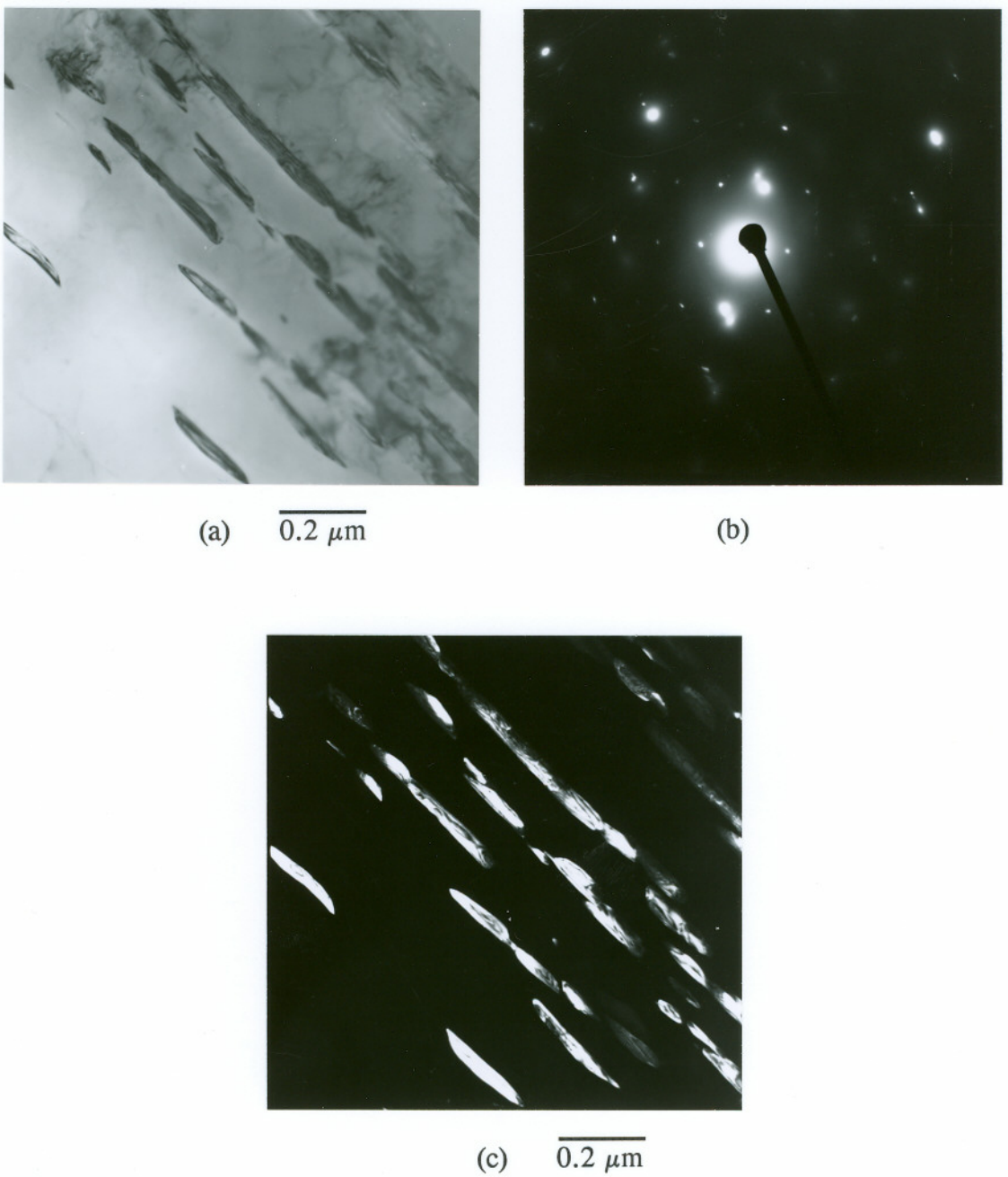

Figure 59. TEM-BF micrograph (a) showing transgranular Cr_2N precipitates present in cold-rolled DPSC 2100 material aged at 900°C for 1 hour. SADP (b) taken from Cr_2N shown in (a), ZA $[14\bar{5}\bar{3}]$. TEM-CDF micrograph of same area as (a).

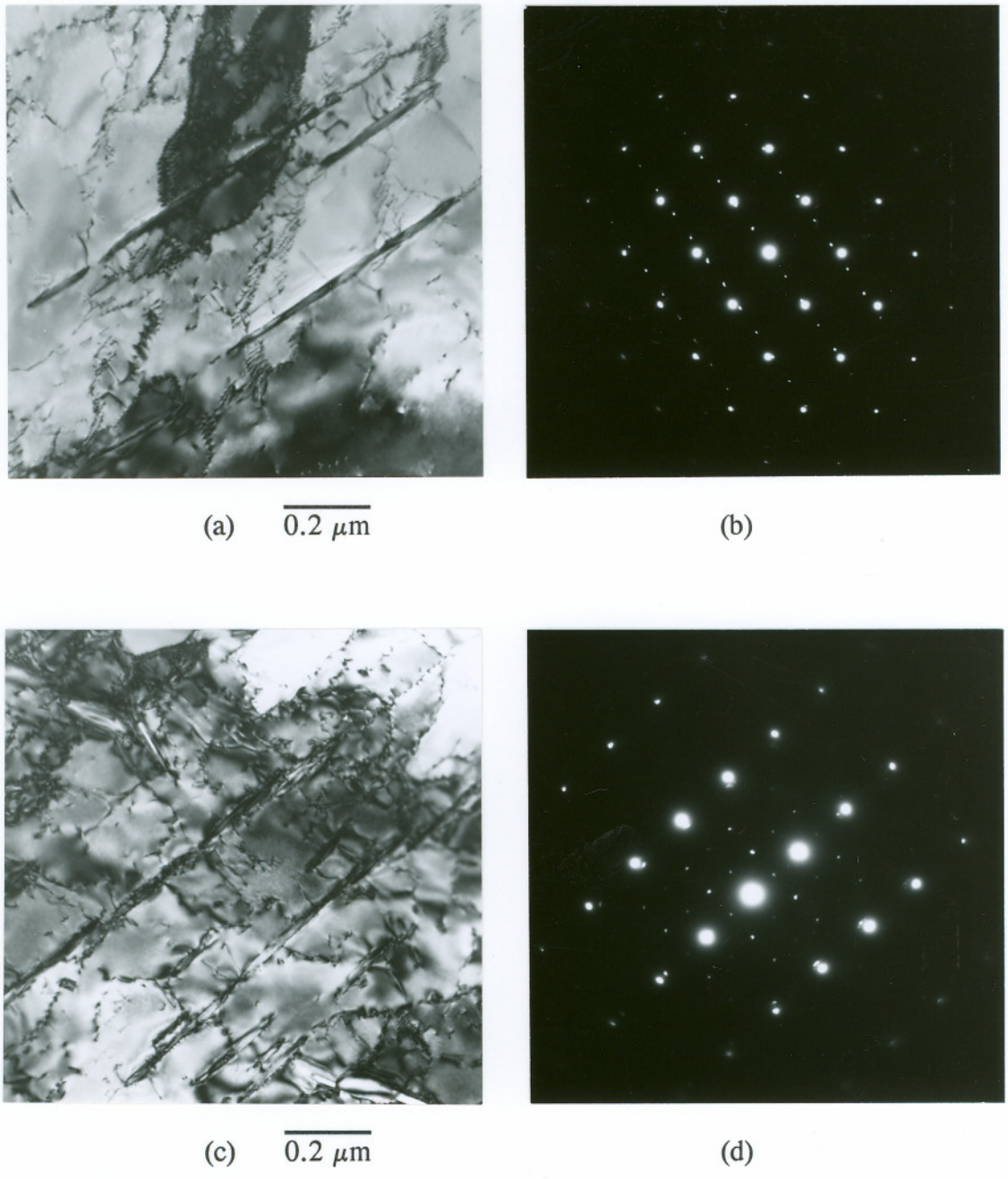

Figure 60. TEM-BF micrographs (a) and (c) showing transgranular Cr_2N precipitates present in cold-rolled DPSC 2100 materials aged at 900°C for 1 hour. SADPs of austenite and Cr_2N (b) from region (a) with $[110]\gamma$ and $[\bar{1}100]Cr_2N$), and (d) from region (c) with $[\bar{1}12]\gamma$ and $[\bar{1}\bar{1}20]Cr_2N$.

association between the twinning defects and Cr_2N nucleation and growth could not be established. In samples aged at 700°C, the specific regions in which twins were observed did not contain Cr_2N precipitates. Kinetics of nitride precipitation in samples aged at 700°C were much slower than at 900°C so the observation of Cr_2N precipitates in TEM samples at the lower aging temperatures was more difficult. More TEM work would be required to establish a more definite association between the deformation twins and Cr_2N precipitates.

Transgranular precipitates formed in deformed materials generally had the same orientation relationship with the matrix as described earlier for transgranular precipitation in solution annealed materials. This was true for specimens heat treated at temperatures below 1000°C as illustrated in the SADPs of *Figure 60*, taken from a specimen aged at 900°C. In some regions of specimens heat treated at 1000°C in which transgranular precipitation was observed, precipitates showed an orientation relationship with the matrix. However, in other areas, there did not seem to be any orientation relationship between the matrix and Cr_2N.

Strain recovery occurred to a significant extent during heat treatment at 1000°C. Subgrains were well developed in the material after aging for one hour at 1000°C. The polygonized structure and subgrain boundaries, made up of dislocations, are shown in the TEM-BF micrographs of *Figure 61*. Recovery occurred to a much smaller extent in specimens aged at 950 and 900°C. Isolated regions of subgrain formation, identical to those shown in *Figure 61*, were observed.

Summary - Prior Deformation Effects

Prior deformation enhanced GB and transgranular precipitation in DPSC 2100 materials heat treated at temperatures of 600 to 1000°C. Precipitation occurred at shorter times for a given aging temperature compared to annealed materials. The effect was directly observed for GB precipitation of Cr_2N at temperatures below 800°C. Grain boundary precipitation was so rapid in annealed materials aged

between 800 and 1000°C that precipitation enhancement due to prior deformation could not be measured within this temperature range. Aged structures of cold-rolled materials contained only a small fraction of the cellular precipitation products present in annealed materials.

Acceleration of transgranular Cr_2N precipitation in cold-rolled materials was dramatic for aging in the temperature range of 600-950°C. The TTP curve for transgranular precipitation shifted to much shorter times and lower temperatures. In annealed materials, transgranular precipitation was not observed until 30 hours of aging at 700°C, compared to 0.4 hours in cold-rolled materials. The crystal structure of the precipitates seemed to be unchanged by prior deformation. However, the morphology of the transgranular precipitates changed from plates, to elongated needles.

Strain recovery, characterized by formation of subgrain structures, started to have an effect on microstructural development at temperatures of about 900°C, but became significant in samples aged at 1000°C. Due to strain recovery at 1000°C, prior deformation provided little enhancement of transgranular precipitation kinetics at this temperature.

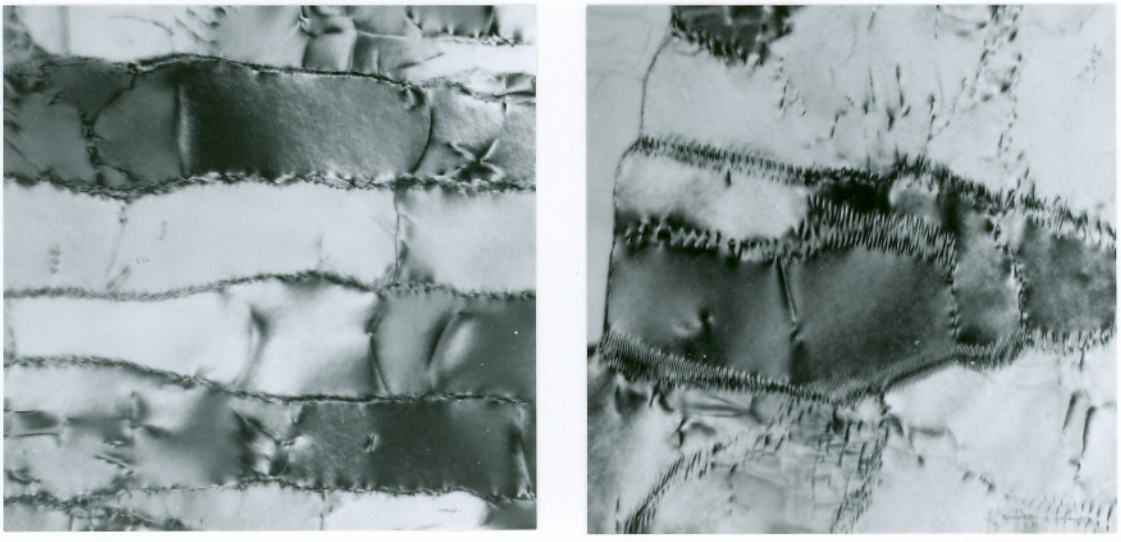

(a) 0.2 μm (b) 0.1 μm

Figure 61. TEM-BF micrographs of polygonized microstructure taken from cold-rolled DPSC 2100 material aged at 1000°C for 1 hour. Subgrain boundaries consisted of aligned dislocation structures as shown in (b).

PRECIPITATION-INDUCED CHROMIUM-DEPLETION

The purpose of the work presented in this section was to determine whether or not the precipitation of Cr_2N (primarily GB and cellular precipitate products) would induce GB and/or transgranular Cr-depletion in aged DPSC 2100 materials. It did not provide an in-depth study of the parameters controlling Cr-depletion in these materials, but merely determined their susceptibility to sensitization.

Indirect Measurement

The results of EPR testing on DPSC 2100 solution annealed materials aged at 700 and 900°C, and cold rolled material aged at 700°C, are shown in *Table 14.*

None of the samples aged at 900°C showed any reactivation during EPR testing. Thus, sensitization of this material did not occur for aging at 900°C. This was in spite of the large amount of Cr_2N precipitated within the samples, present both at grain boundaries and as lamellar Cr_2N in the cellular decomposition products. Transgranular precipitation was also present in some of the samples aged at 900°C, specifically, those aged for 1 or more hours.

Aging at 700°C caused sensitization in annealed materials for aging times equal to or greater than 1 hour. Reactivation during EPR testing did not occur in solution annealed materials for aging times less than 1 hour. For cold-rolled materials, sensitization occurred at 700°C for the shortest aging time of 0.2 hours. Cold working significantly enhanced sensitization development for aging at 700°C. Comparison of sensitization development at 700°C for solution annealed and cold worked materials is shown in *Figure 62.* Cold worked material aged for 0.2 hours had an EPR value equal to solution annealed material aged for 1 hour. Also, the DOS values reached in the cold worked material after aging at 10 hours was more than 4 times greater than that for the solution annealed material.

TABLE 14 - EPR Testing Results for Heat DPSC 2100			
Aging Temp./Time (°C - Hours)	Initial Material Condition*	Integrated Charge Value Q (coulombs)	Normalized EPR-DOS Pa (coul./cm^2)
700 - 0.2	SA	NR	NR
700 - 0.4	SA	NR	NR
700 - 1.0	SA	0.0025	0.4
700 - 3.0	SA	0.0315	5.0
700 - 10	SA	0.0905	14.4
700 - 0.2	SA + CW	0.0028	0.5
700 - 0.4	SA + CW	0.0154	2.5
700 - 1.0	SA + CW	0.0445	7.1
700 - 3.0	SA + CW	0.1687	26.9
700 - 10	SA + CW	0.4215	67.1
900 - 0.1	SA	NR	NR
900 - 0.2	SA	NR	NR
900 - 0.4	SA	NR	NR
900 - 1.0	SA	NR	NR
900 - 3.0	SA	NR	NR
900 - 10	SA	NR	NR

* SA = Solution Annealed at 1150°C for 2 hours
CW = Cold Rolled 22%
NR = No Reactivation During EPR Test
(Material Not Sensitized)

Optical micrographs taken from SA and CW materials aged at 700°C for 1 and 10 hours (*Figure 63*), directly after EPR testing, show the corrosive attack caused during the EPR test. Attack for the SA material aged at 700°C for 1 hour was very slight while basically 100% GB attack was present in the cold worked sample with the

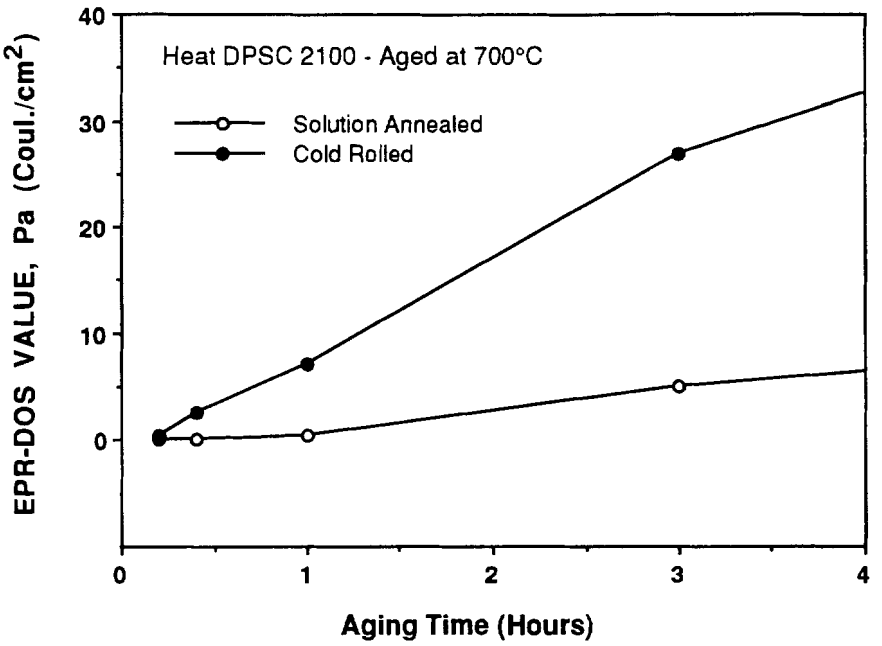

(a)

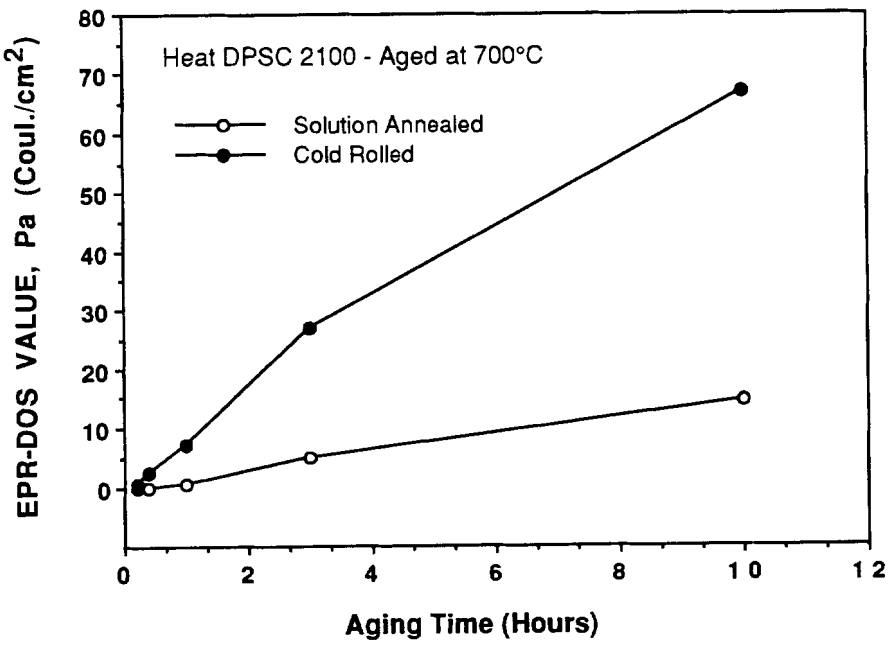

(b)

Figure 62. Degree of sensitization measured by EPR test for solution annealed and cold-rolled DPSC 2100 materials aged at 700°C.

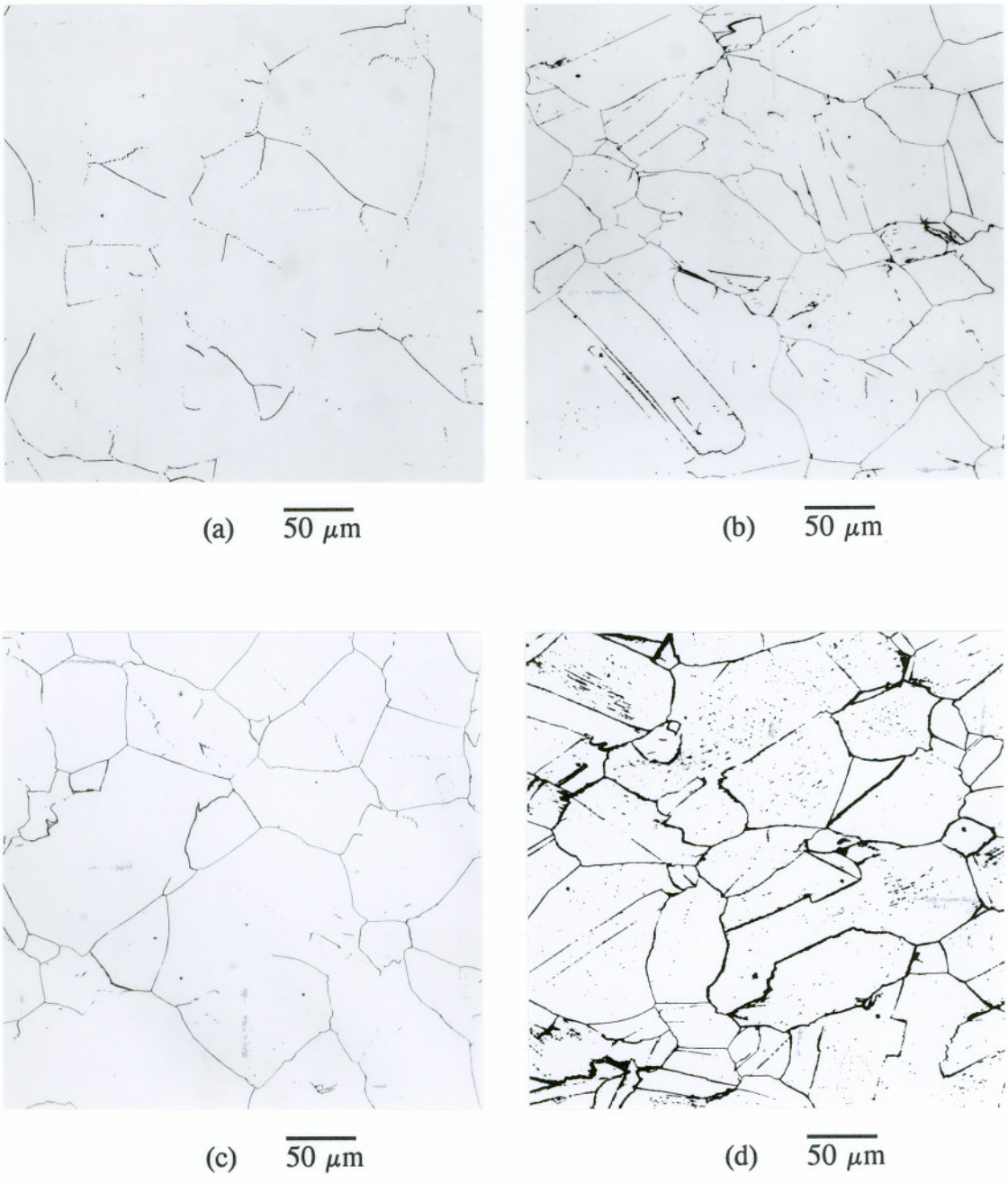

Figure 63. Optical micrographs taken from (a,c) solution annealed and (b,d) cold-rolled DPSC 2100 materials after aging and EPR testing. Aging was done at 700°C for (a,b) 1 hour and (c,d) 10 hours.

same heat treatment. Note that attack of twin boundaries also occurred in the cold worked material *(Figure 63)*. Very slight transgranular attack occurred in this CW sample. The SA sample aged at 700°C for 10 hours *(Figure 63)* had 100% grain boundary attack, but showed no evidence of attack at twin boundaries although the DOS of this sample was greater than the cold worked sample aged at 700°C for 1 hour. The grain boundary attack during EPR testing of the cold worked sample aged at 700°C for 10 hours was more significant than the SA material *(Figure 63)*. This sample also had the most transgranular attack of any of the EPR test specimens indicating that Cr-depletion was present due to transgranular as well as grain boundary precipitation. Still, the contribution of the transgranular Cr-depletion to the over-all DOS value, as compared to the GB contribution, is not considered as being significant.

Direct Measurement

Very fine spacing of Cr_2N precipitates at GBs was characteristic of both DE 257 and DPSC 2100 materials aged below 950°C. Fine spacing of GB precipitates prevented the direct measurement of GBCD using STEM/EDS analysis because the high chromium content of the Cr_2N precipitates influenced the profiles measured. However, an attempt was made to measure GBCD using STEM/EDS (spatial resolution of approximately 25 nm) for the EPR specimen of DPSC 2100 aged at 700°C for one hour. This specimen was known to be sensitized from the EPR results. Unfortunately, due to the small nitride spacing present in this sample, and other samples heat treated at 700°C, direct measurement of GBCD in the EPR specimens was not successful.

Although heat treatment at higher temperatures yielded well-spaced nitrides suitable for measurement of GB Cr-depletion profiles, sensitization did not occur for these heat treatments, as illustrated by the EPR test results.

Therefore, direct GBCD measurements were only conducted in the specially heat treated DPSC 2100 material. This specimen was aged successively at 1050°C/1 hour, 750°C/1 hours, and 650°C/1.5 hours. Even this sample was not ideal for GBCD measurement. This is illustrated by the TEM-BF micrographs of *Figure 64* showing two of the GB regions used for Cr-depletion profile measurements. There were two problems with this sample. The first problem was that, although the high temperature heat treatment produced grain boundary regions with widely spaced nitrides, grain boundary migration occurred between the nitrides. This condition is known to produce asymmetric Cr-depletion profiles in sensitized materials.[71] The second complication was that the lower temperature heat treatment designed to produce low chromium concentrations at the GBs, also initiated additional precipitation of finely spaced GB nitrides, which eliminated much of the well-spaced regions between the large nitrides formed at 1050°C.

In spite of these complications, Cr-depletion was measured at several grain boundary regions in the special heat treatment sample, with GB chromium minimums as low as 10 wt% measured. Two of the Cr-depletion profiles measured are shown in *Figure 65 (a,b)*. The GBCD profiles measured from this sample were generally asymmetric and a fairly wide range of Cr-minimum values were measured from boundary to boundary. The minimum chromium values measured directly at several GBs are shown in *Figure 66*. Although there is a wide range between the chromium values measured, they are well below the bulk chromium value of about 18.5 wt% measured by STEM/EDS.

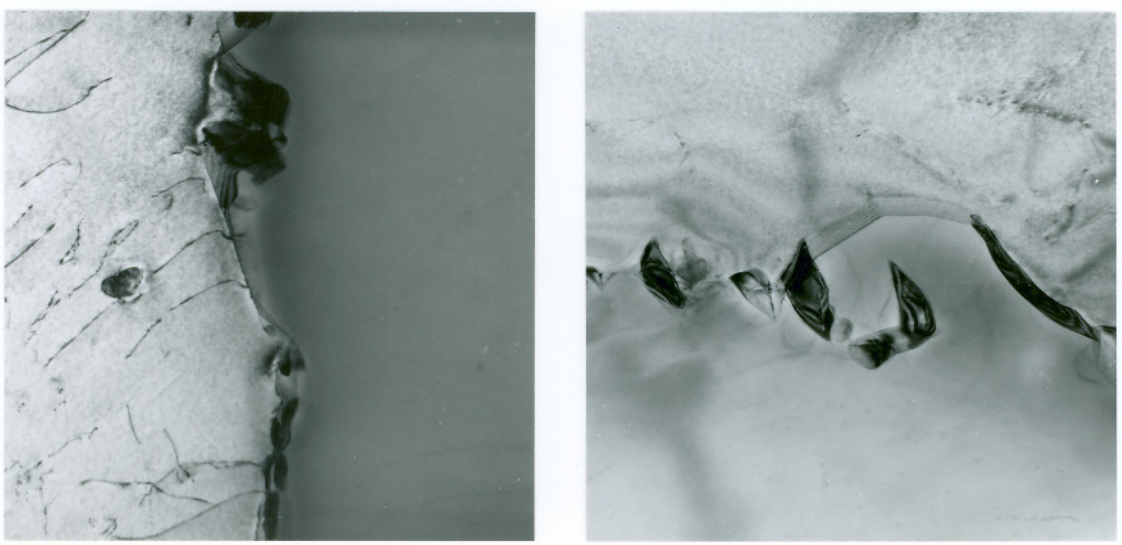

(a) 0.2 μm (b) 0.2 μm

Figure 64. TEM-BF micrographs of typical grain boundary regions in DPSC 2100 material aged successively at 1050°C for 1 hour, 750°C for 1 hour, and 650°C for 1.5 hours. Chromium concentration profiles were measured across, and normal to, grain boundaries.

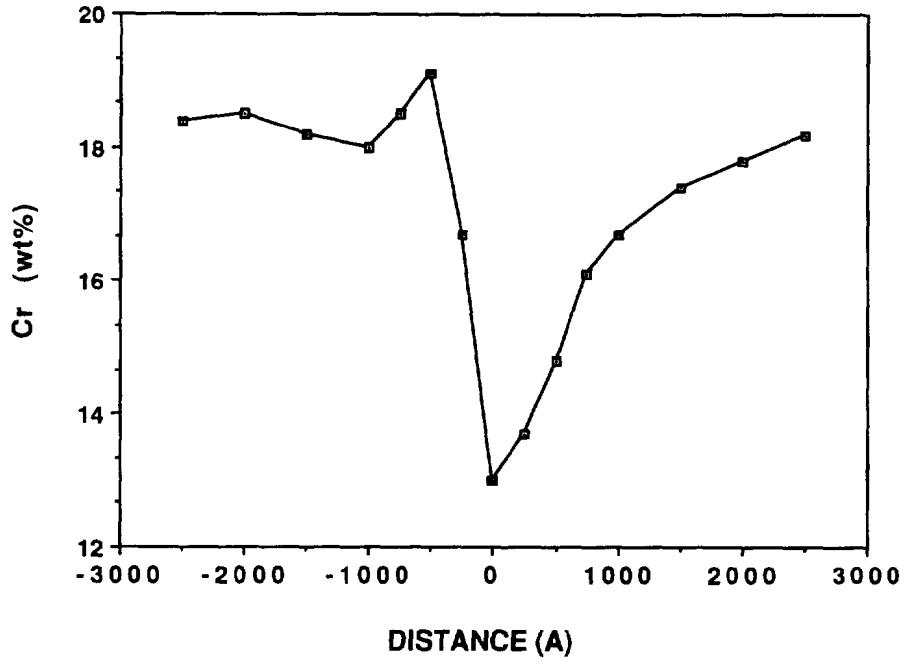

(a)

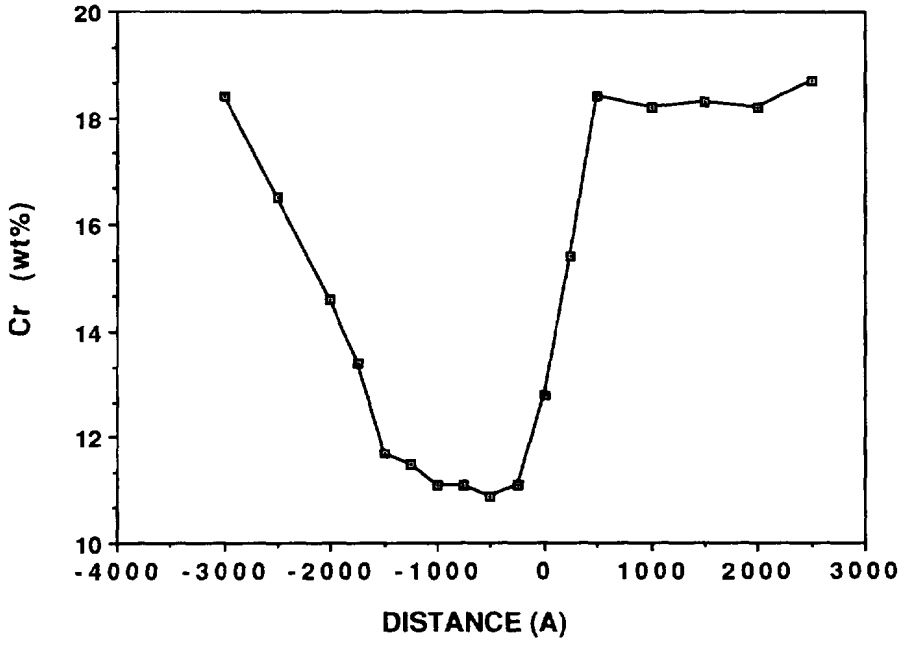

(b)

Figure 65. Cr-depletion profiles measured at grain boundaries (GB at 0 DISTANCE) of "specially" aged DPSC 2100 material (see text).

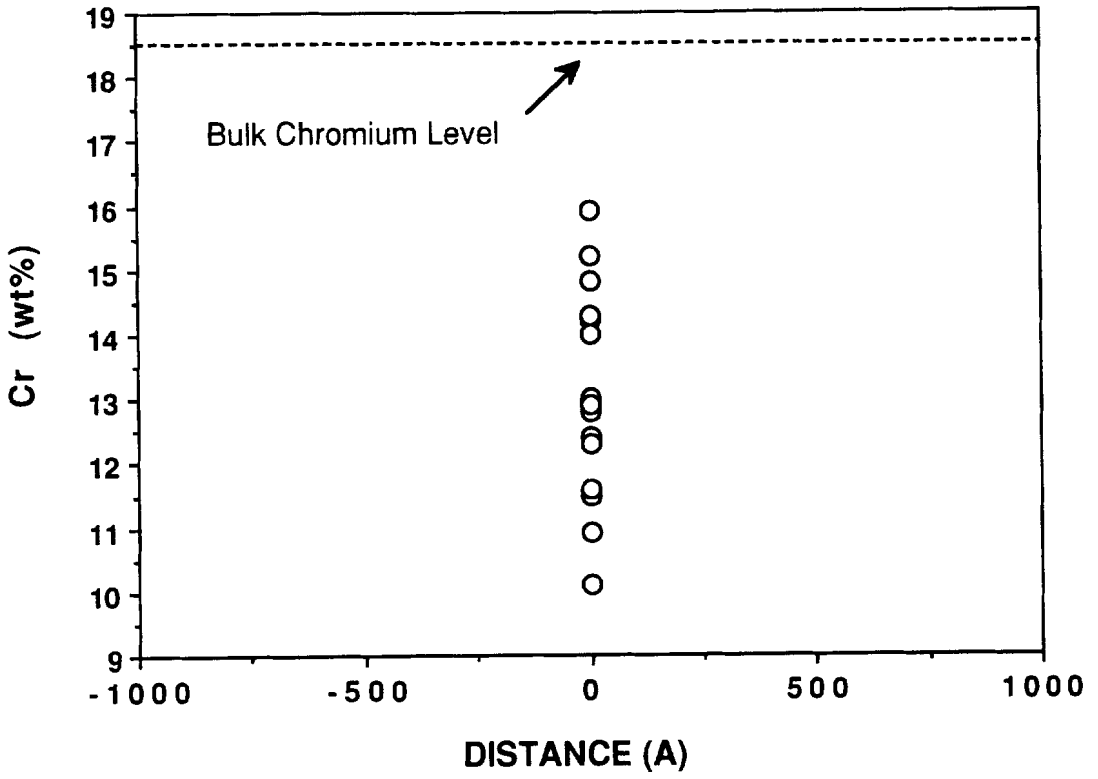

Figure 66. Cr-minimums measured at grain boundaries of "specially" aged DPSC 2100 material (see text).

IMPACT TOUGHNESS TESTING - AGED MATERIALS

As detailed in a previous section, DPSC 2100 specimens heat treated at 700°C contained Cr_2N GB precipitates, with the amount of GB precipitation increasing with increasing aging time. However, no cellular precipitation occurred in specimens heat treated at 700°C. Heat treating at 900°C resulted in both Cr_2N GB precipitation and cellular precipitation. The amount of cellular precipitation increased with increasing aging time at 900°C *(reference Figure 36a)*. The GB precipitate coverage after aging at 900°C was significant for times as short as 0.1 hour. Probably 100% of the GBs after this heat treatment contained precipitates, with the actual amount of GB coverage increasing with increasing aging times.

Effects of isothermal aging at temperatures of 700 and 900°C on the room temperature impact toughness of heat DPSC 2100 are shown in *Table 15* and *Figure 67*. Aging at 700°C caused about a 50% reduction in impact toughness (compared to the solution annealed material) after 1 hour (reduction from 144 to 77 J). Aging to 3 hours at 700°C reduced the impact toughness to only 4 J. As shown in the fractographs of *Figure 68 (a,b)*, fracture of this sample was completely intergranular, and no macroscopic ductility, at all, was observed. The grain facets on this sample were fairly smooth, but not totally featureless. Small dimples, indicative of some microscopic ductility at the grain boundaries was visible.

Aging at 900°C also caused embrittlement of the DPSC 2100 material. Reductions in impact energy occurred at shorter times for aging at 900°C as compared to 700°C. After aging for only 0.1 hour (6 minutes) at 900°C, the absorbed energy dropped to 33 J, from 144 J. SEM fractographs taken from this sample are shown in *Figure 68 (c,d)*. Although fracture of this sample was almost completely intergranular, more microscopic ductility was present as compared to the sample shown in *Figure 68 (a,b)*. This may suggest that nitride coverage of the GBs in the sample aged at 900°C/0.1 hour was not as complete as that in the 700°C/3 hour sample, thus having retained greater GB ductility and toughness.

TABLE 15 - Impact Testing of Aged DPSC 2100 Material*		
Annealing (°C - Hours)	Aging (°C - Hours)	CVN Energy joules (ft-lbs)
1150 - 2	----	144.4 (106.5)
	700 - 0.2	143.0 (105.5)
	700 - 0.4	141.0 (104.0)
	700 - 1.0	76.6 (56.5)
	700 - 2.0	21.7 (16.0)
	700 - 3.0	4.0 (3.0)
	900 - 0.1	33.2 (24.5)
	900 - 0.2	24.4 (18.0)
	900 - 1.0	6.8 (5.0)
	900 - 3.0	4.7 (3.5)
* Impact testing done at ambient temperature		

After one hour of aging at 900°C, CVN values were only 7 J, compared to 77 J for aging at 700°C. After 3 hours of aging, the impact toughness dropped to about the same level as for aging at 700°C, but the fracture morphology was significantly different. Unlike the sample aged at 700°C which had complete intergranular failure, fracture occurred both intergranularly and transgranularly through regions of cellular precipitation *(Figure 69)*. In the cellular regions of the sample fracture occurred by decohesion of the interfacial regions between the austenite and lamellar Cr_2N as shown in the fractograph of *Figure 69c*.

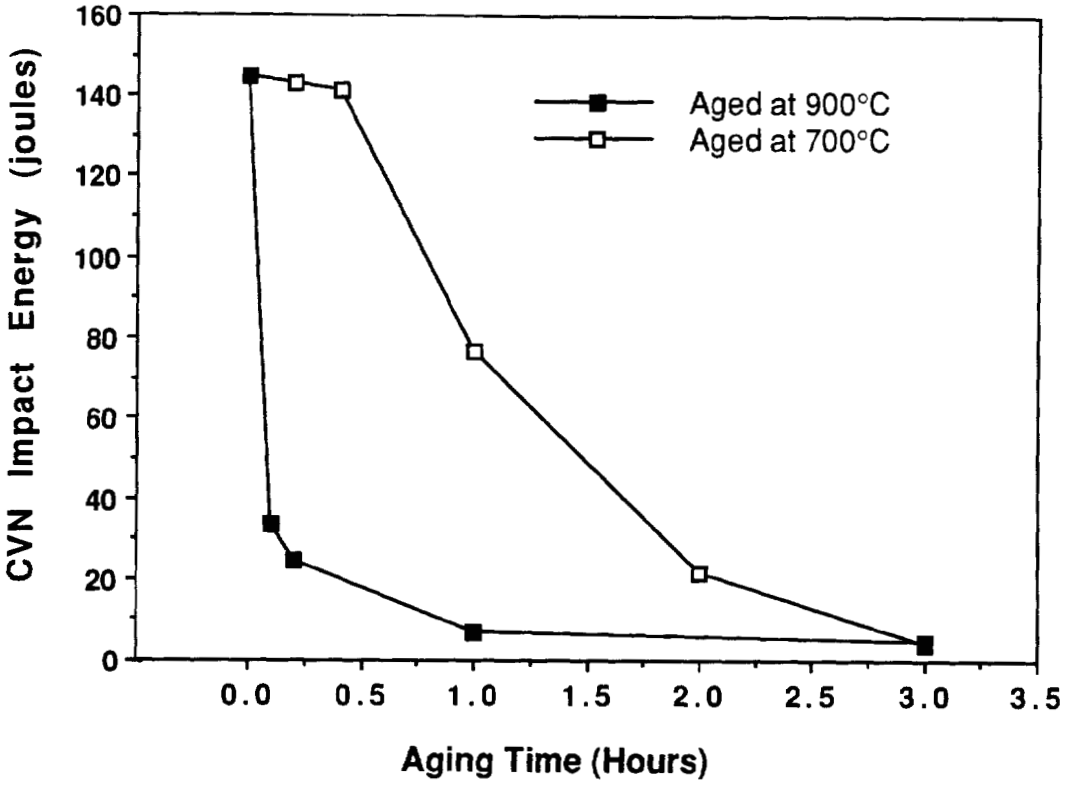

Figure 67. Impact toughness (CVN) of DPSC 2100 materials as a function of aging time at temperatures of 700 and 900°C.

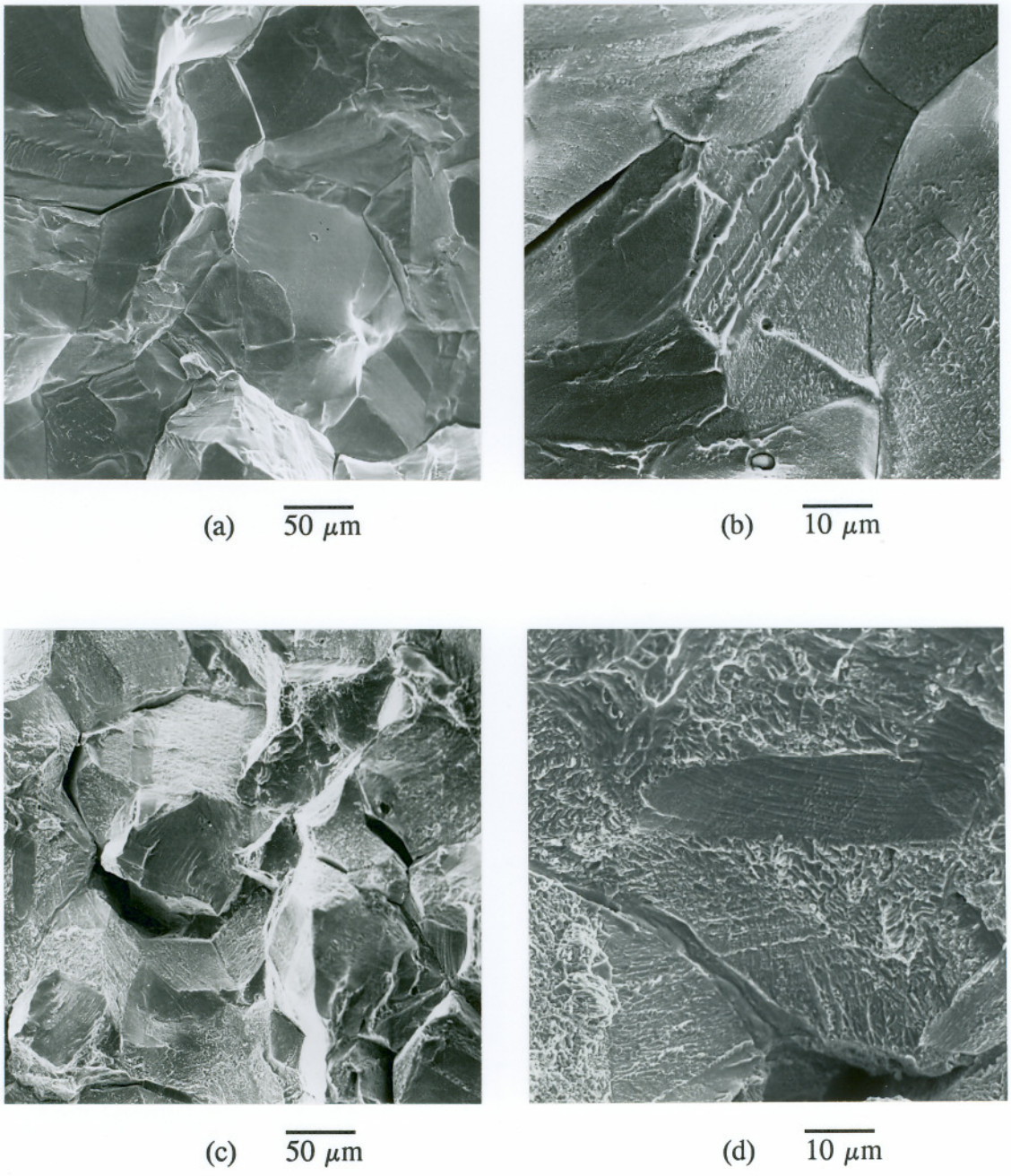

Figure 68. Secondary electron fractographs from heat DPSC 2100 impact toughness specimen aged at (a,b) 700°C for 3 hours (CVN = 4 J) and (c,d) 900°C for 0.1 hour (CVN = 33 J).

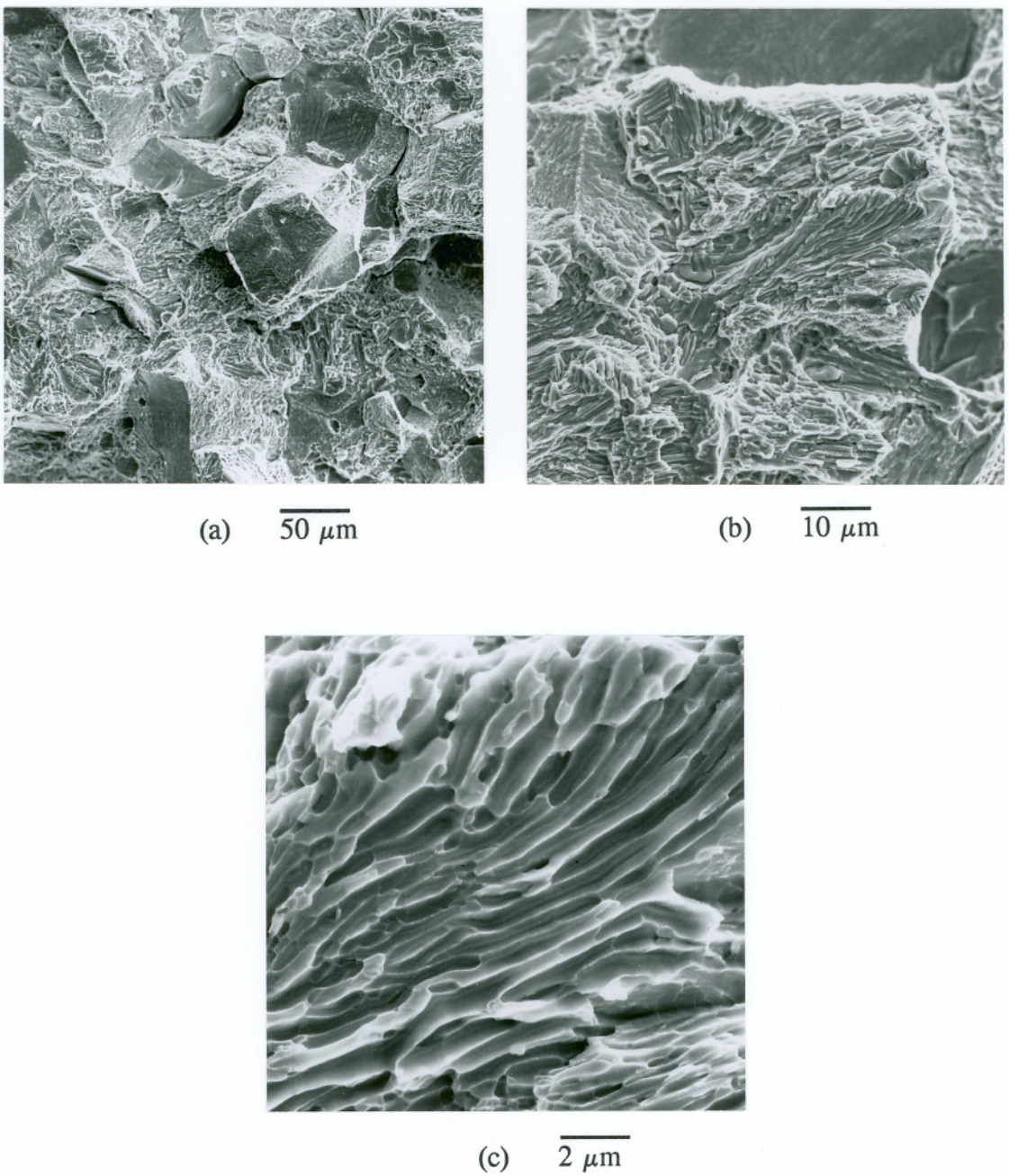

Figure 69. Secondary electron fractographs from heat DPSC 2100 impact toughness specimen aged at 900°C for 3 hours (CVN = 5 J).

DISCUSSION

AS-FORGED and SOLUTION ANNEALED MATERIALS

As-forged DE 257 and DPSC 2100 materials contained large volume fractions of Cr_2N. The Cr_2N in the as-forged materials was present predominantly at GBs and provided essentially complete GB coverage. However, no cellular or transgranular precipitates, such as those formed in isothermally aged materials, were present in the as-forged structures. It was concluded from these observations that the billets had been forged at a temperature between about 1025 and 1075°C.

The NbCrN nitrides and other inclusions present in heat DE 257 (Al or Si rich oxides/nitrides) most likely formed during solidification of the PESR ingot. Since the original DE 257 billet was 100Kg in size, the reduction and working during forging was not sufficient to affect any segregation and/or break-up the inclusion clustering present in the original PESR billet. The very low density of inclusions present in heat DPSC 2100 was primarily due to the difference in composition between the two heats. Heat DPSC 2100 did not contain the strong nitride forming elements, such as Nb and Al, which were present in heat DE 257.

Response of the two heats to solution annealing treatments in the temperature range of 1100-1250°C for times up to 10 hours was significantly different. As shown previously, grain growth in heat DE 257, which contained a large fraction of NbCrN inclusions, was much slower than in heat DPSC 2100 at temperatures below 1250°C. It is presumed that grain growth in alloy DE 257 was inhibited due to GB pinning caused by the large volume fraction of inclusions present. Grain boundary pinning by inclusions was observed in DE 257 solution annealed materials as shown in the TEM micrograph of *Figure 70* taken from a sample annealed at 1150°C for 2 hours.

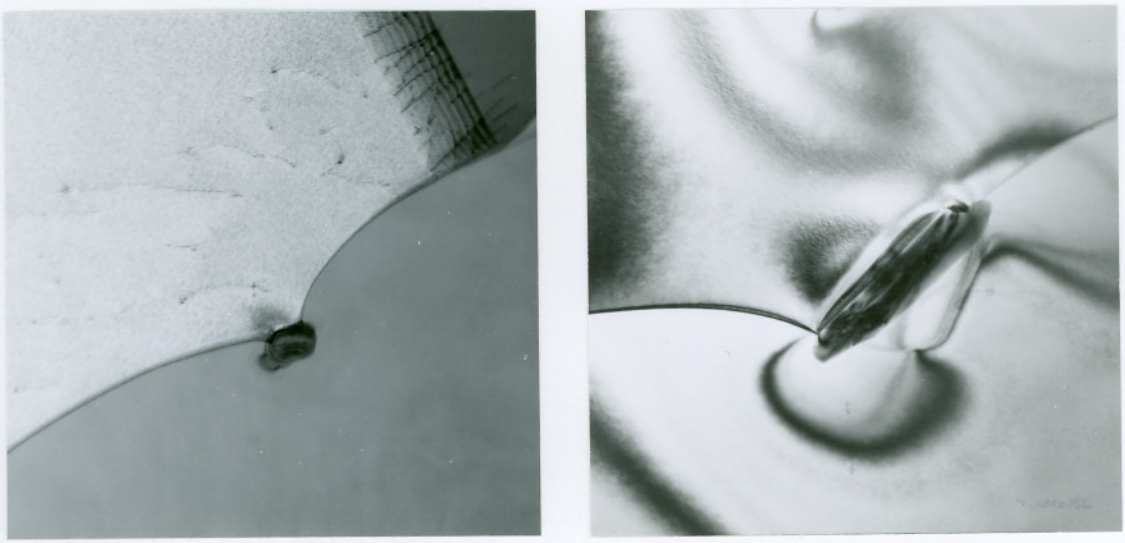

(a) 0.15 μm (b) 0.20 μm

Figure 70. TEM-BF micrograph of NbCrN precipitate at grain boundary in solution annealed (1150°C for 2 hours) DE 257 materials.

Significant bowing of the GB around the inclusion is evident in the micrograph. Increased grain growth rates in DE 257 materials at elevated temperature (1250°C) coincided with a significant decrease in the density and clustering of inclusions.

The presence of a high-density of NbCrN inclusions caused the observed low-energy room temperature impact properties of solution annealed materials from alloy DE 257. Inclusion clustering was the dominant factor in the extremely low toughness values observed for DE 257 materials solution annealed at temperatures below 1150°C. The inclusion clusters were essentially eliminated by solution annealing at 1150-1250°C, but complete dissolution of the NbCrN nitrides was not achieved even after annealing at 1250°C for 10 hours. Rayaprolu and Hendry[11] also reported the incomplete dissolution of transgranular NbCrN nitrides at a solution annealing temperature of 1200°C in a SS containing 0.18 wt% Nb and 0.24 wt% N.

Room temperature impact values for all solution annealed DE 257 materials (from 23 to 60 J) were significantly lower than alloy DPSC 2100 (144 J) and also much lower than expected for an austenitic SS. A typical CVN impact value

(subsized, 5 mm thick samples) for an annealed AISI type 316 SS, is about 120 J.[16] The higher impact toughness of the DPSC 2100 and 316 materials can be attributed to their low inclusion volumes.

Although additions of strong nitride forming elements such as Ti, Nb, and V can increase the solubility of nitrogen in the liquid, solid-solubility is reduced. However, there are two possible beneficial aspects to the addition of elements such as those to high-nitrogen austenitic SSs. The first being that these additions could result in stabilized materials similar to the AISI type 321 and 347 steels. Additions of Ti, Nb, or V would be expected to slow Cr_2N precipitation by reducing the effective nitrogen content in solid-solution (reduction in N supersaturation). However, there are also possible detrimental effects associated with the presence of the additional nitrides, such as loss of ductility and interstitial nitrogen (lower strength). Also, if the main objective were to reduce precipitation kinetics, it would be just as reasonable to reduce the amount of total nitrogen in the material. The second possible beneficial effect of adding strong nitride formers is dispersion hardening due to the formation of stable nitrides. For this mechanism to be effective, the size and dispersion characteristics (e.g. mean particle spacing, volume fraction, homogeneity) of the nitrides would have to be carefully controlled through alloying and thermomechanical processing. Dispersion strengthening in high-nitrogen steels seems to be achievable since nitrides, with very limited solubility, can be formed using alloying additions of Nb, V, Ti, and possibly other elements. Also, the present work demonstrated that nitride structures can be altered/controlled through thermomechanical processing.

Kunakov et al.[7] reported that dispersion hardening of austenitic alloys using V and/or Nb is feasible. In their work, the necessary combination of strength and ductility was obtained by the formation of uniformly dispersed VN after quenching from 1200°C and aging at 650-700°C (materials contained between 0.35 and 0.55 wt% N). The combined effect of the two mechanisms, solid-solution hardening by nitrogen and dispersion hardening, was reported to be effective for both Fe-Cr-Mn-Ni and Fe-Cr-Ni alloys. They reported similar positive results for an austenitic material

alloyed with 0.2 wt% Nb and 0.3 wt% N where the dispersed phase was the NbCrN nitride. Volkov et al.[104] also reported dispersion strengthening in austenitic 18Cr-20Mn-(0.4 to 0.8N) materials containing and up to 0.25 wt% C with additions of 1 wt% V which induced dispersive nitride formation.

Although Nb additions were detrimental to the impact toughness properties of the DE 257 materials, literature reports indicate that dispersion strengthening using low-solubility nitrides is feasible. It seems that thermomechanical processing of the materials plays a major role in determining the effectiveness of this alloying approach.

ISOTHERMALLY AGED MATERIALS

Cr_2N Precipitation

Generally, although minor differences were observed, the aging characteristics of the DE 257 and DPSC 2100 alloys were quite similar. Nitride precipitation occurred first at GBs, followed by cellular, and finally, by transgranular precipitation.

Time-temperature-precipitation curves established for both materials had C-curve shapes typical of reactions which are controlled by the thermodynamics of phase stability (driving force due to nitrogen supersaturation) and the kinetics of diffusion. The shape of the TTP curves can be explained on the basis of the variation of nucleation and growth rates with increasing undercooling below the nitride dissolution temperature (T_d). At temperatures close to T_d the driving force for precipitation is very small, and critical nuclei very large, so that nucleation is slow. When the undercooling is very large, below the nose of the C-curve, slow diffusion rates limit the rate of transformation. In the case of Cr_2N formation, the diffusivity of interstitial nitrogen is so much greater than the substitutional chromium, that the Cr-diffusivity is the rate controlling factor. A maximum rate of precipitation, corresponding to the nose of the C-curve, is obtained at intermediate temperatures where the driving force is significant and diffusion rates are reasonable.

Grain boundary Cr_2N precipitation occurred in both alloys after aging times of less than 0.1 hour (6 minutes) within a wide temperature range (from 800 to 1075°C). Results of isothermal aging studies using the Gleeble showed that GB nucleation occurred within about 36 seconds at temperatures between about 850 and 950°C. The kinetics of GB precipitation were slightly faster in heat DPSC 2100 than in the DE 257 alloy containing Nb additions. For example, Cr_2N precipitation at GBs was observed after 10 hours of aging at 600°C in alloy DPSC 2100, but was not observed during aging at this temperature in heat DE 257 after times as long as 30 hours.

Cellular precipitates nucleated over a wider temperature range in heat DPSC 2100 (700-1000°C) than in heat DE 257 (750-1000°C). Although the difference in the temperature range for cellular precipitation does not seem to be significantly different, large differences in cell development were observed between the two heats of material. Cellular precipitate volume fractions were significantly greater in heat DPSC 2100 than in heat DE 257 for a given aging temperature/time (refer to *Figures 36-38).* Virtually no cell growth occurred in heat DE 257 at 1000°C while aging at this temperature produced almost 10% cellular precipitate coverage in heat DPSC 2100 after 3 hours of aging. Also, the interlamellar spacing of the Cr_2N precipitates in heat DE 257 were larger than in DPSC 2100 materials for identical aging temperatures. The wider interlamellar spacings indicate that the nitrogen supersaturation in heat DE 257 materials was less than that in DPSC 2100 materials.

The orientation relationship between the Cr_2N and austenite lamellae described as $\{111\}\gamma//\{0001\}Cr_2N$ and $<110>\gamma//<\bar{1}100>Cr_2N$ correlated with the results reported by Kikuchi et al.[9] and Rayaprolu and Hendry.[11] The general growth features for cellular precipitation in the materials of the current work also followed those reported by Kikuchi et al. for Cr_2N cellular precipitation in Fe-Cr-Ni alloys which contained lower bulk nitrogen levels. [9,10] These features were detailed in the "Background" section of this manuscript and comparisons to the current work are given below.

The volume fraction of cells vs. reaction time in four Fe-25Cr-20Ni-N austenitic steels studied by Kikuchi and his co-workers[9] is shown in *Figure 71*. Their results correlate well with the results obtained for heats DE 257 and DPSC 2100 (refer to *Figure 36*). Cell coverage increased with increasing aging time until a maximum was reached and cell growth essentially stopped. Kikuchi et al. concluded that the reduction in cell growth rate and development was due to a reduction in the cell boundary migration rate primarily caused by a decrease in the nitrogen supersaturation in the untransformed matrix. Their work showed that long range diffusion of nitrogen occurs from the untransformed matrix into the growing cellular region resulting in an increase in nitrogen in the transformed region compared to the original austenite matrix. The nitrogen concentration in the untransformed austenite regions continually decreases as cell growth continues. This phenomenon causes a reduction in the driving force for transformation and results in decreasing reaction rates until cell growth eventually stops even though the untransformed austenite remains supersaturated with nitrogen.

Transgranular precipitates nucleated in both heats after GB Cr_2N coverage reached 100% and also, in most cases, after cellular precipitation was well developed. Transgranular precipitation, for aging times of 10 hours or less, occurred over a significantly narrower temperature range than GB precipitation. Compared to cellular precipitation, transgranular precipitation occurred over a similar temperature band, but transgranular precipitates formed at higher temperatures. For transgranular precipitation, differences between the two materials followed similar trends as for GB and cellular precipitation, that is, precipitation occurred at shorter times and over a wider temperature range in heat DPSC 2100. For aging times up to 10 hours, transgranular precipitates were observed in the temperature range of 700-1050°C in heat DPSC 2100 materials and 850-1050°C in heat DE 257 materials.

An interesting feature of the transgranular precipitation was that it occurred in regions of untransformed austenite after cellular precipitation had ceased. This observation indicates that the supersaturation of nitrogen required for transgranular

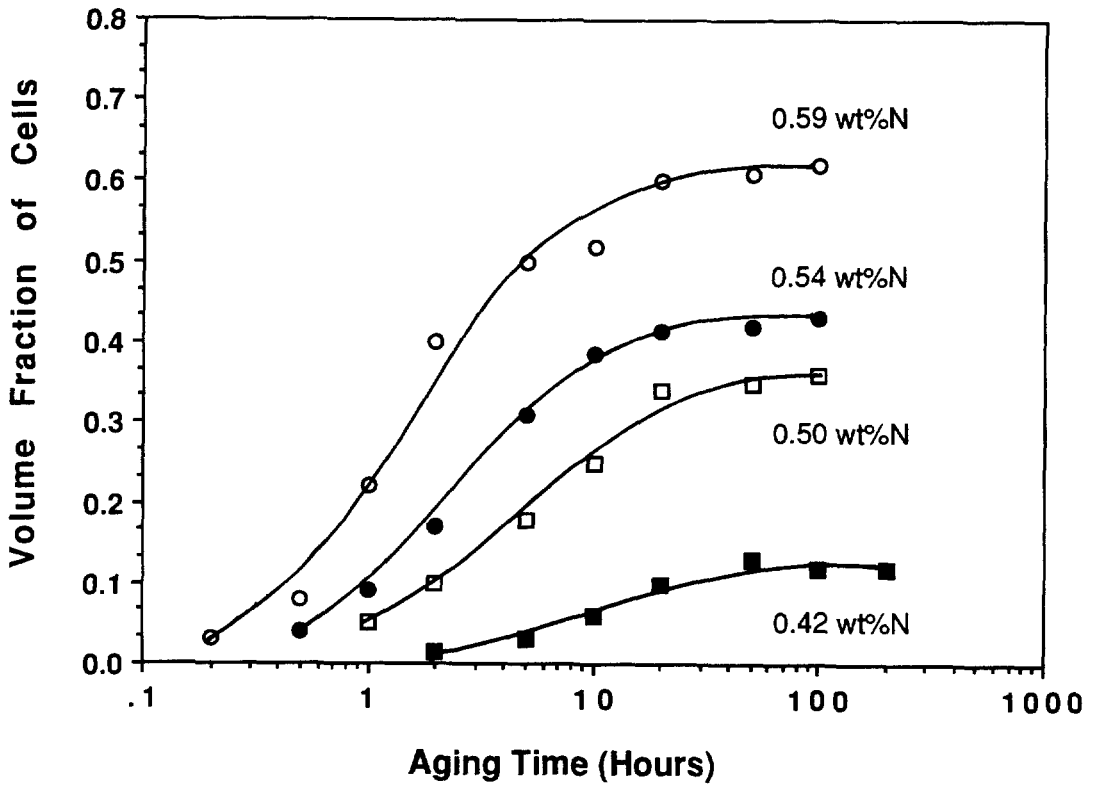

Figure 71. Cellular precipitation development in Fe-25Cr-20Ni (wt%) high-nitrogen stainless steels at an aging temperature of 800°C (from the work of Kikuchi et al.)[53]

precipitation of Cr_2N is less than for cellular precipitation growth. However, since nucleation of cellular precipitation occurs at GB, it can occur at much shorter times than transgranular nucleation due to GB diffusion short-circuiting and the benefit in free-energy by nucleating at a defect as opposed to within a "defect free" matrix.

Kikuchi et al.[9] studied the aging characteristics of a series of Fe-25Cr-20Ni-N alloys with nitrogen contents up to 0.6 wt% and no other significant alloying additions. They reported that transgranular precipitation did not occur in their alloys during aging at 800°C for times up to 500 hours. These results differ significantly from those of the current work. It is possible that transgranular precipitation of Cr_2N in alloys DE 257 and DPSC 2100 was enhanced and stabilized by alloying additions not present in the heats studied by Kikuchi. It is unlikely that defect structures in the

DE 257 and DPSC 2100 solution annealed materials could have been responsible for the observed differences. This is because the solution annealed structures of both materials had typically low dislocation densities and were void of other defect structures which could have enhanced transgranular precipitation.

Precipitation Kinetics

Although heat DE 257 contained more nitrogen than heat DPSC 2100, 0.78 compared to 0.69 wt%, GB, cellular, and transgranular precipitation kinetics were faster in heat DPSC 2100. In addition, nitride precipitation and stability occurred over a wider temperature range in heat DPSC 2100. The Cr_2N lamellae in cellular precipitate colonies in heat DPSC 2100 also had the distinction of having narrower interlamellar spacing than heat DE 257, for samples heat treated under identical (temperature/time) conditions.

These results suggest that the amount of nitrogen supersaturation was greater in heat DPSC 2100 than DE 257. At first glance the reason for this would seem obvious, that the amount of interstitial nitrogen in heat DE 257 materials was reduced, due to the large amount of nitrides present, to a level below that in DPSC 2100 materials. However, if all of the Nb, Al, and V present in heat DE 257 formed nitrides, the reduction in the nitrogen level should have been on the order of 0.02 wt%, 0.04 wt% at the most. This should still have left DE 257 materials with greater levels of interstitial nitrogen than DPSC 2100 materials. At this time, the effects of these elements on Cr-diffusivity in the austenite is not known. However, if Nb, V, or Al additions decrease the rate of chromium diffusion, then precipitation kinetics would be retarded to some degree.

There were other alloying differences between the two materials, heat DPSC 2100 contained about 1 wt% more Ni and 2 wt% less Cr than heat DE 257. According to the work of Kikuchi and co-workers[53] both of these conditions would tend to decrease the interstitial nitrogen solubility in heat DPSC 2100 and increase the

driving force for precipitation as seen in this work. However, the magnitude of the effect of these small alloying differences is not currently known.

One other major difference between the two heats of material in the solution annealed (1150°C for 2 hours) condition, was that the grain size of heat DPSC 2100 samples was much greater than that of DE 257 samples, 72 μm compared to only 40 μm. This also fails to explain the observed kinetic differences because the smaller grain size should be conducive to acceleration of GB and cellular precipitation kinetics. The smaller the grain size, the more GB area, and thus nucleation should be enhanced as compared to a large grain sized material.

Composition - Metallic Elements

Precipitates (Cr_2N) analyzed from alloys DE 257 and DPSC 2100 aged at temperatures between 800 and 1000°C were relatively constant in composition and contained approximately 90 wt%Cr, small amounts of Fe and Mo, and trace amounts of Si and V (refer to *Table 13*). The Cr_2N compositions were independent of whether the precipitates were present at GBs or as lamellae in cellular precipitate regions.

Grain boundary precipitates in DE 257 material aged at 700°C for 1 hour contained considerably less chromium (76 wt%) and higher levels of Mo, Fe, and Si than Cr_2N precipitates formed at higher aging temperatures. Although only ten precipitates from the sample aged at 700°C were analyzed, their compositions were consistent with one another. The results indicate the precipitates in the earlier stages of development to be richer in Fe, Mo, and Si than more developed, larger precipitates. However, a more systematic study involving a greater number of precipitates from both materials aged within the lower temperature region (600-800°C), for a variety of times, is required to substantiate these preliminary results.

It is reasonable that precipitates change in composition as a function of aging temperature/time since substitutional diffusion plays an important role in the precipitation process. Nucleation of precipitates with metallic element compositions

which reflect the local matrix composition more closely, that is with higher iron contents, should be easier than nucleation of precipitates with compositions much different than the matrix.

Compositions of Cr-rich $M_{23}C_6$ nitrides in type 304 SSs have been reported to vary as a function of temperature and aging time. Carbides have been reported to be iron-rich at early growth stages, with the Cr:Fe ratio increasing with time at a given aging temperature. Also, the Cr:Fe ratio in the carbides approached a different final value at each isothermal aging temperature.[105]

Long-term Stability of Cr_2N

As reported earlier, Kikuchi et al.[9,10,53,54] found that after longer aging times in Fe-Cr-Ni alloys (greater than 100 hours) the Cr_2N transformed to a π-phase nitride (ß-manganese structure) which they considered to be the equilibrium nitride in their materials. They also reported that the nickel concentration in the alloy must exceed about 10 wt% for the π-phase to be stable. The π-phase did not form in alloys DE 257 and DPSC 2100 aged for times up to 10 hours. This is not unexpected since the time required for π-phase formation would be expected to be much greater in alloys that are prone to its formation. It is likely, given the low nickel content in the DE 257 and DPSC 2100 alloys, that they would not be susceptible to π-phase formation even at longer aging times. However, long-time aging treatments of these alloys are necessary to determine if the Cr_2N precipitates, primarily the cellular precipitation products, would decompose to form another, more stable nitride, after longer isothermal exposures. At this time, the long-term stability of the Cr_2N nitrides which were formed in the DE 257 and DPSC 2100 materials cannot be predicted.

Role of Carbon in Precipitation

Chromium-rich $M_{23}C_6$ carbides, the primary precipitate phase in carbon-alloyed austenitic SSs such as types 304 and 316, were not detected in any of the aged DPSC 2100 or DE 257 materials. The level of carbon in the DE 257 and DPSC 2100 heats would be considered low for an austenitic SS. This amount of carbon ($\sim$0.025 wt%) is above the solubility limit, and therefore isothermal aging within the temperature range of approximately 600-900°C should eventually produce carbide precipitation. However, at this level of carbon, the time to nucleate carbide precipitates at 700°C, ignoring the effects of nitrogen, would be longer than 10 hours.[71] Mixed carbo-nitride formation may also be possible but no positive identification of them has been reported. The level of carbon exchange as a replacement for nitrogen in the Cr_2N nitrides is unknown and additional work needs to be done to try to measure carbon levels in the nitrides.

Presser and Silcock[12] studied the isothermal aging response (within the range 400-800°C) of a cold-worked high nitrogen austenitic SS with a nominal composition (wt%) of Fe-17Mn-20Cr-0.08C-0.6N (much more carbon than was present in heats DE 257 and DPSC 2100). They reported that for aging at temperatures below 700°C, $M_{23}X_6$ precipitation was dominant whereas at higher aging temperatures the cellular precipitation of M_2N primarily occurred. The Ms represent the metallic species in the phases which are Cr-rich but also contain Mn and Fe, and the X represents C and/or N. However, analyses to determine the composition of the $M_{23}X_6$ phases, identified by XRD, was not undertaken in their work. Holm et al.[106] studied the isothermal aging response of a steel with a similar composition to the material studied by Presser and Silcock. They also reported the precipitation of a phase with the $M_{23}(CN)_6$ structure but did not analyze the composition of the precipitates.

In high-nitrogen austenitic materials the primary precipitate phase is the Cr_2N nitride. It appears that increasing levels of carbon in high-nitrogen steels result in the increasing presence of $M_{23}(CN)_6$ structures which are stabilized by the presence of

carbon and are carbon-rich. The role of carbon in alloys DE 257 and DPSC 2100, considering its low concentration and the lack of carbide precipitation, was certainly limited. Additional aging studies of high-nitrogen materials with high levels of carbon may be necessary in order to define the level of interaction between carbon and nitrogen in forming mixed carbo-nitrides and the interstitial carbon-nitrogen exchange in nitrides and carbides. Emphasis on analysis techniques to determine the atomic exchange between nitrogen and carbon would be necessary.

Intermetallic Phase Formation

For both heats of material in this study, nitride precipitation was followed by χ-phase precipitation at about 10 hours of aging within the temperature range of 800-1000°C. As expected for intermetallic formation, χ-phase precipitates were located primarily at grain boundaries. The preferential nucleation of intermetallic phases at high-energy sites in 316 SSs was documented by Weiss and Stickler[58] and Lai[62].

Weiss and Stickler determined the precipitation sequence in 316 SSs aged at approximately 800°C to be $M_{23}C_6$ at an aging time of about 0.1 hour, followed at much longer aging times (about 100 hours) by χ-phase, and subsequently by η and σ phases. Lai reported the same basic precipitation sequence in another 316 SSs. Longer nucleation times for the intermetallic phases have been attributed to the slower diffusion rates of the several substitutional elements involved in the intermetallic formation compared to the interstitial carbon and/or nitrogen diffusion involved in the $M_{23}C_6$ and Cr_2N reactions.

Chi-phase formation was found to occur at much shorter times in the high-nitrogen DE 257 and DPSC 2100 materials than reported for the 316 SSs. The χ-phase reportedly can accommodate more interstitial atoms than either the η or σ phases, and even has been reported to exist as a carbide of the type $M_{18}C$.[58] It is possible that the presence of the χ-phase at shorter aging times in the high nitrogen alloys is linked to the much greater amount of interstitial, particularly nitrogen,

present. If the χ-phase can accommodate large amounts of nitrogen and is stabilized by it, then χ-phase formation may be enhanced in high-nitrogen materials. More analysis is necessary to determine how much nitrogen was incorporated into the χ-phase structures formed in the DE 257 and DPSC 2100 materials. Additional aging treatments of the high-nitrogen alloys, for times in excess of 100 hours within the temperature range of about 800-1000°C would be required to access their susceptibility to η and σ phase formation.

GLEEBLE vs. FURNACE AGING

The primary purpose of the Gleeble work was to employ fast heating rates, to offset the effect of slow heating in the furnace, so that measurement of precipitation kinetics at short times (less than 3 minutes) could be measured. Fast quenching from the isothermal hold temperature was also imperative so that precipitation could not occur during cooling. It was necessary for safety and logistics reasons, since gas cooling with high-pressure argon was to be employed, that the heat treatments be done in air as quenching within a vacuum was not practical. The initial cooling rate (down to 600°C) obtained with the high-pressure argon blast was about 100°C/sec, which was sufficient to prevent any effect of cooling rate on precipitation.

A series of heat treatments were conducted so that microstructural comparisons could be made between samples heat treated in the furnace and Gleeble. The purpose of these was basically to determine, through microstructural comparisons, whether or not the temperatures measured in the Gleeble were the same as those in the furnace. Heat DPSC 2100 Gleeble specimens were heat treated at temperatures of 850°C, 900°C, and 950°C for 1 hour. These thermal treatments were done in an air atmosphere and heated at a rate and profile equal to the furnace. The Gleeble samples aged at 850 and 900°C had microstructures very similar to the samples aged in the furnace. The samples aged at 850°C each contained about 5% (volume fraction) cellular precipitation products and the samples aged at 900°C about 28%

(reference *Figure 36a* for furnace measurements). With reference to *Figure 36a*, it should be remembered that the samples aged in the furnace at 900 and 950°C for 1 hour contained the same volume fraction of cells.

In addition to the Gleeble sample heat treated in air at the furnace heating rate, two additional Gleeble samples were subjected to treatments at 950°C (1 hour aging); (1) at a 50°C/sec heating rate in air, and (2) at the furnace heating rate in a vacuum. Both of the Gleeble samples heat treated at 950°C for 1 hour in air contained less than 10% volume fraction cellular precipitates. Their microstructures were very similar to samples heat treated in the furnace at 1000°C. Samples heat treated in the furnace at 950°C contained significantly more cellular precipitation, about 28%. The Gleeble sample heat treated in a vacuum had a microstructure which was much more similar to the furnace treated sample than were the other two Gleeble samples. The micrographs of *Figure 72* illustrate these microstructures. These results indicated that the actual temperatures of the Gleeble specimens heated in air, at least for temperatures above 900°C, were about 50°C greater than those measured by the surface thermocouple. Even if the actual temperature of the 900°C Gleeble sample was 950°C, the volume fraction of cellular precipitates would have been about the same as the furnace sample. The microstructural observations indicate that the surface temperature measurements for the 950°C Gleeble specimen heat treated in a vacuum were more indicative of the actual sample temperature. It should be remembered that temperatures in the furnace were measured using three different thermocouples, all of which displayed temperatures within about $\pm$ 5°C of one another. So the confidence level is very high for the accuracy of the temperature measurements within the furnace.

The reason for the discrepancy in the temperature measurements made in the Gleeble seems to be surface cooling effects when the treatments were done in air such that temperatures measured by the thermocouple attached to the surface were about 50°C below those of the actual bulk sample. This effect is expected to be greater at higher temperatures and is also expected to be much greater for treatments in air as

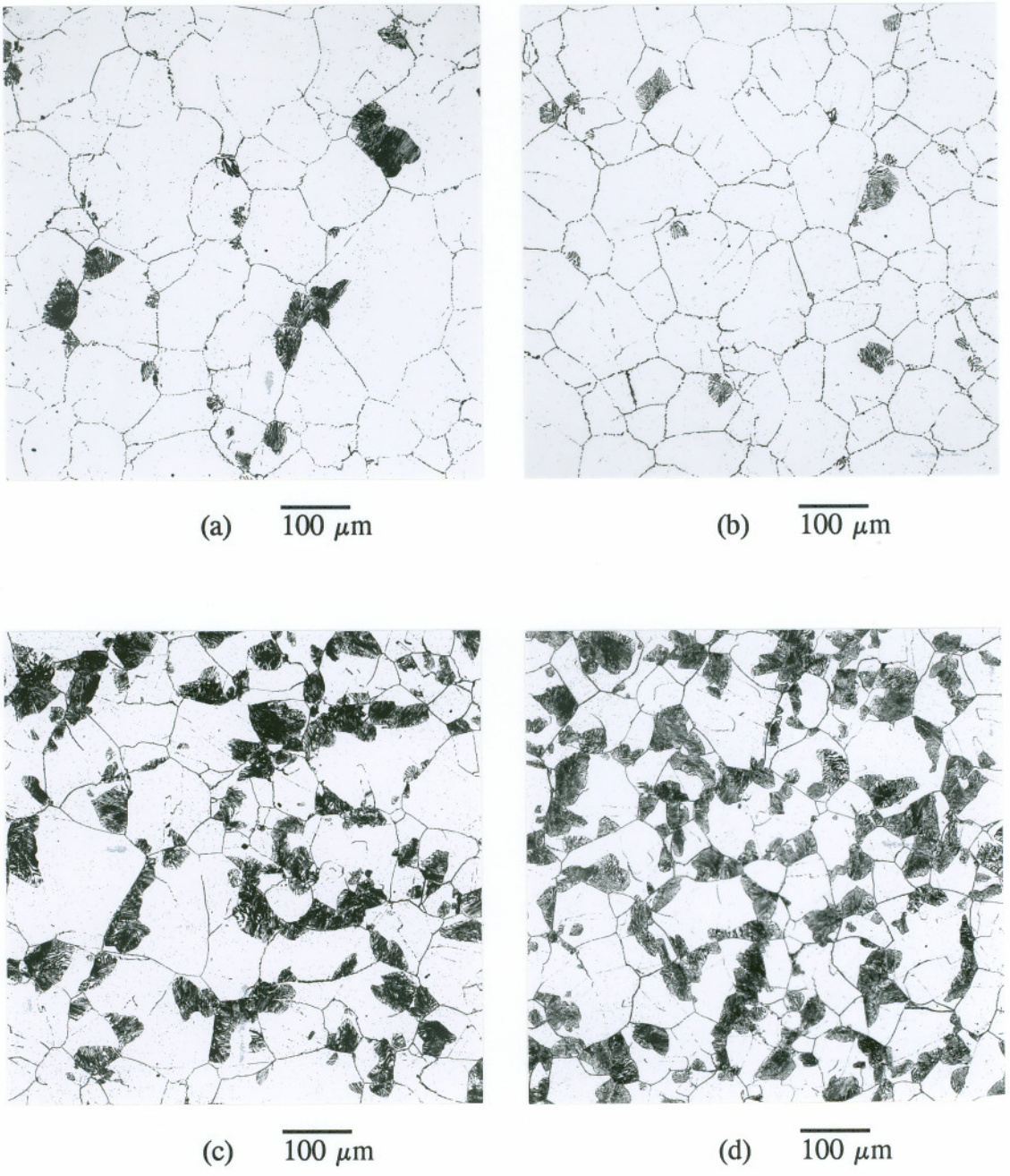

Figure 72. Optical micrographs of specimens from heat DPSC 2100 aged at 950°C for 1 hour in (a, b, c) the Gleeble and (d) furnace. Gleeble specimen shown in (a) heated at a rate of 50°C/sec (Air), (b) at the furnace heating rate (Air), and (c) at the furnace heating rate (Vacuum).

compared to a vacuum. In a vacuum, surface heat losses are only due to radiation, but in air, conduction contributes significantly to the heat losses.[107]

Although the thermal treatments done in the Gleeble did not correspond exactly to the furnace treatments, the results obtained for short-time heat treatments in the Gleeble are still valid for determining the materials susceptibility to precipitation. This point is very important because the primary purpose of the Gleeble work was to determine precipitation susceptibility at short times. Unfortunately, the temperature correspondence of the Gleeble to the furnace work could not be relied upon. It was hoped that heating rate effects on precipitation development at higher temperatures could be directly measured using Gleeble specimens and correlated to the furnace results. However, the temperature discrepancy obtained between the two thermal treatment procedures prevented these direct comparisons.

STRAIN EFFECTS on ISOTHERMAL AGING

The initial deformation structure of the as-rolled (22% thickness reduction) DPSC 2100 material contained a high-density of slip-bands and deformation twins. Cellular and planar dislocation structures were not observed in the as-rolled material. Cellular dislocation structures, which are typical of high SFE materials that readily cross-slip, are not expected to form in austenitic SSs which typically have low SFEs. Planar dislocation structures, which are indicative of a low SFE material with a reduced ability to cross-slip, become more predominant in austenitic materials as the nitrogen concentration is increased. The fact that well-defined planar dislocation arrays were not present in the as-rolled material was probably due to the large amount of deformation present after the 22% reduction.

Dislocation structures become more complicated with increased deformation, and as slip is concentrated along specific directions, planar dislocation arrays become less evident and are replaced by slip-bands which contain a high density of dislocations. The slip-bands and deformation twins in the structure have a similar

appearance but can be distinguished through SADP analysis in the TEM. Deformation twinning as a predominant deformation mechanism is consistent with reported observations of reduced cross-slip and the formation of planar dislocation structures in high-nitrogen austenitic SSs.

Prior deformation substantially accelerated the onset and subsequent development of GB and transgranular Cr_2N nitride precipitates for all temperatures below 1000°C. The effect of strain on the nucleation TTP curve for GB precipitation was directly measured for temperatures below 800°C (refer to *Figure 56*). The rapid development of transgranular Cr_2N precipitates in deformed materials is indicative of the effect of strain on creating defect sites and the site-specific nature of nitride nucleation. Transgranular nucleation in annealed materials occurred only after significant GB and cellular precipitation had already developed. Nucleation of nitrides within the austenite matrix in solution annealed materials is not thermodynamically favorable since high-energy sites, needed to help reduce the free-energy barrier for nucleation, are not present. The high-density of defect sites present in the cold-worked material, such as slip-band intersections, dislocations, and deformation twins, reduced the free-energy barrier to nucleation within the matrix and promoted transgranular precipitation. It can also be postulated that enhanced matrix Cr-diffusion, due to diffusion short-circuiting through a dislocation pipe diffusion mechanism, also enhanced transgranular precipitation development.

Cellular precipitation development was significantly retarded in the cold worked material as compared to solution annealed materials. Volkov et al.[104] also reported in their work that prior deformation suppressed cellular precipitation of Cr_2N during aging and created a finely dispersed transgranular nitride structure. In earlier discussions, it was emphasized that the degree of nitrogen supersaturation is a controlling factor in the development of cellular precipitation structures. Cellular precipitation seems to require a high-degree of nitrogen supersaturation since the process ceases even though some nitrogen saturation may be present. However, due

to the slow nucleation kinetics of transgranular precipitation in annealed materials, cellular precipitation was dominant and transgranular precipitation was minimal.

Retardation of cellular precipitation in cold worked materials is most likely associated with several of the following phenomena: (1) Rapid transgranular precipitation lowers the total nitrogen supersaturation and therefore lowers the driving force for cellular precipitation; the long-range diffusion of nitrogen into the cells does not occur since nitrogen is consumed locally in the formation of transgranular precipitates; and (2) The presence of transgranular precipitates along several directions within a grain, generally along slip-bands and deformation twins, probably retards boundary movement, which is essential for cellular decomposition. Apparently, from the optical examinations, not only is cell growth retarded in cold-worked materials, but initial cellular development (nucleation) is also retarded.

Much of the early transgranular precipitation development in the cold-worked materials occurred preferentially near GB regions as opposed to the center of grains. Near-interface (GB) dislocation densities and dislocation structures are generally more developed than within interior grain regions due to GB deformation and obstruction of dislocation movement by GBs.[108,109] Therefore, in the initial stages of transgranular precipitation in cold-worked materials. nitrogen levels near the GBs are probably lower than in the grain interiors. This phenomenon would retard the nucleation and development of cellular precipitation more than would be indicated just by the total fraction of transgranular precipitates.

PRECIPITATION-INDUCED CHROMIUM-DEPLETION

High-nitrogen austenitic SS materials were shown to be susceptible to sensitization development as a result of isothermal aging. Sensitization was associated with the GB precipitation of Cr_2N with the amount of Cr_2N precipitation and degree of sensitization increasing with increasing aging time at 700°C. Type 304 or 316 alloys containing the same carbon content as that present in alloy DPSC 2100 would

be considered as "low-carbon" alloys but would still be susceptible to $Cr_{23}C_6$ precipitation and a low degree of sensitization. Bruemmer[71] showed that the time to sensitize a type 316 SS at 700°C, containing approximately 0.02 wt%C, is about 20 hours. The time-to-sensitize annealed heat DPSC 2100 samples at 700°C was about 1 hour.

Although materials isothermally aged at 900°C contained a significant amount of GB and cellular Cr_2N precipitates, they were not sensitized. This is because the Cr-depletion associated with nitride precipitation at 900°C was insufficient to produce attack during EPR testing. As presented previously, the degree of sensitization is controlled by the Cr-minimum present at the GBs and the width of the Cr-depletion zone. Reactivation during EPR testing occurs in materials with GB Cr-minimums which are less than about 13.5 wt%.

In carbon-alloyed austenitic SSs, such as types 304 and 316, GB Cr-minimums have been shown to increase with increasing temperature. The GB Cr-minimum is a complex function of the carbon activity ($a_c = \gamma_N X_N$), reaction equilibrium constant (K_{eq}), and chromium activity coefficient (γ_{Cr}) as defined by equation [15]. In carbon-alloyed SSs, the activity coefficient of chromium (γ_{Cr}) has been shown to be a complex function of temperature. Above about 800°C in carbon-alloyed materials, γ_{Cr} decreases dramatically with increasing temperature resulting in an increase in the minimum GB chromium concentration with increasing temperature.[71] It is not unreasonable to assume that a similar trend occurs for Cr_2N precipitation in high-nitrogen steels. Increasing matrix Cr-diffusion with increasing temperature results in smaller depletion widths with increasing annealing temperatures and is also a major factor in reducing material sensitization (GBCD).

Sensitization development was accelerated dramatically by cold-working prior to isothermal aging at 700°C. The EPR test results for aging at 700°C (refer to *Figure 62*) illustrate the significant effect of prior deformation on the development of GB precipitation in heat DPSC 2100. This work is in agreement with previous work of the author[90,110] and others[91,92] which showed prior deformation to significantly

enhance carbide precipitation/sensitization development in carbon-alloyed 316 SSs. Prior deformation also induced transgranular Cr_2N precipitation and associated Cr-depletion regions which were attacked during EPR testing.

One of the primary implications of the substantially increased sensitization kinetics in cold-worked materials is their application at temperatures between about 300 and 500°C. Enhanced sensitization kinetics of deformed materials may make them susceptible to low-temperature sensitization within temperature regimes where annealed materials do not sensitize. High strengths achieved in high-nitrogen steels as a result of cold deformation processing make their use in these conditions very likely. The phenomenon of GB sensitization is important since it can lead to material susceptibility to IGC and IGSCC. Although cold working enhances the rate of sensitization development, it is possible that transgranular sensitization could reduce a materials overall IGSCC susceptibility by providing a discontinuous crack propagation network and thereby reducing intergranular crack propagation.

Indirect Measurement

The EPR test was shown to be applicable to the measurement of sensitization in high-nitrogen SSs despite the fact that their compositions can be quite different than the standard 304 and 316 alloys for which the test was developed. Passivation of the high-nitrogen alloys during EPR testing was done at the same potential (+0.200 volts) as for the 304 and 316 alloys. No reactivation current was measured during EPR testing of solution annealed materials, as expected. One of the important factors in the application of the EPR test to these materials was that the Cr-rich Cr_2N nitrides were not directly attacked during testing. Thus, the reactivation current achieved during testing was directly attributed to attack of Cr-depletion regions. This was shown for samples aged at 900°C which contained massive amounts of Cr_2N nitrides but which did not show any evidence of sensitization (reactivation) or nitride attack during EPR testing. The EPR test can be successfully applied to sensitization

measurement in high-nitrogen SSs induced by the precipitation of Cr-rich Cr_2N nitrides instead of $Cr_{23}C_6$ carbides.

Direct Measurement

Direct measurement of the Cr-depletion zones in the high-nitrogen DPSC 2100 materials proved to be more difficult than in type 304 and 316 SSs. This was, however, not due to the fact that the materials contained Cr_2N nitrides instead of $Cr_{23}C_6$ carbides or that the samples were not sensitized. Direct measurement of Cr-depletion zones in DPSC 2100 was only possible, with the equipment used, in specially heat treated samples. This was because samples heat treated within the sensitization range (approximately 600-850°C) contained high-densities of GB nitrides which, by the nature of their location, were subject to secondary fluorescence during STEM/EDS analysis of the adjacent matrix and contributed to the chromium spectral peaks. Use of a STEM equipped with a smaller probe size, on the order of 2 nm (instead of the ~20 nm used in this study) would enhance the analysis capabilities by reducing the chance that nitrides, located at GBs, would be included in the area analyzed.

In spite of the limitations of the current analysis, Cr-depletion profiles were directly measured in a specially treated DPSC 2100 sample. These results confirmed that the precipitation of Cr_2N causes Cr-depletion (sensitization) and potentially provides a method of obtaining thermodynamic data (e.g. Cr activity coefficient, γ_{Cr}, see *equation [15]*) for nitride/austenite equilibria as a function of aging temperature/time.

IMPACT TOUGHNESS - AGED MATERIALS

Aging of samples from heat DPSC 2100 at 700 and 900°C resulted in low-energy room temperature impact toughness properties. Embrittlement resulted from

GB precipitation of Cr_2N nitrides at 700°C and both GB and cellular precipitation of Cr_2N at 900°C. Increasing aging times at 700°C resulted in decreasing impact energies and lead to 100% intergranular fracture after less than 3 hours of aging. Increasing nitride coverage of GBs with increasing time at temperature was responsible for this trend. For short aging times at 900°C intergranular fracture dominated, but after longer aging fracture was mixed-mode, being intergranular and transgranular. Transgranular fracture after aging at 900°C occurred by decohesion of austenite matrix/Cr_2N lamellae interfacial regions. The fractographic evidence suggests that fracture at GBs and through regions of cellular precipitation was dominated by decohesive failure between the austenite and Cr_2N, and not brittle fracture of the nitrides.

Current results correlate with research that showed types 304 and 316 SSs to be susceptible to embrittlement at ambient and low-temperatures due to the presence of Cr-rich $Cr_{23}C_6$ GB carbides. Bruemmer et al.[16] and others[14,17-19] noted significant reductions in impact properties of 304 and 316 alloys at low-temperatures (-196°C), and moderate reductions at ambient temperature as a result grain boundary precipitation of $Cr_{23}C_6$ carbides. Decohesion at austenite/carbide interfaces was concluded to be the primary fracture mechanism. Losses in tensile ductility have also been attributed to the presence of GB carbides.[17,19] Ductility losses during impact testing at ambient temperature in high-nitrogen SSs caused by the formation of GB and cellular Cr_2N nitrides appear to be much more severe than previously observed in 304 and 316 alloys, which was attributed to $Cr_{23}C_6$ GB precipitates. This may be because high density coverage of Cr_2N precipitates at GBs occurred at shorter aging times in the high-nitrogen materials of the current work than for $Cr_{23}C_6$ precipitation in 304 and 316 SSs. It may also be that austenite/Cr_2N interfacial regions are weaker than austenite/$Cr_{23}C_6$ interfaces resulting in lower-energy decohesive failures.

EFFECT of AGING on PROCESSING and APPLICATIONS

The extremely fast precipitation kinetics of the high-nitrogen alloys studied, at temperatures between 600 and 1075°C, has a major impact on the processing of these, and related, alloys. This work has shown that billets and forgings cooled from annealing temperatures are susceptible to precipitation of Cr_2N precipitates during cooling. The detrimental effect of this precipitation on the toughness and sensitization response of the materials has been clearly demonstrated. It can also be speculated that the slow-strain rate tensile ductility and general corrosion resistance of the materials are also adversely affected by the nitride precipitation. The extremely attractive benefits of high-nitrogen levels in solid-solution on the yield and tensile strengths of these materials may ultimately have to be balanced by the effect of increasing nitrogen levels on precipitation kinetics.

The present work has shown the dramatic effect that prior deformation has on the precipitation kinetics and precipitate morphologies in high-nitrogen steels. The increased susceptibility of cold-worked materials to nitride precipitation and sensitization is very important since work hardening of high-nitrogen steels has been shown to be an extremely effective strengthening mechanism. Deformed materials are susceptible to precipitation/sensitization in temperature regimes where annealed materials are unaffected.

The addition of strong nitride forming elements to high-nitrogen austenitic materials, such as Ti, V, Al, and/or Nb, result in the presence of nitrides in annealed materials since nitrides of these elements have limited solubility. From the current results, and considering those reported in the literature, the presence of these nitrides could either act to cause embrittlement or dispersion strengthening, and that the specific effect is strongly dependent upon thermomechanical processing. In any case, nitrogen removed from solid-solution will reduce the positive effect of the overall nitrogen concentration on interstitial solid-solution strengthening.

CONCLUSIONS

This work showed that although large amounts of interstitial nitrogen can be dissolved in austenite to increase strength levels, rapid precipitation of Cr_2N occurs during exposure at elevated temperatures. Their presence can adversely affect mechanical properties and their formation leads to material sensitization which may cause alloy susceptibility to IGC and IGSCC. Minor additions of strong nitride forming elements such as Nb, V, and Al were shown to influence microstructures and mechanical properties of annealed materials, as well as precipitation kinetics during aging. It was also demonstrated that nitride precipitation kinetics and morphologies can be altered/engineered through thermomechanical processing. The ability to control nitride structures makes the production of dispersioned strengthened alloys, with enhanced mechanical properties, feasible.

The primary observations of this study on microstructural development in high-nitrogen austenitic stainless steels are listed below:

1. Niobium additions resulted in transgranular Nb-rich (NbCrN) nitride formation in as-forged and solution annealed materials. Solubility of NbCrN increased with increasing solution annealing temperature, but complete dissolution was not achieved, even after soaking at 1250°C for 10 hours.
2. Transgranular NbCrN nitrides significantly reduced the room temperature impact properties of annealed materials.
3. Precipitation of Cr-rich Cr_2N nitrides occurred in the temperature range of 600-1075°C during isothermal aging. Precipitation kinetics were most rapid at 900-950°C where nucleation occurred within 0.01 hour (36 seconds). Precipitation occurred first at GBs, followed by cellular, and finally, by

transgranular precipitation. Precipitation kinetics were slightly faster in heat DPSC 2100 than in heat DE 257.

4. Cold-working, prior to aging, increased GB, and most dramatically, transgranular precipitation kinetics. Cellular precipitation development was retarded by prior deformation.
5. Room temperature embrittlement, measured by Charpy V-notch impact toughness testing, was induced by the presence of GB and cellular Cr_2N precipitates.
6. Sensitization in annealed materials was induced by the GB precipitation of Cr-rich Cr_2N nitrides. Prior deformation significantly increased the rate of sensitization development at 700°C and also induced transgranular Cr-depletion.

In this study, the initial forging operation (done at between 1025 and 1075°C) resulted in the presence of a nearly continuous film of Cr_2N nitrides at GBs. The Cr_2N was dissolved by solution annealing at temperatures above 1100°C. However, isothermal aging resulted in removal of the nitrogen from solid-solution and precipitation of Cr_2N. Nitride nucleation was non-homogeneous and occurred preferentially at high energy sites such as GBs. Grain boundary precipitates formed continuous structures at very short times, and cellular and transgranular precipitation resulted in lamellar and platelet nitride morphologies, respectively. The kinetics of these reactions were described using TTP curves.

Prior deformation (cold working) results in accelerated rates of GB and transgranular Cr_2N precipitation. This occurs primarily through two mechanisms, first, the activation of nucleation sites at high-energy defects within the matrix, such as dislocations and deformation twins, and secondly, through enhanced Cr-diffusion due to a dislocation pipe diffusion mechanism. The results of this work indicate that cold worked structures should be susceptible to deformation-induced precipitation in temperature ranges (approximately 400-600°C) where precipitation kinetics in annealed materials are very slow.

Additions of strong nitride forming elements such as Nb, V, and/or Al (also applicable to alloys containing Ti) result in the presence of nitrides which have limited solubility in austenite. The presence of these nitrides can either have a significant detrimental (embrittlement) effect on mechanical properties as shown in this study, or a positive (dispersion strengthening) effect as illustrated by others.[7,104] Nitride characteristics such as morphology, size, spacing, volume fraction, and homogeneity control material response. These factors are primarily controlled by bulk chemistry and thermomechanical processing.

Precipitation of Cr_2N causes the formation of GB Cr-depletion zones and results in material sensitization. Therefore, high nitrogen SSs subjected to thermal treatments within the sensitization regime (about 600-850°C) are likely to be susceptible to IGC and IGSCC. Prior deformation enhances the rate of sensitization development but induces significant transgranular Cr-depletion along with the intergranular Cr-depletion observed in annealed structures. Transgranular Cr-depletion may act to slow crack development in SCC environments by diverting crack development away from GBs and into discontinuous transgranular Cr-depletion regions.

Finally, it can be stated that thermomechanical treatments which result in the presence of GB and cellular Cr_2N nitrides are detrimental to material properties (i.e toughness) and can result in embrittlement after short exposures within the temperature range from about 700-1000°C. Low fracture toughness properties induced by nitride precipitation could cause failure of austenitic SS components generally thought to have "inherently" high fracture toughness.

FUTURE WORK RECOMMENDATIONS

The effect of alloying, temperature, and pressure on the solubility of nitrogen in liquid iron-based alloys is now well understood. High-nitrogen alloys with controlled compositions can be engineered with great accuracy. The primary focus of future research should be one of quantitatively defining nitrogen solid-solubility as a function of alloying. The purpose of this work would be to maximize interstitial nitrogen and thus, strength levels, through judicious alloying additions while minimizing precipitation susceptibility.

One important area of research, given the high work hardening rate of nitrogen austenites and their likely use in the cold worked condition, is the study of mechanical properties of aged materials with prior cold working. The present work has shown that precipitate morphologies are very different in solution annealed and cold worked materials which should have an effect on resultant mechanical properties.

The sensitization susceptibility of high-nitrogen SSs was demonstrated in this work. Additional research could be done to define the parameters controlling sensitization (i.e. alloying, prior deformation, and temperature). The corrosion response, in a variety of environments, of materials containing large volume fractions of Cr_2N, but which are not sensitized, is also very important.

An important aspect to the development and expansion of high-nitrogen steel technologies is the search for new applications. For example, they may be used in applications where austenitic SSs could not be considered before because of their low strength, such as a possible substitute for nickel-base superalloys, where they can provide a cost savings over an existing material. Joining technologies are also important to the expanded use of high-nitrogen steels. This is an especially challenging area since these materials are thermally unstable and joining processes, such as welding, would be expected to cause significant nitride precipitation within heat-affected zones.

REFERENCES

1. Bain, E.C., R.H. Aborn, J.J.B. Rutherford, Trans. Amer. Soc. Steel Treating, 21 (1933) p. 481.

2. M.O. Speidel, "Properties and Applications of High Nitrogen Steels", in Proceedings of the International Conference on High Nitrogen Steels, HNS 88, Lille, France, May 1988, edited by J. Foct and A. Hendry, The Institute of Metals, London (1989) p. 92.

3. J. Foct, "Hign Nitrogen Steels: From Science to Technology," in Proceedings of the 2nd International Conference on High Nitrogen Steels, HNS 90, Aachen, Germany, October 1990, edited by G. Stein and H. Witulski, Verlag Stahleisen mbH, Dusseldorf, Germany (1990) p. 1.

4. G. Stein, J. Menzel, and M. Wagner, "N-Alloyed Steels for Retaining Rings and Other Applications", in Proceedings of the 2nd International Conference on High Nitrogen Steels, HNS 90, Aachen, Germany, October 1990, edited by G. Stein and H. Witulski, Verlag Stahleisen mbH, Dusseldorf, Germany (1990) p. 399.

5. A. Nyilas and B. Obst, "Tensile and Fracture Properties of High Nitrogen Bearing Austenitic Steels at Cryogenic Temperatures, in Proceedings of the International Conference on High Nitrogen Steels, HNS 88, Lille, France, May 1988, edited by J. Foct and A. Hendry, The Institute of Metals, London (1989) p. 194.

6. R.P. Reed and N.J. Simon, "Nitrogen Strengthening of Austenitc Stainless Steels at low Temperatures," in Proceedings of the International Conference on High Nitrogen Steels, HNS 88, Lille, France, May 1988, edited by J. Foct and A. Hendry, The Institute of Metals, London (1989) p. 180.

7. P.J. Uggowitzer and M.O. Speidel, "Ultrahigh-Strength Austenitic steels," in Proceedings of the 2nd International Conference on High Nitrogen Steels, HNS 90, Aachen, Germany, October 1990, edited by G. Stein and H. Witulski, Verlag Stahleisen mbH, Dusseldorf, Germany (1990) p. 156.

8. E. Werner, P. Uggowitzer, and M.O. Speidel, "Mechanical Properties and Aging Behavior of Nitrogen Alloyed Austenitic Steels", Proceedings of the Fifth International Conference on the Mechanical Behavior of Materials, Vol. 1, Bejing, China, June (1987) p. 419.

9. M. Kikuchi, M. Kajihara, and S Choi, "Cellular Precipitation Involving Both Substitutional and Interstitial Solutes: Cellular Precipitation of Cr_2N in Cr-Ni Austenitic Steels", Mat. Sci. and Engr., Vol. A146 (1991) p. 131.

10. M. Kajihara, M. Kikuchi, and S.K. Choi "Cellular Precipitation of Cr_2N in Chromium-Nickel Austenitic Steels" in Phase Transformations '87, G.W. Lorimer, ed., The Institute of Metals, London (1988) p. 265.

11. D.B. Rayaprolu and A. Hendry, "Cellular Precipitation in a Nitrogen Alloyed Stainless Steel", Mat. Sci. and Tech., Vol. 5, April (1989) p. 328.

12. R. Presser and J.M.Silcock, Metal Science, Vol. 17, May (1983) p. 241.

13. S.M. Bruemmer, Materials Science Forum, Vol. 46 (1989) p. 309.

14. S. Danyluk and I. Wolke, "Low Temperature Impact Properties of Phosphorus and Sulfur Doped and Sensitized Type 304 Stainless Steel", Met. Trans. A, Vol. 17A (1986) p. 663.

15. P.T. Purtscher, Scripta Metall., Vol. 26, No. 3 (1992) p. 343.

16. S.M. Bruemmer, L.A. Charlot, A. Bagchi, and D.G. Atteridge, "Influence of Grain Boundary Carbides and Phosphorus Segregation on the Low-Temperature Intergranular Embrittlement of Type 316 Stainless Steel", Scripta Metallurgica, Vol. 23 (1989) p. 1549.

17. D. Gan, "Tensile and Fracture Properties of Type 316 Stainless Steel after Creep", Met. Trans. A, Vol. 13A (1982) p. 2155.

18. T. Tseng, D. Gan, and Po-We Kao, "The Effects of Grain Boundary Carbides on the Low Temperature Impact Properties of Type 316 Stainless Steel", Mat. Sci. and Engr., Vol. 95 (1987) p. 73.

19. S.Y. Chen and D. Gan, "Effects of Grain Boundary Carbides on the Tensile and Impact Properties of Type 316 Stainless Steel", Mat. Sci. and Engr., Vol. 84 (1986) p. 65.

20. R.D. Pehlke and J.F. Elliott, Trans. AIME, Vol. 218, December (1960) p. 1088.

21. A.H. Satir-Kolorz and H.K. Feichtinger, Z. Metallkde, Bd. 82, H.9, (1991) p. 689.

22. H. Feichtinger, A. Satir-Kolorz, and Z. Xiao-hong, "Solubility of Nitrogen and Liquid Iron Aloys with Special regard to the Melting Range," in Proceedings of the International Conference on High Nitrogen Steels, HNS 88, Lille, France, May 1988, edited by J. Foct and A. Hendry, The Institute of Metals, London (1989) p. 92.

23. A.Y. Stomakhin et al., "Thermodynamics of Nitrogen Solutions in Liquid Steel and Optimisation of Nitride-Forming Microadditions" in Proceedings of the 2nd International Conference on High Nitrogen Steels, HNS 90, Aachen, Germany, October 1990, edited by G. Stein and H. Witulski, Verlag Stahleisen mbH, Dusseldorf, Germany (1990) p. 109.

24. A. Sieverts and G. Zapf, Z. Phys. Chem., Abt. A, Vol. 172 (1935) p. 314.

25. W.M. Small and R.D. Pehlke, Trans. AIME, Vol. 242, December (1968) p. 2501.

26. P.H. Turnock and R.D. Pehlke, Trans. AIME, Vol. 236, November (1966) p. 1540.

27. Y.M. Pomarin and G.M. Grigorenko, "Equation for Calculation of Nitrogen Solubility in Nitrogen-Containing Steels and Aloys," in Proceedings of the 2nd International Conference on High Nitrogen Steels, HNS 90, Aachen, Germany, October 1990, edited by G. Stein and H. Witulski, Verlag Stahleisen mbH, Dusseldorf, Germany (1990) p. 27.

28. H. Feichtinger, "Alternative Routes to the Production of High-Nitrogen Steels," in Proceedings of the 2nd International Conference on High Nitrogen Steels, HNS 90, Aachen, Germany, October 1990, edited by G. Stein and H. Witulski, Verlag Stahleisen mbH, Dusseldorf, Germany (1990) p. 298.

29. R.P. Reed, J. Metals, March (1989) p. 16.

30. G. Stein, J. Menzel, and H. Dorr, "Industrial Manufacture of Massively Nitrogen-Alloyed Steels," in Proceedings of the International Conference on High Nitrogen Steels, HNS 88, Lille, France, May 1988, edited by J. Foct and A. Hendry, The Institute of Metals, London (1989) p. 32.

31. J. Menzel, G. Stein, and P. Dahlmann, "Manufacture of N-Alloyed Steels in a 20t PESR Furnace", in Proceedings of the 2nd International Conference on High Nitrogen Steels, HNS 90, Aachen, Germany, October 1990, edited by G. Stein and H. Witulski, Verlag Stahleisen mbH, Dusseldorf, Germany (1990) p. 365.

32. E. Werner, Mat. Sci. and Engr. A, Vol. 101 (1988) p. 93.

33. M.L.G. Byrnes, M. Grujicic, and W.S. Owen, Acta Metall., Vol. 35, No. 7 (1987) p. 1853.

34. E. Werner and H.P. Stuwe, Mat. Sci. and Engr., Vol. 68 (1984-1985) p. 175.

35. P.J. Uggowitzer and M. Harzenmoser, "Strengthening of Austenitic Stainless Steels by Nitrogen," in Proceedings of the International Conference on High Nitrogen Steels, HNS 88, Lille, France, May 1988, edited by J. Foct and A. Hendry, The Institute of Metals, London (1989) p. 174.

36. A. Soussan, S. Degallaix, and J. Foct, "Combined Influence of Nitrogen and Grain Size on the Flow Stress in Type AISI 316L-316LN Austenitic Stainless Steels," in Proceedings of the 2nd International Conference on High Nitrogen Steels, HNS 90, Aachen, Germany, October 1990, edited by G. Stein and H. Witulski, Verlag Stahleisen mbH, Dusseldorf, Germany (1990) p. 67.

37. V.K. Rao, D.M.R. Taplin, and P.R. Rao, Met. Trans. A, Vol. 6A, January (1975) p. 77.

38. L.A. Norstrom, Metal Science, June (1977) p. 208.

39. D. Peckner and I.M. Bernstein, Handbook of Stainless Steels, McGraw-Hill Book Co., New York (1977) p. 21-5.

40. V.G. Garilijuk, V.A. Duz, and S.P. Jephimenko, "The Structure and Mechanical Properties of Cold Worked High-Nitrogen Austenite," in Proceedings of the 2nd International Conference on High Nitrogen Steels, HNS 90, Aachen, Germany, October 1990, edited by G. Stein and H. Witulski, Verlag Stahleisen mbH, Dusseldorf, Germany (1990) p. 100.

41. A.S. Tetelman and A.J. McEvily, Fracture of Structural Materials, John Wiley and Sons, New York (1967).

42. M. Harsenmoser et al., "The Influence of Nickel and Nitrogen on the Mechanical Properties of High-Nitrogen Austenitic Steels at Cryogenic Temperatures," in Proceedings of the 2nd International Conference on High Nitrogen Steels, HNS 90, Aachen, Germany, October 1990, edited by G. Stein and H. Witulski, Verlag Stahleisen mbH, Dusseldorf, Germany (1990) p. 67.

43. V.A. Volkov et al., "Approach to High-Nitrogen Alloyign and Production in the USSR," in Proceedings of the 2nd International Conference on High Nitrogen Steels, HNS 90, Aachen, Germany, October 1990, edited by G. Stein and H. Witulski, Verlag Stahleisen mbH, Dusseldorf, Germany (1990) p. 277.

44. L.E. Murr, Res Mechanica, Vol. 9 (1983) p. 159.

45. V. Gerold and H.P. Karthaler, Acta Metall., Vol. 37, No. 8 (1989) p. 2177.

46. R.E. Stoltz and J.B. Vander Sande, Met. Trans. A, Vol. 11A, June (1980) p. 1033.

47. G. Thomas, Acta Metallurgica, Vol. 11 (1963) p. 1369.

48. M. Grujicic et al., "Basic Deformation Mechanisms in Nitrogen Strengthened Stable Austenitic Stainless Steels," in Proceedings of the International Conference on High Nitrogen Steels, HNS 88, Lille, France, May 1988, edited by J. Foct and A. Hendry, The Institute of Metals, London (1989) p. 151.

49. J. Sassen, A.J. Garratt-Reed, and W.S. Owen, "Electron Microscopy of Austenitic Fe-Ni-Cr Alloys Containing Nitrogen," in Proceedings of the International Conference on High Nitrogen Steels, HNS 88, Lille, France, May 1988, edited by J. Foct and A. Hendry, The Institute of Metals, London (1989) p. 159.

50. R.W.K. Honeycombe, The Plastic Deformation of Metals, William Clowes and Sons, London (1971) p. 176.

51. M. Kikuchi et al. Met Trans. A, Vol. 7A, June (1976) p. 906.

52. M. Deighton, J. Iron Steel Inst., November (1970) p. 1012.

53. M. Kikuchi, M Kajihara, and K. Frisk, "Solubility of Nitrogen in Austenitic Stainless Steels," in Proceedings of the International Conference on High Nitrogen Steels, HNS 88, Lille, France, May 1988, edited by J. Foct and A. Hendry, The Institute of Metals, London (1989) p. 63.

54. M. Kawase, H. Emoto, and M. Kikuchi, "Cellular Precipitation of a Ni-40Cr-4Al Alloy" in Phase Transformations '87, G.W. Lorimer, ed., The Institute of Metals, London (1988) p. 254.

55. D.A. Porter and K.E. Easterling, Phase Transformations in Metals and Alloys, Van Nostrand Reinhold, Berkshire, United Kingdom (1987) p. 271.

56. C.J. Bechtoldt and H.C. Vacher, J. Res. Nat. Bur. Stand., Vol. 58, (1957) p. 7.

57. J.K.L. Lai, Mat. Sci. and Engr., Vol. 61 (1983) p. 101.

58. R. Weiss and R. Stickler, Met. Trans., Vol. 3, April (1972) p. 851.

59. R. Stickler and A. Vinckier, Rev. Met., Vol. 60 (1963) p. 489.

60. H. Wiegand and M. Doruk, Arch. Eisenhuttenw., Vol. 8 (1962) p. 559.

61. H. Goldschmidt, Interstitial Alloys, Plenum Press, New York (1967).

62. J.K.L. Lai, Mat. Sci. and Engr., Vol. 58 (1983) p. 195.

63. S.M. Bruemmer, L.A. Charlot, and D.G. Atteridge, Corrosion, Vol. 44, No. 7, July (1988) p. 427.

64. S.M. Bruemmer, Corrosion, Vol. 46, No. 9, September (1990) p. 698.

65. T.A. Mozhi et al., Corrosion, Vol. 41, No. 10, October (1985) p. 555.

66. H.S. Betrabet et al., Corrosion, Vol. 43, No. 2, February (1987) p. 77.

67. E.L. Hall and C.L. Briant, Met. Trans. A, Vol. 15A, May (1984) p. 793.

68. C.L. Briant and E.L. Hall, Corrosion, Vol. 42, No. 9, September (1986) p. 522.

69. S.M. Bruemmer, L.A. Charlot, Scripta Metall., Vol. 20 (1986) p. 1019.

70. C. Stawstrom, M. Hillert, J. Iron Steel Inst., January (1969) p. 77.

71. S.M. Bruemmer, PhD Dissertation, "Quantitative Measurement and Modeling of Sensitization Development in Stainless Steels," Oregon Graduate Institute of Science and Technology (OGI), Beaverton, OR, May (1988).

72. C.L. Briant, R.A. Mulford, and E.L. Hall, Corrosion, Vol. 38, No. 9, September (1982) p. 468.

73. C.S. Tedmon, Jr., D.A. Vermilyea, J.H. Rosolowski, J. Electrochem. Soc., Vol. 118, No. 2 (1971) p. 192.

74. C.L. Briant, E.L. Hall, Corrosion, Vol. 42, No. 9, September (1986) p. 523.

75. E.C. Bain, R.H. Aborn, Trans. Amer. Soc. Steel Treat., Vol. 18 (1930) p. 837.

76. T. Thorvaldsson and A. Salwen, Scripta Metallurgica, Vol. 18, No. 7 (1984) p. 739.

77. ASTM Book of Standards, A 262, ASTM, Philadelphia, Pennsylvania, Vol. 10 (1978) p. 1.

78. W.L. Clarke, R.L. Cowan, W.L. Walker, "Comparative Methods for Measuring Degree of Sensitization in Stainless Steel," Intergranular Corrosion of Stainless Alloys, ASTM STP 656, R.F. Steigerwald, Ed., ASTM (1978) pp. 99-132.

79. ASTM Committee G-1 - Corrosion of Metals, Subcommittee G01.08 - Corrosion of Nuclear Materials, "Test Method for Electrochemical Potentiokinetic Reactivation (EPR) Method for Detecting Sensitization of AISI-304 and 304L Stainless Steels," ASTM.

80. A. Mignone, A. Borello, and A. La Barbera, Corrosion, Vol. 38, No. 7, July (1982) p. 391.

81. S.M. Bruemmer, Corrosion, Vol. 42, No. 1, January (1986) p. 27.

82. J.B. Lee, Corrosion, Vol. 42, No. 2, February (1986) p. 106.

83. C.L. Briant, A.M. Ritter, Met. Trans. A, Vol. 11A, December (1980) p. 2010.

84. J.W. Christian, "The Theory of Transformations in Metals and Alloys, Part I - Equilibrium and General Kinetic Theory," Pergamon Press Ltd., 2nd ed. (1975).

85. E.W. Hart, Acta Metall., Vol. 5, October (1957) p. 597.

86. F.A. Huntley, F.W. Willoughby, J. Electrochem. Soc., Vol. 120, No. 3, March (1973) p. 415.

87. J.M. Hill, Scripta Metall., Vol. 13, No. 11 (1979) p. 1027.

88. R.W. Balluffi, Phys. Stat. Sol., Vol. 42 (1970) p. 11.

89. A.L. Ruoff, R.W. Balluffi, J. Applied Phys., Vol. 34, No. 7, July (1963) p. 1848.

90. J.W. Simmons, D.G. Atteridge, L.E. Murr, and S.M. Bruemmer, "Effects of Prior Deformation on the Sensitization of Type 316 Austenitic Stainless Steel II: Continuous Cooling Sensitization," Recent Trends in Welding Science and Technology, Proc. 2nd Int. Conf. on Trends in Welding Research, S.A. David and J.M. Vitek, eds., ASM International, Metals Park, Ohio (1990) p. 321.

91. A.H. Advani et al., Metall. Trans. A, Vol. 22A (1991) p. 2917.

92. A.H. Advani et al., Corrosion, Vol. 47, No. 12, (1991) p. 939.

93. A.H. Advani et al., Scripta Metallurgica, Vol. 25 (1991) p. 349.

94. C.L. Briant and A.M. Ritter, Scripta Metallurgica, Vol. 13, No. 3 (1979) p. 177.

95. J.E. Spruiell et al., Met. Trans., Vol. 4, June (1973) p. 1533.

96. H.D. Solomon, Corrosion, Vol. 40, No. 2, February (1984) p. 51.

97. W.L. Clarke, "The EPR Method for the Detection of Sensitization in Stainless Steels," NUREG-0251-1, U.S. Nuclear Regulatory Commission (1976).

98. ASTM Book of Standards, Vol. 3.01, E 23-88, ASTM, Philadelphia, Pennsylvania (1989) p. 198.

99. H. Hughes, "Complex Nitride in Cr-Ni-Nb Steels", JISI, Vol. 205 (1967) p. 775.

100. D.H. Jack and K.H. Jack, "Structure of Z-Phase, NbCrN", JISI, October (1972) p. 790.

101. D.B. Rayaprolu and A. Hendry, "High nitrogen stainless steel wire", Mat. Sci. and Tech., Vol. 4, February (1988) p. 136.

102. "Powder Diffraction File," JCPDS International Center for Diffraction Data 1986, Pennsylvania (1986).

103. Y.A. Kunakov et al., "Nitrogen-Alloyed Austenitic Steels for the High-Temperature and Cryogen Application," in Proceedings of the 2nd International Conference on High Nitrogen Steels, HNS 90, Aachen, Germany, October 1990, edited by G. Stein and H. Witulski, Verlag Stahleisen mbH, Dusseldorf, Germany (1990) p. 448.

104. V.A. Volkov, S.V. Shlepkov, A.A. Kasakov, "Current State and Trends in Scientific Research and Industrial Application of Nitrogen Containing Steels," in Proceedings of the 2nd International Conference on High Nitrogen Steels, HNS 90, Aachen, Germany, October 1990, edited by G. Stein and H. Witulski, Verlag Stahleisen mbH, Dusseldorf, Germany (1990) p. 411.

105. C. DaCasa, V.B. Nileshwar, D.A. Melford, J. Iron Steel Inst., October (1969) p. 1325.

106. H. Holm. P.J. Uggowitzer, and M.O. Speidel, Scripta Metall., Vol. 21, No. 4, (1987) p. 513.

107. "Dynamic Thermal/Mechanical Metallurgy, Using the Gleeble 1500," 2nd Edition, Duffers Scientific, Inc., Troy, NY, p. 22.

108. L.E. Murr and S.H. Wang, Res. Mech., Vol. 4 (1982) p. 237.

109. L.E. Murr and S.H. Wang, Res. Mech. Letters, Vol. 1 (1981) p. 85.

110. J.W. Simmons, M.S. Thesis, "Effects of Prior Deformation on the Continuous Cooling Sensitization of Type 316 Austenitic Stainless Steel," Oregon Graduate Institute of Science and Technology (OGI), Beaverton, OR, October (1989).

APPENDIX A

Crystal Data for Cr_2N, π, and NbCrN (Z-Phase) Nitrides

TABLE A1 - Cr_2N Nitride Crystal Data[1]

Crystal Type: hexagonal
Space Group = 162, P-31m
a = b = 0.4811, c = 0.4484, c/a = 0.932
$\alpha = ß = 90^{\circ}, \gamma = 120^{\circ}$

hkil	d-spacing (nm)
0001	0.4484
$1\bar{1}00$	0.4167
$1\bar{1}01$	0.3052
$11\bar{2}0$	0.2406
0002	0.2242
1120	0.2119
2200	0.2083
$1\bar{1}02$	0.1974
2021	0.1889
$2\bar{1}\bar{1}2$	0.1640
$3\bar{1}20$	0.1575
0003	0.1495
$3\bar{1}21$	0.1486
$1\bar{1}03$	0.1407
$30\bar{3}0$	0.1389
$30\bar{3}1$	0.1327
3122	0.1288

[1] From JCPDF-ICDD card #35-803[102]

TABLE A2 - π-Phase (Nitride) Crystal Data	
Crystal Type: cubic, ß-Mn Structure a = b = c, $\alpha = ß = \gamma = 90°$	
Chemical Formula[1]	Lattice Parameter
$(Cr_{13}Ni_7)N_4$	0.6316
$(Cr_{13}Fe_3Ni_4)N_4$	0.6335
$(Cr_{12}Fe_4Ni_2Si_2)N_4$	0.6362
$(Cr_{11}W_1Ni_8)N_4$	0.6370
hkl	d-spacing (nm) (a = 0.6316)
110	0.4465
111	0.3645
210	0.2824
211	0.2578
220	0.2232
221	0.2105
310	0.1997
311	0.1904
222	0.1823
320	0.1751
321	0.1688
330	0.1488
331	0.1448
[1] From Kikuchi et al.[53]	

TABLE A3 - NbCrN Nitride Crystal Data[1]

Crystal Type: tetragonal
Space Group = 129, P4/nmm
a = b = 0.3037, c = 0.7391, c/a = 2.434
$\alpha = \beta = \gamma = 90^{\circ}$

hkl	d-spacing (nm)
001	0.7390
002	0.3690
101	0.2809
003	0.2464
102	0.2346
110	0.2148
111	0.2052
103	0.1913
112	0.1857
004	0.1848
113	0.1619
104	0.1848
200	0.1519
201	0.1488
005	0.1478
202	0.1404

[1] From Jack and Jack[100]

APPENDIX B

Isothermal Aging Schedules for Heats DE 257 and DPSC 2100

TABLE B1 - Isothermal Aging Schedule of Annealed Materials
(1150°C/2 Hours) from Heats DE 257 (+) and DPSC 2100 (◂)

Temperature °C	Aging Time (Hours)									
	0.01[1]	0.02[1]	0.05[1]	0.1	0.2	0.4	1.0	3.0	10	30
600							+ ◂	+ ◂	+ ◂	+ ◂
650						◂	+ ◂	+ ◂	+ ◂	
700					+ ◂		+ ◂	+ ◂	+ ◂	+ ◂
750			◂	◂	+ ◂		+ ◂	+ ◂	+ ◂	
800		◂		+ ◂	+ ◂		+ ◂	+ ◂	+ ◂	
850			◂	+ ◂	+ ◂	+ ◂	+ ◂	+ ◂	+ ◂	
900	◂	◂		+ ◂	+ ◂	+ ◂	+ ◂	+ ◂	+ ◂	
950		◂		+ ◂	+ ◂	+ ◂	+ ◂	+ ◂	+ ◂	
1000	◂		◂	+ ◂	+ ◂		+ ◂	+ ◂	+ ◂	
1050				+ ◂	+ ◂		+ ◂	+ ◂		
1075				+ ◂	+ ◂		+ ◂			

1 - These samples were heat treated in the Gleeble

TABLE B2 - Isothermal Aging Schedule for Heat DPSC 2100 Solution Annealed (◂) and Cold-Rolled Materials (☼)										
Temperature °C	Aging Time (Hours)									
	0.01[1]	0.02[1]	0.05[1]	0.1	0.2	0.4	1.0	3.0	10	30
600							☼ ◂	☼ ◂	◂	◂
650				☼	☼	☼ ◂	☼ ◂	◂	◂	
700				☼	☼ ◂	☼	☼ ◂	☼ ◂	☼ ◂	◂
750			◂	☼ ◂	☼ ◂	☼	☼ ◂	☼ ◂	◂	
800		◂		☼ ◂	☼ ◂	☼	☼ ◂	☼ ◂	☼ ◂	
850			◂	☼ ◂	☼ ◂	☼ ◂	☼ ◂	☼ ◂	☼ ◂	
900	◂	◂		☼ ◂	☼ ◂	☼ ◂	☼ ◂	☼ ◂	☼ ◂	
950		◂		☼ ◂	☼ ◂	☼ ◂	☼ ◂	☼ ◂	☼ ◂	
1000	◂		◂	☼ ◂	☼ ◂		☼ ◂	◂	◂	
1050				◂	◂		◂	◂		
1075				◂	◂		◂			
1 - These samples were heat treated in the Gleeble										

APPENDIX C

Selected Area Diffraction Pattern (SADP) Schematics

and

Stereographic Projections

NbCrN SADP Schematic
Crystal Type: tetragonal
Space Group = 129, P4/nmm
a = b = 0.304 nm
c = 0.739 nm
Zone Axis = [100]

Camera Constant = 2.90 Å-cm
(Reference Figure 13c)

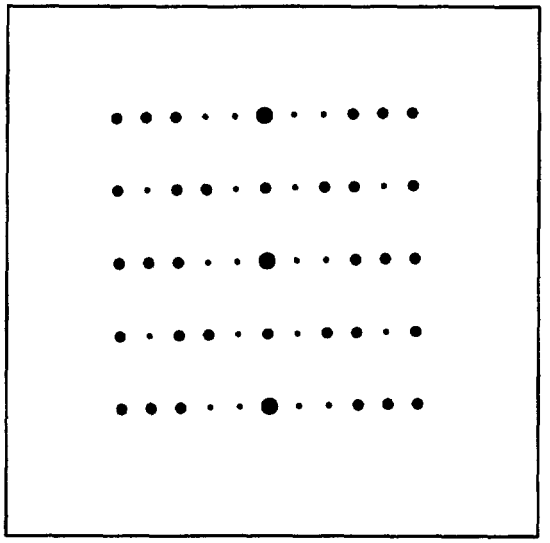

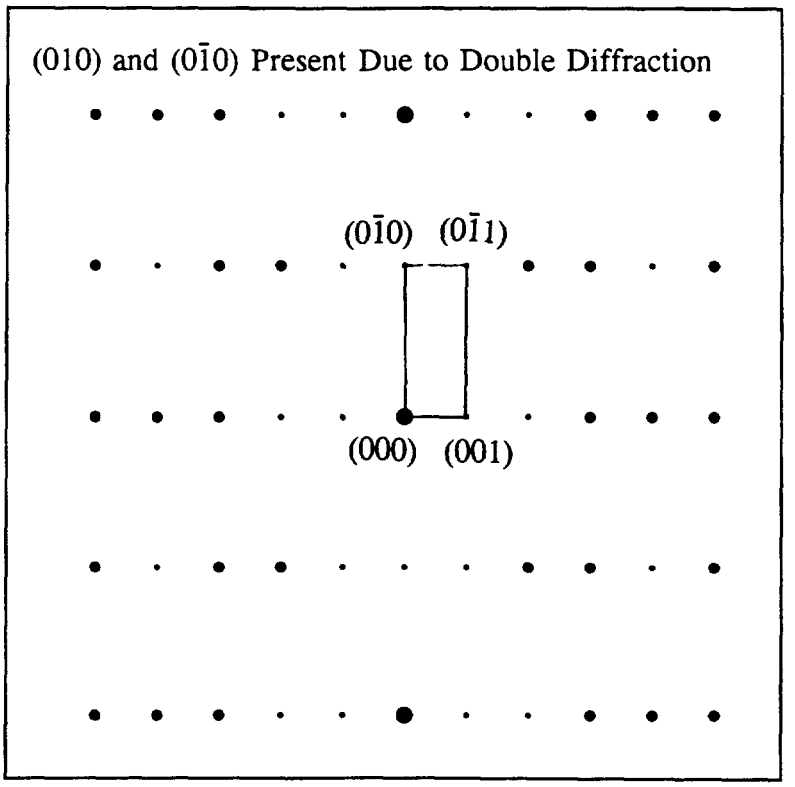

NbCrN SADP Schematic
Space Group = 129, P4/nmm
a = b = 0.304 nm
c = 0.739 nm
Zone Axis = [111]

Camera Constant = 2.90 Å-cm
(Reference Figure 13d)

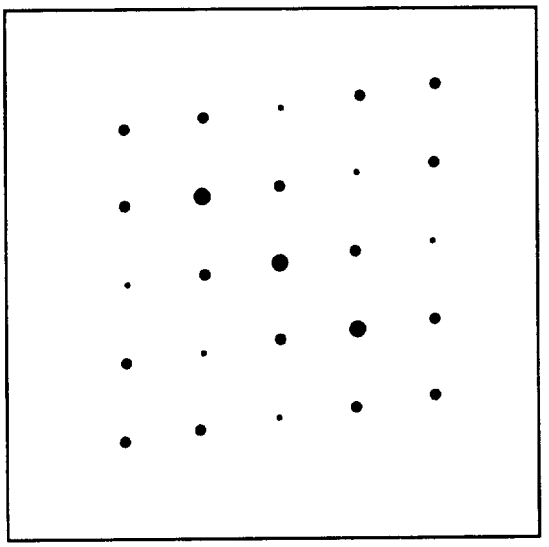

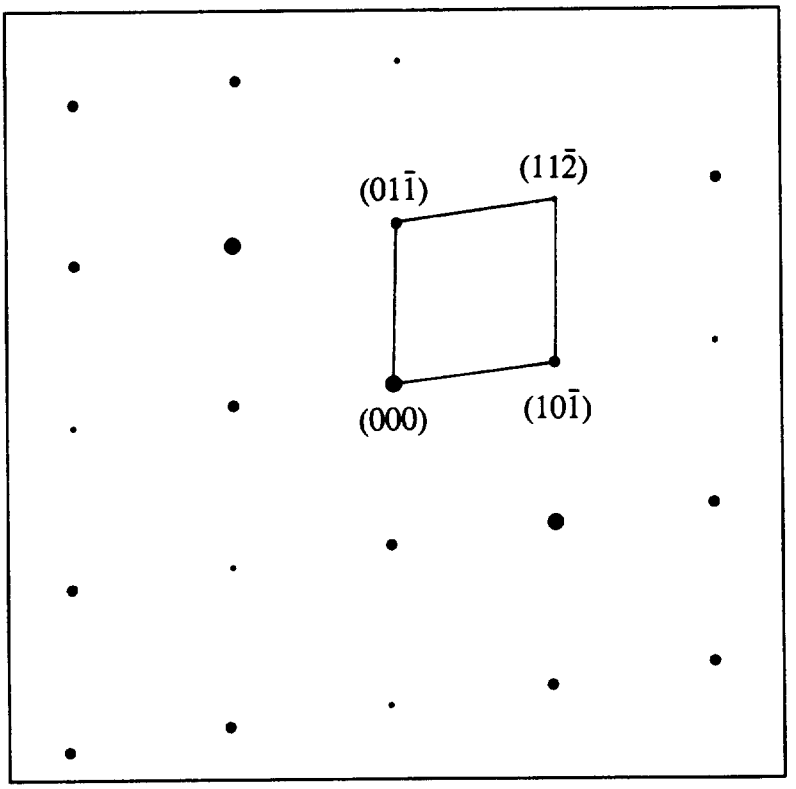

Cr_2N SADP Schematic
Crystal Type: hexagonal
Space Group = 162, P-31m
a = b = 0.481 nm
c = 0.448 nm
Zone Axis = $[\bar{1}100]$

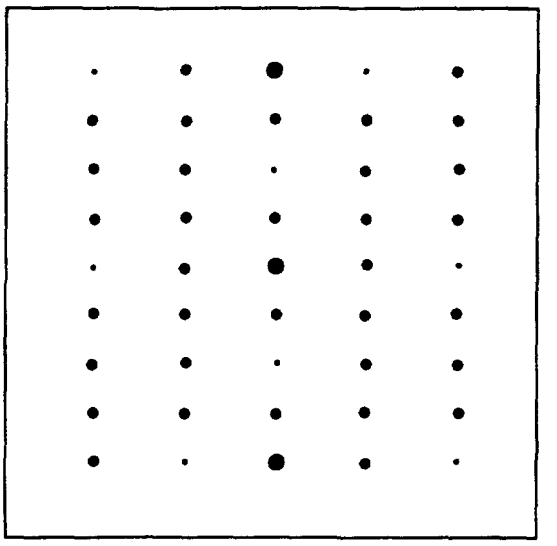

Camera Constant = 2.90 Å-cm
(Reference Figures 29b, 30b, 40c, and 41d)

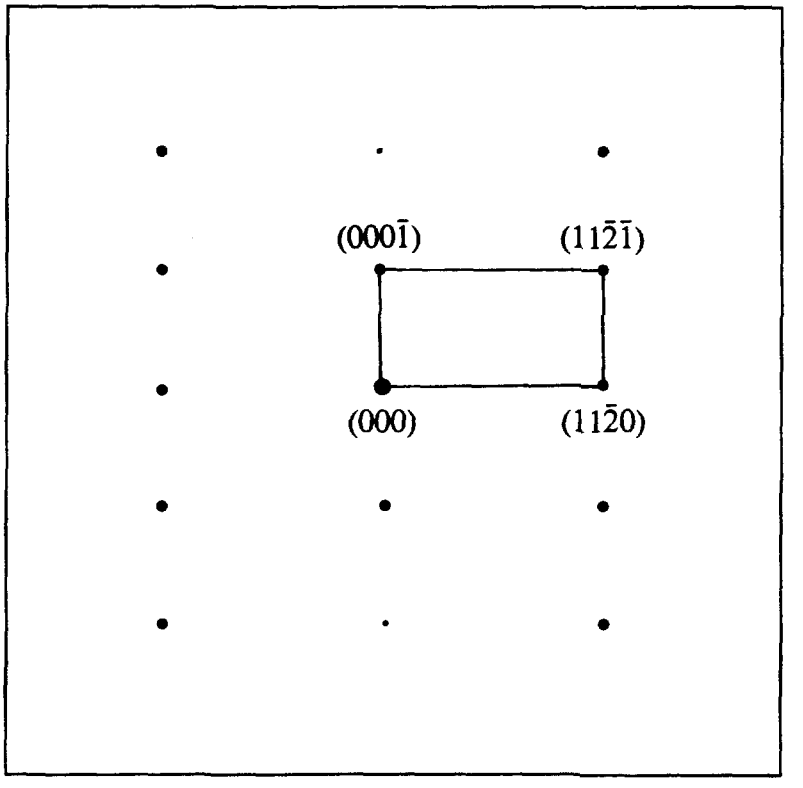

Cr_2N SADP Schematic
Crystal Type: hexagonal
Space Group = 162, P-31m
a = b = 0.481 nm
c = 0.448 nm
Zone Axis = $[1\bar{1}03]$

Camera Constant = 2.90 Å-cm
(Reference Figure 29c)

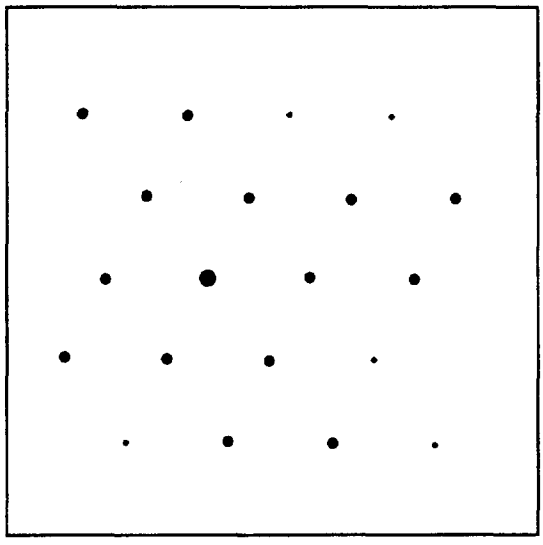

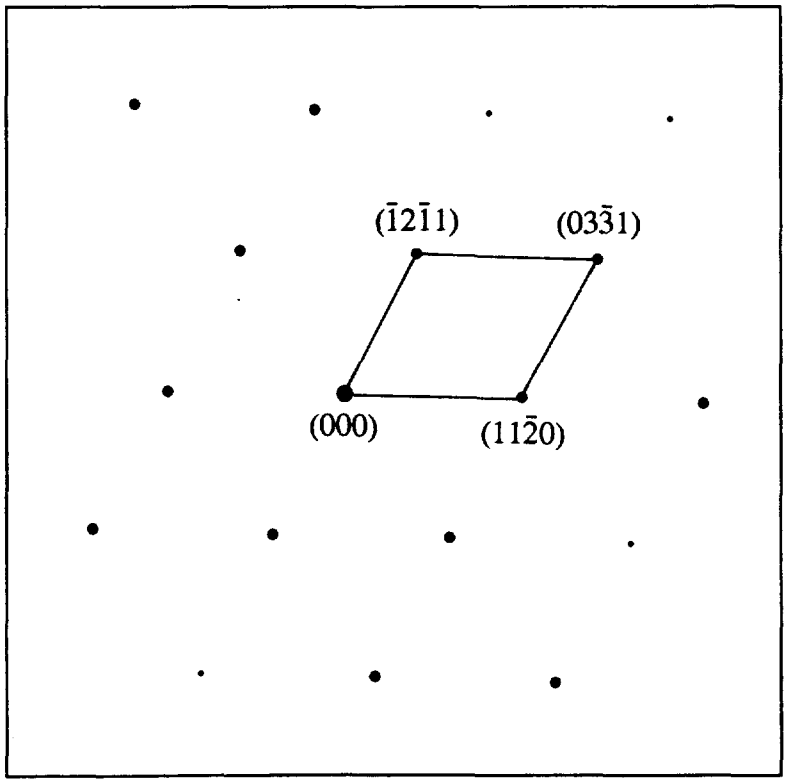

Cr_2N SADP Schematic
Crystal Type: hexagonal
Space Group = 162, P-31m
a = b = 0.481 nm
c = 0.448 nm
Zone Axis = $[20\bar{2}3]$

Camera Constant = 2.90 Å-cm
(Reference Figure 29d)

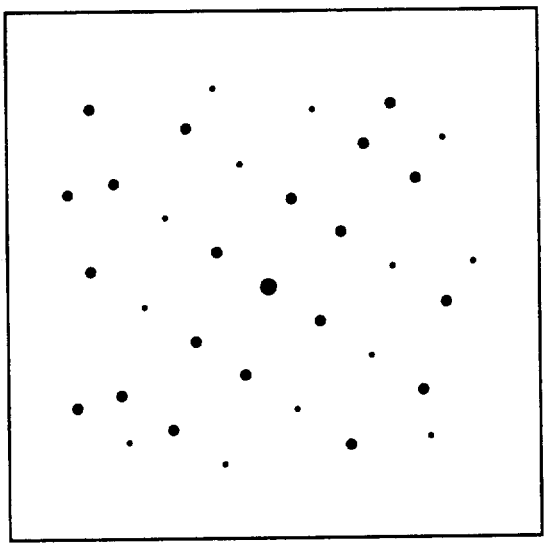

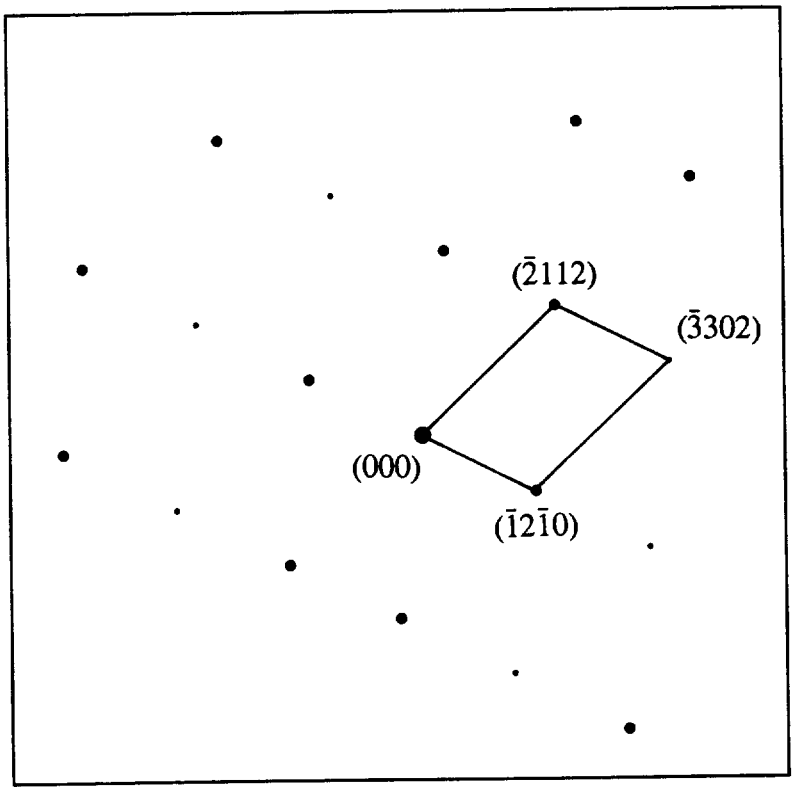

Cr_2N SADP Schematic
Crystal Type: hexagonal
Space Group = 162, P-31m
a = b = 0.481 nm
c = 0.448 nm
Zone Axis = $[3\bar{2}\bar{1}\bar{3}]$

Camera Constant = 1.97 Å-cm
(Reference Figure 45b)

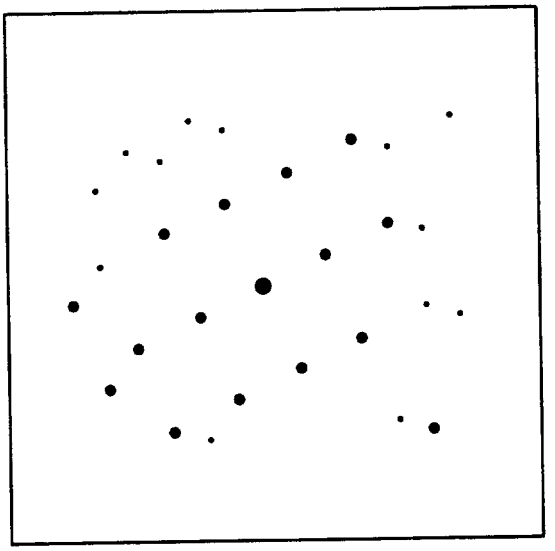

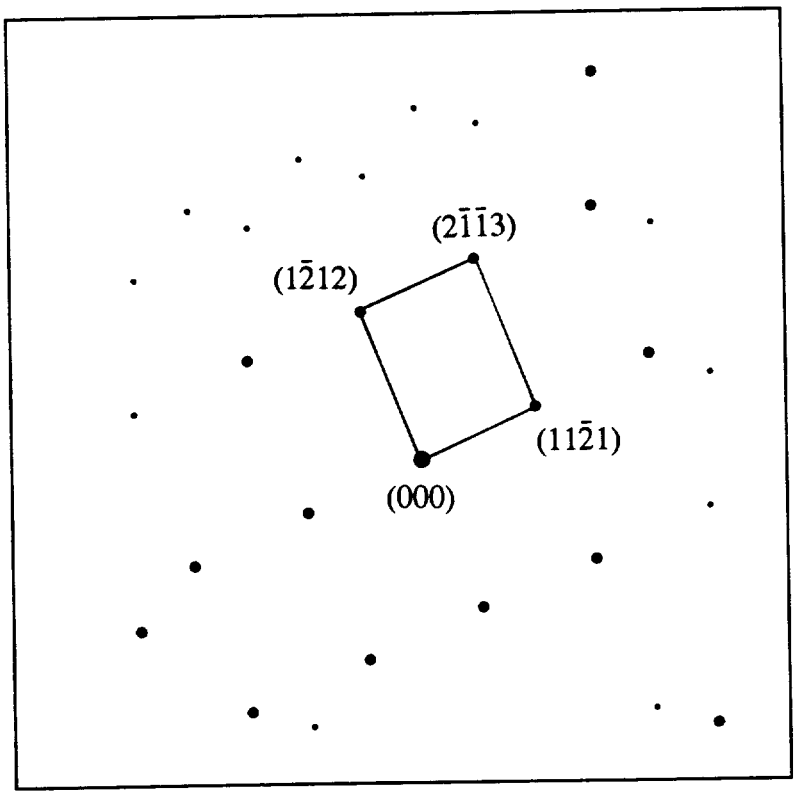

γ/Cr_2N SADP Schematic

$[110]\gamma//[\bar{1}100]Cr_2N$

Camera Constant = 2.90 Å-cm
(Reference Figures 47b & 60b)

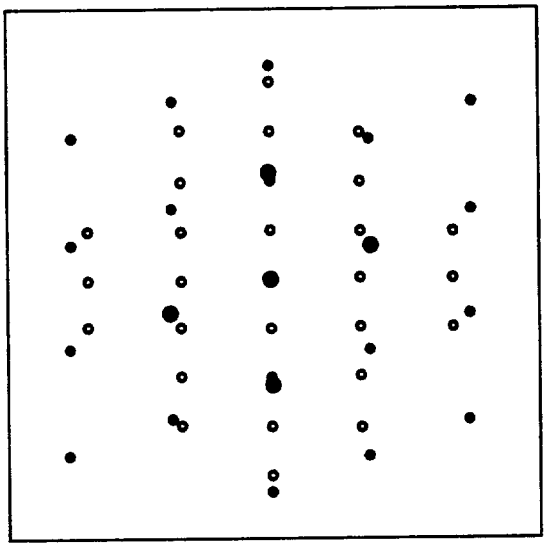

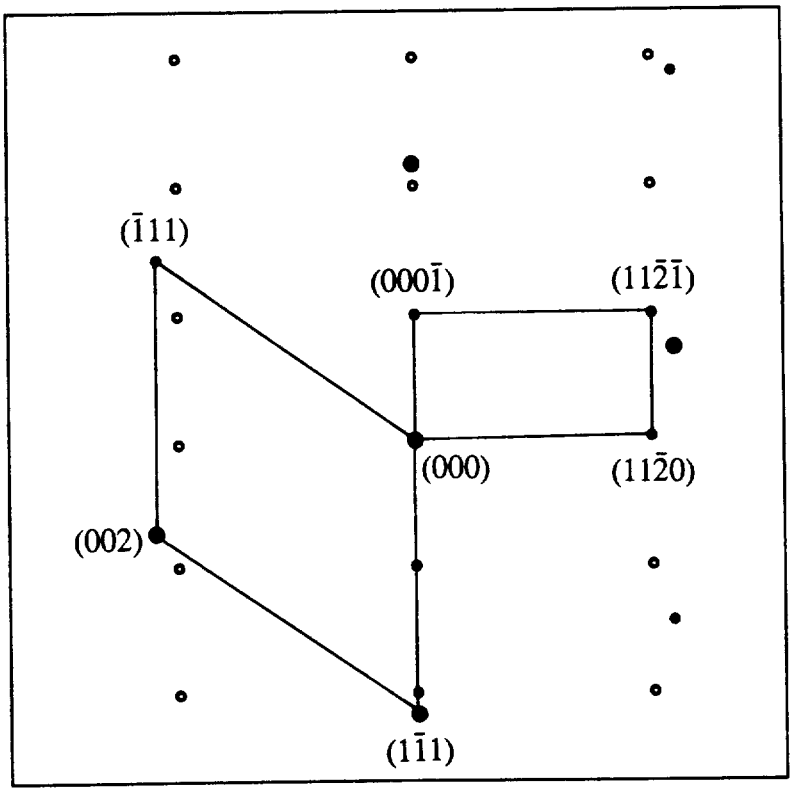

γ/Cr_2N SADP Schematic

$[1\bar{1}\bar{2}]\gamma//[11\bar{2}0]Cr_2N$

Camera Constant = 1.97 Å-cm
(Reference Figures 47d & 60d)

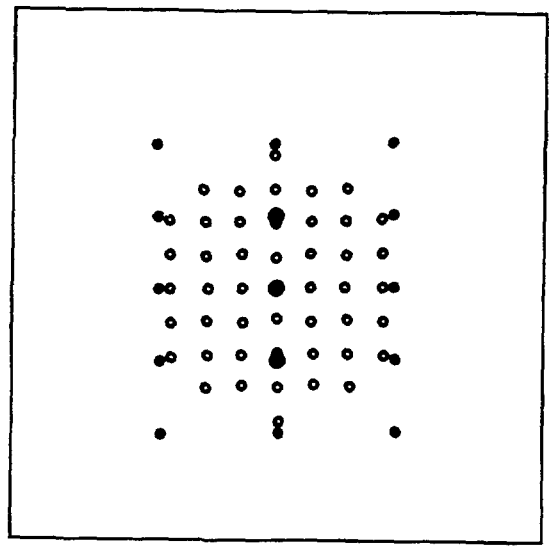

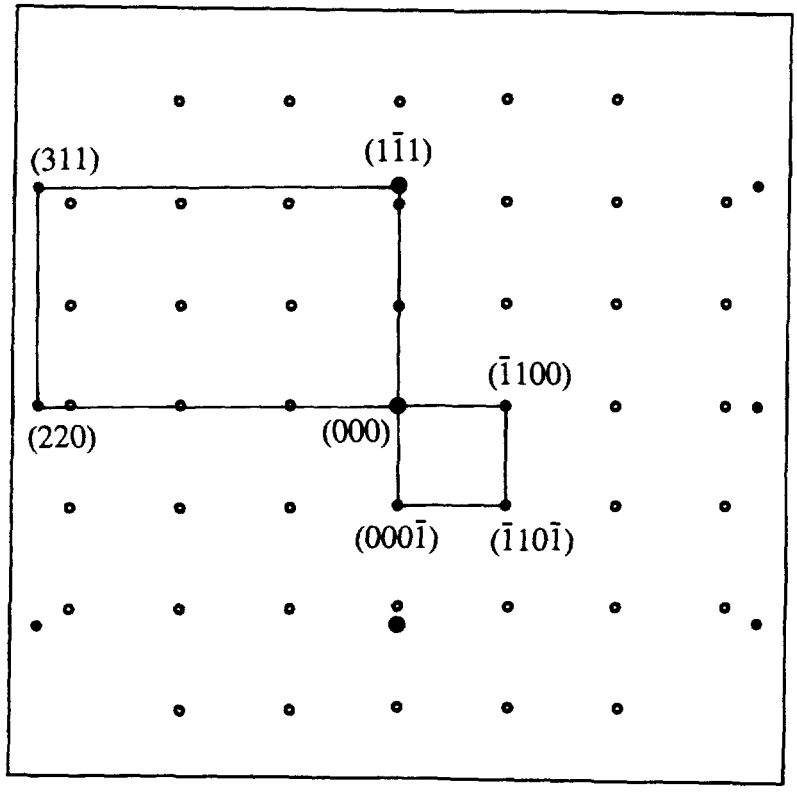

γ/Cr_2N SADP Schematic

for ZA $[\bar{1}11]\gamma$
Close to $[5\ 5\ \bar{1}\bar{0}\ 6]Cr_2N$

Camera Constant = 1.97 Å-cm
(Reference Figures 48b)

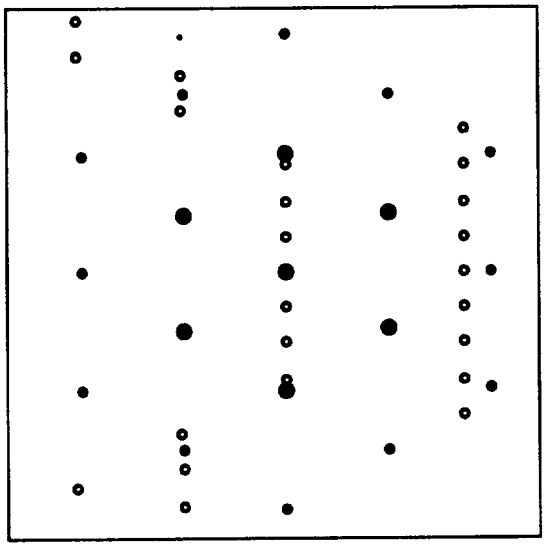

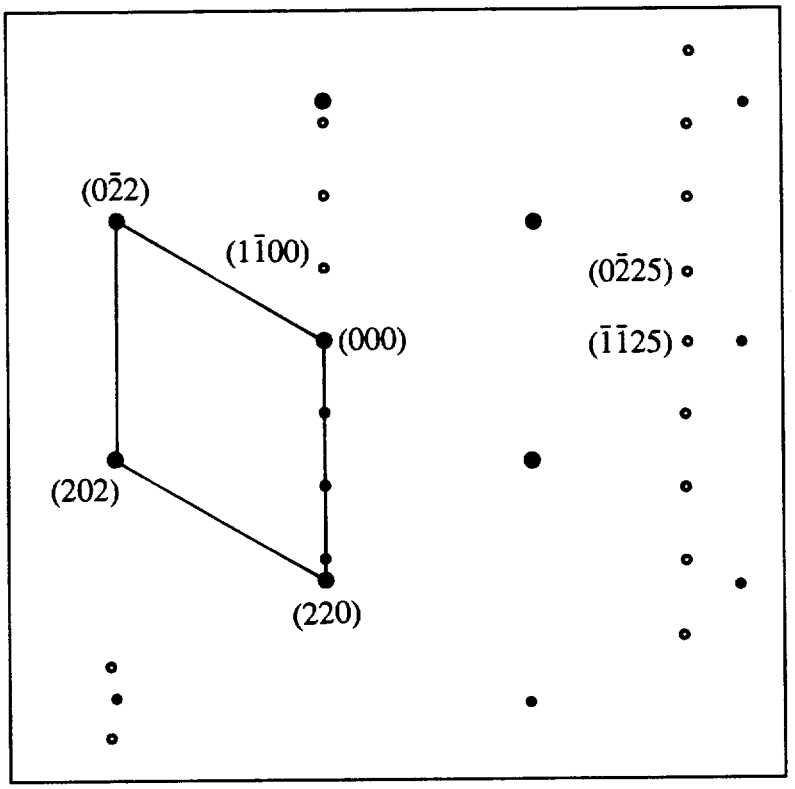

χ-Phase SADP Schematic
Crystal Type: cubic
Space Group = 217, I-43m
a = 0.889 nm
Zone Axis = [111]

Camera Constant = 2.90 Å-cm
(Reference Figure 52b)

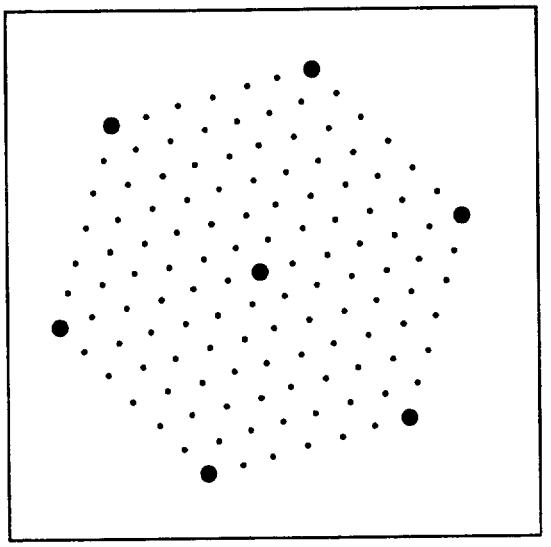

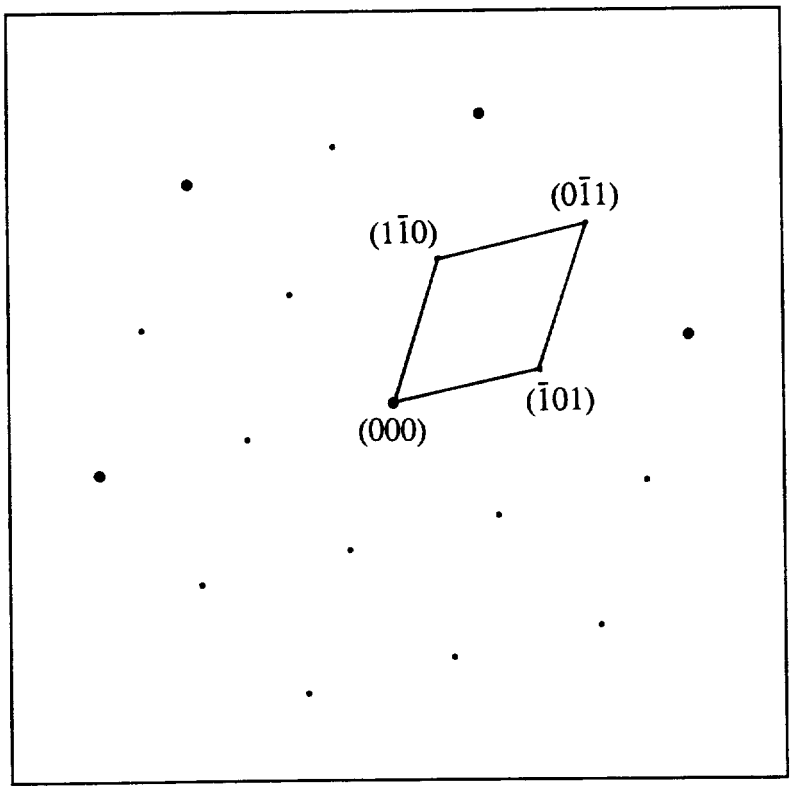

χ-Phase SADP Schematic
Crystal Type: cubic
Space Group = 217, I-43m
a = 0.889 nm
Zone Axis = [110]

Camera Constant = 2.90 Å-cm
(Reference Figure 52d)

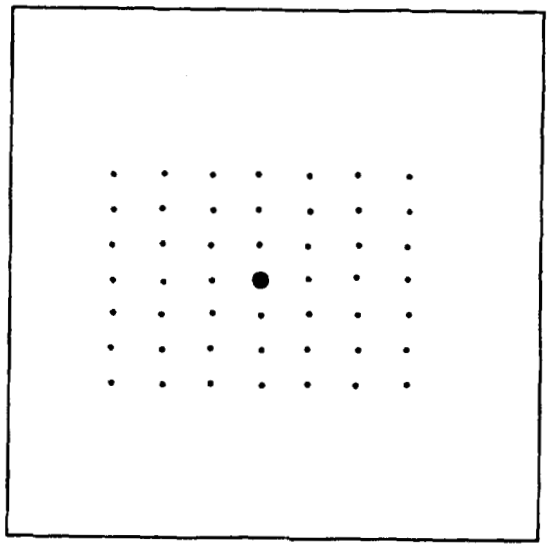

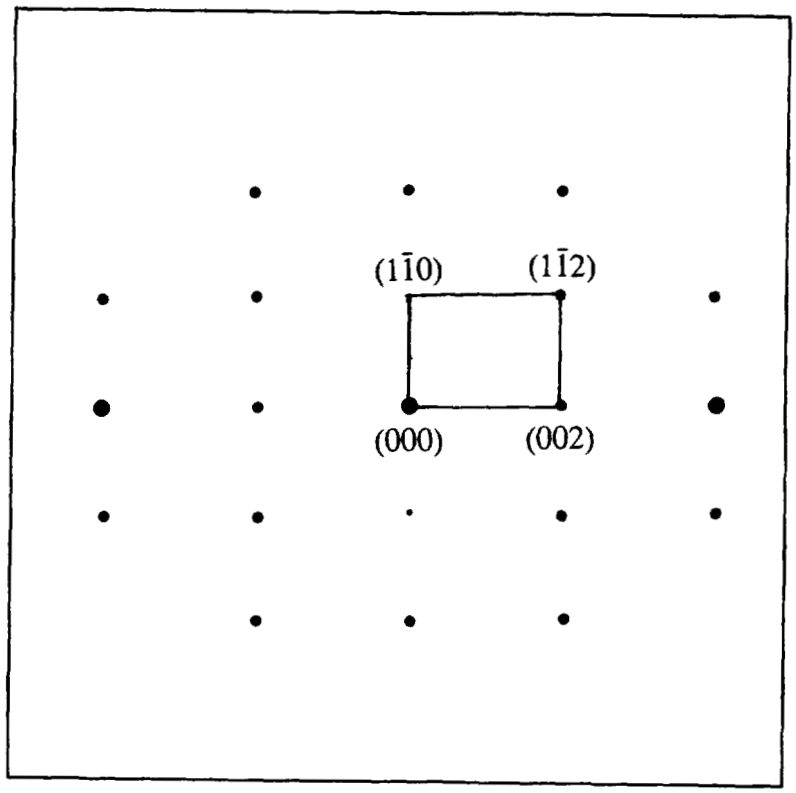

Matrix (γ) SADP Schematic
Crystal Type: fcc
a = 0.358 nm
Zone Axis = [110]

Twinning {111} <112>

Camera Constant = 1.97 Å-cm
(Reference Figure 58c)

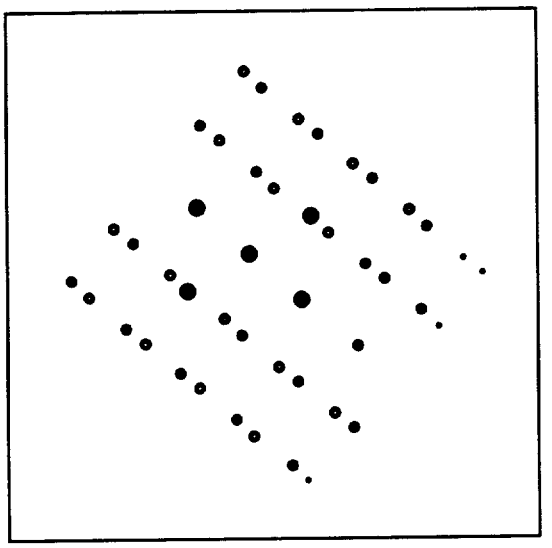

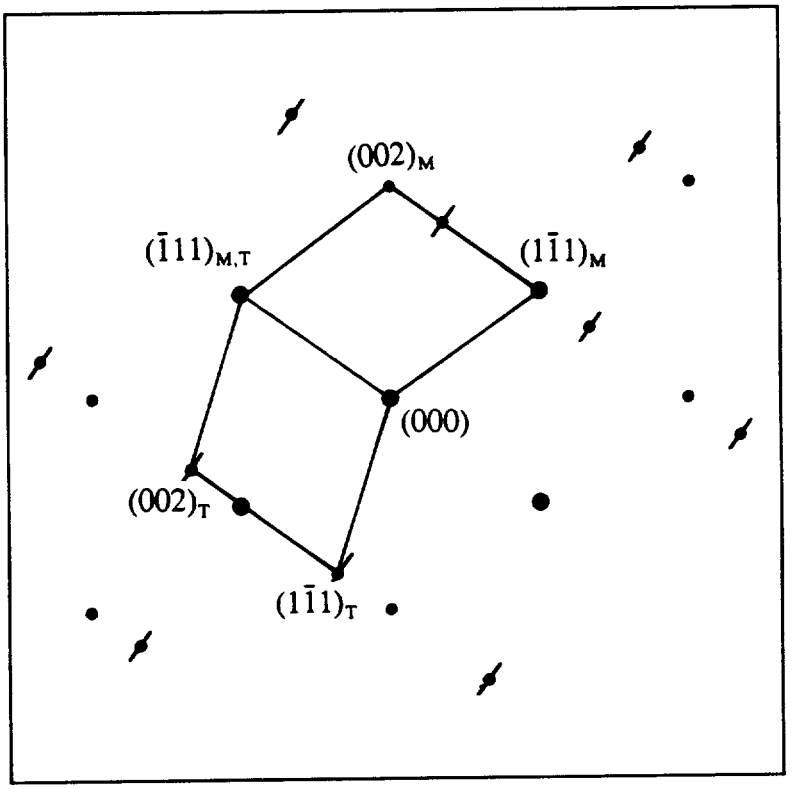

Cr_2N SADP Schematic
Crystal Type: hexagonal
Space Group = 162, P-31m
a = b = 0.481 nm
c = 0.448 nm
Zone Axis = $[14\bar{5}\bar{3}]$

Camera Constant = 1.97 Å-cm
(Reference Figure 59b)

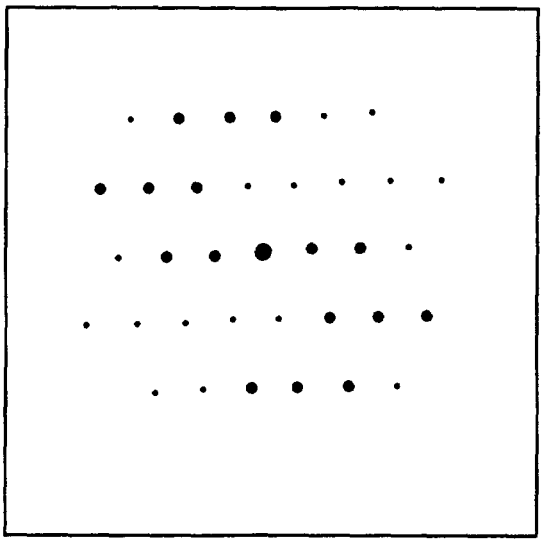

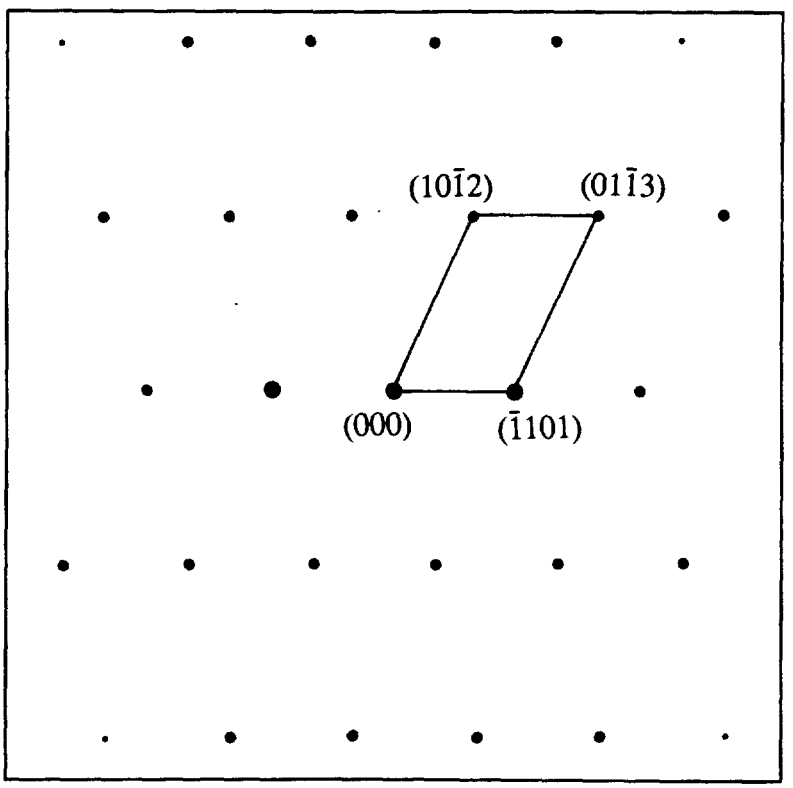

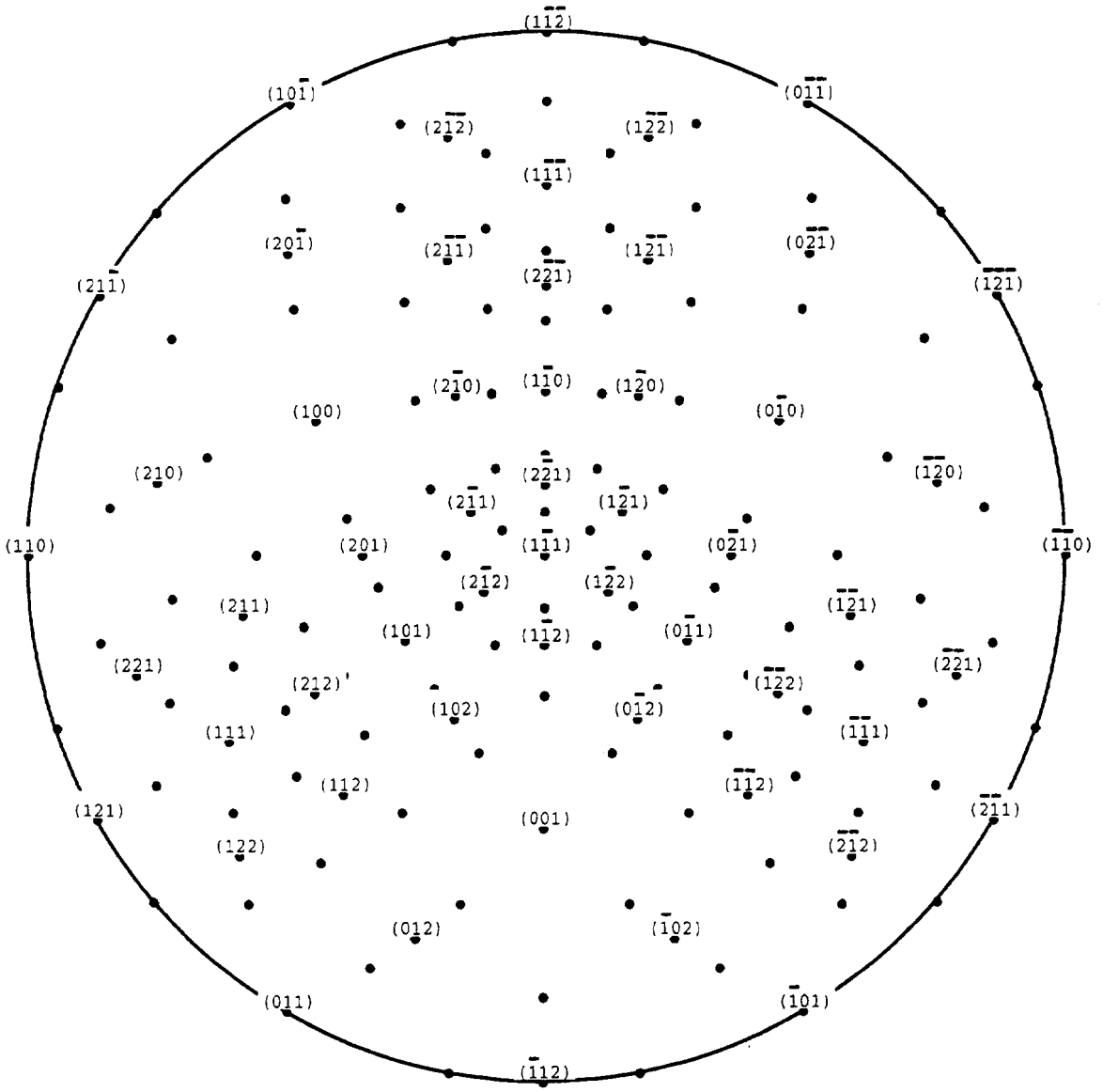

Stereographic Projection for Matrix (γ) Centered on (1$\bar{1}$1)

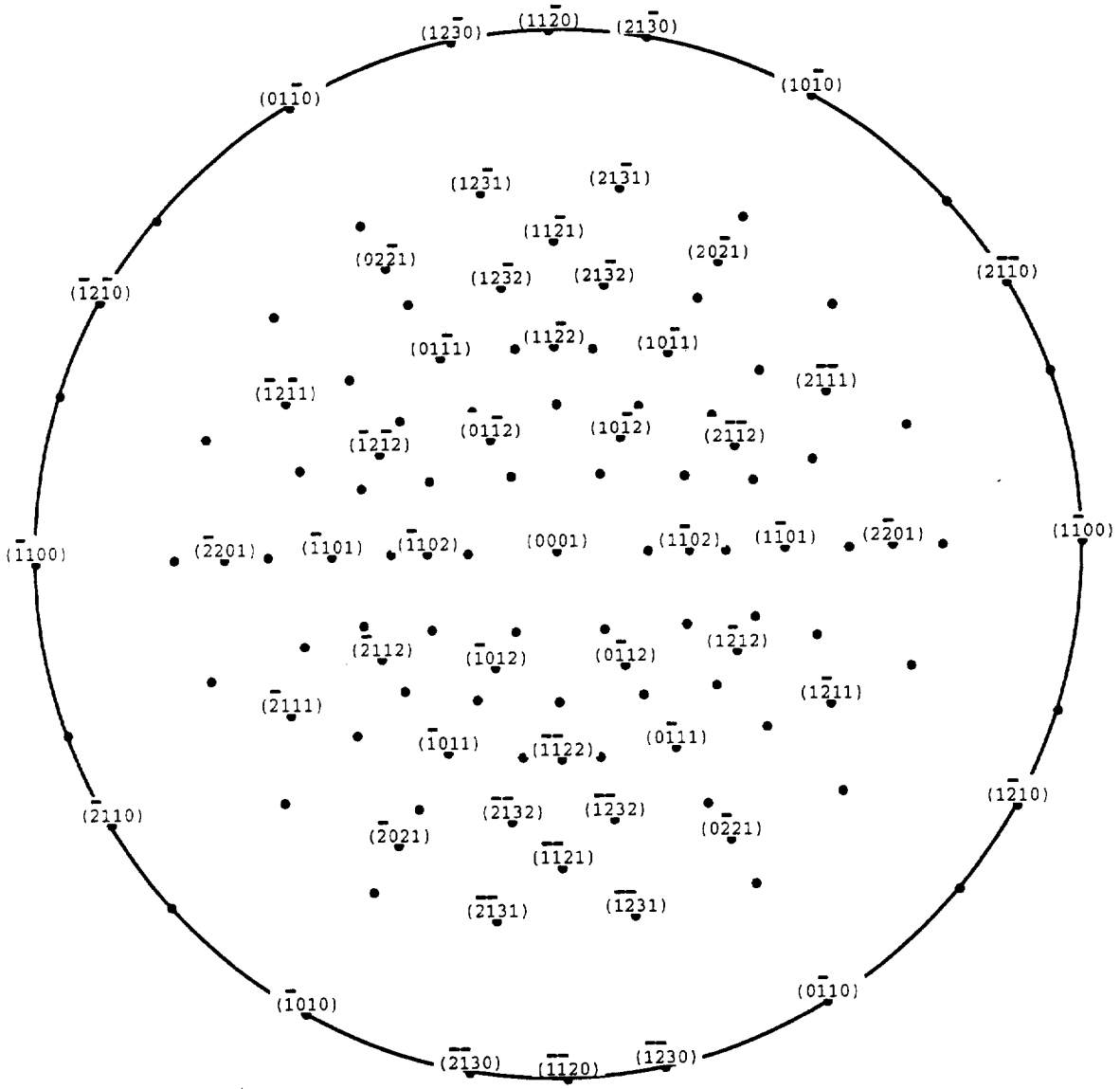

Stereographic Projection for Cr_2N Centered on (0001)

APPENDIX D

Legend

LEGEND

AEM	analytical electron microscopy
bcc	body-centered cubic
BF	bright-field
CDF	centered dark field
CVN	Charpy V-notch
DOS	degree of sensitization
EDS	energy dispersive spectroscopy
EPR	electrochemical potenitokinetic reactivation
fcc	face-centered cubic
GB	grain boundary
GBA	grain boundary area
GBCD	grain boundary chromium-depletion
hcp	hexagonal close-packed
HIP	hot-isostatic-pressure
IGC	intergranular corrosion
IGSCC	intergranular stress corrosion cracking
PESR	pressurized electroslag remelting
SADP	selected area diffraction pattern
SCC	stress corrosion cracking
SEM	scanning electron microscopy
SSs	stainless steel(s)
SF	stacking fault
SFE	stacking fault energy
SRO	short-range order
STEM	scanning transmission electron microscopy
TEM	transmission electron microscopy
TTP	time-temperature-precipitation
WDS	wavelength dispersive spectroscopy
XRD	X-ray diffraction
YSs	yield strength(s)

VITA

The author was born the youngest of five children to Joe and Zeta Simmons on November 5, 1960, in Salinas, California. His parents moved with their children to Santa Maria in 1961 where the author lived until his high school graduation in 1978. He attended California Polytechnic State University in San Luis Obispo where he received his Bachelor of Science degree in Metallurgical Engineering in 1982.

After graduation the author worked as a Materials Engineer with Lockheed Missiles and Space Co. Inc., in Sunnyvale, California from 1982 to 1988. While at Lockheed, he gained extensive experience in metallography and performed failure analysis on a variety of aerospace materials and components.

He returned to the "academic world" in 1988 and received a Master of Science degree from the Oregon Graduate Institute of Science & Technology in 1990 based on his thesis entitled "Effects of Prior Deformation on the Continuous Cooling Sensitization of Type 316 Austenitic Stainless Steel." The author stayed at OGI and became a cooperative employee with the U.S. Bureau of Mines Albany Research Center which sponsored his research towards his PhD. He has authored and co-authored several papers based on his graduate work in sensitization of stainless steels and high-nitrogen alloying. He is planning to continue doing research work at the U.S. Bureau of Mines Albany Research Center.